

**Geochemical and textural indicators of syn-eruptive degassing during  
recent rhyolitic eruptions**

Rebecca Paisley

Department of Earth & Planetary Sciences

McGill University

Montreal, Quebec, Canada

April 2019

A thesis submitted to McGill University in partial fulfilment of the requirements  
of the degree of Doctor of Philosophy

© Rebecca Paisley, 2019

## Abstract

Silicic volcanoes are capable of producing dangerous explosive eruptions and the effusion of lava and domes. Observations from recent rhyolitic eruptions demonstrated how the transition between these two end-member behaviours is markedly complex. Fractures, commonly preserved as tuffisite veins, are transient permeable pathways that allow for the punctuated but efficient escape of volatiles. They are considered key enablers of degassing but their interactions with deeper, gas-rich reservoirs and influence on melt chemistry are not fully understood. Preserved  $^{210}\text{Pb}$ - $^{226}\text{Ra}$  isotope disequilibria, volatile trace element heterogeneity, and complex vein and breccia textures in volcanic bombs have been previously associated with gas fluxing within the conduit. In this thesis I utilise both textural and chemical heterogeneity preserved in samples from the first observed rhyolite eruptions, Chaitén (2008) and Cerdón Caulle (2011-2012), to assess how degassing processes are preserved from the dm to nm scale.

$^{210}\text{Pb}$ - $^{226}\text{Ra}$  isotope and trace element analyses were conducted on 'mini-bulk' samples of tuffisite veins and their respective hosts to understand gas flow through fractures, from deeper reservoirs. The lack of  $^{210}\text{Pb}$ - $^{226}\text{Ra}$  disequilibria preserved in veins constrains the upper limit for the volume of magma that can be degassed by a tuffisite vein during its lifetime. Whilst trace element enrichments and depletions in veins record preferential gas fluxing (e.g. Li, Cu, Pb, Tl, Bi), results are limiting because tuffisites and breccias, which preserve the fracturing process, are comprised of clasts that have each undergone differing degrees of degassing. To further constrain gas fluxing and clasts' individual histories, electron microprobe and laser ablation ICP-MS analyses were undertaken across mm to  $\mu\text{m}$ -scale textures in samples from Cerdón Caulle. Chemical and textural heterogeneity are strongly linked, depletions of metals

(e.g. Zn, Pb, Tl) in veins highlight scavenging by the fluxing volatile phase. Trace element systematics constrain minute-hour fracture lifespans and show how these increase towards the surface and with eruption duration. Trace element analyses are analytically limited to the order of 10s of microns to yield accurate and precise results. But texturally fracturing processes can be investigated to the nm scale. The study of the interfaces between host and vein material show how veins exploit pre-existing bubble networks and can infill them with ash. Rheological weaknesses are exploited to allow cycles of fragmentation, degassing, sintering and healing of melts. Post-fracture melt compaction highlights how even small veins can degas vesicular magmas on the cm-scale.

By investigating fracture processes texturally and chemically at differing analytical scales, I constrain (1) the degree to which fractures and permeable gas reservoirs interact; (2) the timescales fractures outgas for; and (3) how heterogeneity is preserved as a function of depth in the conduit and eruption duration. Fractures exploit pre-existing permeable networks at depth, extracting volatiles on a cm-scale, but not enough magma is degassed to induce  $^{210}\text{Pb}$ - $^{226}\text{Ra}$  isotope disequilibria in tuffsite veins. The channelling of volatiles from reservoirs through fractures in the conduit plug results in metal exchange with transported shards and localised volatile exchange at fracture-host interfaces (constraining fracture lifespans). Outgassing at the near-surface, later in the eruption, occurs for longer resulting in a greater degree of metal and textural heterogeneity. In conclusion, I show fractures play a fundamental spatial and temporal role in degassing of silicic magmas and can directly impact the changing explosive-effusive behaviour observed during eruptions.

## Résumé

Les volcans siliciques sont capables de produire des éruptions explosives dangereuses, où de mener à l'épanchement de lave et la formation de dômes. Les observations d'éruptions rhyolitiques récentes ont montré à quel point la transition entre ces deux comportements extrêmes est complexe. Les fractures, généralement préservées sous forme de veines tuffisitiques, sont des voies perméables transitoires qui permettent l'échappement ponctuel mais efficace des éléments volatiles. Elles sont considérées comme des catalyseurs essentiels du dégazage, mais leurs interactions avec des réservoirs plus profonds et riches en gaz et leur influence sur la chimie des masses fondues ne sont pas entièrement comprises. L'enregistrement du déséquilibre isotopique  $^{210}\text{Pb}$ - $^{226}\text{Ra}$ , l'hétérogénéité des éléments-traces volatils et les textures complexes des veines et des brèches dans les bombes volcaniques ont déjà été associés à des flux de gaz dans le conduit. Dans cette thèse, j'utilise l'hétérogénéité texturale et chimique préservée dans des échantillons des premières éruptions observées de rhyolite, Chaitén (2008) et Cordón Caulle (2011-2012), pour évaluer la façon dont les processus de dégazage sont préservés de l'échelle décimétrique à nanométrique.

Des analyses d'isotopes  $^{210}\text{Pb}$ - $^{226}\text{Ra}$  et d'éléments-traces ont été effectuées sur des échantillons représentatifs de veines tuffisitiques et de leurs encaissants respectifs afin de comprendre le flux de gaz à travers les fractures à partir de réservoirs plus profonds. L'absence de déséquilibre isotopique  $^{210}\text{Pb}$ - $^{226}\text{Ra}$  enregistré dans les veines contraint la limite supérieure du volume de magma qui peut être dégazé par une veine tuffisite pendant sa durée de vie. Bien que les enrichissements ou appauvrissements en éléments-traces dans les veines indiquent un flux gazeux préférentiel (par exemple, Li, Cu, Pb, Tl, Bi), les résultats sont mitigés, car les tuffisites



et les brèches, qui préservent le processus de fracturation, sont constituées de fragments ayant subi différents degrés de dégazage. Pour contraindre davantage le flux de gaz et les histoires individuelles des clastes, des analyses par microsonde électronique et par ICP-MS à ablation laser ont été effectuées sur des textures allant d'échelle millimétrique à micrométrique sur des échantillons du Cordón Caulle. Les hétérogénéités chimiques et texturales sont fortement liées, et des appauvrissements en métaux (par exemple, Zn, Pb, Tl) dans les veines mettent en évidence la récupération par le passage de la phase volatile. La systématique des éléments-traces contraint les durées de vie des fractures avec une précision allant de la minute à l'heure et montre comment la durée de vie augmente vers l'avant lorsque l'on se rapproche de la surface et augmente avec la durée de l'éruption. Les analyses d'éléments-traces sont limitées analytiquement à des tailles de l'ordre de 10 microns pour donner des résultats exacts et précis, mais les processus de fracturation texturale peuvent être étudiés à l'échelle nanométrique. L'étude des interfaces entre la roche encaissante et le matériau de la veine montre comment les veines exploitent les réseaux de bulles préexistants et peuvent les remplir de cendres. Les faiblesses rhéologiques sont exploitées pour permettre des cycles de fragmentation, de dégazage, de frittage et de cicatrisation des masses fondues. La compaction post-fracture du magma souligne le fait que même de petites veines peuvent dégazer des magmas vésiculaires à l'échelle centimétrique.

En examinant les processus de fracture selon leur chimie et textures, à échelles analytiques différentes, je contraindre (1) le degré d'interaction des fractures et des réservoirs de gaz perméables; (2) les échelles de temps selon lesquelles les fractures dégazent ; et (3) la façon dont l'hétérogénéité est préservée en fonction de la profondeur dans le conduit et de la durée de l'éruption. Les fractures exploitent les réseaux perméables préexistants en profondeur, en extrayant les éléments volatils à l'échelle centimétrique, mais une quantité insuffisante de

magma est dégazée pour induire des déséquilibres isotopiques de  $^{210}\text{Pb}$ - $^{226}\text{Ra}$  dans les veines tuffisitiques. La canalisation des éléments volatils des réservoirs à travers les fractures du bouchon conduit à un échange de métaux avec les éclats transportés et à un échange volatil localisé aux interfaces fracture-roche encaissante (contraignant la durée de vie des fractures). Le dégazage près de la surface, plus tard au cours de l'éruption, dure plus longtemps, ce qui entraîne un degré plus élevé d'hétérogénéité des métaux et textures. En conclusion, je montre que les fractures jouent un rôle spatial et temporel fondamental dans le dégazage des magmas siliciques et peuvent influencer directement le changement de comportement explosif-effusif observé lors des éruptions.

## **Contribution of Authors**

This manuscript-based thesis is composed of three central chapters. Chapter One was submitted to the Journal of Volcanology and Geothermal Research (JVGR) in October 2018. I am the main author on this chapter along with three co-authors: my supervisor Kim Berlo, Bassam Ghaleb (GEOTOP, Canada) and Hugh Tuffen (Lancaster University, UK). BG and I both carried out isotope method development and analyses on samples. Chapter Two is in preparation for the open access journal Volcanica. I am the lead author on this chapter with several co-authors: Kim Berlo, Hugh Tuffen, Jack Whattam and C. Ian Schipper (both from Victoria University of Wellington, New Zealand). JW and I collected electron microprobe data for this study with support and guidance from CIS. Chapter Three is in preparation for submission to Contributions to Mineralogy and Petrology. I am the central author along with co-authors Kim Berlo, Hugh Tuffen, Jacqueline Owen (Lancaster University, UK) and Stephan Kolzenburg (McGill University).

The initial basis of the project was devised by KB. I developed the ideas for each chapter with KB (Chapters One and Two) and HT (Chapter Three). I carried out the bulk of sampling during fieldwork although additional samples were provided by KB, HT and CIS for analytical work in Chapters One and Two. I performed all the chemical analyses, data processing and numerical modelling. All figures, tables and supplementary material are of my design. All three chapters were written by me with feedback for each chapter provided by the respective co-authors.

## Acknowledgements

I wish to thank my supervisor Kim Berlo and co-supervisors Hugh Tuffen and Bassam Ghaleb. Thank you for keeping me curious, I would not be the scientist I am today without you all. Further thanks to Ian Schipper, Jacqui Owen, Nathan Magnall and Jack Whattam for our discussions about Cordón Caulle, rhyolites and much more. I would like to extend my thanks to John Stix, Boswell Wing and Stephan Kolzenburg for all contributing to my advisory committee and asking the hard and left-field questions. My time in the field would not have been nearly as fulfilling or fruitful without Alex Corgne, Nicolas Vergara Pontigo and Felipe Ignacio P. Gallardo. Getting to see Cordón Caulle system in its entirety was a once in a lifetime opportunity that would not have been possible without you.

Many people around the globe have supported me with my analytical work. Thank you to Anna Jung, Vincent van Hinsberg, Isabelle Richer, Brigitte Dionne and Lang Shi at McGill; André Poirier at UQAM; and Bruce Charlier, Luisa Ashworth, and Elliot Swallow at Victoria University of Wellington. You have all been so patient with me and answered my many questions. Thank you to Anne Kosowski, Angela Di Ninno, Kristy Thronton and Brandon Bray for letting me pester you repeatedly. My PhD would not have run as smoothly without you.

Financial support from NSERC, McGill University, UQAM, Victoria University of Wellington, Geological Society of America, Society of Economic Geologists and Mineralogical Association of Canada was fundamental to the success of this PhD. I would not have had half the opportunities I've experienced in the last 4 years without it.

I have been lucky to meet some excellent humans and life-long friends during my time in Montreal. Special shout out to the past and present members of the 131A family and the 'magma chamber' crew. To Rowan, Shane, Lauren and Sam your friendship is something I will cherish and your support in the last few months has been vital to getting me over the finish line.

Finally to my family, words cannot convey how grateful I am. You are the reason I'm still here. Mum thank you for always being on the end of the phone and being the greatest role model I could ask for. Your strength of character is something no-one can match. Charlotte your support has been unwavering and so important to me. I couldn't have asked for a greater sister. Dad, Michael I know you two would have loved this crazy adventure, I dedicate this to you.

## Table of Contents

<b><u>Abstract</u></b>	<b><u>I</u></b>
<b><u>Résumé</u></b>	<b><u>III</u></b>
<b><u>Contribution of Authors</u></b>	<b><u>VI</u></b>
<b><u>Acknowledgements</u></b>	<b><u>VII</u></b>
<b><u>Table of Contents</u></b>	<b><u>IX</u></b>
<b><u>Summary of Figures</u></b>	<b><u>XIII</u></b>
<b><u>Summary of Tables</u></b>	<b><u>XVI</u></b>
<b><u>Summary of Appendices</u></b>	<b><u>XVIII</u></b>
<b><u>General Introduction</u></b>	<b><u>1</u></b>
<b>1. Introduction</b>	<b>1</b>
<b>2. Thesis Rationale</b>	<b>3</b>
<b><u>Link to Chapter One</u></b>	<b><u>7</u></b>
<b><u>Chapter One</u></b>	<b><u>8</u></b>
<b><u>Abstract</u></b>	<b><u>9</u></b>
<b>1. Introduction</b>	<b>10</b>
1.1 Tuffisite Veins	11
1.2 Volatiles, trace species and Ra-Rn-Pb systematics during degassing	13
1.3 Two Case Studies: Chilean Rhyolites	14
<b>2. Methods</b>	<b>15</b>
<b>3. Results</b>	<b>17</b>
3.1 Sample Petrology	17

3.2	$^{210}\text{Pb}$ - $^{226}\text{Ra}$ Isotopes	19
3.3	Trace Elements	20
<b>4.</b>	<b>Discussion</b>	<b>22</b>
4.1	Degassing-induced chemical heterogeneity	23
4.2	Why are no $^{210}\text{Pb}$ excesses preserved in veins?	30
4.3	Other processes inducing tuffisite vein trace element heterogeneity	36
4.4	Isotopic outliers: Samples not in secular equilibrium	40
4.5	Why is degassing preserved differently at Chaitén and Cordón Caulle?	41
<b>5.</b>	<b>Conclusions</b>	<b>44</b>
<b>6.</b>	<b>Acknowledgements</b>	<b>45</b>
<b>7.</b>	<b>References</b>	<b>46</b>
<b>8.</b>	<b>Tables and Figures</b>	<b>55</b>
<b>9.</b>	<b>Supplementary Figure</b>	<b>64</b>
<b>10.</b>	<b>Appendices</b>	<b>65</b>
	Appendix A: Trace Element Data and 2SD Errors	65
	Appendix B: Details of Equations in Section 4.2	74
	Appendix C: Model Sensitivity	80
	<b><u>Link to Chapter Two</u></b>	<b>83</b>
	<b><u>Chapter Two</u></b>	<b>84</b>
	<b>Abstract</b>	<b>85</b>
<b>1.</b>	<b>Introduction</b>	<b>86</b>
<b>2.</b>	<b>Case Study: The Puyehue-Cordón Caulle Volcanic Complex</b>	<b>87</b>
2.1	Eruption Background	87
2.2	Petrology Background	89
<b>3.</b>	<b>Methods</b>	<b>90</b>
3.1	Sampling Methods	90

3.2	Analytical Methods	91
<b>4.</b>	<b>Results: Textural and Chemical Observations</b>	<b>94</b>
4.1	Domain Petrology	94
4.2.	Chemical Analyses	98
<b>5.</b>	<b>Discussion</b>	<b>103</b>
5.1	Degassing: from eruption onset to decline	103
5.2	Degassing: from depth to the surface	105
5.3	Timescales of Degassing Events	118
5.4	Summary: Fracturing Processes at Cordón Caulle	122
<b>6.</b>	<b>Conclusions</b>	<b>124</b>
<b>7.</b>	<b>Acknowledgements</b>	<b>125</b>
<b>8.</b>	<b>References</b>	<b>126</b>
<b>9.</b>	<b>Tables and Figures</b>	<b>138</b>
<b>10.</b>	<b>Supplementary Figures</b>	<b>155</b>
<b>11.</b>	<b>Appendices</b>	<b>161</b>
	Appendix A: Data Table for Major and Trace Elements	161
	Appendix B: Data Table for Trace Element Diffusion Profiles	172
	<b><u>Link to Chapter Three</u></b>	<b>180</b>
	<b><u>Chapter Three</u></b>	<b>181</b>
	<b>Abstract</b>	<b>182</b>
<b>1.</b>	<b>Introduction</b>	<b>183</b>
1.1	The 2011-2012 Cordón Caulle Eruption	185
<b>2.</b>	<b>Sample Studied</b>	<b>186</b>
<b>3.</b>	<b>Methodology</b>	<b>186</b>
<b>4.</b>	<b>Results &amp; Petrology</b>	<b>187</b>
4.1	Host Material	188



4.2	Vein One (V1)	189
4.3	Vein Two (V2)	190
4.4	Host-V1 Interface	191
4.5	V2-Host Interface	191
4.6	Failed Fractures and Injection veins	192
4.7	Element Maps	193
<b>5.</b>	<b>Discussion</b>	<b>193</b>
5.1	Discerning between syn-eruptive and post-eruptive textural features	194
5.2	Pre-existing porous network	195
5.3	Fracturing of vesicular melts, tuffisite sources, and timescale estimates	198
5.4	Evidence for gas fluxing	203
<b>6.</b>	<b>Conclusions</b>	<b>205</b>
<b>7.</b>	<b>Acknowledgements</b>	<b>206</b>
<b>8.</b>	<b>References</b>	<b>208</b>
<b>9.</b>	<b>Figures</b>	<b>216</b>
<b>10.</b>	<b>Supplementary Figures</b>	<b>232</b>
<b><u>General Conclusions</u></b>		<b><u>236</u></b>
<b>1.</b>	<b>Major Findings</b>	<b>236</b>
<b>2.</b>	<b>Contributions to Original Knowledge</b>	<b>239</b>
<b>3.</b>	<b>Topics for Further Research</b>	<b>241</b>
<b><u>References</u></b>		<b><u>242</u></b>

## Summary of Figures

### Chapter One

Figure 1: Summary of key textural features of samples from Cordón Caulle and Chaitén.	55
Figure 2: $(^{210}\text{Pb}/^{226}\text{Ra})_0$ versus $(^{210}\text{Pb})_0$ and $(^{226}\text{Ra})_0$ .	59
Figure 3: Elemental concentrations from Bomb A sub-samples normalised to Bomb A Host composition (Chaitén Volcano).	60
Figure 4: Element concentrations from select tuffisite veins from Cordón Caulle normalised to host composition.	61
Figure 5: Schematic vein model summarising interaction between vein and degassing cell.	62
Figure 6: Contoured plot showing required R values to generate certain $(^{210}\text{Pb}/^{226}\text{Ra})_0$ for a known fracture lifespan.	63
Figure S.1: Elemental concentrations from Bomb A sub-samples and modeled compositions normalised to Bomb A Host composition (Chaitén Volcano).	64
Figure C.1: R value vs Timespan of fracturing event with varying $\tau$ values.	81
Figure C.2: R value vs Timespan of fracturing event with varying f values.	82

### Chapter Two

Figure 1: Schematic timeline of eruption and overview map with sampling localities.	138
Figure 2: Schematic overview of the conduit and the relative depths of degassing that are preserved by different domains.	140
Figure 3: Comparison of median Tl, In and Bi concentrations of <i>bomb</i> , <i>flow</i> and <i>vent</i> samples from the 2011-2012 eruption.	141

Figure 4: Violin plot highlighting median Cl concentrations and distributions for each textural domain. _____	142
Figure 5: Domain-host ratios for select elements. _____	143
Figure 6: Trace element profiles across an oxidised breccia matrix between two clasts from a <i>vent</i> sample. _____	145
Figure 7: Pb and Tl elemental gradients away from a fracture surface in a nozzle. _____	149
Figure 8: Elemental variations in oxidised, near-surface samples. _____	150
Figure 9: Li and Na elemental variation in a banded obsidian clast away from the matrix-clast interface in a non-oxidised pumice breccia. _____	151
Figure 10: Li and Rb elemental variation across juxtaposing bands in a banded obsidian bomb. _____	152
Figure 11: Summary figure highlighting chemical interpretations of the degassing processes throughout the eruption. _____	153
Figure S.1: Element-element plots (majors and traces) highlighting minor positive correlations between certain elements. _____	155
Figure S.2: Profile of TiO <sub>2</sub> and Cl concentrations obtained via EMP across a banded obsidian domain. _____	156
Figure S.3: Comparison of elements away from a fracture surface in a nozzle. _____	157
Figure S.4: Comparison of elements away from a matrix-clast interface in a dense clast. _____	158
Figure S.5: Comparison of elements in a banded obsidian clast away from the matrix-clast interface in a non-oxidised pumice breccia. _____	159
Figure S.6: Comparison of elements across juxtaposing bands in a banded obsidian bomb. _____	160

## Chapter Three

Figure 1: Overview of tuffisite-hosting volcanic bomb.	216
Figure 2: Images of typical textures in host.	217
Figure 3: Images of typical textures in V1.	219
Figure 4: Images of typical textures in V2.	221
Figure 5: Textures found at V1-host interface.	223
Figure 6: Textures found at V2-host interface.	225
Figure 7: Examples of injection veins and fracturing into host material.	226
Figure 8: Annotated compositional maps and BSE image of partially-healed vein.	228
Figure 9: Calculated timescales of rounding/sintering of particles as a function particle radius and H <sub>2</sub> O concentrations of the melt.	229
Figure 10: Schematic summary of the four key stages of fracturing and degassing.	230
Figure S.1: BSE image and compositional map of sintered ash intruding into bubbles within host.	232
Figure S.2: BSE image and compositional map of sintered ash intruding into bubbles within tuffisite vein.	234

## Summary of Tables

### Chapter One

Table 1: Activities and activity ratios (back calculated to time of eruptions) of samples and sub-samples analysed.	58
Table A.1: Elemental concentrations (ppm) of samples from Chaitén and Cordón Caulle analysed via ICP-MS.	66
Table A.2: Associated errors (2 SD) of elemental concentrations of samples from Chaitén and Cordón Caulle analysed via ICP-MS.	70
Table C.1: Summary of R value required for 1.6 hour and 7.5 hour events given a known f and f' value and varying $\tau$ .	81

### Chapter Two

Table 1: Summary of elements that have domain-host ratios outside of unity.	144
Table 2: Summary of diffusion coefficients ( $D$ , $\text{m}^2/\text{s}^{-1}$ ) calculated at an eruptive temperature of 895 °C (Castro et al., 2013) and their references.	147
Table 3: Summary of the length scales of element variability preserved at certain domain interfaces and the calculated timescales of the related degassing processes.	148
Table A.1: Data table of sample descriptions and calculated averages for major and trace elements.	162
Table A.2: Data table of sample errors (1 Standard Deviation).	165

Table A.3: Data table of sample % Relative Standard Deviations. _____	168
Table A.4: Calculated averages of secondary standards used for EPMA. _____	171
Table B.1: Figure 7 Profile Concentrations (ppm). _____	173
Table B.2: Figure 7 Profile Internal Standard Errors (2SE) in ppm. _____	174
Table B.3: Figure 8 Profile Concentrations (ppm). _____	175
Table B.4: Figure 8 Profile Internal Standard Errors (2SE) in ppm. _____	176
Table B.5: Figure 9 Profile Concentrations (ppm). _____	177
Table B.6: Figure 9 Profile Errors Internal Standard Errors (2SE) in ppm. _____	177
Table B.7: Figure 10 Profile Concentrations (ppm). _____	178
Table B.8: Figure 10 Profile Internal Standard Errors (2SE) in ppm. _____	179

## Summary of Appendices

### Chapter One

Appendix A: Trace Element Data and 2SD Errors	65
Appendix B: Details of Equations in Section 4.2	74
Appendix C: Model Sensitivity	80

### Chapter Two

Appendix A: Data Table for Major and Trace Elements.	161
Appendix B: Data Table for Trace Element Diffusion Profiles.	172

# General Introduction

## 1. Introduction

Volcanic eruptions can produce far-reaching hazards that impact both local and global populations (Brown et al., 2017). The first step to mitigating the socio-economic impacts of eruptions is to understand the sub-surface processes that contribute and control eruptive behaviour (Cassidy et al., 2018). Rhyolitic eruptions can produce explosive and voluminous eruption columns, as well as sizeable domes or obsidian flows (Eichelberger, 1995). However, eruptions at silicic centres are infrequent and consequently our understanding of their eruptive dynamics is lacking when compared to more common basaltic eruptions, despite their arguably more hazardous potential. Therefore, there is a need to explore the syn-eruptive processes that control silicic volcanism.

Volatiles are species (e.g.  $\text{H}_2\text{O}$ ,  $\text{CO}_2$ ) and trace elements (e.g. Po, Rn) that have an affinity for a gas phase. As magma ascends from depth the solubility of volatile species decreases, when supersaturation is reached the exsolution of a volatile phase occurs and bubble nucleation and growth commences (Papale et al., 2006; Zhang et al., 2007; Cashman and Sparks, 2013). Volatiles are known drivers of eruptions. Their ability to degas from melts (i.e. be lost to the gas phase) and segregate from ascending magmas determines whether eruptive behaviour is explosive or effusive (Edmonds, 2008). The high viscosities of silicic magmas precludes the movement of individual bubbles (Sparks, 1978), therefore volatile segregation and outgassing (i.e. loss of volatiles to the surface) occurs via the development of permeable networks of bubbles (e.g. magmatic foams) or fractures (e.g. tuffisite veins) (Eichelberger et al., 1986;



Gonnermann and Manga, 2003). Two 21<sup>st</sup> century eruptions at Chaitén and Cordon Caulle in Chile demonstrated that high-silica systems can undergo simultaneous explosive and effusive behaviour (Pallister et al., 2013; Schipper et al., 2013). These new observations emphasised the need to understand processes that facilitate the transition between these end-member behaviours, and highlighted the role of fracturing as an outgassing mechanism. This is the process I focus on and explore in this thesis.

Fractures, commonly preserved as tuffisite veins, have been hypothesised as pathways for gases since the late 1980s (e.g. Heiken et al., 1988). The channelling of gases through fractures can account for the observed punctuated explosions, but also the progressive depletion of volatiles and formation of effusive products (Schipper et al., 2013). Studies have focused on the textures, chemistry and physical properties of tuffisite veins to constrain their roles from initial fracturing through to healing. Fractures form via shearing or hydrofracturing of the ascending melt (Heiken et al., 1988; Tuffen et al., 2003). Tuffisite textures in volcanic bombs and conduits point to the repeating nature of magma fracturing, and the fluidised flow of gas and ash through these transient networks that span 10-100s of metres (Stasiuk et al., 1996; Tuffen and Dingwell, 2005; Saubin et al., 2016). They are shown to be highly permeable when open but can also completely anneal due to the sintering of transported ash and their later compaction (Kolzenburg et al., 2012; Farquharson et al., 2016; Kendrick et al., 2016). Chemical studies suggest their primary role must be pathways for gases because diffusive degassing at their margins is not efficient enough given their short lifespans (Castro et al., 2012; Berlo et al., 2013).

Although H<sub>2</sub>O, CO<sub>2</sub> and halogens are the major components of an exsolved volatile phase, it is also comprised of lower concentration trace elements, including alkalis (e.g. Li, Rb, Cs), metals (e.g. Cu, Tl, Pb, Bi) and metalloids (e.g. As, Sb) that complex with ligands (Hinkley et al., 1994; Williams-Jones et al., 2002). Providing there is a volatile phase present, these lower concentration elements can degas by diffusing through a silicate melt towards a gas-melt interface before partitioning into the volatile phase (e.g. MacKenzie and Canil, 2008). From their deposition in the sub-surface as ore-deposits, to their preservation in aerosol layers in ice cores, trace volatile elements have long been used to study volcanic fluids, vapours, and emissions during hydrothermal and magmatic events (Wei et al., 2008; Mather et al., 2012; Pokrovski et al., 2013; Henley and Berger, 2013; van Hinsberg et al., 2015). Despite this, only two studies have focused on the trace element chemistry of tuffisite veins. Elemental variations recorded in tuffisites at Chaitén (Chile), Torfajökull (Iceland) and Soufrière Hills Volcano (Montserrat) preserve preferential gas fluxing through these features, and point towards the interaction of veins with deeper magmas and gases (Berlo et al., 2013; Plail et al., 2014). These studies contribute to our understanding of fractures as outgassing pathways for volatiles to escape from gas-rich reservoirs at depth. They further show the wealth of information that can be obtained by analyses of trace elements, which cannot be acquired by alternative types of studies, and I build on these studies to further our understanding of fracturing processes.

## **2. Thesis Rationale**

This thesis is divided into three chapters each investigating the fracturing and degassing of silicic melts by utilising chemical and textural heterogeneity from the dm to nm scale. This was undertaken with the aim of better understanding (1) how fractures interact and channel gases

from gas-rich reservoirs; (2) how long fractures can be open for; and (3) how the preserved heterogeneity is a function of depth in the conduit and eruption duration. Conducting studies at three differing scales of spatial resolution, using several analytical techniques, allows for a more complete and comprehensive study of the fracturing process than using a single approach.

### ***Chemically constraining gas flow through tuffisites***

In Chapter One I conduct a dm-cm scale trace element and  $^{210}\text{Pb}$ - $^{226}\text{Ra}$  isotope study to constrain the degree of interaction between tuffisite veins and volatile-rich melts. Trace element heterogeneity can record preferential gas fluxing through fractures (Berlo et al., 2013) whilst  $^{210}\text{Pb}$ - $^{226}\text{Ra}$  isotope disequilibria preserved in erupted products have been successfully used to constrain the redistribution of gases within conduits (e.g. Gauthier and Condomines, 1999; Berlo and Turner, 2010; Condomines et al., 2010). However, isotope disequilibria have not been used before to study gas flow through tuffisite veins, nor have bulk trace element analyses been conducted of these features. It is important to constrain the degree of interaction veins have with their gas-rich sources and how much gas can be removed, as they are considered to be gas pathways spanning hundreds of metres within the conduit (e.g. ~150 m calculated via differences in  $\text{H}_2\text{O}$  concentrations between host glasses and clastic vein material, Castro et al., 2012; Saubin et al., 2016). Analyses were conducted on samples from both Chaitén and Cordón Caulle volcanoes. I was able to model estimates for the upper limits on the amount of magma that can be degassed by a vein during its lifespan, and explored the chemical heterogeneity induced by degassing at Cordón Caulle.

### ***The use of trace volatiles as degassing indicators when $\text{H}_2\text{O}$ has been lost***

In Chapter Two I use an in situ approach and conduct a cm- $\mu$ m scale trace element study of a complex suite of rocks from Cordón Caulle to better understand the causes of chemical heterogeneity preserved in veins. I further show how trace elements can be used to study degassing in systems where other volatiles (e.g. H<sub>2</sub>O and CO<sub>2</sub>) are extensively degassed. Water variations surrounding fractures and tuffisite veins have been used to constrain their lifespans (Berlo et al., 2013; Castro et al., 2014; Saubin et al., 2016). However, the erupted products from Cordón Caulle are water-poor (<0.35 wt. %) and studies so far have not been able to precisely define its degassing history or the role of fractures (Schipper et al., 2013; Castro et al., 2014). Volatile trace elements diffuse through melts but at a slower rate than H<sub>2</sub>O and thus can be used to estimate timescales of diffusion-inducing processes such as degassing (MacKenzie and Canil, 2008; Zhang et al., 2010; Zhang and Ni, 2010; Berlo et al., 2013; Gardner et al., 2012). I utilise systematic trace element heterogeneity to address degassing at Cordón Caulle and better constrain how degassing varies with time during an eruption and with depth from the surface. By studying the chemistry and textures of individual veins at the cm- $\mu$ m scale I was able to constrain minute-to-day fracture lifespans, the scavenging of metals by the fluxing gases; and how progressive degassing reduces the concentrations of trace volatile elements in later erupted products.

### ***Understanding the physical interaction of fracture and porous networks***

For tuffisites to be efficient mechanisms for degassing, they must be capable of outgassing volatiles from depth, and there is a need to understand how fractures physically interact with porous networks (connected bubbles and pore spaces) to allow this to occur. In Chapter Three I undertake a  $\mu$ m-nm scale textural study to address this and understand how fractures propagate through and interact with porous networks, shedding light on their potential volatile

and ash matrix sources. I show how fractures exploit pre-existing porous networks when propagating and how this interaction results in efficient degassing far beyond the scale recorded in dense melts. I also address how melt fracturing is a key process in the formation of the source material for tuffisite matrices.

The general conclusions section summarises the key findings of each of the central chapters, tying together the study of degassing processes with different chemical and petrographic techniques. By studying processes at a variety of different analytical scales I further the understanding of complex sub-surface, syn-eruptive processes that result in the explosive and effusive behaviour observed during eruptions.

## **Link to Chapter One**

In the general introduction I highlight that there have been few studies on the chemical impacts of degassing through fracture networks preserved as tuffisite veins. Only two studies have focused on trace element signatures and only one study has focused on deposits from Cordon Caulle. Whilst there is a common consensus that fractures act as pathways for gases (e.g. Castro et al., 2012; Berlo et al., 2013; Castro et al., 2014; Cabrera et al., 2015; Saubin et al., 2016), there is a need to understand how much melt a fracture is capable of outgassing during its lifespan. As discussed in the introduction, isotopes have been used to understand the redistribution of gases within a conduit as a result of gas fluxing at many volcanic centres (e.g. Berlo et al., 2006; Gauthier and Condomines, 1999; Cunningham et al., 2009; Berlo and Turner, 2010; Condomines et al., 2010). However, this technique has not been previously applied to tuffisites or to rhyolitic eruptions.

In this chapter, I aim to address these outstanding problems via a bulk-rock (dm-cm scale) isotope and trace element study on tuffisite veins from Cordon Caulle and Chaitén in Chile, the world's most recent rhyolitic eruptions. I show that fluxing durations are not sufficient in length to create isotopic disequilibria in veins but trace elements do preserve degassing. Trace element signatures related to degassing and other physical processes are recorded at both volcanoes, highlighting the need to analyse a wide range of elements with differing properties during a single study. Finally, I develop an isotope-based model that can be used to provide constraints on the mass of melt degassed by a vein during its lifetime which can be further applied to other systems.

## Chapter One

### **Geochemical constraints on the role of tuffisite veins in degassing at the 2008-09 Chaitén and 2011-12 Cordón Caulle rhyolite eruptions**

R. Paisley,<sup>1</sup> K. Berlo<sup>1,2</sup>, B. Ghaleb<sup>2</sup>, H. Tuffen<sup>3</sup>

<sup>1</sup>Department of Earth & Planetary Sciences, McGill University, 3450 Rue University, Montreal, Quebec, Canada, H3A 0E8

<sup>2</sup>Geotop, Université du Québec à Montréal, Montréal, Canada

<sup>3</sup>Lancaster Environment Centre, Lancaster University, Lancaster, UK

*Submitted to the Journal of Volcanology and Geothermal Research*

#### **Highlights:**

- Multi-stage degassing signatures preserved in Chaitén's tuffisite veins
- The erupted products at both volcanoes preserve minimal  $^{210}\text{Pb}$ - $^{226}\text{Ra}$  disequilibria
- Geochemical preservation of gas fluxing through tuffisite veins at Cordón Caulle
- Evidence of preferential transport of glass over crystals in tuffisite veins

## Abstract

Hybrid activity during the rhyolitic eruptions of Chaitén (2008-09) and Cordon Caulle (2011-2012) in Chile has offered unprecedented insights into the enigmatic and complex degassing processes occurring during eruptions of silicic magma. Highly permeable, transient fracture networks within the conduit can act as outgassing channels. Their interaction with deeper volatile-rich melt can account for both punctuated explosive activity and large-scale degassing of the system, leading towards predominantly effusive behaviour. In this study we characterise trace element concentrations and  $^{210}\text{Pb}$ - $^{226}\text{Ra}$  systematics within pyroclastic material from the recent eruptions at Chaitén and Cordon Caulle volcanoes. Results reveal how gas fluxing from deep, volatile-rich reservoirs to the surface, within magmatic conduits, can be recorded by trace elements and  $^{210}\text{Pb}$ - $^{226}\text{Ra}$  disequilibria in tuffisite veins.

Tuffisite veins (particle-filled fracture networks) are present in volcanic bombs from both eruptions. Trace element heterogeneity associated with tuffisites preserves evidence for degassing. At Chaitén, enrichments (e.g. Cu) and depletions (e.g. Mo, Li and Bi) are identified in vein material and clasts transported within veins, and record multiple degassing events. At Cordon Caulle, enrichments of volatiles in an early vein (e.g. Tl and Bi) and depletions in a later vein (e.g. Cd, In, Pb and Tl) reflect interactions between glassy clasts and the carrier gas phase that transported them. In contrast,  $^{210}\text{Pb}$  and  $^{226}\text{Ra}$ , which can be fractionated during degassing, are mostly in secular equilibrium. Modelling suggests that the disparity between the signals preserved in these two types of chemical signatures reflects the brevity of degassing events and the relative volumes of tuffisite veins and the bodies of degassing magma that they source gas from. The lack of preserved  $^{210}\text{Pb}$  enrichments in tuffisite veins at both volcanoes



places an upper limit on the mass of deeper, bubble-rich magma outgassed via tuffisites during their lifetime.

This study shows that both the presence, and absence, of sample-scale geochemical heterogeneity can be used to place constraints on syn-eruptive physical processes and underlines the value of analysing a wide suite of trace element species.

## **1. Introduction**

Volatile behaviour during magma ascent governs eruption style at the surface and is recorded in the erupted deposits (Gonnermann and Manga, 2007, Edmonds, 2008). Silicic eruptions commonly shift from explosive to effusive activity with time, despite no change in the initial magma volatile content (Eichelberger et al., 1986, Jaupart and Allègre, 1991). The observation of hybrid activity – simultaneous Vulcanian explosions and lava effusion – during recent rhyolitic eruptions at Chaitén (2008-09) and Cordón Caulle (2011-2012) calls for an investigation into the processes that facilitate the long-term transition towards predominantly effusive behaviour (Schipper et al., 2013, Pallister et al., 2013a). Fracture networks have been hypothesised as permeable degassing pathways within the magma-filled conduit that are transient in time and space. They facilitate the extensive degassing of a system during an eruption and a shift to effusive behaviour, while also accounting for punctuated pressurisation and resulting Vulcanian explosions (Stasiuk et al., 1996, Schipper et al., 2013, Kendrick et al., 2016). These transient fractures, sometimes preserved as particle-filled tuffisite veins, can be up to three orders of magnitude more permeable than their hosts when open, before sintering

and compaction of particles within veins dramatically reduces permeability (Kolzenburg et al., 2012, Heap et al., 2015, Farquharson et al., 2016).

Whilst fractures can act as gas pathways spanning hundreds of metres within the conduit (Castro et al., 2012, Berlo et al., 2013, Castro et al., 2014, Saubin et al., 2016), the degree of interaction between veins and gas-rich sources at depth is poorly constrained. There is a need to quantify how much melt a fracture can degas during its lifespan in order to assess its potential impact on eruption mechanisms. Here we present a trace element and  $^{210}\text{Pb}$ - $^{226}\text{Ra}$  isotope study of volcanic bombs from both Chaitén and Cerdón Caulle in Chile, sourced from the upper conduit plugs from these two volcanoes, as inferred by low residual water concentrations in volcanic bombs from these eruptions (Schipper et al., 2013, Castro et al., 2014). We focus on tuffisite veins to assess geochemical evidence of gas flow through these highly permeable features. The preservation of syn-eruptive degassing signatures allows for a quantitative constraint on the interaction between transient fracture pathways and deeper volatile-rich, magma sources. We find that whilst trace element signatures at both volcanoes can be related to degassing and other physical processes, degassing-induced isotopic disequilibrium in veins is lacking. The disparity between isotopic and trace element signatures at Chaitén and Cerdón Caulle relate to the duration of gas fluxing and the contrasting nature of the upper conduit conditions during the two eruptions, including the fracturing depth and gas compositions.

## 1.1 Tuffisite Veins

Tuffisite veins are fractures filled and propped open by variably sintered, fine-grained material (with particle sizes spanning microns to centimetres). Their lengths can span from centimetres

to hundreds of metres within conduits, country rock and bombs ejected during Vulcanian explosions (e.g. Stasiuk et al. (1996), Tuffen and Dingwell (2005), Castro et al. (2012), Castro et al. (2014)). Veins and fractures result from brittle fracture of magma and country rocks, triggered either by high shear strain rates (Tuffen et al., 2003) or hydrofracturing (Heiken et al., 1988), thus opening potential gas pathways (Gonnermann and Manga, 2003). The lifespan of the veins ends with the sintering and compaction of vein-filling clasts (Tuffen et al., 2003, Kendrick et al., 2016, Saubin et al., 2016). A reduction in the permeability of magma within the upper conduit, the result of processes including viscous densification and porosity loss, can lead to repeated cycles of volatile accumulation, fracturing, gas escape via explosions, and healing of magma on ascent (Okumura and Sasaki, 2014, Heap et al., 2015). This is recorded texturally as anastomosing, cross-cutting veins that preserve evidence of transient fluidised flow as well as subsequent sintering, compaction and ultimately complete destruction of primary porosity and permeability within the vesicle-poor upper conduit (Stasiuk et al., 1996, Tuffen et al., 2003, Tuffen and Dingwell, 2005). Fracturing can briefly create a highly permeable pathway and deplete major volatiles in the neighbouring dense melt, but only localised depletions develop, within hundreds of microns of fracture surfaces. In this case, repeated, mm-scale brecciation would be required for effective degassing (Okumura et al., 2010, Castro et al., 2012). Thus, for melt fracturing to be an enabler of efficient degassing it must provide a pathway for gases to escape from more permeable, vesicular magmas at depth through the vesicle-poor 'plug' in the upper conduit. Element enrichment in tuffisite veins and detailed textural records of intra-vein clasts show evidence for this interaction with deeper magma and gases, for example using H<sub>2</sub>O differences between tuffisite clasts and host material as a proxy for depth at Chaitén, vein connectivity is shown to occur over ~150 metres (Berlo et al., 2013, Castro et al., 2014, Saubin et al., 2016). However, questions remain over what

mass of magma can be efficiently degassed by a tuffisite during its lifespan, which we address with a combination of trace element and  $^{210}\text{Pb}$ - $^{226}\text{Ra}$  isotope analyses of veins.

## 1.2 Volatiles, trace species and Ra-Rn-Pb systematics during degassing

A volcanic vapour phase is dominated by major volatile species (e.g.  $\text{H}_2\text{O}$ ,  $\text{CO}_2$ , S, Cl and F) that act as complexing agents for semi-volatile metals (e.g. Cu, Tl, Sn), and carrier gases for low concentration volatiles (e.g. Rn, Po) that can be enriched in gas plumes and at fumaroles (Lambert et al., 1985, Hinkley et al., 1994, Williams-Jones et al., 2002). As metal-bearing gases stream through fractures they interact with melt-rich clasts being carried by the gas, as well as the surrounding host melt. Fluxing will end when gas supply ceases or clasts sinter and compact, sealing the vein. Conditions (e.g. pressure, temperature, oxygen fugacity) can change within fractures during gas fluxing, affecting the vapour-melt partition coefficients of metals and the stability of their complexing agents (Williams-Jones and Heinrich, 2005), and induce chemical heterogeneity in the vein material and neighbouring fracture host melt. Metals can be scavenged from clasts resulting in depletions, e.g. Berlo et al. (2013), or deposited onto clast surfaces via adsorption forming metal-bearing mineral phases as seen in fumaroles resulting in enrichments, e.g. Williams-Jones et al. (2002) and Berlo et al. (2013). If conditions allow volatile elements in the gas phase can re-equilibrate with the surrounding melt and be reabsorbed into the melt structures also leading to metal enrichments, e.g. Plail et al. (2014).

The Uranium ( $^{238}\text{U}$ ) decay-series contains many short-lived isotopes with varied geochemical properties and half-lives ( $t_{1/2}$ ). Fractionating processes such as crystallisation, partial melting or changing oxygen fugacity ( $f\text{O}_2$ ), can cause disequilibrium between different isotopes within

the series (e.g. Bourdon et al, 2003; Berlo and Turner, 2010 and references therein). Degassing can induce disequilibrium between  $^{226}\text{Ra}$ ,  $^{222}\text{Rn}$  and  $^{210}\text{Pb}$ .  $^{210}\text{Pb}$ - $^{226}\text{Ra}$  disequilibria have been used to study the timing and redistribution of Rn-rich gases from deeper to shallower magmas in recent andesitic and dacitic eruptions including Mt St Helens (USA), Rabaul (Papa New Guinea) and Mt Pinatubo (Philippines) (Berlo et al., 2006, Cunningham et al., 2009, Kayzar et al., 2009). During degassing  $^{222}\text{Rn}$  ( $t_{1/2} = \sim 3.8$  days), the volatile daughter isotope of  $^{226}\text{Ra}$  ( $t_{1/2} = \sim 1600$  years), prefers the exsolved gas phase. With time  $^{222}\text{Rn}$  decays through several short-lived intermediate daughters to  $^{210}\text{Pb}$  ( $t_{1/2} = 22.6$  years), which is less volatile and resorbed back into the melt (Lambert et al., 1985). Persistent gas-melt segregation can result in the redistribution of the nuclides between melt that has lost gas and melt that has undergone gas fluxing. It is recorded in the erupted products as  $^{210}\text{Pb}$  ‘deficits’, where  $(^{210}\text{Pb}/^{226}\text{Ra}) < 1$ , and  $^{210}\text{Pb}$  ‘excesses’, where  $(^{210}\text{Pb}/^{226}\text{Ra}) > 1$ . Here we characterise  $^{210}\text{Pb}$ - $^{226}\text{Ra}$  disequilibria to quantify interactions between tuffisites and deeper magma and their exsolved gases.

### 1.3 Two Case Studies: Chilean Rhyolites

Chaitén and Cordon Caulle volcanoes both within the Chilean Southern Volcanic Zone (SVZ), produced the world’s most recent rhyolitic eruptions in 2008 and 2011 respectively. The two eruptions have many similarities in both their eruption dynamics and eruptive products. Chaitén erupted unexpectedly on May 1<sup>st</sup> 2008 with two weeks of explosive activity ( $\sim 0.3 \text{ km}^3$  dense rock equivalent, DRE), with a  $< 21$  km eruption column before transitioning into 20 days of hybrid activity (Pallister et al., 2013a, Major and Lara, 2013). Dome extrusion ( $\sim 0.8 \text{ km}^3$ ) continued until late 2009 (Major and Lara, 2013). The 2011-2012 eruption of Cordon Caulle commenced on June 4<sup>th</sup> with a persistent  $< 15$  km high Plinian eruption column for 27 hours, that transitioned into sub-Plinian behaviour, with lava effusion starting  $\sim 11$  days later and

simultaneous emplacement of a shallow (20-200 m deep) laccolith (Silva Parejas, 2012, Castro et al., 2016). The eruption continued into a prolonged phase of explosive activity accompanied by lava effusion that terminated in March 2012 with  $\sim 1.4 \text{ km}^3$  DRE of magma being erupted in total (Tuffen et al., 2013, Pistolesi et al., 2015), together with  $\sim 0.8 \text{ km}^3$  of magma intruded within the laccolith. Chaitén magma was sourced from a depth of  $\sim 5 \text{ km}$  ( $\sim 50\text{-}200 \text{ MPa}$ ),  $\sim 780\text{-}825 \text{ }^\circ\text{C}$ , (Castro and Dingwell, 2009) while depth estimates for Cordon Caulle range from 2.5 km to 7 km ( $895\text{-}920 \text{ }^\circ\text{C}$ ,  $f\text{O}_2 \sim \text{QFM}$ ); and both are volatile-saturated at depth (Castro et al., 2013a, Jay et al., 2014). Erupted products for both eruptions are sparsely phyrlic ( $<5 \text{ vol. } \%$ ), particularly the earlier explosively erupted material. Chaitén has a phenocryst assemblage of plagioclase, orthopyroxene and Fe-Ti oxides with rare biotite. The Cordon Caulle assemblage is similar, with plagioclase, orthopyroxene and Fe-Ti oxides, plus additional clinopyroxene, and accessory apatite and pyrrhotite (Castro and Dingwell, 2009, Castro et al., 2013a). Recorded precursory activity at Chaitén was on the order of hours compared to the months of heightened seismic activity and years of pre-eruptive inflation phases at Cordon Caulle, although there is a recording bias as no seismometers were placed close to Chaitén prior to the 2008 eruption. The effusive components to the eruptions differ, with a dome forming at Chaitén whilst a lava flow formed at Cordon Caulle. The groundmass glass water concentrations of the final products from each eruption are markedly different. Chaitén samples vary from  $\sim 0.1$  to  $1.6 \text{ wt. } \%$   $\text{H}_2\text{O}$  and have been used to trace degassing in the upper  $\sim 1 \text{ km}$  of the conduit, whereas Cordon Caulle samples are ubiquitously degassed to near-atmospheric pressures ( $<0.35 \text{ wt. } \%$   $\text{H}_2\text{O}$ ) (Schipper et al., 2013, Castro et al., 2014), and are thought to reflect an origin in the upper 200 metres of the conduit.

## **2. Methods**

Tuffisite veins and other sub-samples were cut and isolated from their host hand specimens with a micro-rotary tool and powdered with a pestle and mortar. Aliquots of powders, weighing 0.1-0.9 g, underwent closed vessel digestion in a concentrated HF-HNO<sub>3</sub>-HCl-H<sub>3</sub>BO<sub>3</sub> mixture. After digestion, solutions were centrifuged, and any insoluble materials were re-attacked until sample solutions appeared clear. Separate powder aliquots were digested for Po isotope, Ra isotope and trace element determinations. <sup>210</sup>Pb (t<sub>1/2</sub> = 22.6 years) activities were determined via alpha-spectrometry of its granddaughter isotope <sup>210</sup>Po (t<sub>1/2</sub> = 138.4 days), as secular equilibrium between the two is re-established ~2 years after eruption. Samples were analysed a minimum of 4 years after eruption and thus it is valid to use <sup>210</sup>Po as a proxy for <sup>210</sup>Pb (Bourdon et al., 2003). To determine <sup>210</sup>Po, a weighed drop of <sup>209</sup>Po spike was dried down in Teflon and sample powders then added, digested, and taken up in 0.5N HCl. Po was autoplated on Ag disks and counted on an alpha spectrometer (EGG-ORTEC at GEOTOP, Université de Quebec à Montreal) for a minimum of 7 days. Some samples underwent an additional chromatographic column purification step, summarised in Reagan et al. (2005), prior to plating. We found no difference in the <sup>210</sup>Pb activity between the two methods, however the latter chromatography method produced spectra with a reduced low-energy tail length and less noise, defining a clearer peak. <sup>226</sup>Ra activities were determined with a VG sector 54 Thermal Ionisation Mass Spectrometer (TIMS) using a <sup>228</sup>Ra spike calibrated against 15 aliquots of BCR-2 powder, that underwent the digestion procedure described above, with an assumed (<sup>226</sup>Ra) of 1.26 dpm/g. The Ra chemistry followed the procedure from Ghaleb et al. (2004). BCR-2 was regularly analysed, as an unknown, for both <sup>210</sup>Pb and <sup>226</sup>Ra and found to be within error of calculated <sup>238</sup>U activities and published values, e.g. Cunningham et al. (2009), on all occasions. Procedural blanks, carried out regularly for both isotope systems, showed <sup>210</sup>Po counts to be below background and negligible <sup>226</sup>Ra. Isotope analyses were conducted between 2014 and 2017, (<sup>210</sup>Pb)<sub>0</sub> and errors are back-calculated to correct for time between eruption and

analysis using the decay equation (Berlo and Turner, 2010). Bracketed isotopes, e.g. ( $^{210}\text{Pb}$ ), denote isotope activities or isotope activity ratios. Trace element concentrations were measured using a Thermo Scientific iCAP Q ICP-MS at McGill University on 2 %  $\text{HNO}_3$  dilutions. Rock standards BCR-2 and UTR-2 were analysed to assess for accuracy and fall within error of published values (Appendix A). Samples were digested in three sessions in May 2016, November 2016 and November 2017. Calibration standards were prepared from multi-element, ICP-MS grade, standard solutions with trace metal grade acids and nano pure water. Up to 9 standards were prepared and diluted to cover the range of expected concentrations. New calibration standards were prepared for each session and a minimum of two analyses per standard, per session were collected to correct for drift. Calibration curves for each element, in each session, were calculated via a robust, linear regression fit through a minimum of 3 calibration standards. Both sample and analytical duplicates were run in each session and data collected in November 2016 and 2017 were median-normalised to the May 2016 dataset. Relative standard deviations (% RSD) were calculated via duplicates in each session for each sample, see Appendix A for calculated errors.

### **3. Results**

#### **3.1 Sample Petrology**

Samples from both volcanoes were selected based on textural features that are indicative of upper conduit fragmentation and localised gas-loss during the transitional phases of both eruptions. Bombs are dense, partially foamed or fully pumiceous and, in addition, can be vein-bearing or brecciated with varying degrees of welding. All sub-samples are described in Figure



1. Two metre-scale bombs from the 2008 Chaitén eruption were collected from inside the crater, from pyroclastic density current deposits, and represent dense, tuffisite-hosting (Bomb A) and breadcrust (Bomb B) bombs, two textural types typical of bombs from the hybrid phase of activity that occurred between the 11<sup>th</sup> and 31<sup>st</sup> of May, 2008 (Castro et al., 2012, Saubin et al., 2016). Bomb A (also described as BTB) is a 30 x 40 x 50 cm dense obsidian bomb found ~800 m from the vent and is extensively described in Saubin et al. (2016). The central tuffisite vein is approximately 3 cm-wide and filled with mm to cm-sized dense obsidian, pale vesicular and banded or crystalline clasts, all set in a fine-grained matrix. Smaller  $\mu\text{m}$  to mm-sized subsidiary veins propagate from, and are found sub-parallel to, this central vein. Bomb B is ~1 m-across, with a dense (2-8 cm) rind that grades into an exposed pumiceous interior. Grey-black (mm-wide) glassy bands delineate separate clasts of white pumice in the bomb interior, with band density increasing towards the bomb edge. Clasts have micro-porosity away from these dense bands and secondary breadcrusting is observed on the exposed faces of some clasts. Six samples (five bombs and one lava sample) from the 2011-2012 eruption of Cordon Caulle represent the different bomb types observed, and the explosive and effusive products of the hybrid activity that commenced after the initial Plinian phase in June 2011 (Castro et al., 2013b). At Cordon Caulle, Bombs 1 and 2 were collected from a ridge ~3.5 km NW of the vent and three further samples (Bombs 3-5) were collected from the vent area within the tephra cone. Bombs found far from the vent (Bombs 1-2) were ejected in explosions during a low intensity explosive phase (7<sup>th</sup> June onwards) and beginning phase of hybrid activity (Schipper et al., 2013, Pistolesi et al., 2015). (Schipper et al., 2013, Pistolesi et al., 2015). Bombs were observed being ejected <1 km from the vent in January 2012 (Schipper et al., 2013) and thus we assume Bombs 3-5 represent the explosive component of the later, waning hybrid activity as they were collected from the tephra cone that built up during the eruption, within 300 m of the vent opening. Veins in Bombs 2 and 3 are predominantly filled by well-sorted, fine ash

(Figure 1). The tuffisite vein in Bomb 2 is ~1-3 cm wide and is laterally continuous throughout the rind of the bomb. Reservoir zones, irregular voids filled by micron-sized ash material that offshoot from central veins as described by Tuffen and Dingwell (2005), can be <7 cm wide. Tuffisite material in Bomb 3 is hosted in concave voids (approximately 5cm-wide and 3 cm-deep) that are part of a series of large coalesced vesicles in this highly sheared sample. The infiltration and clogging of the small vesicles in the neighbouring host by the tuffisite appear to have sealed this large coalesced vesicle train, isolated it from others, and concentrated gas transport along this one path. Bomb 4 is a ~4cm-wide multi-component vein, with coarse-grained beds composed of dense obsidian clasts and glassy, oxidised (pink-coloured), micron-sized ash; and fine-grained beds of heavily sintered glassy ash, which could represent tapping of a more complex heterogeneous conduit (Saubin et al., 2016). The relative timing of the degassing events that resulted in Bombs 3 and 4 are hard to definitively distinguish. Bomb 3 has tuffisite textures commonly seen in bombs ejected during the early phase of the eruption (e.g. Bomb 2) whilst Bomb 4 is more welded and heterogeneous. Thus, we suggest that Bomb 4 likely was erupted later than Bomb 3, and underwent more extensive compaction, but both were later than Bomb 2. The Cordón Caulle obsidian flow (Flow 1) was sampled from a breakout on the NW front of the northern branch that was impeded by a ridge within 60 days of the eruption commencing (Magnall et al., 2017, Magnall et al., 2018).

### 3.2 $^{210}\text{Pb}$ - $^{226}\text{Ra}$ Isotopes

$^{210}\text{Pb}$  and  $^{226}\text{Ra}$  data for Chaitén and Cordón Caulle are presented in Figure 2 and Table 1. Sub-samples of volcanic bombs from Chaitén have activity ratios within error of secular equilibrium, with the exception of Bomb B Exterior ( $(^{210}\text{Pb}/^{226}\text{Ra})_0 = 0.83 \pm 0.12$ ), whose

depletion results from higher  $^{226}\text{Ra}$  and lower  $^{210}\text{Pb}$  activities. At Cerdón Caulle, earlier activity samples (Flow 1, Bombs 1-2), Bomb 3 and the host component of Bomb 4 have  $(^{210}\text{Pb}/^{226}\text{Ra})_0$  activities within error of 1. Bomb 4 (vein) is depleted in  $^{210}\text{Pb}$  relative to  $^{226}\text{Ra}$ ,  $(^{210}\text{Pb}/^{226}\text{Ra})_0 = 0.90 \pm 0.02$ . Bomb 5 is slightly enriched in  $^{210}\text{Pb}$  relative to  $^{226}\text{Ra}$ ,  $(^{210}\text{Pb}/^{226}\text{Ra})_0 = 1.19 \pm 0.17$ .

### 3.3 Trace Elements

The measured trace element abundances of each sample are given in Appendix A, and highlights are discussed below. For ease of comparison elements are grouped into four categories based on their properties and similar behaviours (White, 2013). Group 1 elements (Mg, P, Sc, V, Mn, Co and Sr) are highly compatible in the crystallising assemblages and Group 2 elements (Be, Ga, Ba, La, Ce, Pr, Nd, Sm, Eu, Gd, Tb, Dy, Ho, Er, Tm, Yb, Lu, Y and Th) are the rare earth elements (REEs) and other moderately incompatible elements. Group 3 elements (Zr, Nb, Hf, Ta and U) are the high field strength elements (HFSEs) and U. Group 4 elements (Li, Rb, Cs, Mo, Ag, Cd, In, Sn, Sb, W, Tl, Pb, Bi, Cu, Zn) are a collection of elements known to partition into magmatic and hydrothermal fluids and vapours by forming chloride, sulphide, fluoride and hydroxy complexes (e.g. Webster (1990), Churakov et al. (2000), Wahrenberger (2002), Zajacz et al. (2008), Pokrovski et al. (2013) and references therein). Elemental concentrations of tuffisite veins from Chaitén (Figure 3) and Cerdón Caulle (Figure 4) are compared to their respective hosts.

#### 3.3.1 Chaitén

The higher  $^{210}\text{Pb}$  and  $^{226}\text{Ra}$  activities and concentrations of incompatible elements (e.g. Th, U, Appendix A) reflect the more evolved magma at Chaitén, ~75 wt. %  $\text{SiO}_2$  (Pallister et al., 2013a) compared to ~70 wt. %  $\text{SiO}_2$  (Castro et al., 2013a) at Cerdón Caulle. Trace element concentrations across both sub-samples of Bomb B and Bomb A (Host) are within error of each other and are similar to samples analysed by Pallister et al. (2013b), supporting the theory that melt for this eruption is near homogeneous in major and trace elements and similar to historical Holocene eruptions (Lowenstern et al., 2012). Group 1 and Group 2 elements plus select elements from Group 4 (Zn, Sn, Tl and Pb), in particular, show little variation across both bombs.

However, on a cm-mm scale elemental variation does occur. In the vein material of Bomb A and Banded Clast, a non-juvenile clast type that accounts for ~42% of the vein (Saubin et al., 2016), elemental variation is best studied by examining the compositions vein-host ratio, e.g.  $\text{Li}_{\text{vein}}/\text{Li}_{\text{Host}}$ , allowing for an easy comparison of composition (Figure 3). When compared to the host composition, Group 3 elements are depleted in both the vein material and Banded Clast, along with many Group 4 elements (Figure 3). The Banded Clast has stronger depletions of Bi, Li, Mo, W, Ag, and Cd (ratios averaging ~0.58 when compared to the host) than the vein material (average ratios ~0.88). Cu is depleted within the Banded Clast but shows enrichment in the vein matrix (Figure 3). The Banded Clast is enriched in Ni relative to all other samples (not shown in Figure 3).

### 3.3.2 Cerdón Caulle

At Cordon Caulle, Group 2 and 3 elements, and select Group 4 elements (Li, Mo, Ag, Sb and Zn), show little variation across the sample suite (see Appendix A). Key observations noted in elemental variation of samples are: (1) Bomb 2 (Interior) is elevated in Cu and Sn over the rest of the samples; (2) Bomb 3 is enriched in Bi and depleted in P and In with respect to the average Cordon Caulle composition; and (3) the host component of Bomb 3 is further enriched in Tl.

When vein material from Bomb 2, Bomb 3 and Bomb 4 are compared to their respective hosts a similar ratio signature pattern between veins is observed (Figure 4). Veins are depleted in Group 1 elements. Group 2 and 3 elements are similar in the veins to their respective hosts. Group 4 elements show variability within the veins. Bi is enriched in veins in Bombs 2-3. The vein in Bomb 2 is enriched in Tl. The vein from Bomb 3 has an apparent depletion in Tl relative to the host, but the depletion is exaggerated due to the host's higher than average Tl concentration ( $0.8 \pm 0.3$  ppm vs an average of  $0.43 \pm 0.07$  ppm). The vein in Bomb 4 is depleted in Cd, In, Tl and Pb, and enriched in Cu and Rb.

#### **4. Discussion**

Neither Chaitén nor Cordon Caulle have significant  $^{210}\text{Pb}$ - $^{226}\text{Ra}$  disequilibria, however trace element variation is preserved and can be linked to several processes that occur before and during eruption, and at the conduit- and fracture-scales. The discussion is divided into sections that address degassing signatures, other physical processes, and how heterogeneity relates to conditions in the upper conduit. Section 4.1 discusses degassing-induced heterogeneity in

isotopes and trace elements and the implications for the disparity between them. Section 4.2 outlines how the lack of isotope disequilibria within fractures can be used to constrain the mass of melt that outgas via a fracture during their open lifespans, we use Chaitén as an example before discussing its applicability to other systems. We discuss trace element variations that can be attributed to other processes in Section 4.3 and the anomalous  $^{210}\text{Pb}$ - $^{226}\text{Ra}$  disequilibria in Section 4.4. Finally, the last section links the preservation of chemical heterogeneity to the physical conditions of the upper conduit and summarises the potential causes for differences in chemical signatures between these two volcanic eruptions.

## **4.1 Degassing-induced chemical heterogeneity**

### **4.1.1 Isotopic Evidence for Degassing**

Disequilibria in  $^{210}\text{Pb}$ - $^{226}\text{Ra}$  isotopes can be preserved at a conduit scale and induced by both pre-eruptive and syn-eruptive degassing (Berlo and Turner, 2010). Therefore it is important to first assess for any heterogeneity between samples before assessing disequilibria within samples related to individual fracturing events.

#### **Pre-Eruptive Degassing**

The majority of samples at Chaitén and Cerdón Caulle are in secular equilibrium, and this lack of large-scale  $^{210}\text{Pb}$ - $^{226}\text{Ra}$  disequilibria indicates no extensive, pre-eruptive degassing was

recorded in the magmas at either volcano. At Chaitén the last recognized eruption was a few hundred years before present, and there was no extensive documented precursory activity prior to the 2008 eruption to indicate the accumulation of shallow magma, thus it is unlikely a large volume of degassing magma was present below this system (Major and Lara, 2013, Amigo et al., 2013). Similarly, at Cordón Caulle, whilst the two previous eruptions occurred in the last 100 years (1922 and 1960), any moderate  $^{210}\text{Pb}$  excesses or deficits produced during these eruptions would be nearing re-equilibration today, given the 58-96 years between the eruptions and 2018, and  $^{210}\text{Pb}$  being within ~94 % of  $^{226}\text{Ra}$  after 4 half-lives (~88 years).

### **Syn-Eruptive Degassing**

Volatile data, including preserved  $\text{H}_2\text{O}$  concentrations (Section 1.3) and trace element variations (Section 4.1.2), from both eruptions suggest that syn-eruptive degassing did occur extensively during these eruptions. However, the main phases of the eruptions were ~12 months in duration, too brief for significant isotopic deficits to form (Gauthier and Condomines, 1999).  $^{210}\text{Pb}$  excesses could be formed within this time (Condomines et al., 2010) but no disequilibria were preserved at either volcano. This suggests there was not enough gas fluxing, Rn transfer, or Rn accumulation within the timeframe of the eruptions to induce significant disequilibria in the Rn system. Similarly, no isotope excesses were recorded in tuffisite veins (within samples), which are channels of volcanic material known to have undergone a large amount of gas fluxing. This lack of disequilibria provides constraints on the degassing through veins and is discussed in Section 4.2.

#### **4.1.2 Trace Element Evidence for Degassing**

Heterogeneity preserved in Group 4 elements within sub-samples (e.g. tuffisite veins) from both volcanoes are related to degassing processes. The behaviour of these elements during degassing depend on their melt-vapour partition coefficients (how favourably they will partition into an available vapour) which in turn depends on the ligand availability in the vapour phase (elements they will form complexes with), which vary with pressure and temperature within the conduit (Zajacz et al., 2008, MacKenzie and Canil, 2008, Pokrovski et al., 2013). Their behaviour further depends on their diffusivities in silicic melts (how quickly they will diffuse towards melt-vapour interfaces), which is a function of the H<sub>2</sub>O concentration in the melt, pressure and temperature (Zajacz et al., 2008, MacKenzie and Canil, 2008, Pokrovski et al., 2013). The evolution of these factors during both eruptions is largely unknown and prevents robust and quantitative modelling of trace element partitioning and behaviour. Texturally, tuffisite veins preserve the last major fracturing and degassing event a parcel of melt underwent prior to fragmentation and bomb ejection. Chemical heterogeneity within tuffisite veins largely relate to that final syn-eruptive event. However, it is possible for older degassing events to be preserved within host material and entrained lithics, and so careful sub-sample analyses of differing bomb components allows for the distinction between different events.

#### **Chaitén**

The biggest compositional variations in the Chaitén samples are within the vein matrix samples and Banded Clast found in the vein of Bomb A (Figure 3). Banded Clasts have previously been



interpreted as non-juvenile material from a previous eruption that had undergone shearing events and cristobalite precipitation (Saubin et al., 2016). The clast is depleted in many Group 4 elements, known to be volatile under magmatic conditions (e.g. Mo, Li, Bi, Ag, Cd and Cu), which suggests outgassing occurred simultaneously with these shearing events resulting in the extensive depletion of volatiles in the melt bands within the clast. However, the clast shows no evidence of degassing preserved in its  $^{210}\text{Pb}$  isotope signature. We propose that these clasts are part of the old dome, from a previous eruption that preceded the 2008 eruption by more than 120 years, so any initial disequilibria have been lost. In the less likely scenario it is a juvenile clast, the degassing events recorded as trace element depletions were insufficiently lengthy to be recorded in the  $^{210}\text{Pb}$  isotope signature. Depletions in the Group 3 elements (HFSEs and U) are discussed in Section 4.3.

Cu is enriched in the vein matrix but depleted in the Banded Clast, whilst Bi, Li and Mo are depleted in the vein matrix. Cu, Mo and Sb are among the elements known to be enriched in vein matrices at Chaitén, whilst Li is depleted in the vein matrix but enriched in the pumice clasts within veins (along with Cu and Sb) (Berlo et al., 2013). Bi was not analysed by Berlo et al. (2013). Our bulk vein results appear, at first, contradictory to the in-situ study conducted by Berlo et al. (2013). However, the Mo, Li and Bi depletions in this vein are likely the result of the mixing signature from the Banded Clast overprinting any vein enrichment, as discussed in Section 4.3. Combined, Berlo et al. (2013) and our study show that Cu, Mo, Li, Sb and Bi are mobile and are evidence of gas streaming through tuffisite veins. Gas streaming is the process whereby magmatic gases are channelled through permeable pathways in magma, e.g. fractures that can be preserved as tuffisite veins, which are transient throughout the conduit during eruption. The ligands present in the gases aid in transporting metals from depth towards the surface, as discussed in Section 1.2, and elements such as Cu, Mo, Sb and Bi are found to

more favourably partition into fluids with a low chlorinity, often forming hydroxy complexes (Zajacz et al., 2008, Berlo et al., 2013). Chemical heterogeneity is caused by the interaction of the gases and the transported glass shards and preserves the gas streaming event. The ‘purer’ Vein Matrix sub-sample shows the highest level of Cu enrichment. This could be due to more efficient Cu adsorption onto the finer particles that provide a high surface area for adsorption, or absorption of metals by the sintering melt. The origin of the Cu enrichment remains unclear.

### **Cordón Caulle**

Group 4 elements display a wide range of signatures in the Cordón Caulle veins. Bi and Tl are commonly amongst the most enriched trace elements found in gases, favourably partitioning into available vapours at high temperatures (e.g. Symonds et al. (1987), Mather et al. (2012), Zelenski et al. (2013)), and show the greatest variability across this suite of samples. The Bi and Tl enrichment in the tuffsite vein of Bomb 2 (Figure 4) could be due to adsorption of these elements onto the glass shards, the result of interaction with the fluxing gas phase. Bi and Tl would be transported within the vapour phase but changing conditions upon ascent could have promoted deposition and adsorption from the gas phase (as melt-vapour partition coefficients decreased with changing conditions), the fine-grained glass shards of these veins providing a high surface area to volume ratio, ideal for adsorption. This would be analogous to metal deposition in fumaroles. Alternatively, the glass shards absorbed metals into their silicate melt structure during vein sintering and compaction; or have higher Bi and Tl concentrations suggesting tapping of deeper, less degassed melts. Distinguishing between adsorption and absorption is beyond the scope of the methods of this paper.

Bi is also enriched in the vein of Bomb 3, but Tl is depleted (Figure 4). The apparent depletion of Tl within this vein component is due to the enrichment of Tl in the vesiculated host with respect to all other samples. The elongated and connected vesicles in this highly sheared sample suggest open channels for gas flow were present prior to tuffsite formation. Adsorption of Tl onto the channel walls during fluxing could account for its higher than average concentration, and thus lower vein-host ratio. Bi is much higher in concentration in this sample than all others from Cordón Caulle as well, supporting the theory of gas adsorption in the host component of this sample. Alternatively, the sample has lost less Tl and Bi through degassing than other samples, pointing to a larger-scale control on concentrations of volatiles preserved than individual fracture-degassing events.

The vein within Bomb 4 (Figure 4) is depleted in Tl (Bi is similar to the host), suggesting this later vein tapped a more degassed source or that conditions within the vein resulted in scavenging of metals and not metal deposition. Cd, In and Pb depletions are observed in this vein only. Depletions would suggest the system either progressively degassed over time, with earlier veins tapping gas-rich melts and later veins tapping more gas-depleted melts, or conditions changed such that earlier veins underwent metal deposition whilst later veins underwent scavenging.

In each of these cases, the affinity of both Bi and Tl for a gas phase and the textural association of the enrichments and depletions with gas pathways suggest that interactions between melt and fluxing gas was the driver for the preserved heterogeneity. However, the processes

responsible remain unclear pending detailed studies on the behaviour of these elements under similar conditions. In-situ studies into Tl and Bi variation could be key to understanding the complex degassing history and Cordón Caulle.

#### **4.1.3 Why is there a disparity between the isotope and trace element signatures?**

As discussed in Section 1.2,  $^{210}\text{Pb}$ - $^{226}\text{Ra}$  disequilibria and trace element heterogeneity can be induced by degassing of a magma before and during an eruption. At both Cordón Caulle and Chaitén there is little evidence of degassing preserved in the isotope record but trace element variations in tuffisite veins at both localities do provide evidence for degassing. One key parameter for a chemical signature of degassing to be preserved is time.  $^{210}\text{Pb}$  deficits can only be formed over months to years of continuous degassing because of the need for continuous extraction of  $^{222}\text{Rn}$  from the system (Gauthier and Condomines, 1999).  $^{210}\text{Pb}$  excesses can be formed in less time, with weeks to months of gas fluxing required to transfer  $^{222}\text{Rn}$  from one location to another, and for it to then decay to  $^{210}\text{Pb}$  (Condomines et al., 2010). The timing required to generate an excess is also dependent on the mass of magma Rn is being removed from and redistributed into. If the ratio is large then less time is required to generate an excess, and we address this within the context of tuffisite veins in Section 4.2. However, trace element heterogeneity induced by degassing is a function of the characteristic diffusivities of elements in silicate melts and their vapour-melt partition coefficients and not by decay, thus they require only minutes to hours to generate sub-mm scale heterogeneity in tuffisite vein material (MacKenzie and Canil, 2008, Berlo et al., 2013). The preservation of degassing signatures in trace elements at Chaitén and Cordón Caulle but not in isotopes suggests that individual degassing events through fractures were transient (not longer than days at a time), otherwise

we would expect to see preserved signatures in both trace elements and isotopes. Furthermore, this places limits on the mass of magma that is being degassed through these channels.

#### 4.2 Why are no $^{210}\text{Pb}$ excesses preserved in veins?

The redistribution or streaming of gas (containing  $^{222}\text{Rn}$ ) through a system can result in  $^{210}\text{Pb}$  excesses. Therefore, if a fracture or tuffisite vein underwent sufficient gas streaming over time it would be expected to have a  $^{210}\text{Pb}$  excess.  $^{210}\text{Pb}$  that has decayed from volatile  $^{222}\text{Rn}$ , concentrated within the gas phase, would be resorbed by melt particles within the fracture (Lambert et al., 1985). However, despite evidence for gas streaming (e.g. metal enrichments and clastic textures), no vein material from Cordón Caulle or Chaitén has preserved a significant  $(^{210}\text{Pb})_0$  excess. We adapt the model from Condomines et al. (2010) to explain why no excesses have been preserved in veins at either volcano and which conditions could potentially form excesses at other eruptions.

Condomines et al. (2010) numerically modelled how  $^{210}\text{Pb}$  excesses ( $^{210}\text{Pb}/^{226}\text{Ra} > 1$ ) can be derived from the accumulation of  $^{222}\text{Rn}$  (and its subsequent decay to  $^{210}\text{Pb}$ ). Their model accounts for the mass ratio ( $R$ ) of the magma degassing cells losing gas ( $M_d$ ) and accumulating Rn ( $M_a$ ); the fraction of Rn extracted from the degassing cell ( $f$ ) and from the accumulating cell ( $f'$ ); as well as the volatile content of the undegassed magma ( $\alpha$ ) and the magma's residence time in the degassing cell ( $\tau$ ) (Figure 5). We present a model adapted from Condomines et al. (2010) and the original differential decay equations as derived by Bateman (1910). The model constrains the mass ratio required to generate an excess of  $^{210}\text{Pb}$  in the vein given a degassing event of  $X$  hours. It is divided into two parts. Part One calculates the evolution of  $(^{210}\text{Pb})_0$ ,

( $^{222}\text{Rn}$ ) and ( $^{226}\text{Ra}$ ) with time while the fracture is open and  $^{222}\text{Rn}$  is being redistributed from the degassing cell to the fracture via gas streaming (Figure 5). Part Two allows for the assessment of the final ( $^{210}\text{Pb}/^{226}\text{Ra}$ ) of the bulk fracture assuming no further loss of  $^{222}\text{Rn}$  or  $^{210}\text{Pb}$  following closure and sealing of the vein. Only re-equilibration and decay of the nuclides present at the time of vein closure occurs during this time.

#### 4.2.1 Part One: Radon Redistribution during fracturing and gas streaming

Following the approach of Condomines et al. (2010), the  $^{222}\text{Rn}$  variation per unit time in the fracture is given by:

$$\frac{d(\text{Rn})_a}{dt} = \frac{1}{M_a} [(\phi_{\text{Rn}}^{\text{in}}) - (\phi_{\text{Rn}}^{\text{out}})] + \lambda_{\text{Rn}}(\text{Ra})_a - \lambda_{\text{Rn}}(\text{Rn})_a \quad (1)$$

Where  $\phi_{\text{Rn}}^{\text{in}}$  and  $\phi_{\text{Rn}}^{\text{out}}$  are defined as the flux of Rn in and out of the accumulating cell, in this case the fracture preserved as the tuffisite vein.  $M_a$  is the mass of the tuffisite vein;  $\lambda_{\text{Rn}}$  is the decay constant of Rn; and  $(\text{Ra})_a$  and  $(\text{Rn})_a$  are the  $^{226}\text{Ra}$  and  $^{222}\text{Rn}$  activities of the tuffisite material respectively. The parameters  $f$  and  $f'$  denote the fraction of Rn effectively extracted from the degassing magma cell, and accumulating magma cell respectively:

$$f = \frac{(\phi_{\text{Rn}}^{\text{in}})}{[\lambda_{\text{Rn}}M_d + (1-\alpha)\phi_0](\text{Ra})_d} \quad (2)$$

$$f' = \frac{(\phi_{\text{Rn}}^{\text{out}})}{[\lambda_{\text{Rn}}M_a(\text{Ra})_a + (\phi_{\text{Rn}}^{\text{in}})]} = \frac{(\phi_{\text{Rn}}^{\text{out}})}{[\lambda_{\text{Rn}}M_a(\text{Ra})_a + f(\lambda_{\text{Rn}}M_d + (1-\alpha)\phi_0)(\text{Ra})_d]} \quad (3)$$

Where  $M_d$  is the mass of the degassing cell,  $\phi_0$  is the influx of undegassed magma into the degassing reservoir,  $\alpha$  is the volatile content of the undegassed magma, and  $(\text{Ra})_d$  is the  $^{226}\text{Ra}$  activity of the degassing cell (see Fig. 5). Condomines et al. (2010) simplify their equations

because  $(\text{Rn}/\text{Ra})_a$  will reach a steady state after several weeks as Rn, and other intermediary nuclides, are in secular equilibrium with Ra. This is an assumption we are unable to make as the fractures are only open on the order of hours to days (Castro et al., 2012, Berlo et al., 2013). Thus we combine the above equations and simplify by introducing the parameters residence time,  $\tau = M_d/\phi_o$ , and mass ratio,  $R = M_d/M_a$ , as suggested by Condomines et al. (2010), and restricting our model to  $(\text{Ra})_a = (\text{Ra})_d$ . This is a valid assumption as ( $^{226}\text{Ra}$ ) is immobile, does not partition into a gas phase (Lambert et al., 1985), and these systems show no significant Ra variation over time (see Section 3, Fig. 2). The changing ( $^{222}\text{Rn}$ ) with time can then be represented by:

$$\frac{d(\text{Rn})_a}{dt} = \lambda_{\text{Rn}}(\text{Ra})_a C - \lambda_{\text{Rn}}(\text{Rn})_a \quad (4)$$

Where:

$$C = (1 - f') \left[ 1 + fR \left[ 1 + \frac{(1 - \alpha)}{\lambda_{\text{Rn}}\tau} \right] \right] \quad (5)$$

This modified equation takes into account the additional  $^{222}\text{Rn}$  from the decay of  $^{226}\text{Ra}$  in the degassing cell, the  $^{222}\text{Rn}$  lost from the fracture, and  $^{222}\text{Rn}$  that comes from the decay of  $^{226}\text{Ra}$  in the tuffsite material within the fracture. Appendix B provides further details on the derivation of this equation and equations underpinning both parts of the model presented.

The model uses the complete solutions to the decay equations, as described by Bateman (1910), assuming that  $^{226}\text{Ra}$  and its products,  $^{222}\text{Rn}$  and  $^{210}\text{Pb}$ , start in secular equilibrium. The additional  $^{222}\text{Rn}$  is accounted for in the equations for both ( $^{222}\text{Rn}$ ) and ( $^{210}\text{Pb}$ ) variation with time. There are several, short-lived intermediate nuclides between  $^{222}\text{Rn}$  and  $^{210}\text{Pb}$  that we have not included within the model. We assume that  $^{218}\text{Po}$  ( $t_{1/2} \sim 3.05$  mins) and  $^{214}\text{Po}$  ( $t_{1/2} \sim 1.64 \times 10^{-4}$  s)

<sup>4</sup> s) are in secular equilibrium the whole time due to their short half-lives and can be ignored. If the fracture is open for <2 ½ hours then <sup>214</sup>Pb and <sup>214</sup>Bi stay trapped and do not need to be considered separately as <sup>214</sup>Pb would be resorbed into melt particles, and <sup>214</sup>Bi would stay volatile with Rn. If the vein is open longer, they are in secular equilibrium with <sup>222</sup>Rn. Finally, we assume negligible Rn flux from vein walls when compared to contribution from depth, due to slow Rn diffusion (Gauthier et al., 1999), thus R represents purely the mass ratio between the fracture and degassing cell. The model numerically calculates the activities of Pb, Rn and Ra and the activity ratios (<sup>222</sup>Rn/<sup>226</sup>Ra) and (<sup>210</sup>Pb/<sup>226</sup>Ra) for a fracture open between 0 and 36 hours (t), a timespan that applies to veins at both these and other volcanoes such as Torfajökull (Iceland) and Lipari (Italy) (Cabrera et al., 2010, Castro et al., 2012, Berlo et al., 2013). The parameters inputted into the calculations representing Rn extraction from the degassing chamber (f) and the fracture (f') vary from 0 to 1, and R (the mass ratio, M<sub>d</sub>/M<sub>a</sub>) varies from 0.1 to 1x10<sup>6</sup> to provide a full range of potential scenarios.

#### **4.2.2 Part Two: Vein Closure and Subsequent Decay**

Eventually, radon gas transport will cease because particles within the vein will have sintered to the point at which the system becomes closed to gases (Farquharson et al., 2017). Excess Rn trapped within the isolated porosity of the vein will decay to Pb and be reintroduced into the melt (Condomines et al., 2010). Part two of the model calculates the decay of <sup>210</sup>Pb, <sup>222</sup>Rn and <sup>226</sup>Ra and activity ratios Rn/Ra and Pb/Ra for scenarios with varying f, f', R and t values. After ~50 days the activity of <sup>222</sup>Rn has returned to within error of its original activity, <sup>210</sup>Pb and <sup>222</sup>Rn are in secular equilibrium, and (<sup>210</sup>Pb/<sup>226</sup>Ra) has reached its maximum. Contoured plots generated show the R value required, for given f' and τ values, to generate (<sup>210</sup>Pb/<sup>226</sup>Ra) ~1.10



(a ratio that deviates from secular equilibrium by more than analytical error). This is for a fracture open over a range of timescales, e.g. Figure 6 where  $\tau = 0.019$ ,  $f = 1$ ,  $f' = 0.5$  and  $t = 0-15$  hours.

### 4.2.3 Applying the model: Chaitén

Previous studies on tuffsite veins from Chaitén make this a prime case study to test this model. Diffusion modelling of H<sub>2</sub>O towards fractures in bombs from the 2008 Chaitén eruption suggests fractures are open on the order of hours (Castro et al., 2012). We assume the degassing cell is an isolated parcel of magma, isolated prior to and upon ascent within the conduit. As the system becomes closed,  $\tau \rightarrow \infty$ . Appendix C summarises the effect of varying  $\tau$  on the required R values, with negligible differences in required R when  $\tau > 1$ . Here we use a  $\tau$  value of 0.019 (equivalent to the cell being isolated for 1 week before being degassed by the fracture). Castro and Dingwell (2009) indicate that magma at depth at Chaitén contained <4 wt. % H<sub>2</sub>O thus we choose  $\alpha = 0.04$ , this is the volatile content of the undegassed magma that is ultimately exsolved. Sensitivity analysis indicates that variation of  $\alpha$  has a negligible impact on the final values of the model. Assuming complete extraction of Rn from the degassing chamber ( $f = 1$ ) for a fracture open for 7.5 hours, mass ratios ( $R = M_d/M_a$ ) of ~3000-9000 are required to generate an activity ratio of ( $^{210}\text{Pb}/^{226}\text{Ra}$ ) ~1.10 (the minimum  $^{210}\text{Pb}$  excess that would be outside of error) depending on the amount of Rn extracted from the vein to the surface ( $f' = 0.25-0.75$ ). Here an  $f'$  value of 0.25 implies 25 % of available Rn is extracted out of the vein during the time the vein is open. R increases fourfold from 4,500 to 20,000 as fracture lifespan decreases from ~7.5 hours to ~1.6 hours (assuming  $f = 1$ ,  $f' = 0.5$  and  $\tau = 0.019$ , see Figure 6). These values would increase if  $f < 1$ , therefore these are minimum values. The model sensitivity

to varying  $f$  values is discussed in Appendix C. The model provides an estimate on the size of a melt pocket that can be degassed by a fracture during its lifetime. As an example, a sheet-shaped vein with a 5 cm aperture, 6-50 m wide, with 150 m of vertical length, would have a  $M_a$  between  $9.3 \cdot 10^4$  and  $7.8 \cdot 10^5$  kg assuming a bulk density of  $2070 \text{ kg/m}^3$  (Saubin et al., 2016). This would correspond to a degassing cell mass ( $M_d$ ) between  $4.7 \cdot 10^8$  and  $3.9 \cdot 10^9$  kg (or  $\sim 2 \cdot 10^5$ - $1.7 \cdot 10^6 \text{ m}^3$  of magma, assuming a density of  $2281 \text{ kg/m}^3$ ) at  $R \sim 5,000$ . Geometrically, this is equivalent to a single vein efficiently degassing a cylindrical parcel of magma  $\sim 350$  m in length with a radius between 14 and 40 m, within a lifespan of several hours.  $\text{H}_2\text{O}$  cannot diffuse in a dense melt over a metre length scale on these timescales (e.g. Castro et al. (2012)). Furthermore, these calculations highlight the implausible cylinder radii required for wider veins (e.g. 40 m), that suggest they were degassing a melt wider than the conduit itself. For this unlikely scenario to occur the magma being degassed would require an extensively connected bubble network across its length and width for gas to segregate into and move these distances before then outgassing through the fracture. Thus, the model highlights that disequilibria, induced within a single fracture and gas fluxing event, are highly unlikely to be preserved in veins open for such a short a period of time.

#### **4.2.4 Applying the model: Other Systems**

The model outputs imply that if veins are open long enough,  $>1$  day, it could be possible to generate a small  $^{210}\text{Pb}$  excess under favourable conditions (Figure 6, Appendix C). For this model to be applied to other systems fracture opening timescales are required, via measurement or estimation. This can be done via diffusion studies, e.g. Castro et al. (2012) or via visual observation, e.g. Schipper et al. (2013), if the assumption is made that vents or sub-vents are

the surface manifestation of gas fluxing through fractures at depth. Once a time estimate is known, isotope disequilibria will aid in constraining the mass of magma being degassed by fractures during those events. Tuffisite veins in volcanic centres, such as those in a ~70 ka dissected conduit at Torfajökull in Iceland, show evidence of being longer-lived (Berlo et al., 2013). However, isotope systematics dictate that this model can be only used only recent eruptions, as all  $^{210}\text{Pb}$  disequilibria will decay away after ~120 years (~5 half-lives of  $^{210}\text{Pb}$ ).

### **4.3 Other processes inducing tuffisite vein trace element heterogeneity**

Some of the chemical heterogeneity in the tuffisite veins are in elements that are not commonly associated with degassing because of their immobility, non-volatility, and general preference for mineral phases (e.g. Group 1 and Group 3 elements). Thus, degassing is unlikely to be the cause of the heterogeneity. At Chaitén HFSEs and U are depleted in the Bomb A vein subsamples with respect to the host, and at Cerdón Caulle many major elements and transition elements (e.g. Mg, Sr, and V) are depleted in the three separate veins with respect to their hosts. These variations though can be explained through different physical processes than degassing as discussed below and highlight the importance of analysing a wide suite of elements with varying properties.

#### **Chaitén**

The biggest compositional variations in the Chaitén samples are within the vein matrices and Banded Clast components of Bomb A (Figure 3). As previously mentioned, the Banded Clast

is interpreted as non-juvenile material (Saubin et al., 2016). Group 3 elements (HFSEs and U) are generally highly incompatible in many mineral phases, but are commonly found in elevated concentrations in the refractory mineral zircon (Belousova et al., 2002). Zr, Hf and Nb are the most depleted elements in the Banded Clast (excluding the volatile elements discussed in Section 4.1), followed by U, Ta, the heavy REEs (Dy to Lu) and Y. Apparent partition coefficients calculated from the observed deficits are consistent with that of zircon crystallisation ( $D_{Zr} > D_{Hf} > D_U \gg D_{HREEs} \sim D_Y$ , Fujimaki (1986), Thomas (2003)). This would require these clasts to have undergone a different cooling history to the zircon undersaturated, main 2008 melt (Boehnke et al., 2013). We propose that the Banded Clast represents a previous rhyolitic dome, which would have cooled more slowly through the zircon saturation temperature ( $\sim 712$  °C based on calculations by Boehnke et al. (2013) assuming a similar composition to the 2008 melt), allowing for the formation of micron-sized zircons. This would explain why the zircon signature is only found in these clasts and not in the juvenile melt of Bombs A and B.

The elemental composition of the Banded Clast will affect the vein sub-samples from Bomb A as the clasts are a sizable component of the vein's textural make-up. The Banded Clast analysed is  $\sim 1$  cm in across, however most clasts of this type range from  $\sim 0.1$  to  $\sim 8$  mm in size (Saubin et al., 2016). Saubin et al. (2016) report that banded clasts accounted for  $42 \pm 3$  % of this tuffisite vein, with dense clasts accounting for  $35 \pm 3$  % and pale vesicular clasts  $22 \pm 4$  %. Using this information, we construct a simple three component mixing model, assuming this component ratio (42:35:22), to predict the concentrations of elements in the tuffisite vein, and account for the apparent elemental depletions within the Vein Matrix and Matrix & Clasts sub-samples (Fig. S.1). These sub-samples are depleted in HFSEs, U, and some volatiles (Li, Mo, Bi) but to a lesser extent than the Banded Clast (see Section 3.3, Fig. 3). Dense clasts are

assumed to have a composition identical to the host, the banded clasts' composition is known, and we use average element concentrations for the pumice clasts from Berlo et al. (2013) for the three-component model. Certain elements (Yb, Y, Zr, Nb, W, Cs, Ag, Cd and Bi) were not analysed by Berlo et al. (2013) so their concentration in the pumice clasts are assumed to be the same as that of the host. This is a valid assumption as Saubin et al. (2016) state these clasts fragmented deep in the system and were brought up into the vein, suggesting they are part of the 2008 juvenile melt that is chemically well constrained (see Section 3.3). This reduces the 3-component mixing model to a two-component mixing model between Host (~57 %) and Banded Clast (~42 %). These models reproduce, within error, observed depletions in Figure 3 (Fig. S.1) with exception of Nb that is just outside of error, Cu (Matrix sub-sample), Mo and Bi (in both sub-samples). The underestimation of Cu, Sb, Mo and Bi concentrations by the model suggests that these elements have been added to the vein, supporting the theory of gas streaming discussed in Section 4.1 and by Berlo et al. (2013). Thus, the depletions in the more immobile elements, and most volatile elements, within the vein at Chaitén are due to mixing and bulk analysis of clasts, with subtle compositional differences, that have been transported along with the gas phase. The compositions of these individual clasts represent their histories (degassing, crystallisation etc.) prior to entrainment within the tuffisite vein. This mixing of three clast types with subtly different compositions has likely masked the enrichment of certain volatile elements (Cu, Mo and Bi) that have been fluxed through with the gas phase and adsorbed onto the clast surfaces within the vein.

## **Cordón Caulle**

Three tuffisite samples show similar trace element ratios when normalised to their respective hosts (Figure 4). Anomalies in the Group 1 elements are unlikely to result from degassing but could be the result of preferential fracturing and transportation of glass over the phenocryst assemblage (plagioclase, orthopyroxene, clinopyroxene, Fe-Ti oxides and accessory apatite) during fragmentation. Horwell et al. (2001) found that the components of different size fractions of the pyroclastic flow deposits at Soufrière Hills volcano were altered due to physical processes. Larger size fractions are found to be phenocryst-enriched whilst the finer size fractions of the concurrent ash fall deposits are glass-enriched and this fractionation is reflected in the deposits' geochemistry. Laser ablation analysis of volcanic glass from Cordón Caulle (Paisley et al., in prep.) indicates these Group 1 elements (e.g. V, Mg, P, Sr, Mn) are lower in concentration than the bulk (crystals + glass) analyses described in Section 3. Furthermore, petrographic studies on other tuffisite samples from Cordón Caulle show that fine-grained laminae within tuffisite veins are often devoid of crystals or fragments when compared to coarser beds (Paisley et al., in prep.). Rare phenocrysts are hosted within clasts with complex banded textures, in coarse-grained beds, or are in the form of microlites within glass shards of different sizes that grew upon ascent. Finally, the crystal content of the Cordón Caulle deposits is relatively low (~5 %), and crystals are commonly found as glomerocrysts (Castro et al., 2013a), which are not widely observed in the tuffisite veins. Thus, we suggest that the preferential fracturing and transport of glass through tuffisites is the cause in the depletions of these elements within veins. This discovery has implications regarding the formation of source material for tuffisites and whether the pressurisation and fragmentation of crystal-poor, vesicular melt at depth results in the preferential movement of the glass-rich shards through propagating fracture networks.

#### 4.4 Isotopic outliers: Samples not in secular equilibrium

Although the majority of samples at both volcanoes are within secular equilibrium there are notable outliers that can be addressed.

##### Chaitén

Bomb B (Exterior) from Chaitén is not in secular equilibrium. Bomb B (Exterior) has a  $(^{226}\text{Ra}) = 42.01 \pm 3.46$  Bq/kg, a value within error of its predicted activity based on its U concentration ( $3.41 \pm 0.19$  ppm). In contrast the Bomb B (Interior) has a lower  $(^{226}\text{Ra})$  than predicted but a  $^{210}\text{Pb}$ - $^{226}\text{Ra}$  ratio within secular equilibrium. Degassing is unlikely the cause of this deficit, as Ra is not a volatile element. Ra is highly incompatible too and Ra partition coefficients are usually smaller than those of Pb. However, an explanation that fractional crystallisation could have played a role in this deficit is implausible as textures show negligible in-situ microlite growth within the bomb. Therefore, the  $^{226}\text{Ra}$  depletion is not readily explained.

##### Cordón Caulle

The tuffisite vein within Bomb 4, representing later hybrid activity, is the only sub-sample to show internal isotope variation with  $(^{210}\text{Pb}/^{226}\text{Ra})_o = 0.90 \pm 0.02$  (Figure 1), and its origin can be decoded using  $(^{210}\text{Pb})_o/\text{Pb}$ . Significant degassing ( $^{222}\text{Rn}$  removal) or fluxing ( $^{222}\text{Rn}$  addition) will decrease or increase this ratio respectively, as common lead is not influenced by this

process (Turner et al., 2004). The vein component of Bomb 4 has a  $(^{210}\text{Pb})_o/\text{Pb} = 0.083 \pm 0.002$ , similar to other Cordon Caulle samples, and  $(^{210}\text{Pb})_o/\text{Pb} \sim 0.086$ . The vein is depleted in total Pb compared to the host (Figure 4), with a ratio of  $\sim 0.9$ , and has a  $(^{210}\text{Pb})_{\text{Vein}}/(^{210}\text{Pb})_{\text{Host}} \sim 0.94$ . In comparison, other veins have a  $(^{210}\text{Pb})_{\text{Vein}}/(^{210}\text{Pb})_{\text{Host}}$  within error of 1. Thus, the vein's reduced  $(^{210}\text{Pb})_o$  may result from extraction of total lead (all isotopes, not only  $^{210}\text{Pb}$ ) during a later degassing event, e.g. during fracturing and vein formation, and not prior degassing. Only one sample, Bomb 5, has a  $^{210}\text{Pb}$  excess relative to  $^{226}\text{Ra}$ ,  $(^{210}\text{Pb}/^{226}\text{Ra})_o = 1.19 \pm 0.17$  (Figure 2). Its  $(^{210}\text{Pb})_o/\text{Pb} = 0.107 \pm 0.006$  which is significantly higher than the average and could indicate abundant gas streaming. Adsorption of Po and Pb from the outgassing vapour by the vesicular sample within the vent would account for its elevated ratios.

#### **4.5 Why is degassing preserved differently at Chaitén and Cordon Caulle?**

Trace elements have recorded a clear signal of degassing. Chaitén veins have volatile trace element enrichments whilst Cordon Caulle veins have some enrichments but also have depletions (e.g. Bomb 4). This initially appears counterintuitive as the veins at both volcanoes act as gas flow pathways whilst the fractures are open and thus similar gas flow signatures might be expected. We suggest that the difference in the depth of upper conduit fracturing at the two volcanoes can explain the contrasting signatures. Fracturing at Chaitén is thought to range from the surface to a depth of  $\sim 500$  m with extensive connectivity (Castro et al., 2014, Saubin et al., 2016, Farquharson et al., 2017). In contrast, at Cordon Caulle extensive fracturing has been shown to occur in the near surface environment ( $< 20$  m), only extending down to  $\sim 200$  m (Schipper et al., 2013, Castro et al., 2016). Farquharson et al. (2017) suggest that veins will undergo different degassing regimes depending on the relative timescales of three



processes: fluid flow ( $\tau_{Da}$ ), porosity reduction (i.e. compaction,  $\tau_C$ ); and volatile exchange with the sintering melt ( $\tau_D$ ). Providing  $\tau_C > \tau_{Da}$ , veins sit in an outgassing regime as pore fluid pressures continually equilibrate as compaction occurs. If  $\tau_{Da} > \tau_C$  then pore pressure equilibrium is not maintained, and veins will undergo either volatile exchange with the melt ( $\tau_{Da} > \tau_C > \tau_D$ ) or pore pressure increases ( $\tau_{Da} > \tau_D > \tau_C$ ) which results in favourable conditions for explosive fragmentation. This is summarised by a critical permeability threshold ( $k_{cr}$ ). If fracture permeability ( $k_f$ ) is less than or equal to  $k_{cr}$  it implies pore fluid pressures will increase and potentially result in explosive fragmentation. Although initially  $k_f$  is high, compaction and sintering reduces this value with time, tending towards the magma's initial permeability ( $k_o$ ) (Kolzenburg et al., 2012, Farquharson et al., 2017).

In shallower environments Farquharson et al. (2017) predict that fractures would sit in an outgassing regime as lower pressures result in lower  $k_{cr}$  values and longer  $\tau_D$  times. Fractures remain open longer, before compaction reduces their permeability so that  $k_f < k_{cr}$ , and more time would be required for volatiles to diffusively resorb into the sintering vein particles and element enrichment occurring. This matches observations from Cordon Caulle. Low  $H_2O$  groundmass concentrations and oxidation suggest fracturing and quenching are occurring at shallower depths than Chaitén (<200 m vs <500 m), and there is direct outgassing to the atmosphere from certain fractures (Schipper et al., 2013, Castro et al., 2014, Castro et al., 2016). We observe minimal elemental enrichments (with the exception of Bi) suggesting less interaction between particles and the gas phase (due to longer  $\tau_D$ ). Furthermore, as stated by Farquharson et al. (2017) Cordon Caulle has a relatively high calculated  $k_{cr}$  which would result in frequent pressure build ups (when  $k_f < k_{cr}$ ), incomplete sintering (as observed in Figure 1) and frequent explosions (as observed by Schipper et al. (2013)). Thus, elemental enrichments in tuffisite veins in early Cordon Caulle bombs are unlikely the result of diffusive absorption

of volatiles but it is unclear if adsorption processes would occur under these conditions. Thus, Tl and Bi enrichments could be due to shards having higher concentrations prior to entrainment in the vein (a richer Tl and Bi source melt) or elemental adsorption. Depletions in the Bomb 4 vein could be the result of diffusion out of glass shards (element scavenging as observed at Torfajökull by Berlo et al. (2013)), which could be resolved by in situ analysis. At Chaitén bombs are excavated from deeper (Castro et al., 2014) and veins record vertical clast transport over hundreds of metres (Berlo et al., 2013, Saubin et al., 2016). Such conditions would result in higher  $k_{cr}$  values and shorter  $\tau_D$  times than Cerdón Caulle, and be ideal for volatile exchange (Farquharson et al., 2017). Veins equilibrate with trapped gases in isolated pockets as particles sinter, exchanging volatiles and resulting in enrichments (see Figure 3), before entering the pore pressure increase regime ( $\tau_{Da} > \tau_D > \tau_C$ ) where pressure build-up results in fragmentation and bomb ejection. Differing gas compositions and eruptive temperatures would also influence the exchange of volatile species, as well as which elements are available to exchange.

Studying trace elemental variation in tuffisite veins, brecciated conduit margins, and shear zones at other volcanoes would aid in understanding the depth to which these channels are open, available for degassing, and their role in the trace metal budget of eruptions. This would be a particularly useful approach to look at near-surface degassing processes occurring during fracturing and dome formation, where volatiles such as H<sub>2</sub>O would have already been largely lost. This study also has implications in the study of vapours as a method of metal transport, e.g. Williams-Jones and Heinrich (2005) and van Hinsberg et al. (2016), highlighting that deeper veins forming during volcanic activity appear to show more metal enrichments than their shallower counterparts.

## 5. Conclusions

Our study of tuffisite veins from the two recent rhyolitic eruptions provides an insight into how syn-eruptive physical processes, such as degassing, are geochemically preserved. Although both Chaitén and Cordon Caulle have undergone gas streaming it is recorded differently in trace elements and isotopes. Cu enrichments record gas streaming and volatile exchange at Chaitén. At Cordon Caulle trace element depletions (e.g. Cd, In, Pb and Tl) indicate degassing during fracturing events. However, no systematic evidence of degassing has been preserved in the isotope record at either volcano, suggesting degassing events were of insufficient duration and efficiency for the formation of disequilibria between  $^{210}\text{Pb}$  and  $^{226}\text{Ra}$ . The lack of  $^{210}\text{Pb}$  excesses preserved in veins from both eruptions allows us to calculate an upper limit on the magma mass being degassed by individual tuffisite veins during these eruptions. We have also shown that other physical processes, such as the preferential movement of glass over crystals, can be chemically preserved in tuffisites.

This study reinforces the idea that trace elements are valuable tools for understanding syn-eruptive physical processes, particularly at systems with erupted deposits depleted in major volatiles such as  $\text{H}_2\text{O}$  (e.g. Cordon Caulle). By analysing for a wide suite of elements, both non-volatile and volatile, it is possible to distinguish between degassing processes and physical processes redistributing clasts, crystals and glass during fracturing and vein formation. It is also possible to discriminate between early degassing events (preserved within clasts in veins) and syn-fracture degassing by analysing the different components of individual tuffisites. This method of analysis could be easily applied to other volcanoes to assess the role of fracturing in

degassing in different volcanic environments and be extended to the micron-scale using in situ methods.

## **6. Acknowledgements**

RP would like to thank Alex Corgne, Nicolas Vergara Pontigo and Felipe Ignacio P. Gallardo for assistance in the field; Anna Jung and André Poirier for instrument assistance; and Vincent van Hinsberg for constructive analytical advice. The authors appreciate constructive comments on an earlier manuscript from Jacqueline Owen, Jamie Farquharson, and from an anonymous reviewer and the rapid and thorough reviews on this manuscript from Fabian Wadsworth and an anonymous reviewer. RP was supported by travel and research grants from the Mineralogical Association of Canada and the Geological Society of America. This work is supported by a NSERC Discovery Grant to KB. Certain samples from Cordón Caulle (Flow 1, Bomb 1 and Bomb 2) and Chaitén (Bombs A and B) were collected during fieldwork supported by the European Research Council under the European Union's Seventh Framework Programme FP7/2007-2013 grant agreement No 307356 to KB. HT and KB would like to thank Jon Castro, Ian Schipper, Fabian Wadsworth, Amy Chadderton and Peter Sammonds for their time and assistance in the field. HT is supported by a Royal Society University Research Fellowship and thanks Sports Centre and Facilities staff at Lancaster University for assistance.

Declarations of Interest: none

## 7. References

- AMIGO, A., LARA, L. E. & SMITH, V. C. 2013. Holocene record of large explosive eruptions from Chaitén and Michinmahuida Volcanoes, Chile. *Andean Geology*, 40, 227-248.
- BATEMAN, H. The solution of a system of differential equations occurring in the theory of radioactive transformations. *Proc. Cambridge Philos. Soc*, 1910. 423-427.
- BELOUSOVA, E., GRIFFIN, W., O'REILLY, S. Y. & FISHER, N. 2002. Igneous zircon: trace element composition as an indicator of source rock type. *Contributions to Mineralogy and Petrology*, 143, 602-622.
- BERLO, K., TUFFEN, H., SMITH, V. C., CASTRO, J. M., PYLE, D. M., MATHER, T. A. & GERAKI, K. 2013. Element variations in rhyolitic magma resulting from gas transport. *Geochimica et Cosmochimica Acta*, 121, 436-451.
- BERLO, K. & TURNER, S. 2010.  $^{210}\text{Pb}$ – $^{226}\text{Ra}$  disequilibria in volcanic rocks. *Earth and Planetary Science Letters*, 296, 155-164.
- BERLO, K., TURNER, S., BLUNDY, J., BLACK, S. & HAWKESWORTH, C. 2006. Tracing pre-eruptive magma degassing using ( $^{210}\text{Pb}/^{226}\text{Ra}$ ) disequilibria in the volcanic deposits of the 1980–1986 eruption of Mount St. Helens. *Earth and Planetary Science Letters*, 249, 337-349.
- BOEHNKE, P., WATSON, E. B., TRAIL, D., HARRISON, T. M. & SCHMITT, A. K. 2013. Zircon saturation re-revisited. *Chemical Geology*, 351, 324-334.
- BOURDON, B., GEOCHEMICAL, S. & MINERALOGICAL SOCIETY OF, A. 2003. *Uranium-series geochemistry*, [St. Louis, Mo.]; Washington, DC, Geochemical Society ; Mineralogical Society of America.

- CABRERA, A., WEINBERG, R. F., WRIGHT, H. M. N., ZLOTNIK, S. & CAS, R. A. F. 2010. Melt fracturing and healing: A mechanism for degassing and origin of silicic obsidian. *Geology*, 39, 67-70.
- CASTRO, J. M., BINDEMAN, I. N., TUFFEN, H. & IAN SCHIPPER, C. 2014. Explosive origin of silicic lava: Textural and  $\delta D-H_2O$  evidence for pyroclastic degassing during rhyolite effusion. *Earth and Planetary Science Letters*, 405, 52-61.
- CASTRO, J. M., CORDONNIER, B., SCHIPPER, C. I., TUFFEN, H., BAUMANN, T. S. & FEISEL, Y. 2016. Rapid laccolith intrusion driven by explosive volcanic eruption. *Nat Commun*, 7, 13585.
- CASTRO, J. M., CORDONNIER, B., TUFFEN, H., TOBIN, M. J., PUSKAR, L., MARTIN, M. C. & BECHTEL, H. A. 2012. The role of melt-fracture degassing in defusing explosive rhyolite eruptions at volcán Chaitén. *Earth and Planetary Science Letters*, 333-334, 63-69.
- CASTRO, J. M. & DINGWELL, D. B. 2009. Rapid ascent of rhyolitic magma at Chaiten volcano, Chile. *Nature*, 461, 780-3.
- CASTRO, J. M., SCHIPPER, C. I., MUELLER, S. P., MILITZER, A. S., AMIGO, A., PAREJAS, C. S. & JACOB, D. 2013a. Storage and eruption of near-liquidus rhyolite magma at Cordón Caulle, Chile. *Bulletin of Volcanology*, 75:202.
- CASTRO, J. M., SCHIPPER, C. I., TUFFEN, H., JAMES, M. R. & MILITZER, A. S. 2013b. Reassembling a volcanic conduit using bombs at Cordón Caulle, Chile. *IAVCEI 2013 Scientific Assembly*. Kagoshima, Japan.
- CHURAKOV, S. V., TKACHENKO, S. I., KORZHINSKII, M. A., BOCHARNIKOV, R. E. & SHMULOVICH, K. I. 2000. Evolution of Composition of High-Temperature Fumarolic Gases from Kudryavy Volcano, Iturup, Kuril Islands: the Thermodynamic Modeling. *Geochemistry International*, 38, 436-451.

- CONDOMINES, M., SIGMARSSON, O. & GAUTHIER, P. J. 2010. A simple model of  $^{222}\text{Rn}$  accumulation leading to  $^{210}\text{Pb}$  excesses in volcanic rocks. *Earth and Planetary Science Letters*, 293, 331-338.
- CUNNINGHAM, H. S., TURNER, S. P., PATIA, H., WYSOCZANSKI, R., NICHOLS, A. R. L., EGGINS, S. & DOSSETO, A. 2009. ( $^{210}\text{Pb}/^{226}\text{Ra}$ ) variations during the 1994–2001 intracaldera volcanism at Rabaul Caldera. *Journal of Volcanology and Geothermal Research*, 184, 416-426.
- EDMONDS, M. 2008. New geochemical insights into volcanic degassing. *Philos Trans A Math Phys Eng Sci*, 366, 4559-79.
- EICHELBERGER, J. C., CARRIGAN, C. R., WESTRICH, H. R. & PRICE, R. H. 1986. Non-explosive silicic volcanism. *Nature*, 323, 598-602.
- FARQUHARSON, J. I., HEAP, M. J., LAVALLÉE, Y., VARLEY, N. R. & BAUD, P. 2016. Evidence for the development of permeability anisotropy in lava domes and volcanic conduits. *Journal of Volcanology and Geothermal Research*, 323, 163-185.
- FARQUHARSON, J. I., WADSWORTH, F. B., HEAP, M. J. & BAUD, P. 2017. Time-dependent permeability evolution in compacting volcanic fracture systems and implications for gas overpressure. *Journal of Volcanology and Geothermal Research*, 339, 81-97.
- FUJIMAKI, H. 1986. Partition coefficients of Hf, Zr, and REE between zircon, apatite, and liquid. *Contributions to Mineralogy and Petrology*, 94, 42-45.
- GAUTHIER, P.-J. & CONDOMINES, M. 1999.  $^{210}\text{Pb}$ – $^{226}\text{Ra}$  radioactive disequilibria in recent lavas and radon degassing: inferences on the magma chamber dynamics at Stromboli and Merapi volcanoes. *Earth and Planetary Science Letters*, 172, 111-126.
- GAUTHIER, P.-J., CONDOMINES, M. & HAMMOUDA, T. 1999. An experimental investigation of radon diffusion in an anhydrous andesitic melt at atmospheric pressure:

- implications for radon degassing from erupting magmas. *Geochimica et Cosmochimica Acta*, 63, 645-656.
- GHALEB, B., PONS-BRANCHU, E. & DESCHAMPS, P. 2004. Improved method for radium extraction from environmental samples and its analysis by thermal ionization mass spectrometry. *Journal of Analytical Atomic Spectrometry*, 19, 906-910.
- GONNERMANN, H. M. & MANGA, M. 2003. Explosive volcanism may not be an inevitable consequence of magma fragmentation. *Nature*, 426, 432-435.
- GONNERMANN, H. M. & MANGA, M. 2007. The Fluid Mechanics Inside a Volcano. *Annual Review of Fluid Mechanics*, 39, 321-356.
- HEAP, M. J., FARQUHARSON, J. I., WADSWORTH, F. B., KOLZENBURG, S. & RUSSELL, J. K. 2015. Timescales for permeability reduction and strength recovery in densifying magma. *Earth and Planetary Science Letters*, 429, 223-233.
- HEIKEN, G., WOHLLETZ, K. & EICHELBERGER, J. 1988. Fracture fillings and intrusive pyroclasts, Inyo Domes, California. *Journal of Geophysical Research: Solid Earth*, 93, 4335-4350.
- HINKLEY, T. K., LE CLOAREC, M. F. & LAMBERT, G. 1994. Fractionation of families of major, minor, and trace metals across the melt-vapor interface in volcanic exhalations. *Geochimica et Cosmochimica Acta*, 58, 3255-3263.
- HORWELL, C. J., BRANÄA, L. P., SPARKS, R. S. J., MURPHY, M. D. & HARDS, V. L. 2001. A geochemical investigation of fragmentation and physical fractionation in pyroclastic flows from the Soufrière Hills volcano, Montserrat. *Journal of Volcanology and Geothermal Research*, 109, 247-262.
- JAUPART, C. & ALLÈGRE, C. J. 1991. Gas content, eruption rate and instabilities of eruption regime in silicic volcanoes. *Earth and Planetary Science Letters*, 102, 413-429.



- JAY, J., COSTA, F., PRITCHARD, M., LARA, L., SINGER, B. & HERRIN, J. 2014. Locating magma reservoirs using InSAR and petrology before and during the 2011–2012 Cordón Caulle silicic eruption. *Earth and Planetary Science Letters*, 395, 254-266.
- KAYZAR, T. M., COOPER, K. M., REAGAN, M. K. & KENT, A. J. R. 2009. Gas transport model for the magmatic system at Mount Pinatubo, Philippines: Insights from (210Pb)/(226Ra). *Journal of Volcanology and Geothermal Research*, 181, 124-140.
- KENDRICK, J. E., LAVALLÉE, Y., VARLEY, N. R., WADSWORTH, F. B., LAMB, O. D. & VASSEUR, J. 2016. Blowing Off Steam: Tuffisite Formation As a Regulator for Lava Dome Eruptions. *Frontiers in Earth Science*, 4:41.
- KOLZENBURG, S., HEAP, M. J., LAVALLÉE, Y., RUSSELL, J. K., MEREDITH, P. G. & DINGWELL, D. B. 2012. Strength and permeability recovery of tuffisite-bearing andesite. *Solid Earth*, 3, 191-198.
- LAMBERT, G., LE CLOAREC, M. F., ARDOUIN, B. & LE ROULLEY, J. C. 1985. Volcanic emission of radionuclides and magma dynamics. *Earth and Planetary Science Letters*, 76, 185-192.
- LOWENSTERN, J. B., BLEICK, H., VAZQUEZ, J. A., CASTRO, J. M. & LARSON, P. B. 2012. Degassing of Cl, F, Li, and Be during extrusion and crystallization of the rhyolite dome at Volcán Chaitén, Chile during 2008 and 2009. *Bulletin of Volcanology*, 74, 2303-2319.
- MACKENZIE, J. M. & CANIL, D. 2008. Volatile heavy metal mobility in silicate liquids: Implications for volcanic degassing and eruption prediction. *Earth and Planetary Science Letters*, 269, 488-496.
- MAGNALL, N., JAMES, M. R., TUFFEN, H. & VYE-BROWN, C. 2017. Emplacing a Cooling-Limited Rhyolite Lava Flow: Similarities with Basaltic Lava Flows. *Frontiers in Earth Science*, 5, 44.

- MAGNALL, N., JAMES, M. R., TUFFEN, H., VYE-BROWN, C., SCHIPPER, C. I., CASTRO, J. M. & DAVIES, A. G. 2018. The origin and evolution of breakouts in a cooling-limited rhyolite lava flow. *GSA Bulletin*.
- MAJOR, J. J. & LARA, L. E. 2013. Overview of Chaitén Volcano, Chile, and its 2008-2009 eruption. *Andean Geology*, 40, 196-215.
- MATHER, T. A., WITT, M. L. I., PYLE, D. M., QUAYLE, B. M., AIUPPA, A., BAGNATO, E., MARTIN, R. S., SIMS, K. W. W., EDMONDS, M., SUTTON, A. J. & ILYINSKAYA, E. 2012. Halogens and trace metal emissions from the ongoing 2008 summit eruption of Kīlauea volcano, Hawai'i. *Geochimica et Cosmochimica Acta*, 83, 292-323.
- OKUMURA, S., NAKAMURA, M., NAKANO, T., UESUGI, K. & TSUCHIYAMA, A. 2010. Shear deformation experiments on vesicular rhyolite: Implications for brittle fracturing, degassing, and compaction of magmas in volcanic conduits. *Journal of Geophysical Research*, 115, B06201.
- OKUMURA, S. & SASAKI, O. 2014. Permeability reduction of fractured rhyolite in volcanic conduits and its control on eruption cyclicity. *Geology*, 42, 843-846.
- PALLISTER, J. S., DIEFENBACH, A. K., BURTON, W. C., MUÑOZ, J., GRISWOLD, J. P., LARA, L. E., LOWENSTERN, J. B. & VALENZUELA, C. E. 2013. The Chaitén rhyolite lava dome: Eruption sequence, lava dome volumes, rapid effusion rates and source of the rhyolite magma. *Andean Geology*, 40, 277-294.
- PISTOLESI, M., CIONI, R., BONADONNA, C., ELISSONDO, M., BAUMANN, V., BERTAGNINI, A., CHIARI, L., GONZALES, R., ROSI, M. & FRANCALANCI, L. 2015. Complex dynamics of small-moderate volcanic events: the example of the 2011 rhyolitic Cordón Caulle eruption, Chile. *Bulletin of Volcanology*, 77:3.

- PLAIL, M., EDMONDS, M., HUMPHREYS, M.C.S., BACLAY, J., HERD, R.A., 2014. Geochemical evidence for relict degassing pathways preserved in andesite. *Earth Planet. Sci. Lett.* 386, 21–33. <https://doi.org/10.1016/j.epsl.2013.10.044>
- POKROVSKI, G. S., BORISOVA, A. Y. & BYCHKOV, A. Y. 2013. Speciation and Transport of Metals and Metalloids in Geological Vapors. *Reviews in Mineralogy and Geochemistry*, 76, 165-218.
- REAGAN, M., TEPLEY, F. J., GILL, J. B., WORTEL, M. & HARTMAN, B. 2005. Rapid time scales of basalt to andesite differentiation at Anatahan volcano, Mariana Islands. *Journal of Volcanology and Geothermal Research*, 146, 171-183.
- SAUBIN, E., TUFFEN, H., GURIOLI, L., OWEN, J., CASTRO, J. M., BERLO, K., MCGOWAN, E. M., SCHIPPER, C. I. & WEHBE, K. 2016. Conduit Dynamics in Transitional Rhyolitic Activity Recorded by Tuffisite Vein Textures from the 2008–2009 Chaitén Eruption. *Frontiers in Earth Science*, 4:59.
- SCHIPPER, C. I., CASTRO, J. M., TUFFEN, H., JAMES, M. R. & HOW, P. 2013. Shallow vent architecture during hybrid explosive–effusive activity at Cordón Caulle (Chile, 2011–12): Evidence from direct observations and pyroclast textures. *Journal of Volcanology and Geothermal Research*, 262, 25-37.
- SILVA PAREJAS, C. L., L. E.; BERTIN, D.; AMIGO, A.; OROZCO, G. 2012. The 2011–2012 eruption of Cordón Caulle volcano (Southern Andes): Evolution, crisis management and current hazards. *EGU General Assembly 2012*. Vienna, Austria.
- STASIUK, M. V., BARCLAY, J., CARROLL, M. R., JAUPART, C., RATTE, J. C., SPARKS, R. S. J. & TAIT, S. R. 1996. Degassing during magma ascent in the Mule Creek vent (USA). *Bulletin of volcanology.*, 58, 117.
- SYMONDS, R. B., ROSE JR, W. I., REED, M. H., LICHTER, F. E. & FINNEGAN, D. L. 1987. Volatilization, transport and sublimation of metallic and non-metallic elements in high

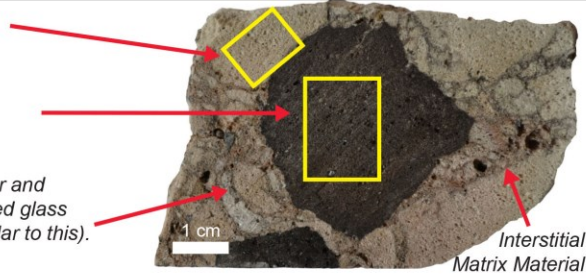
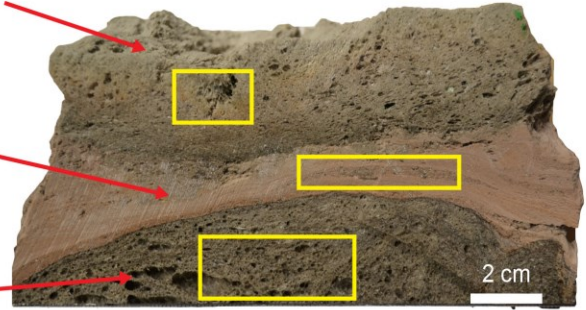
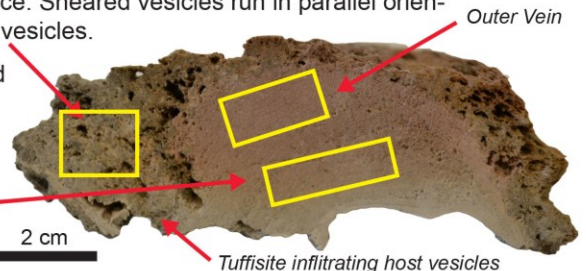
- temperature gases at Merapi Volcano, Indonesia. *Geochimica et Cosmochimica Acta*, 51, 2083-2101.
- THOMAS, J. B., BODNAR, R. J. , SHIMIZU, N., CHESNER, C. A.; 2003. Melt Inclusions in Zircon. *Reviews in Mineralogy and Geochemistry*, 53, 63-87.
- TUFFEN, H. & DINGWELL, D. 2005. Fault textures in volcanic conduits: evidence for seismic trigger mechanisms during silicic eruptions. *Bulletin of Volcanology*, 67, 370-387.
- TUFFEN, H., DINGWELL, D. B. & PINKERTON, H. 2003. Repeated fracture and healing of silicic magma generate flow banding and earthquakes? *Geology*, 31, 1089-1092.
- TUFFEN, H., JAMES, M. R., CASTRO, J. M. & SCHIPPER, C. I. 2013. Exceptional mobility of an advancing rhyolitic obsidian flow at Cordon Caulle volcano in Chile. *Nat Commun*, 4, 2709.
- TURNER, S., BLACK, S. & BERLO, K. 2004.  $^{210}\text{Pb}$ – $^{226}\text{Ra}$  and  $^{228}\text{Ra}$ – $^{232}\text{Th}$  systematics in young arc lavas: implications for magma degassing and ascent rates. *Earth and Planetary Science Letters*, 227, 1-16.
- VAN HINSBERG, V. J., BERLO, K., MIGDISOV, A. A. & WILLIAMS-JONES, A. E. 2016.  $\text{CO}_2$ -fluxing collapses metal mobility in magmatic vapour. *Geochemical Perspectives Letters*, 2, 169-177.
- WAHRENBERGER, C., SEWARD, T. M. & DIETRICH, V. 2002. Volatile trace-element transport in high-temperature gases from Kudriavy volcano (Itrup, Kurile Islands, Russia). *The Water-Rock Interactions, Ore Deposits, and Environmental Geochemistry: A tribute to David A. Crerar*.
- WEBSTER, J. D. 1990. Partitioning of F between  $\text{H}_2\text{O}$  and  $\text{CO}_2$  fluids and topaz rhyolite melt. *Contributions to Mineralogy and Petrology*, 104, 424-438.
- WHITE, W. M. 2013. *Geochemistry*, John Wiley & Sons.

- WILLIAMS-JONES, A. E. & HEINRICH, C. A. 2005. 100th Anniversary Special Paper: Vapor Transport of Metals and the Formation of Magmatic-Hydrothermal Ore Deposits. *Economic Geology*, 100, 1287-1312.
- WILLIAMS-JONES, A. E., MIGDISOV, A. A., ARCHIBALD, S. M. & XIAO, Z. 2002. Vapor-transport of ore metals. *The Water-Rock Interactions, Ore Deposits, and Environmental Geochemistry: A tribute to David A. Crerar*.
- ZAJACZ, Z., HALTER, W. E., PETTKE, T. & GUILLONG, M. 2008. Determination of fluid/melt partition coefficients by LA-ICPMS analysis of co-existing fluid and silicate melt inclusions: Controls on element partitioning. *Geochimica et Cosmochimica Acta*, 72, 2169-2197.
- ZELENSKI, M. E., FISCHER, T. P., DE MOOR, J. M., MARTY, B., ZIMMERMANN, L., AYALEW, D., NEKRASOV, A. N. & KARANDASHEV, V. K. 2013. Trace elements in the gas emissions from the Erta Ale volcano, Afar, Ethiopia. *Chemical Geology*, 357, 95-116.

## 8. Tables and Figures

Figure 1:

Summary of key textural features of samples from Cordón Caulle (Flow 1 & Bombs 1-5) and Chaitén (Bombs A & B). Sub-samples are noted in bold and briefly described. Additional descriptions in italics. Yellow boxes are representative of material analysed for each sub-sample.

	Size	Sub-Sample Descriptions	Sub-Sample Interpretations
Cordón Caulle	Flow 1 ~10 cm sub-sample of northern breakout lobe	Breakout lobe at flow front. Breakouts are described by Schipper et al. (2015) and Magnall et al. (2018) as vesiculated obsidian with ~40 % plagioclase and 10 % pyroxene microlites set in a glass groundmass. No tuffisite veins are present in the flow samples. Vesicles in this sample are <1 cm in size, are elongate to spherical, and coated with vapour-deposited cristobalite.	Parallel cristobalite bands are thought to record vesicle collapse.
	Bomb 1 ~10 cm sub-sample of a ~30 cm scale bread-crustured bomb	<p><b>Beige:</b> Rounded to elongate cm-sized clasts. Vesicle size increases towards clast centre.</p> <p><b>Black:</b> Rarer clasts, both vesiculated and dense clasts present.</p> <p><i>Interstitial matrix material is dark-grey to black in colour and forms sintered veins between larger clasts. Fine-grained glass can be oxidised to orange-red in certain samples (similar to this).</i></p> 	No tuffisite vein present but breccia bombs resemble tuffisite vein fill material. It is likely breccias represent the same process fracturing and gas fluxing process in the upper conduit as tuffisites.
	Bomb 2 Sub-sample of a ~1.5 m scale bread-crustured bomb	<p><b>Exterior:</b> A metre-scale grey pumice bomb. Quenched, light grey, vesiculated (mm-sized) pumice. Melt rinds at the vein-host interface.</p> <p><b>Vein:</b> Located near bomb rim, 1-3 cm wide. Pale pink colour (oxidation), with fine and coarse-grained laminations and some inflated clasts. Subsidiary and injections veins present offshooting from main vein.</p> <p><b>Interior:</b> Vesicles (10s cm) due to bomb expansion post-ejection. Smaller vesicles &lt;1 cm from vein walls result of local syn-eruptive or post-eruptive degassing into vein. Volatile depleted melt foamed less than bomb interior far from vein.</p> 	Melt rinds at vein-host interface could be due to shearing or material quenching upon ejection. Tuffisite textures indicative of fluidised flow. Inflated clasts within beds of coarse-grained fill indicate material of different volatile contents were tapped when fracture was open and have subsequently inflated differently as bomb was ejected. Vein shape altered by melt relaxation and bomb inflation.
	Bomb 3 ~15 cm long pumice bomb with large ash-filled vesicles	<p><b>Host:</b> Highly sheared, vesiculated tube pumice. Sheared vesicles run in parallel orientation to vein. Tuffisite material found in host vesicles.</p> <p><b>Outer Vein:</b> Pale pink (oxidation), fine-grained sintered ash in concave laminations. Tuffisite material is variably sintered.</p> <p><b>Inner Vein:</b> Sintered ash, colour grades from orange to white.</p> 	Tuffisite infiltrating into host implies host vesicularity developed and connected prior to tuffisite formation. Changing vein colour suggests it started open to the atmosphere (and was heavily oxidised) becoming less open (and oxidised) with time.



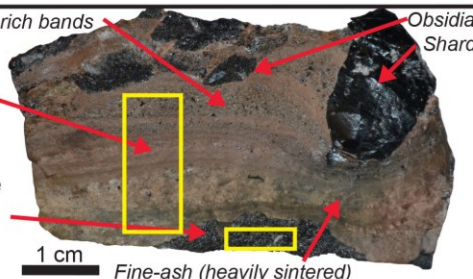
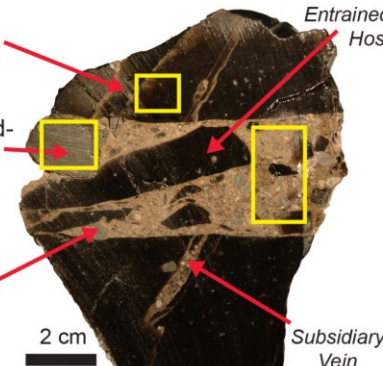

		Size	Sub-Sample Descriptions	Sub-Sample Interpretations
Cordón Caulle	<b>Bomb 4</b>	~15 cm bomb fragment	<p><b>Vein:</b> Multiple pink-orange laminations distinguished by variable particle sintering, particle-size, % obsidian shard and vesicularity. Banding deflected around large, dense-obsidian shards.</p> <p><b>Host:</b> Black vesiculated obsidian. Melt relaxation at the host-vein interface (not shown). Vesicles (mm-sized) and rare mm-sized plagioclase crystals are observed.</p> 	Observations from this and other tuffisite veins at Cordón Caulle suggest later veins have more variability in vein components.
	<b>Bomb 5</b>	~8 cm wide small vesicular bomb	Black vesicular bomb fragment with no vein. The bomb rim is quenched and vesicles are mm scale. There are rare plagioclase crystals visible (1-2 mm in size). Material adhered to the outside of the samples is oxidised ash and mm-sized obsidian shards (surface material was not analysed). The cone structure around the vein is predominantly composed of pumice bombs, grey and black in colour, varying from cm scale to metre scale.	Ash and obsidian shards were likely welded to the bomb surface when they were still hot.
Chaitén	<b>Bomb A</b>	Sub-sample from a ~0.5 m wide dense obsidian bomb	<p><b>Host:</b> Dense obsidian, hosting a 3 cm-wide tuffisite vein and subsidiary veins. Host, vein and clasts are described in detail by Saubin et al. (2016).</p> <p><b>Banded Clast:</b> cm-sized, sub-rounded clast with uneven boundaries. Have greatest size range of vein clasts (mm to cm sized) and most irregular shapes. Are heterogeneous with glassy and SiO<sub>2</sub>-enriched bands (~93 wt. %). Latter bands correspond to fractured areas, have greater porosity and crystallinity.</p> <p><b>Vein:</b> ~3 cm wide, parallel-walled vein composed of banded (~35 %), dense (~42 %) and vesicular (~22 %) clasts in a fine-grained, oxidised matrix.</p> 	SiO <sub>2</sub> -enriched bands interpreted as zones of cristobalite precipitation. Banded Clast interpreted as non-juvenile material from previous activity in caldera.  <b>Vein Matrix</b> represents isolated matrix. <b>Vein Matrix &amp; Clasts</b> represents bulk vein.
	<b>Bomb B</b>	Two ~30 cm sub-samples from a ~1.5 m bomb with dense rind and pumiceous core	<p><b>Exterior:</b> 2-8 cm dense, glassy rind, cracks &lt;10 cm into interior. Grades into pumice interior. Thin black bands of glass are found in the transition zone between the bomb and interior. Open (&lt;10 cm deep) cooling fractures in rind.</p> <p><b>Interior:</b> Elongate clasts of white pumice surrounded by mm-wide grey bands of dense glass. There is visible micro-porosity in the interior of clasts. Secondary bread-crusting (&lt;1 cm) can be found on the surface of some of the white pumice clasts. Sample comes from an area with more abundant grey bands in the bomb interior. Interior also has &lt;10 cm long open fractures.</p> 	



Table 1:

Activities and activity ratios (back calculated to time of eruptions) of samples and sub-samples analysed via alpha spectrometry ( $^{210}\text{Pb}$ ) and TIMS ( $^{226}\text{Ra}$ ).

Sample ID	$(^{210}\text{Pb})_0$ (Bq/kg)	$\pm 2$ SD (Bq/kg)	$(^{226}\text{Ra})$ (Bq/kg)	$\pm 2$ SD (Bq/kg)	$(^{210}\text{Pb}/^{226}\text{Ra})_0$	$\pm 2$ SD
Bomb A Host	37.16	2.88	35.58	1.25	1.04	0.09
Bomb A Vein Matrix & Clasts	38.07	3.15	36.01	2.67	1.06	0.12
Bomb A Vein Matrix	38.73	7.32	38.72	2.35	1.00	0.20
Bomb A Banded Clast	36.55	4.76	39.98	1.40	0.91	0.12
Bomb B Interior	36.79	3.34	35.77	2.65	1.03	0.12
Bomb B Exterior Flow 1	34.85	4.34	42.01	3.46	0.83	0.12
Bomb 1 Black	29.91	4.16	28.25	2.14	1.06	0.17
Bomb 1 Beige	30.30	2.58	29.49	2.21	1.03	0.12
Bomb 2 Exterior	29.52	2.27	29.17	0.35	1.01	0.08
Bomb 2 Vein	31.51	1.98	30.53	0.41	1.03	0.07
Bomb 2 Interior	30.65	2.97	32.07	0.71	0.96	0.09
Bomb 3 Host	29.31	1.30	30.07	0.37	0.97	0.04
Bomb 3 Outer Vein	31.16	0.81	30.16	2.32	1.03	0.08
Bomb 3 Inner Vein	31.54	2.22	31.41	1.86	1.00	0.09
Bomb 4 Host	30.15	2.55	29.72	0.36	1.01	0.09
Bomb 4 Vein	28.57	2.94	28.81	0.56	0.99	0.10
Bomb 5	26.81	0.43	29.62	0.36	0.90	0.02
BCR-2*	36.85	3.47	29.45	0.36	1.19	0.17
	21.62	1.49	21.74	3.22		

\*Average values for BCR-2, 5 duplicates were run for  $^{210}\text{Pb}$  and 3 duplicates were run for  $^{226}\text{Ra}$ .

Figure 2:

$(^{210}\text{Pb}/^{226}\text{Ra})_o$  versus (a)  $(^{210}\text{Pb})_o$  and (b)  $(^{226}\text{Ra})$  showing the excesses and deficits in the Cordón Caulle samples (white) are solely due to  $^{210}\text{Pb}$  variation. Chaitén samples (black) show  $^{226}\text{Ra}$  variability. Annotations are outliers discussed in Section 4.4. The red box denotes a 10 % error window, equivalent to the average two standard deviation value on calculated ratios in Table 1.

Table 1.

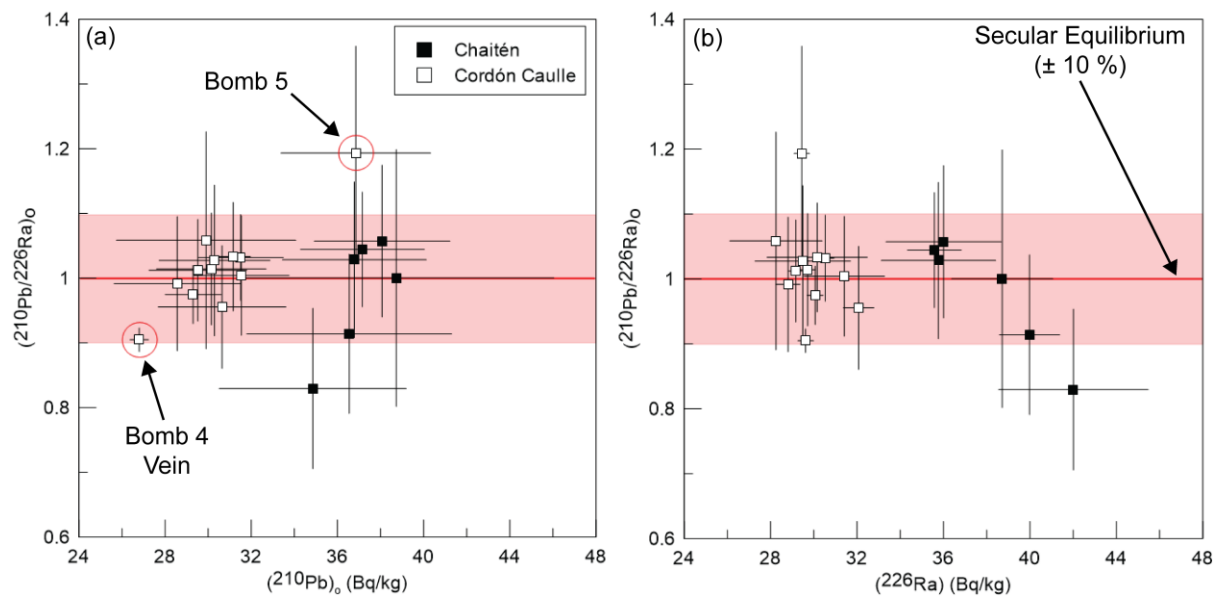


Figure 3:

Select elemental concentrations of Vein Matrix, Vein Matrix & Clasts (bulk tuffisite) and Banded Clast normalised to Bomb A Host composition (Chaitén Volcano). Depletions in HFSEs and volatile elements (e.g. Mo, Li, Bi) are evident in both clast and vein samples, as is Cu enrichment in the vein. Errors are 2 standard deviation.

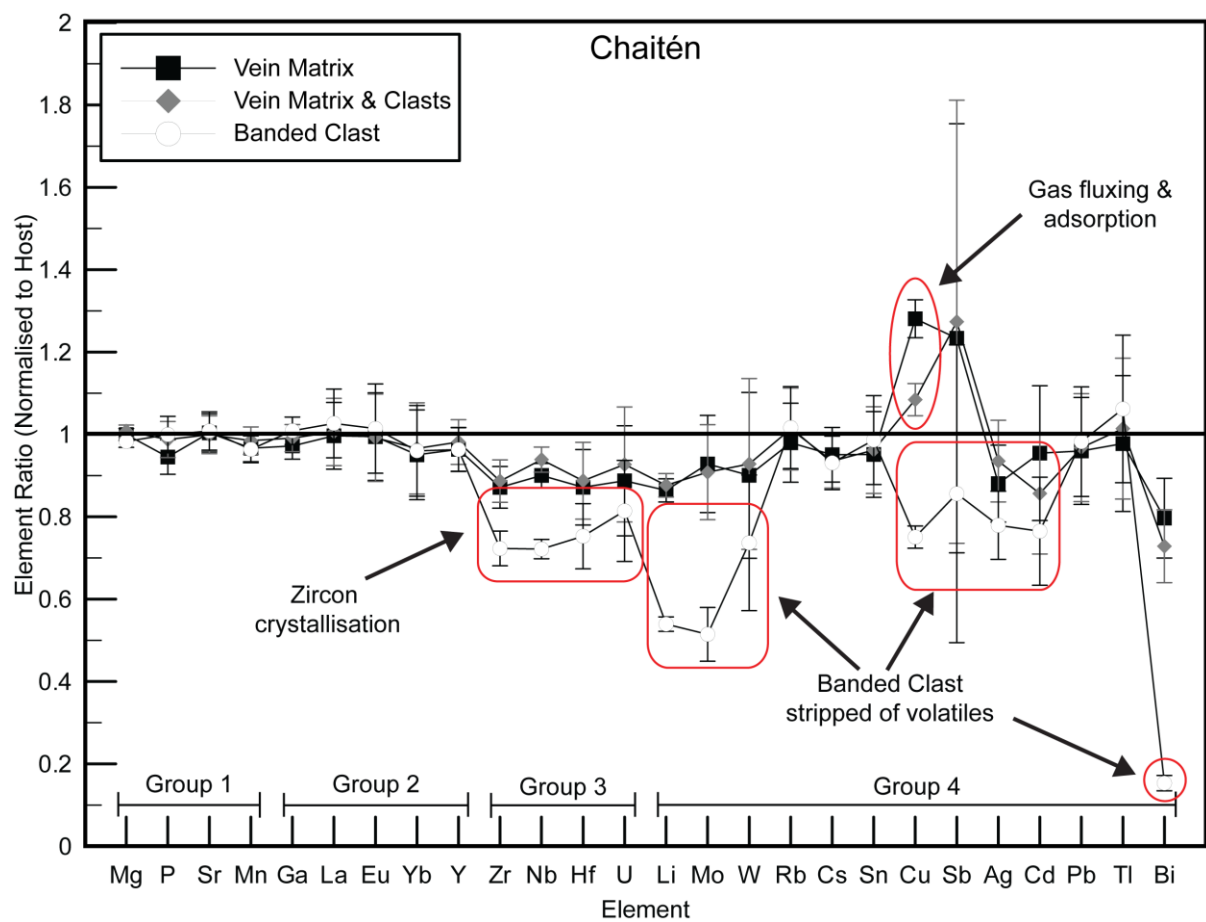


Figure 4:

Element concentrations from select tuffisite veins from Cordón Caulle normalised to host composition. Bomb 2 (vein) is normalised to Bomb 2 (Interior) concentration (black squares). Bomb 3 (Outer Vein) is normalised to Bomb 3 (Host) (grey diamonds) and the Bomb 4 (vein) is normalised to Bomb 4 (Host) (white circles). Errors are 2 standard deviation.

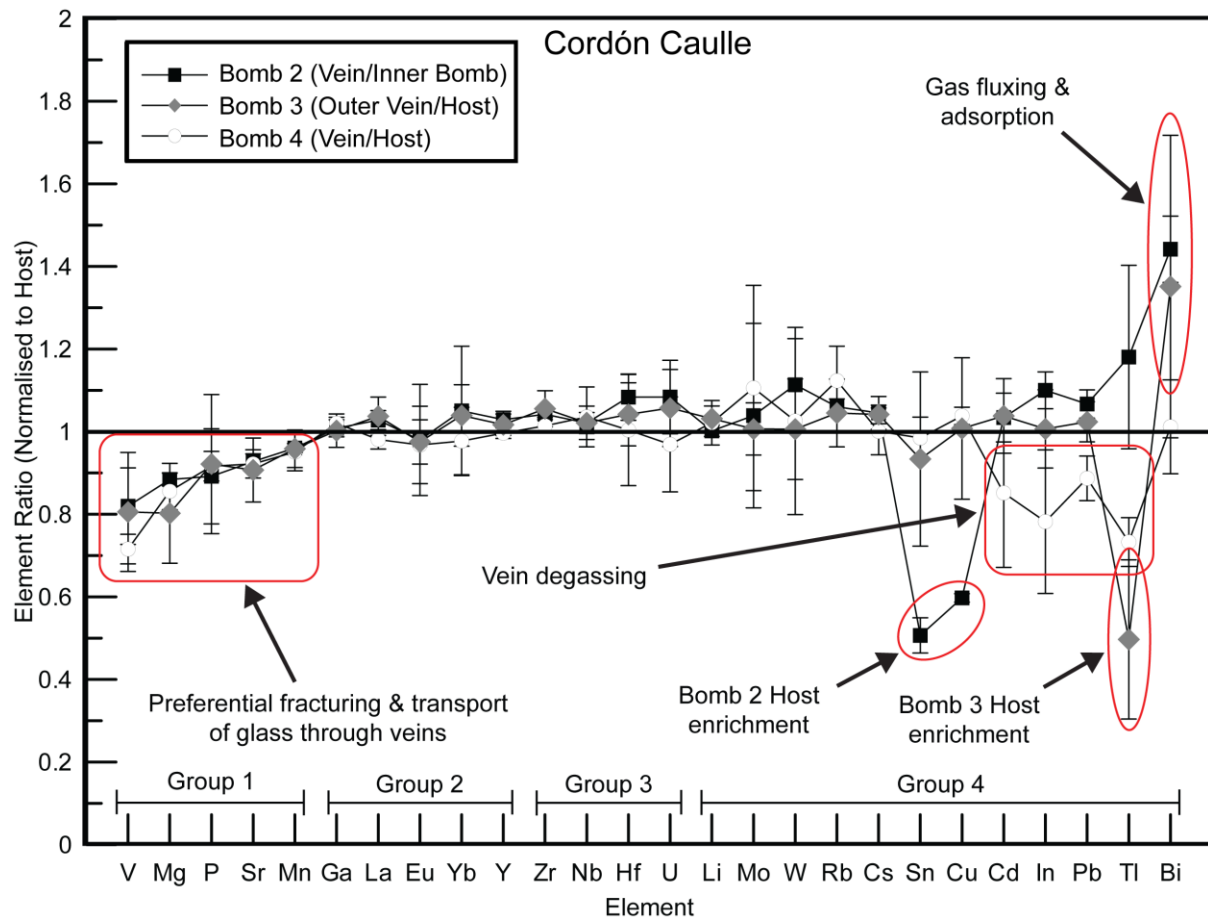


Figure 5:

Schematic model of a fracture sourcing Rn from a degassing cell. Yellow arrows indicate gas transfer in and out of the fracture. Magma fluxes ( $\Phi_o$ ) into a degassing cell that has a mass,  $M_d$ , and Ra activity,  $(Ra)_d$ , and volatiles exsolve. Volatiles, including Rn, are extracted from the degassing cell and into the fracture (mass,  $M_a$ , and Ra activity,  $(Ra)_a$ ),  $f$  denotes the fraction of Rn extracted from the degassing cell. Volatiles outgas through the fracture to the surface,  $f'$  denotes the fraction of Rn lost from the fracture. This model assumes all Rn that enters the fracture comes solely from the degassing cell and not the tuffisite host thus calculated mass ratios (R values) can be used to estimate the upper limit of the volume size of the degassing cell.

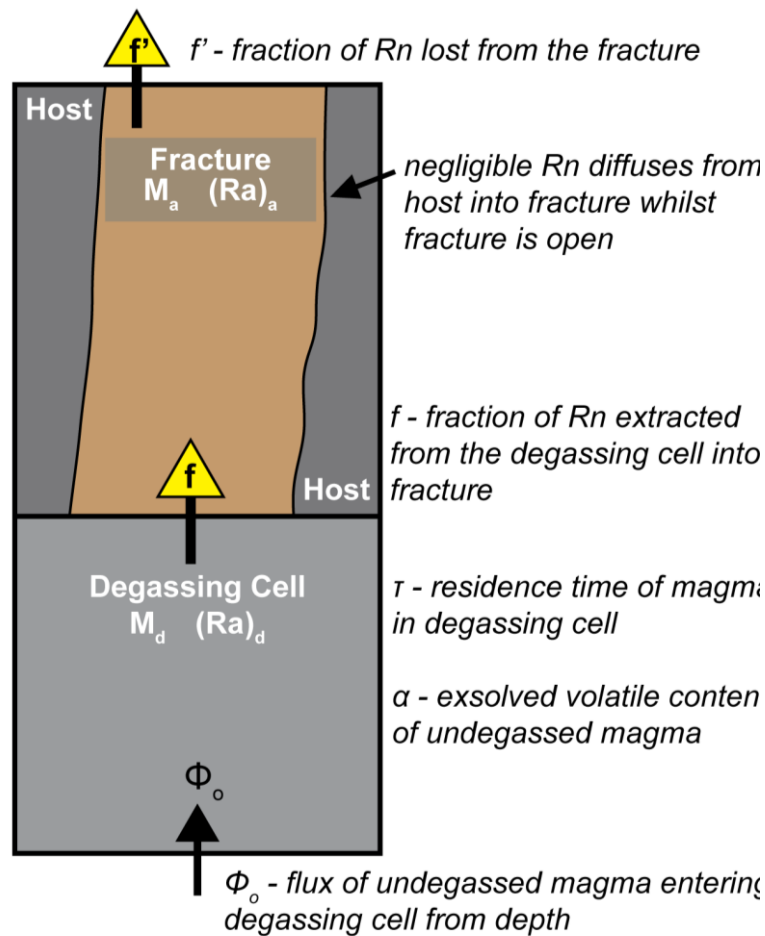
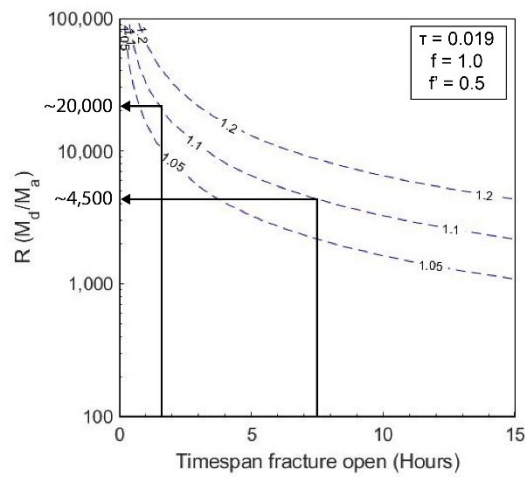


Figure 6:

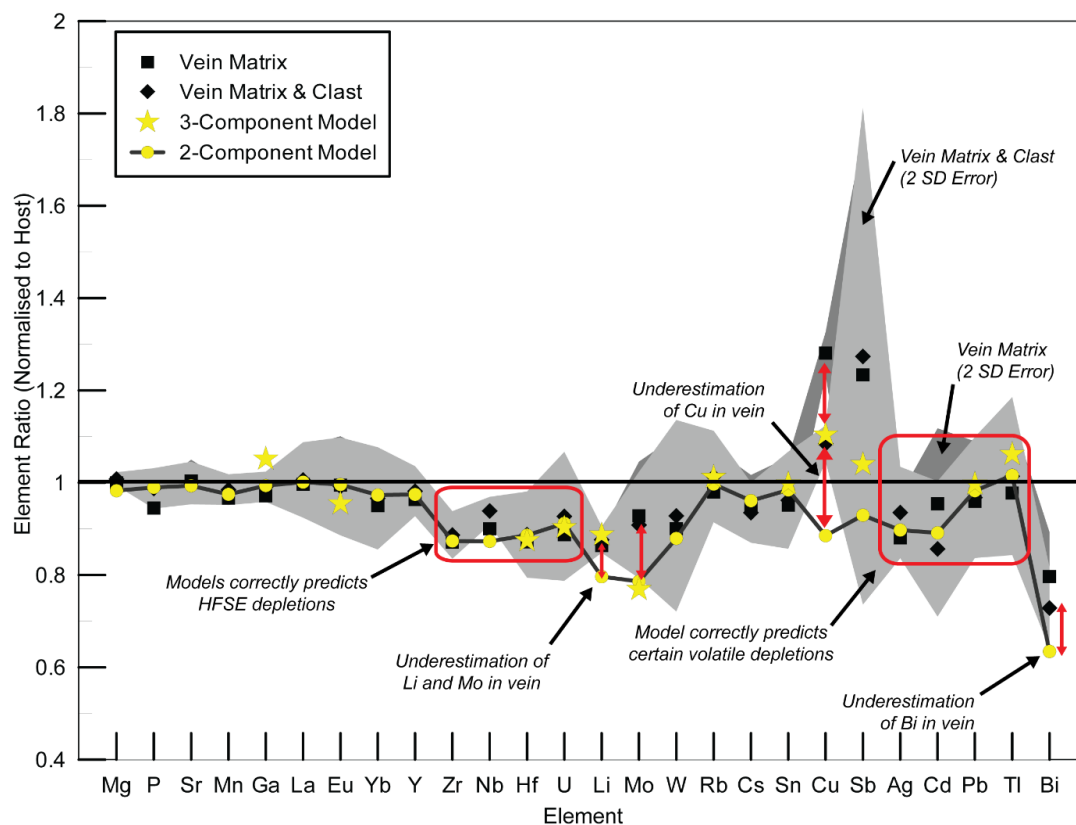
Contoured plot showing required R values to generate certain ( $^{210}\text{Pb}/^{226}\text{Ra}$ ) for a known fracture lifespan assuming  $\tau = 0.019$ ,  $f = 1$  and  $f' = 0.5$ . Black lines highlight the required R values, given minimum (1.6 hour) and maximum (7.5 hour) lifespan estimates of example fractures from Chaitén, to generate a ( $^{210}\text{Pb}/^{226}\text{Ra}$ ) = 1.10 (see Section 4.2) (Castro et al., 2012).



## 9. Supplementary Figure

Figure S.1:

Select elemental concentrations of Vein Matrix (black squares), Vein Matrix & Clasts (bulk tuffisite, black diamonds) and predicted vein concentrations from a three-component (yellow stars) and two-component (yellow circles) model normalised to Bomb A Host composition (Chaitén Volcano). Shaded zones represent 2 SD errors on vein-host ratios. Three-component model data only available for elements analysed in vesicular clasts by Berlo et al. (2013). With the exception of Nb, both models correctly predict the calculated vein-host ratio for HFSE suggesting depletions are the result of banded clast entrainment in the vein. Underestimation of volatile elements (red arrows) such as Mo, Cu and Bi are the result of these elements being added to the vein via gas streaming.



## **10. Appendices**

### **Appendix A: Trace Element Data and 2SD Errors**



Table A.1: Elemental concentrations (ppm) of samples from Chaitén and Cordon Caulle analysed via ICP-MS. Li concentrations were calculated from  $^6\text{Li}$  values using the natural abundance ratio of  $^6\text{Li}/^7\text{Li}$ . \*Average value of the 2 duplicates run for BCR -2.

<b>Sample ID</b>	<b>Li</b>	<b>Be</b>	<b>Mg</b>	<b>P</b>	<b>Sc</b>	<b>V</b>	<b>Cr</b>	<b>Mn</b>	<b>Co</b>	<b>Ni</b>	<b>Cu</b>	<b>Zn</b>
Bomb A Host	47.3	1.92	1560	260	3.0	3.3	0.4	426	1.03	0.62	4.23	35.6
Bomb A Matrix	40.9	1.80	1560	246	3.3	3.4	1.4	412	1.09	1.68	5.41	34.0
Bomb A Matrix & Clasts	41.4	1.91	1573	257	3.8	3.7	0.5	419	1.09	0.76	4.58	35.1
Bomb A Banded Clast	25.5	1.93	1534	260	3.4	3.0	0.2	410	0.98	4.32	3.17	34.5
Bomb B Interior	47.4	1.95	1559	253	3.4	3.5	0.3	429	1.04	0.51	4.18	35.4
Bomb B Exterior	47.7	1.95	1581	263	3.4	3.2	0.5	433	1.03	0.46	4.18	36.0
Flow 1	23.8	2.20	3653	585	15.2	12.1	<d.l.	860	3.48	0.66	18.51	81.7
Bomb 1 Black	22.8	2.13	3719	655	14.6	14.0	2.8	858	3.65	5.50	25.56	81.3
Bomb 1 Beige	23.5	2.16	3798	611	15.5	12.2	<d.l.	872	3.51	2.15	19.42	81.1
Bomb 2 Exterior	22.8	2.13	3418	577	14.4	12.3	2.1	829	3.35	3.11	20.28	79.5
Bomb 2 Vein	23.4	2.16	3080	505	13.1	8.9	2.3	806	2.92	5.68	18.70	79.2
Bomb 2 Interior	23.3	2.16	3484	567	14.2	10.9	<d.l.	839	3.22	3.33	31.30	78.9
Bomb 3 Host	23.3	2.15	3726	444	15.1	10.9	2.9	849	3.33	3.43	18.85	81.8
Bomb 3 Outer Vein	24.0	2.20	2990	409	13.9	8.8	1.2	813	2.94	3.53	18.99	79.9
Bomb 3 Inner Vein	23.4	2.16	3263	404	14.0	10.6	1.7	821	3.13	3.74	16.84	80.7
Bomb 4 Host	23.1	2.22	3484	567	15.0	11.4	1.3	852	3.31	2.56	17.96	81.5
Bomb 4 Vein	23.6	2.21	2981	519	14.4	8.2	1.2	809	2.91	2.89	18.65	77.8
Bomb 5	23.6	2.19	3467	579	14.8	11.8	1.3	837	3.33	3.16	17.85	80.4
BCR -2*	7.7	1.72	18723	1414	31.5	398.9	13.9	1368	34.01	10.80	17.10	130.3
UTR	50.6	7.82	34	35	2.9	0.4	26.6	695	0.18	1.27	4.60	207.3
Analysed Masses	6	9	24	31	45	51	52	55	59	60	63	66

<b>Sample ID</b>	<b>Ga</b>	<b>Rb</b>	<b>Sr</b>	<b>Y</b>	<b>Zr</b>	<b>Nb</b>	<b>Mo</b>	<b>Ag</b>	<b>Cd</b>	<b>In</b>	<b>Sn</b>	<b>Sb</b>
Bomb A Host	13.6	104.4	140	11.0	101	7.8	1.57	0.20	0.106	0.017	1.89	0.57
Bomb A Matrix	13.2	102.3	141	10.6	88	7.0	1.46	0.18	0.101	0.016	1.79	0.70
Bomb A Matrix & Clasts	13.5	105.8	140	10.8	89	7.3	1.43	0.19	0.091	0.016	1.81	0.73
Bomb A Banded Clast	13.7	106.1	142	10.6	73	5.6	0.81	0.16	0.081	0.015	1.86	0.49
Bomb B Interior	13.4	106.1	137	11.0	101	7.8	1.55	0.20	0.105	0.016	1.83	0.58
Bomb B Exterior	13.7	108.1	143	11.3	105	7.9	1.58	0.20	0.102	0.016	1.92	0.57
Flow 1	18.7	67.6	164	47.7	329	8.9	2.40	0.58	0.267	0.079	2.95	0.79
Bomb 1 Black	18.2	62.2	160	47.0	316	8.7	2.29	0.55	0.269	0.101	4.54	0.79
Bomb 1 Beige	18.3	68.4	160	49.0	326	9.0	2.37	0.59	0.283	0.096	3.40	0.79
Bomb 2 Exterior	18.1	66.9	154	47.5	323	8.8	2.35	0.56	0.266	0.081	3.23	0.82
Bomb 2 Vein	18.5	70.8	142	50.4	343	9.2	2.50	0.61	0.267	0.085	2.95	0.92
Bomb 2 Interior	18.3	66.8	154	49.0	329	9.0	2.41	0.58	0.258	0.077	5.83	0.82
Bomb 3 Host	18.2	66.6	158	46.5	318	8.8	2.40	0.56	0.246	0.067	3.18	0.89
Bomb 3 Outer Vein	18.3	69.6	143	47.2	336	9.0	2.42	0.58	0.256	0.067	2.97	0.83
Bomb 3 Inner Vein	18.1	67.9	150	46.5	325	8.9	2.40	0.58	0.245	0.067	2.74	0.85
Bomb 4 Host	18.1	62.9	159	47.6	324	8.6	2.23	0.58	0.269	0.079	2.98	0.78
Bomb 4 Vein	18.4	70.7	146	47.4	329	8.9	2.47	0.60	0.229	0.062	2.94	0.87
Bomb 5	18.4	67.1	158	47.3	323	8.9	2.41	0.56	0.261	0.078	2.90	0.79
BCR -2*	20.5	41.4	312	30.7	169	11.8	229.68	0.43	0.663	0.084	2.00	0.37
UTR	35.1	130.0	2	110.5	1090	81.5	7.58	1.78	0.867	0.165	9.48	0.17
Analysed Masses	71	85	88	89	90	93	95	107	111	115	118	121

<b>Sample ID</b>	<b>Cs</b>	<b>Ba</b>	<b>La</b>	<b>Ce</b>	<b>Pr</b>	<b>Nd</b>	<b>Sm</b>	<b>Eu</b>	<b>Gd</b>	<b>Tb</b>	<b>Dy</b>	<b>Ho</b>
Bomb A Host	7.15	644	23.9	46.1	4.7	16.0	2.60	0.58	2.41	0.34	1.90	0.38
Bomb A Matrix	6.79	632	23.9	44.8	4.7	15.6	2.51	0.58	2.36	0.33	1.84	0.37
Bomb A Matrix & Clasts	6.68	641	24.1	45.6	4.8	15.9	2.59	0.57	2.44	0.33	1.89	0.38
Bomb A Banded Clast	6.65	644	24.6	46.1	4.8	16.2	2.62	0.59	2.49	0.33	1.89	0.38
Bomb B Interior	7.25	638	23.9	45.5	4.7	15.8	2.57	0.57	2.42	0.34	1.89	0.38
Bomb B Exterior	7.30	648	24.6	46.7	4.9	16.2	2.64	0.58	2.47	0.34	1.93	0.40
Flow 1	4.47	713	29.3	65.7	8.6	35.8	8.09	1.77	8.33	1.39	8.69	1.87
Bomb 1 Black	4.35	693	29.3	66.3	8.6	35.8	8.18	1.73	8.38	1.39	8.79	1.86
Bomb 1 Beige	4.51	698	29.8	67.4	8.7	36.3	8.18	1.73	8.52	1.39	8.82	1.91
Bomb 2 Exterior	4.46	696	29.7	66.2	8.7	36.0	8.16	1.70	8.40	1.38	8.66	1.86
Bomb 2 Vein	4.83	739	31.4	71.9	9.3	38.0	8.82	1.74	9.18	1.46	9.57	2.04
Bomb 2 Interior	4.62	704	30.6	67.7	9.2	36.6	8.48	1.78	8.72	1.42	9.07	1.95
Bomb 3 Host	4.41	684	28.7	64.7	8.2	34.6	7.77	1.60	7.96	1.32	8.40	1.81
Bomb 3 Outer Vein	4.59	715	29.8	66.4	8.6	35.3	8.01	1.56	8.19	1.36	8.59	1.85
Bomb 3 Inner Vein	4.51	702	29.4	65.4	8.3	35.0	7.80	1.62	8.05	1.34	8.56	1.83
Bomb 4 Host	4.59	703	30.3	66.8	8.8	36.2	8.47	1.77	8.53	1.44	9.09	1.95
Bomb 4 Vein	4.59	710	29.7	67.4	8.7	36.0	8.14	1.72	8.33	1.39	8.84	1.91
Bomb 5	4.46	696	29.2	65.9	8.5	35.6	7.99	1.73	8.20	1.35	8.69	1.84
BCR -2*	1.00	607	22.6	47.3	6.2	24.8	6.28	1.95	6.71	1.01	6.24	1.21
UTR	4.75	11	78.4	173.5	20.4	76.1	17.85	1.40	19.25	3.33	20.72	4.35
Analysed Masses	133	137	139	140	141	146	147	153	157	159	163	165

<b>Sample ID</b>	<b>Er</b>	<b>Tm</b>	<b>Yb</b>	<b>Lu</b>	<b>Hf</b>	<b>Ta</b>	<b>W</b>	<b>Tl</b>	<b>Pb</b>	<b>Bi</b>	<b>Th</b>	<b>U</b>
Bomb A Host	1.19	0.18	1.29	0.21	3.09	0.88	4.43	0.52	17.6	0.268	11.62	3.33
Bomb A Matrix	1.14	0.17	1.23	0.19	2.69	0.82	3.99	0.51	16.9	0.214	11.29	2.95
Bomb A Matrix & Clasts	1.18	0.17	1.25	0.20	2.74	0.92	4.11	0.53	17.0	0.195	11.53	3.08
Bomb A Banded Clast	1.15	0.17	1.24	0.20	2.32	0.73	3.26	0.55	17.3	0.041	11.37	2.71
Bomb B Interior	1.19	0.18	1.31	0.21	3.04	0.95	4.37	0.52	17.2	0.282	11.70	3.30
Bomb B Exterior	1.21	0.18	1.33	0.21	3.16	0.88	4.47	0.53	17.6	0.274	12.14	3.41
Flow 1	5.74	0.86	5.89	0.91	8.86	0.82	1.47	0.36	21.3	0.043	8.49	2.37
Bomb 1 Black	5.69	0.86	5.86	0.90	8.78	0.77	1.44	0.48	20.8	0.082	8.24	2.31
Bomb 1 Beige	5.75	0.87	5.83	0.91	8.85	0.78	1.49	0.40	21.3	0.081	8.39	2.34
Bomb 2 Exterior	5.65	0.85	5.85	0.90	8.87	0.75	1.48	0.41	21.1	0.077	8.36	2.33
Bomb 2 Vein	6.18	0.94	6.46	0.99	10.15	0.93	1.79	0.48	24.8	0.083	9.72	2.65
Bomb 2 Interior	6.01	0.89	6.15	0.93	9.36	0.91	1.61	0.41	23.3	0.058	8.93	2.45
Bomb 3 Host	5.51	0.84	5.69	0.89	8.77	0.82	1.49	0.77	20.8	0.148	8.21	2.30
Bomb 3 Outer Vein	5.67	0.86	5.91	0.91	9.13	0.76	1.50	0.38	21.3	0.200	8.50	2.43
Bomb 3 Inner Vein	5.66	0.84	5.86	0.90	8.97	0.81	1.54	0.48	21.1	0.158	8.52	2.35
Bomb 4 Host	5.95	0.88	6.19	0.96	9.26	0.62	1.49	0.41	21.9	0.077	8.67	2.49
Bomb 4 Vein	5.77	0.88	6.05	0.94	9.30	0.83	1.53	0.30	19.4	0.078	8.76	2.41
Bomb 5	5.62	0.85	5.86	0.89	8.93	0.85	1.46	0.39	20.7	0.075	8.26	2.30
BCR -2*	3.60	0.50	3.22	0.49	4.80	1.48	0.70	0.26	8.3	0.061	5.43	1.57
UTR	12.98	1.89	12.48	1.85	24.67	5.36	1.92	0.57	23.1	0.180	16.19	4.88
Analysed Masses	166	169	172	175	178	181	182	205	208	209	232	235

Table A.2: Associated errors (2 SD) of elemental concentrations of samples from Chaitén and Cordón Caulle analysed via ICP-MS. Li concentrations were calculated from  $^6\text{Li}$  values using the natural abundance ratio of  $^6\text{Li}/^7\text{Li}$ . \*Average value of the 2 duplicates run for BCR -2. Errors in ppm.

<b>Sample ID</b>	<b>Li</b>	<b>Be</b>	<b>Mg</b>	<b>P</b>	<b>Sc</b>	<b>V</b>	<b>Cr</b>	<b>Mn</b>	<b>Co</b>	<b>Ni</b>	<b>Cu</b>	<b>Zn</b>
Bomb A Host	1.5	0.07	19.1	10.9	1.6	1.2	0.10	13.8	0.03	0.75	0.13	2.0
Bomb A Matrix	0.4	0.05	12.4	3.7	0.1	0.1	1.11	3.9	0.32	0.22	0.10	0.4
Bomb A Matrix & Clasts	0.4	0.05	12.5	3.9	0.1	0.1	0.42	4.0	0.32	0.10	0.08	0.4
Bomb A Banded Clast	0.2	0.05	12.2	3.9	0.1	0.1	0.17	3.9	0.28	0.57	0.06	0.4
Bomb B Interior	0.4	0.05	12.4	3.8	0.1	0.1	0.27	4.0	0.30	0.07	0.07	0.4
Bomb B Exterior	2.1	0.01	73.2	15.9	0.2	0.3	0.22	15.7	0.03	0.05	0.05	2.1
Flow 1	0.9	0.07	435.7	33.5	1.3	1.3	1.07	34.8	0.19	0.03	0.63	5.0
Bomb 1 Black	0.3	0.04	216.2	52.8	0.3	0.2	0.11	39.3	0.21	2.00	0.04	1.3
Bomb 1 Beige	0.6	0.04	710.7	83.2	1.4	2.2	0.32	100.7	0.55	0.44	1.30	4.2
Bomb 2 Exterior	1.0	0.08	203.5	11.2	0.8	0.8	1.67	23.2	0.10	0.38	2.01	2.1
Bomb 2 Vein	0.2	0.05	37.3	45.9	1.1	0.7	1.34	6.5	0.29	0.41	0.22	0.8
Bomb 2 Interior	0.2	0.05	43.4	52.1	1.1	0.9	0.47	6.8	0.33	0.25	0.39	0.8
Bomb 3 Host	0.2	0.04	472.6	44.0	1.4	1.2	2.35	27.4	0.22	2.49	2.24	1.9
Bomb 3 Outer Vein	0.7	0.15	243.6	62.8	0.2	1.2	0.82	28.3	0.18	2.12	2.30	2.7
Bomb 3 Inner Vein	1.1	0.07	575.2	42.1	1.0	1.9	1.07	47.4	0.32	0.15	0.37	2.5
Bomb 4 Host	1.1	0.25	78.2	15.1	0.4	0.4	0.05	12.2	0.10	0.59	0.33	1.2
Bomb 4 Vein	0.4	0.14	140.5	14.9	0.8	0.3	0.11	36.9	0.08	0.92	0.15	2.7
Bomb 5	0.6	0.13	77.9	16.0	0.3	0.5	0.05	4.8	0.06	0.02	0.06	0.2
<b>Average %RSD</b>	<b>1%</b>	<b>2%</b>	<b>3%</b>	<b>3%</b>	<b>4%</b>	<b>5%</b>	<b>25%</b>	<b>2%</b>	<b>6%</b>	<b>13%</b>	<b>2%</b>	<b>1%</b>
Analysed Masses	6	9	24	31	45	51	52	55	59	60	63	66

<b>Sample ID</b>	<b>Ga</b>	<b>Rb</b>	<b>Sr</b>	<b>Y</b>	<b>Zr</b>	<b>Nb</b>	<b>Mo</b>	<b>Ag</b>	<b>Cd</b>	<b>In</b>	<b>Sn</b>	<b>Sb</b>
Bomb A Host	0.4	10.2	6.3	0.6	5.8	0.2	0.18	0.02	0.018	0.0042	0.2	0.05
Bomb A Matrix	0.2	0.9	1.4	0.1	0.8	0.1	0.08	0.01	0.004	0.0003	0.1	0.29
Bomb A Matrix & Clasts	0.2	0.9	1.4	0.1	0.8	0.1	0.07	0.01	0.004	0.0003	0.1	0.30
Bomb A Banded Clast	0.2	0.9	1.4	0.1	0.6	0.1	0.04	0.01	0.003	0.0002	0.1	0.20
Bomb B Interior	0.2	0.9	1.4	0.1	0.9	0.1	0.08	0.01	0.004	0.0003	0.1	0.24
Bomb B Exterior	0.2	5.4	5.4	0.4	4.3	0.3	0.06	0.01	0.003	0.0010	0.2	0.01
Flow 1	1.5	1.0	8.4	3.3	23.8	0.6	0.24	0.06	0.033	0.0087	0.1	0.09
Bomb 1 Black	0.001	10.6	15.0	1.8	15.3	0.1	0.30	0.02	0.003	0.0033	0.2	0.06
Bomb 1 Beige	1.0	2.9	7.3	4.7	4.1	0.6	0.09	0.05	0.027	0.0035	0.3	0.02
Bomb 2 Exterior	0.3	0.9	2.6	0.4	7.2	0.3	0.08	0.06	0.028	0.0009	0.5	0.16
Bomb 2 Vein	0.3	0.9	2.0	0.7	1.8	0.2	0.38	0.08	0.011	0.0025	0.2	0.19
Bomb 2 Interior	0.3	0.8	2.2	0.7	1.7	0.2	0.36	0.08	0.010	0.0022	0.3	0.17
Bomb 3 Host	0.5	4.0	10.1	0.8	10.4	0.3	0.14	0.04	0.021	0.0045	0.6	0.21
Bomb 3 Outer Vein	0.6	3.5	8.1	0.9	8.5	0.2	0.05	0.02	0.005	0.0044	0.4	0.06
Bomb 3 Inner Vein	0.5	1.3	11.4	1.3	3.8	0.1	0.03	0.05	0.003	0.0075	0.1	0.07
Bomb 4 Host	0.2	1.3	1.9	0.5	2.3	0.2	0.16	0.23	0.057	0.0024	0.1	0.18
Bomb 4 Vein	0.1	5.1	5.1	0.4	4.3	0.6	0.52	0.04	0.002	0.0136	0.1	0.01
Bomb 5	0.5	1.0	2.9	1.1	6.4	0.04	0.15	0.05	0.010	0.0032	0.1	0.01
<b>Average %RSD</b>	<b>1%</b>	<b>2%</b>	<b>2%</b>	<b>1%</b>	<b>1%</b>	<b>1%</b>	<b>4%</b>	<b>5%</b>	<b>3%</b>	<b>3%</b>	<b>4%</b>	<b>9%</b>
Analysed Masses	71	85	88	89	90	93	95	107	111	115	118	121

<b>Sample ID</b>	<b>Cs</b>	<b>Ba</b>	<b>La</b>	<b>Ce</b>	<b>Pr</b>	<b>Nd</b>	<b>Sm</b>	<b>Eu</b>	<b>Gd</b>	<b>Tb</b>	<b>Dy</b>	<b>Ho</b>
Bomb A Host	0.49	44.4	1.9	3.6	0.46	0.9	0.3	0.05	0.3	0.026	0.2	0.04
Bomb A Matrix	0.10	4.7	0.3	0.6	0.09	0.2	0.1	0.04	0.1	0.033	0.1	0.02
Bomb A Matrix & Clasts	0.10	4.8	0.3	0.6	0.10	0.2	0.1	0.04	0.1	0.033	0.1	0.02
Bomb A Banded Clast	0.10	4.8	0.3	0.6	0.10	0.2	0.1	0.04	0.1	0.033	0.1	0.02
Bomb B Interior	0.11	4.8	0.3	0.6	0.09	0.2	0.1	0.04	0.1	0.034	0.1	0.02
Bomb B Exterior	0.34	35.4	1.2	2.1	0.23	0.7	0.1	0.03	0.1	0.019	0.1	0.01
Flow 1	0.22	64.4	2.8	5.5	0.87	3.2	0.9	0.18	0.9	0.139	0.9	0.18
Bomb 1 Black	0.10	6.8	1.0	0.2	0.05	0.9	0.1	0.05	0.2	0.018	0.1	0.02
Bomb 1 Beige	0.24	29.2	1.4	2.8	1.08	1.3	0.3	0.12	0.3	0.063	0.3	0.06
Bomb 2 Exterior	0.13	15.0	0.2	1.6	0.17	0.8	0.2	0.02	0.3	0.023	0.3	0.06
Bomb 2 Vein	0.13	8.9	0.5	1.2	0.44	0.7	0.3	0.17	0.3	0.152	0.5	0.12
Bomb 2 Interior	0.12	8.4	0.5	1.1	0.43	0.7	0.3	0.17	0.3	0.147	0.5	0.11
Bomb 3 Host	0.03	30.4	1.0	1.9	0.74	0.9	0.4	0.07	0.4	0.077	0.4	0.08
Bomb 3 Outer Vein	0.10	13.5	0.9	0.9	0.03	0.3	0.2	0.05	0.1	0.005	0.1	0.02
Bomb 3 Inner Vein	0.01	7.9	0.4	1.6	0.56	1.0	0.2	0.07	0.1	0.011	0.2	0.02
Bomb 4 Host	0.10	4.4	0.4	0.3	0.15	0.4	0.2	0.12	0.2	0.357	0.2	0.23
Bomb 4 Vein	0.24	10.0	0.6	2.2	0.28	0.4	0.5	0.12	0.3	0.088	0.7	0.16
Bomb 5	0.14	9.6	1.4	1.6	0.41	1.3	0.4	0.10	0.5	0.102	0.4	0.14
<b>Average %RSD</b>	<b>1%</b>	<b>1%</b>	<b>2%</b>	<b>1%</b>	<b>2%</b>	<b>1%</b>	<b>2%</b>	<b>3%</b>	<b>2%</b>	<b>4%</b>	<b>2%</b>	<b>3%</b>
Analysed Masses	133	137	139	140	141	146	147	153	157	159	163	165

<b>Sample ID</b>	<b>Er</b>	<b>Tm</b>	<b>Yb</b>	<b>Lu</b>	<b>Hf</b>	<b>Ta</b>	<b>W</b>	<b>Tl</b>	<b>Pb</b>	<b>Bi</b>	<b>Th</b>	<b>U</b>
Bomb A Host	0.11	0.020	0.1	0.024	0.3	0.1	0.55	0.069	2.4	0.029	1.6	0.458
Bomb A Matrix	0.07	0.039	0.1	0.072	0.1	0.6	0.74	0.054	0.3	0.011	0.2	0.181
Bomb A Matrix & Clasts	0.07	0.039	0.1	0.073	0.1	0.7	0.76	0.056	0.3	0.010	0.2	0.189
Bomb A Banded Clast	0.07	0.040	0.1	0.073	0.1	0.6	0.61	0.059	0.3	0.002	0.2	0.166
Bomb B Interior	0.07	0.041	0.1	0.078	0.1	0.8	0.81	0.055	0.3	0.015	0.2	0.203
Bomb B Exterior	0.05	0.005	0.1	0.010	0.1	0.03	0.27	0.027	1.1	0.020	0.4	0.186
Flow 1	0.47	0.084	0.6	0.103	0.9	0.3	0.19	0.077	1.3	0.014	0.8	0.306
Bomb 1 Black	0.04	0.005	0.1	0.001	0.2	0.2	0.05	0.133	0.3	0.036	0.2	0.089
Bomb 1 Beige	0.49	0.005	0.4	0.015	0.3	0.1	0.01	0.001	0.7	0.0002	0.3	0.055
Bomb 2 Exterior	0.04	0.023	0.1	0.030	0.3	0.2	0.22	0.073	0.5	0.010	0.2	0.037
Bomb 2 Vein	0.90	0.039	0.7	0.070	0.4	0.2	0.13	0.064	0.6	0.003	0.3	0.155
Bomb 2 Interior	0.87	0.036	0.6	0.065	0.3	0.2	0.11	0.055	0.5	0.002	0.3	0.141
Bomb 3 Host	0.30	0.035	0.4	0.045	0.6	0.2	0.16	0.267	0.9	0.038	0.4	0.188
Bomb 3 Outer Vein	0.07	0.003	0.1	0.006	0.3	0.1	0.09	0.067	0.4	0.018	0.2	0.080
Bomb 3 Inner Vein	0.18	0.018	0.2	0.016	0.1	0.1	0.11	0.043	0.2	0.010	0.3	0.010
Bomb 4 Host	0.17	0.216	0.2	0.304	0.4	0.7	0.33	0.031	0.8	0.004	0.4	0.230
Bomb 4 Vein	0.29	0.066	0.5	0.041	1.2	0.5	0.05	0.008	0.9	0.008	1.0	0.179
Bomb 5	0.19	0.069	0.2	0.058	0.6	0.1	0.08	0.009	1.3	0.001	0.5	0.175
<b>Average %RSD</b>	<b>3%</b>	<b>5%</b>	<b>3%</b>	<b>7%</b>	<b>2%</b>	<b>19%</b>	<b>5%</b>	<b>6%</b>	<b>2%</b>	<b>5%</b>	<b>2%</b>	<b>0.031</b>
Analysed Masses	166	169	172	175	178	181	182	205	208	209	232	235



## Appendix B: Details of Equations in Section 4.2

### Arriving at Equation (4)

Following the approach of Condomines et al. (2010), the  $^{222}\text{Rn}$  variation per unit time in the fracture is given by:

$$\frac{d(\text{Rn})_a}{dt} = \frac{1}{M_a} [(\phi_{\text{Rn}}^{\text{in}}) - (\phi_{\text{Rn}}^{\text{out}})] + \lambda_{\text{Rn}}(\text{Ra})_a - \lambda_{\text{Rn}}(\text{Rn})_a \quad (1)$$

Where  $\phi_{\text{Rn}}^{\text{in}}$  and  $\phi_{\text{Rn}}^{\text{out}}$  are defined as the flux of Rn in and out of the accumulating cell, in this case the fracture preserved as the tuffisite vein.  $M_a$  is the mass of the tuffisite vein;  $\lambda_{\text{Rn}}$  is the decay constant of Rn; and  $(\text{Ra})_a$  and  $(\text{Rn})_a$  are the  $^{226}\text{Ra}$  and  $^{222}\text{Rn}$  activities of the tuffisite material respectively. The parameters  $f$  and  $f'$  denote the fraction of Rn effectively extracted from the degassing magma cell, and accumulating magma cell respectively:

$$f = \frac{(\phi_{\text{Rn}}^{\text{in}})}{[\lambda_{\text{Rn}}M_d + (1-\alpha)\phi_0](\text{Ra})_d} \quad (2)$$

$$f' = \frac{(\phi_{\text{Rn}}^{\text{out}})}{[\lambda_{\text{Rn}}M_a(\text{Ra})_a + (\phi_{\text{Rn}}^{\text{in}})]} = \frac{(\phi_{\text{Rn}}^{\text{out}})}{[\lambda_{\text{Rn}}M_a(\text{Ra})_a + f(\lambda_{\text{Rn}}M_d + (1-\alpha)\phi_0)(\text{Ra})_d]} \quad (3)$$

Where  $M_d$  is the mass of the degassing cell,  $\alpha$  is the volatile content of the undegassed magma,  $\phi_0$  is the influx of undegassed magma into the degassing reservoir and  $(\text{Ra})_d$  is the  $^{226}\text{Ra}$  activity of the degassing cell (see Fig. 5). Substituting equations (2) and (3) into equation (1) and expanding the terms results in:

$$\begin{aligned} \frac{d(Rn)_a}{dt} = & \frac{f\lambda_{Rn}M_d(Ra)_d}{M_a} + \frac{f(1-\alpha)\phi_0(Ra)_d}{M_a} - \frac{f'\lambda_{Rn}M_a(Ra)_a}{M_a} - \frac{ff'\lambda_{Rn}M_d(Ra)_d}{M_a} \\ & - \frac{ff'(1-\alpha)\phi_0(Ra)_d}{M_a} + \lambda_{Rn}(Ra)_a - \lambda_{Rn}(Rn)_a \end{aligned}$$

This can be simplified by introducing the parameters (1) mass ratio,  $R = M_d/M_a$  and (2) residence time,  $\tau = M_d/\phi_0$  (and thus  $\phi_0/M_a = R/\tau$ ), as suggested by Condomines et al. (2010), and restricting our model to  $(Ra)_a = (Ra)_d$ , thus the equation becomes:

$$\begin{aligned} \frac{d(Rn)_a}{dt} = & \frac{f\lambda_{Rn}R(Ra)_a}{\tau} + \frac{f(1-\alpha)R(Ra)_a}{\tau} - \frac{f'\lambda_{Rn}(Ra)_a}{\tau} - \frac{ff'\lambda_{Rn}R(Ra)_a}{\tau} \\ & - \frac{ff'(1-\alpha)R(Ra)_a}{\tau} + \lambda_{Rn}(Ra)_a - \lambda_{Rn}(Rn)_a \end{aligned}$$

This equation is condensed to:

$$\frac{d(Rn)_a}{dt} = \lambda_{Rn}(Ra)_a \left[ (1-f') + \left( fR(1-f') + \frac{fR(1-\alpha)}{\lambda_{Rn}\tau}(1-f') \right) \right] - \lambda_{Rn}(Rn)_a$$

And finally, to:

$$\frac{d(Rn)_a}{dt} = \left[ (1-f') \left( 1 + fR \left( 1 + \frac{(1-\alpha)}{\lambda_{Rn}\tau} \right) \right) \right] \lambda_{Rn}(Ra)_a - \lambda_{Rn}(Rn)_a$$

The changing ( $^{222}\text{Rn}$ ) with time is then be represented by equation (4):

$$\frac{d(\text{Rn})_a}{dt} = \lambda_{\text{Rn}}(\text{Ra})_a C - \lambda_{\text{Rn}}(\text{Rn})_a \quad (4)$$

Where:

$$C = (1 - f') \left[ 1 + fR \left[ 1 + \frac{(1 - \alpha)}{\lambda_{\text{Rn}}\tau} \right] \right] \quad (5)$$

This modified equation takes into account the additional  $^{222}\text{Rn}$  from the decay of  $^{226}\text{Ra}$  in the degassing cell, the  $^{222}\text{Rn}$  lost from the fracture, and  $^{222}\text{Rn}$  that comes from the decay of  $^{226}\text{Ra}$  in the tuffisite material within the fracture.

### **Equations underpinning Part One of the Rn Model**

Part One of the model assumes Rn is added to the fracture via a gas phase (flux in) and some is also lost from the fracture (flux out). These are assumed to be average fluxes for the period the fracture is open. During this period (<36 hours in the model, T) there will be some decay of Rn and the model assumes that any resultant  $^{210}\text{Pb}$  is instantly resorbed into particles in the fracture. The half-life of  $^{222}\text{Rn}$  is 3.8 days, significantly longer than the fracture lifespan (according to all previous studies of the timescale of tuffisite opening e.g. Castro et al. (2012), Berlo et al. (2013)), the contribution of excess  $^{210}\text{Pb}$  instantly resorbed into the melt particles in the vein during this phase is negligible. The vast contribution of  $^{222}\text{Rn}$ , and thus  $^{210}\text{Pb}$ , which results in the excess is acquired in Part Two (see below). Gas that enters the fracture will be rich in Rn, and although much gas is lost (a high  $f'$  value) volatiles will become trapped in pore

space during progressive compaction and densification of the vein, which drastically reduces its permeability.

The equation in Part One are adapted from the equations of Bateman (1910) but include the constant C, defined above, which is a function of  $\alpha$ ,  $\tau$ ,  $f$ ,  $f'$ , and R. The equations are solved for a time (T, between 0 and 36 hours), for f values (between 0 and 1),  $f'$  (0 and 1) and R ( $10^{-1}$  and  $10^6$ ). Two constants,  $\tau$  and  $\alpha$ , are assumed a priori and do not vary, thus the equations are solved for T, f,  $f'$  and R generating a 4 dimensional matrix of values. The initial number of Ra ( $N_{Ra}^0$ ) is calculated from the known activity of  $^{226}\text{Ra}$  of the initial material (35.58 Bq/kg or 2.13 dpm/g for Chaitén, see Table 1). Rn ( $N_{Rn}^0$ ) and Pb ( $N_{Pb}^0$ ) initial particle numbers are then calculated assuming all activities are initially equal. The equations for ( $^{226}\text{Ra}$ ), ( $^{222}\text{Rn}$ ) and ( $^{210}\text{Pb}$ ) are thus:

$$(^{226}\text{Ra}) = \lambda_{Ra} [N_{Ra}^0 e^{-\lambda_{Ra} T}]$$

$$(^{222}\text{Rn}) = \lambda_{Rn} \left[ \left( \frac{\lambda_{Ra} C N_{Ra}^0}{\lambda_{Rn} - \lambda_{Ra}} \right) e^{-\lambda_{Ra} T} + \left( \frac{\lambda_{Ra} C N_{Ra}^0}{\lambda_{Ra} - \lambda_{Rn}} + N_{Rn}^0 \right) e^{-\lambda_{Rn} T} \right]$$

And

$$(^{210}\text{Pb}) = \lambda_{Pb} \left[ \left( \frac{\lambda_{Ra} \lambda_{Rn} C N_{Ra}^0}{(\lambda_{Rn} - \lambda_{Ra})(\lambda_{Pb} - \lambda_{Ra})} \right) e^{-\lambda_{Ra} T} + \dots \right. \\ \left. \left( \frac{\lambda_{Ra} \lambda_{Rn} C N_{Ra}^0}{(\lambda_{Ra} - \lambda_{Rn})(\lambda_{Pb} - \lambda_{Rn})} + \frac{\lambda_{Rn} N_{Rn}^0}{\lambda_{Pb} - \lambda_{Rn}} \right) e^{-\lambda_{Rn} T} + \dots \right. \\ \left. \left( \frac{\lambda_{Ra} \lambda_{Rn} C N_{Ra}^0}{(\lambda_{Ra} - \lambda_{Pb})(\lambda_{Rn} - \lambda_{Pb})} + \frac{\lambda_{Rn} N_{Rn}^0}{\lambda_{Rn} - \lambda_{Pb}} + N_{Pb}^0 \right) e^{-\lambda_{Pb} T} \right]$$

Activity ratios are calculated by dividing one activity over another, e.g. ( $^{210}\text{Pb}/^{226}\text{Ra}$ ), and are known for all combinations of T, f, f and R.

### Equations underpinning Part Two of the Rn Model

Part Two provides time for the trapped volatile phase to re-equilibrate with the fracture material and the decay of excess  $^{222}\text{Rn}$  to  $^{210}\text{Pb}$ . The equations in Part Two are decay equations for Pb, Rn and Ra as described in Bateman (1910) but do not include the constant C because there is no additional gas fluxing phase during this period:

$$(^{226}\text{Ra}) = \lambda_{\text{Ra}} [N_{\text{Ra}} e^{-\lambda_{\text{Ra}} t}]$$

$$(^{222}\text{Rn}) = \lambda_{\text{Rn}} \left[ \left( \frac{\lambda_{\text{Ra}} N_{\text{Ra}}}{\lambda_{\text{Rn}} - \lambda_{\text{Ra}}} \right) e^{-\lambda_{\text{Ra}} t} + \left( \frac{\lambda_{\text{Ra}} N_{\text{Ra}}}{\lambda_{\text{Ra}} - \lambda_{\text{Rn}}} + N_{\text{Rn}} \right) e^{-\lambda_{\text{Rn}} t} \right]$$

And

$$(^{210}\text{Pb}) = \lambda_{\text{Pb}} \left[ \begin{array}{l} \left( \frac{\lambda_{\text{Ra}} \lambda_{\text{Rn}} N_{\text{Ra}}}{(\lambda_{\text{Rn}} - \lambda_{\text{Ra}})(\lambda_{\text{Pb}} - \lambda_{\text{Ra}})} \right) e^{-\lambda_{\text{Ra}} t} + \dots \\ \left( \frac{\lambda_{\text{Ra}} \lambda_{\text{Rn}} N_{\text{Ra}}}{(\lambda_{\text{Ra}} - \lambda_{\text{Rn}})(\lambda_{\text{Pb}} - \lambda_{\text{Rn}})} + \frac{\lambda_{\text{Rn}} N_{\text{Rn}}}{\lambda_{\text{Pb}} - \lambda_{\text{Rn}}} \right) e^{-\lambda_{\text{Rn}} t} + \dots \\ \left( \frac{\lambda_{\text{Ra}} \lambda_{\text{Rn}} N_{\text{Ra}}}{(\lambda_{\text{Ra}} - \lambda_{\text{Pb}})(\lambda_{\text{Rn}} - \lambda_{\text{Pb}})} + \frac{\lambda_{\text{Rn}} N_{\text{Rn}}}{\lambda_{\text{Rn}} - \lambda_{\text{Pb}}} + N_{\text{Pb}} \right) e^{-\lambda_{\text{Pb}} t} \end{array} \right]$$

These are solved for a time (t) between 0 and 50 days with initial conditions ( $N_{Ra}$ ,  $N_{Rn}$  and  $N_{Pb}$ ) taken from Part One of the model that represent all time intervals from  $T=0$  to  $T= 36$  hours, and is presented as a 5 dimensional matrix. Activity ratios are then calculated for all times (0-50 days) with all starting conditions. The utilisation of matrices in Matlab allow for all scenarios to be considered and a contour function is utilised to generate a figure with T on the x-axis and R on the y-axis. For example, the models input to generate Fig. 6 are  $\alpha=0.04$ ,  $\tau=0.019$  and the ( $^{226}\text{Ra}$ ) for Chaitén Host. Part One calculates all activities from  $T = 0$  to  $T = 36$  hours, Part Two runs for  $t = 0$  to 50 days. The contour map inputs are  $f = 1$ ,  $f^* = 0.5$ ,  $t = 50$ , the result is a contour map of calculated activity ratios depending on the T (0-35 hours) and R values (100-100,000), x and y-axis limits were used for clarity and only contours for 1.05, 1.1 and 1.2 are shown.

## Appendix C: Model Sensitivity

The model summarised in Section 4.2 requires several inputs, including the magma's residence time in the degassing cell ( $\tau$ ) and the fraction of Rn effectively extracted from the degassing cell ( $f$ ) (Gauthier and Condomines, 1999, Condomines et al., 2010), to which the model's outputs are sensitive. If the system is a closed then  $\tau \rightarrow \infty$ , if the system is fully open then  $\tau = 0$ . Within our model,  $\tau$  can influence the final R value required to generate an excess, when  $\tau < 1$ , where R is the mass ratio of the degassing magma cell and fracture,  $R = M_d/M_a$ . As  $\tau$  decreases below 1, the R value required to generate a known excess decreases (Figure B.1, Table B.1), because the degassing cell is being provided with new magma, rich in Rn and Ra, more regularly, which then degases within the cell (Figure 5). Although R values are implausibly high at short timespans, regardless of the  $\tau$  value, at timespans on the order of a few days it would be possible to generate a  $^{210}\text{Pb}$  excess within a vein with an  $R < 500$  providing  $\tau$  is low.

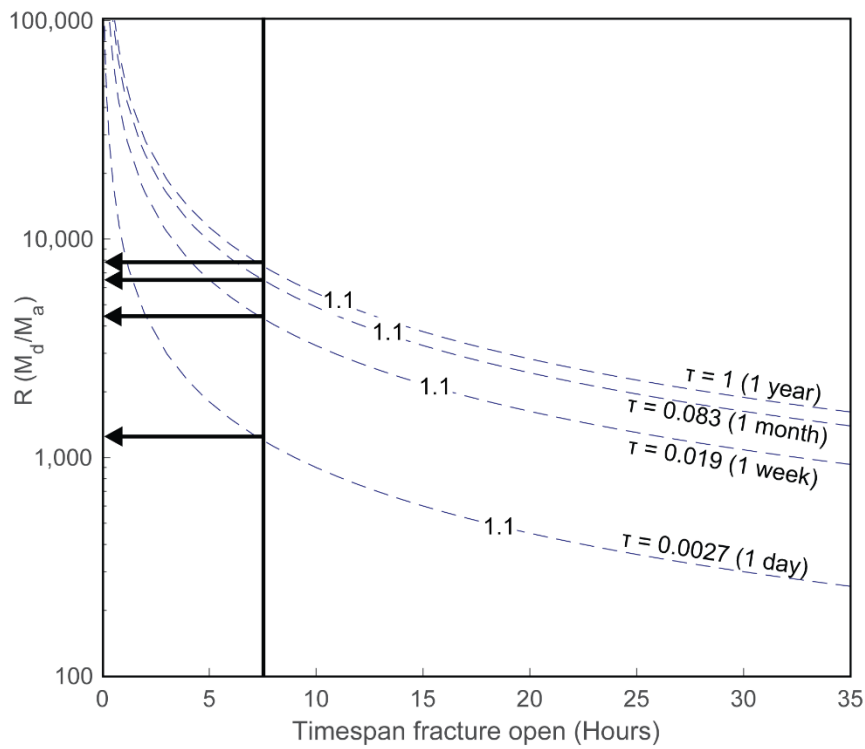


Figure C.1:

R value vs Timespan of fracturing event with varying  $\tau$  values. Black arrows show how, for a 7.5-hour vein lifetime, the R value decreases as the  $\tau$  value decreases.

Table C.1:

Summary of R value required for 1.6 hour and 7.5 hour events given a known  $f$  and  $f'$  value and varying  $\tau$ .

$f = 1, f' = 0.5$	$t = 1.6$ hours	$t = 7.5$ hours
$\tau = 1$ (1 year)	~35 000	~7 500
$\tau = 0.083$ (1 month)	~32 000	~6 500
$\tau = 0.019$ (1 week)	~20 000	~4 500
$\tau = 0.0027$ (1 day)	~5 900	~1 100



The fraction of gas removed from the degassing magma is denoted as  $f$  (Figure 5). In the discussion a value of 1 is assumed, providing us with a minimal  $R$  value estimate for Chaitén. This assumes that all available radon is extracted from the degassing magma into the fracture. If  $f < 1$  then less radon is transferred into the accumulating magma and therefore the mass ratio between the degassing and accumulating magmas must be larger to produce a certain excess, i.e.  $R$  must be larger. Figure B.2 summarises the effect of lowering  $f$  on the  $R$  values required to generate a 10 % excess assuming  $t = 7.5$  hours,  $\tau = 0.019$ ,  $\alpha = 0.04$  and  $f' = 0.5$ . If  $f = 0$  then no radon is extracted from the degassing cell into the fracture so there would be no  $R$  value associated.

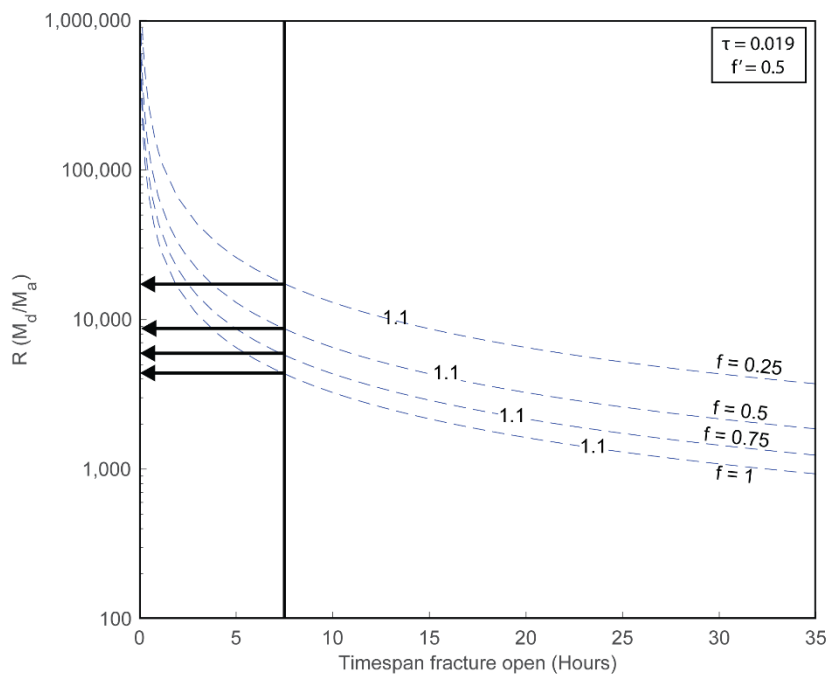


Figure C.2:

$R$  value vs Timespan of fracturing event with varying  $f$  values. Black arrows show how, for a 7.5-hour fracturing event, the  $R$  value increases as the  $f$  value decreases.

## **Link to Chapter Two**

In Chapter One I show that trace element variations at the dm-cm scale in veins at Cordón Caulle were the result of degassing. However, the spatial resolution of this study is analytically limited because isotope analyses require a larger sample volume owing to the low concentrations of  $^{210}\text{Pb}$  and  $^{226}\text{Ra}$  and so whole veins were crushed, powdered and analysed. Thus much of this variation could not be explored further using the methods described in Chapter One. In the general introduction, I highlight how studies into the diffusion of water around fractures have aided in understanding the timescales fractures can be open for. However, the shallowly derived erupted products from the recent Cordón Caulle eruption are water-poor (Schipper et al., 2013; Castro et al., 2014) and thus no timing inferences have been made about processes that occurred during the latest eruption.

In Chapter Two I delve deeper into trace element variation at Cordón Caulle using in situ techniques to assess variation on the  $\mu\text{m}$ -mm scale. I expand on the types of textures analysed, focusing on breccias as well as veins, resulting in a comprehensive study of degassing at different levels within the upper conduit. Sampling of different components of this eruption allows for the assessment of how these processes change as an eruption evolves. Finally, using these techniques I highlight how trace elements can be used to assess timescales of degassing, particularly in water-poor systems where previous studies have been not been fruitful.

## Chapter Two

### Degassing-induced chemical heterogeneity at the 2011-2012 Cordón Caulle eruption

R. Paisley<sup>\*</sup>,<sup>1</sup>, K. Berlo<sup>1</sup>, J. Whattam<sup>2</sup>, C. I. Schipper<sup>2</sup>, H. Tuffen<sup>3</sup>

<sup>1</sup>Department of Earth & Planetary Sciences, McGill University, 3450 Rue University, Montreal, Quebec, Canada, H3A 0E8

<sup>2</sup>School of Geography, Environment and Earth Sciences, Victoria University of Wellington, Wellington, New Zealand

<sup>3</sup>Lancaster Environment Centre, Lancaster University, Lancaster, UK

*In preparation for Volcanica*

#### Highlights:

- Chemical heterogeneity preserved in erupted products records gas flow through syn-eruptive fracture-generated networks
- Evidence for metal scavenging from tuffisite vein material by the fluxing gas phase
- Hour to day fracture lifespans constrained via trace element diffusion
- Volatiles (In, Tl and Bi) progressively depleted from the melt as eruption proceeded

## Abstract

The eruption dynamics of the 2011-2012 rhyolite eruption at Cordón Caulle, Chile, were markedly complex. After a brief Plinian phase, the eruption transitioned into an extended period of simultaneous low-intensity plumes, explosions and lava effusion (behaviour referred to as hybrid activity). This activity reflects the competing processes of fracturing, melt relaxation and gas fluxing occurring within the upper conduit. At Cordón Caulle the erupted products preserve low concentrations of H<sub>2</sub>O and CO<sub>2</sub>, which limits their use as recorders of degassing for this particular eruption and our understanding of these syn-eruptive processes. However, major volatiles act as carrier gases for many volatile trace elements (e.g. Li, Rb, Cs, Cu, In, Zn, Pb, Tl and Bi) and heterogeneity in trace elements is preserved. Trace element and textural heterogeneity at Cordón Caulle are strongly correlated, emphasising how degassing can be preserved by volatile trace elements in the erupted products. Individual samples are subdivided into textural domains with each domain representing a degassing process within the upper conduit. Depletions of Pb and Tl in glass shards in tuffisite veins and interstitial matrices of breccias record scavenging of metals by the fluxing gas phase. Enrichments of Tl in surficial ash domains highlight how changing environmental conditions, as gases flux into the surface environment, can result in scavenging of certain elements by ash. We infer that this occurred during ash jetting events observed from the lava-filled vent during late hybrid activity in 2012. Elemental gradients in alkalis (Li, Na, Rb, Cs) and metals (Cu, Tl and Pb) indicate deep-conduit degassing events are short-lived, with lifespans on the order of minutes, and surface venting can occur (from a single location) for hours, corroborating with observations made during the latter period of hybrid activity during this eruption. Vent samples from later in the eruption sequence are depleted in In, Tl and Bi, relative to earlier erupted volcanic bombs, highlighting the progressive degassing of the system as the eruption proceeded. This study sheds light on

the complex degassing processes that occur in the uppermost conduit and how these processes evolve as an eruption progresses. Combining in-situ textural and chemical analyses is an alternative method for assessing degassing in systems that are depleted in H<sub>2</sub>O and CO<sub>2</sub>.

## **1. Introduction**

Prior to the 2008 eruption of Chaitén in Chile, no explosive rhyolitic eruptions had been scientifically observed in detail (Castro et al., 2014). The Chaitén eruption was closely followed by another Chilean rhyolitic eruption, at Cordon Caulle from 2011 to 2012. During both eruptions simultaneous explosive and effusive activity from the same vent were observed, known as hybrid activity (Pallister et al., 2013; Schipper et al., 2013). Observations of hybrid activity have led to a paradigm shift in our understanding of syn-eruptive degassing of silicic magma and highlight the important role played by melt fracturing in the upper conduit. Such fracturing processes are recorded by tuffisite veins, which are ash-filled fractures formed in shallow magma or country rock and found in the products of many silicic eruptions (e.g. Heiken et al., 1988; Stasiuk et al., 1996; Tuffen et al., 2003; Tuffen and Dingwell, 2005), together with variably-welded breccias (e.g. Kolzenburg and Russell, 2014; Isgett et al., 2017). Geochemical, textural and experimental studies have shown fractures to be highly permeable, transient pathways where volcanic gases can flux over hundreds of metres within the upper conduit, before sintering and compaction leads to porosity and permeability loss in these features (e.g. Kolzenburg et al., 2012; Heap et al., 2015; Farquharson et al., 2016; Kendrick et al., 2016; Saubin et al., 2016). H<sub>2</sub>O diffusion gradients in glasses have been used to constrain the timescale of degassing into fractures at Chaitén (Castro et al., 2012), Lipari (Cabrera et al., 2011) and Mono Craters (Watkins et al., 2017). However, the erupted products from Cordon

Caulle are H<sub>2</sub>O-poor (<0.35 wt. % H<sub>2</sub>O) and lack well-defined degassing trends in both water concentrations and isotopes (Schipper et al., 2013; Castro et al., 2014). Therefore alternative approaches are required to chemically constrain degassing processes during this eruption that are recorded by the texturally complex and heterogeneous erupted products.

Whilst volcanic vapour compositions are dominated by H<sub>2</sub>O, CO<sub>2</sub> and halogens, they are also enriched in trace elements including alkalis, metals and metalloids (Hinkley et al., 1994; Williams-Jones et al., 2002). Trace element variations in tuffisites have been linked to gas fluxing through these permeable pathways at depth (Berlo et al., 2013; Plail et al., 2014; Paisley et al., in review). Their diffusivities are commonly slower than that of H<sub>2</sub>O (Zhang et al., 2010; Zhang and Ni, 2010; Gardner et al., 2012). Thus, whilst H<sub>2</sub>O has been efficiently degassed and removed from the melt at Cordón Caulle, other species potentially have not. In this study, we exploit this alternative approach and evaluate heterogeneity in volatile trace elements (e.g. Li, Rb, Cs, Cu, Tl, Pb) and ligands (e.g. Cl) across textural features indicative of degassing preserved in the erupted products from the most recent Cordón Caulle eruption.

## **2. Case Study: The Puyehue-Cordón Caulle Volcanic Complex**

### **2.1 Eruption Background**

The Puyehue-Cordón Caulle Volcanic complex (PCCVC) is located in the Chilean Southern Volcanic Zone (SVZ). Historical eruptions on the complex range from basaltic to rhyolitic in composition (Gerlach et al., 1988). The Cordón Caulle fissure system is located within a NW-

SE oriented graben, between the Puyehue composite stratovolcano (~2230 m a.s.l) and the Cordillera Nevada caldera (~1800 m a.s.l), and is controlled by a branching fault off-shooting from the 1000+ km-long, N-S striking Liquiñe-Ofqui Fault Zone in the SVZ (Gerlach et al., 1988; Lara et al., 2006; Singer et al., 2008). The two most recent eruptions of the Cordón Caulle fissure zone in 1922 and 1960 were rhyodacitic to rhyolitic in composition (Gerlach et al., 1988), with the latter notably occurring 38 hours after the  $M_w$  9.5 Valdivia subduction zone earthquake, the largest instrumentally recorded seismic event (Lara et al., 2004).

The 2011-2012 eruption commenced on June 4<sup>th</sup> with 27 hours of Plinian activity after months of elevated seismicity, ground deformation and uplift (Silva Parejas et al., 2012; Jay et al., 2014). The column height was initially 15 km, before fluctuating between 3 and 10 km over the next week (Silva Parejas et al., 2012; Castro et al., 2013; and references therein). Ten days into the eruption lava effusion began, from the same vents as the pyroclastic emissions, breaching the NW side of the tephra cone (Silva Parejas et al., 2012; Schipper et al., 2013). Rapid surface uplift of <200 m around the vent is thought to indicate the emplacement of a shallow laccolithic intrusion, at a depth of 20-200 m with a volume  $\sim 0.8 \text{ km}^3$ , in the first month of the eruption (Castro et al., 2016). Pyroclastic emissions continued for several months, with the concurrent coalescence of two partly-overlapping cones formed in the early stages of eruption. In January 2012 two sub-vents within a single tephra cone were observed, each displaying a cycle of behaviour from Vulcanian blasting (with bombs landing <1 km away from the vent) to ash and gas venting (Silva Parejas et al., 2012; Schipper et al., 2013). This hybrid behaviour continued into late March 2012, when recorded tremor ceased, after emission of a total erupted volume of magma of  $\sim 1.4 \text{ km}^3$  dense rock equivalent (Tuffen et al., 2013; Pistolesi et al., 2015). The lava effusion rate averaged  $50 \text{ m}^3\text{s}^{-1}$  during the first 20 days before declining to lower fluxes, and the 35 m-thick lava flow continued to advance via breakouts

from its thermally-insulated core into 2013 (Tuffen et al., 2013; Bertin et al., 2015). Extensive deformation was also recorded post eruption (Delgado et al., 2016).

## 2.2 Petrology Background

Bulk (~69 wt. % SiO<sub>2</sub>) and glass (~72 wt. % SiO<sub>2</sub>) concentrations from the 2011-2012 eruption show minimal variation across the eruption suite and are comparable to the 1922 and 1960 eruptions at Cordón Caulle (Gerlach et al., 1988; Castro et al., 2013; Pistolesi et al., 2015). Phenocryst growth occurring during magma storage accounts for the minor difference between the bulk and glass compositions (Castro et al., 2013). These most recent silicic magmas form an extended trend (in both major and trace elements) when compared to historical bulk analyses of the PCVVC glacial and post-glacial deposits, the result of fractional crystallisation of a plagioclase, clinopyroxene, orthopyroxene and magnetite anhydrous assemblage (Gerlach et al., 1988; Jicha et al., 2007; Castro et al., 2013; Daga et al., 2014; Alloway et al., 2015). The 2011-2012 phenocryst assemblage comprises of plagioclase, orthopyroxene, clinopyroxene, magnetite and ilmenite with rare apatite and pyrrhotite, although samples are near aphyric (<5 vol. %) and crystals are commonly observed as glomerocrysts (Castro et al., 2013). Magmatic storage conditions for this eruption are estimated to be ~2.5-7.5 km, 875-925 °C, fO<sub>2</sub> ~QFM, the hot conditions accounting for the low viscosity of the melt (Castro et al., 2013; Jay et al., 2014). Plagioclase-hosted melt inclusions record pre-eruptive volatile concentrations of <2.5 wt. % H<sub>2</sub>O, and ~40-70 ppm CO<sub>2</sub> (Castro et al., 2013), whilst pyroxene-hosted inclusions contain ~3.9 wt. % H<sub>2</sub>O, ~220 ppm CO<sub>2</sub> and ~130 ppm SO<sub>2</sub> (Jay et al., 2014). The groundmass of the erupted products from the 2011 event is uniformly low in H<sub>2</sub>O (<0.35 wt. %), with no systematic differences in H<sub>2</sub>O or  $\delta D$  between the various eruptive phases (e.g. Plinian pumice,



Vulcanian bombs, and lava) (Schipper et al., 2013; Castro et al., 2014). Thus less is known about magmatic degassing at Cordón Caulle than other eruptions that have expelled more H<sub>2</sub>O-rich upper conduit material, such as the 2008 Chaitén eruption.

### 3. Methods

#### 3.1 Sampling Methods

To accurately assess degassing processes during the 2011-2012 Cordón Caulle eruption samples must represent degassing events both through time (beginning to end) and space (from depth to the surface). This allows for an understanding of how volatiles degas as magma ascends from depth, and how degassing changed in an initially-explosive eruption that transitioned into prolonged hybrid behaviour. To achieve this, relevant samples were collected that encapsulate shifting degassing systematics from the onset to the end of the hybrid phase of activity. They are subdivided into three categories (*bomb*, *vent* and *flow*). Figure 1 summarises sample collection localities and the phases of hybrid activity they represent. *Bomb* samples were predominantly collected from ballistic ejecta mantling a ridge ~2.5 km NW of the vent, which were ejected during the lower intensity explosive phase (7th June onwards) that gave way to the onset of vigorous hybrid activity (Schipper et al., 2013; Pistolesi et al., 2015). Further *bomb* samples were collected near or in the vent complex within the tephra cone, these are bombs or bomb fragments that were ejected later during the eruption, in lower energy explosions whose ejecta failed to escape the crater within the tephra cone (Schipper et al., 2013). *Vent* samples are those collected exclusively from within the vent, with many sampled in situ, and represent the surfaces of fractures within the vent-filling lava that acted as loci for

ash and gas emissions during the waning phases of the hybrid activity in 2012. *Flow* samples are collected from the rhyolite flow, with samples from the flow front of the northern branch likely representing the first-effused lava from the onset of the hybrid phase (June 2011), and the sample from within the vent representing the very end of activity in 2012 (Magnall et al., 2017, 2018).

During explosive eruptions, degassing starts deep within the system with the exsolution of volatiles and continues all the way to the surface with the expulsion of a plume (Cashman and Sparks, 2013). Samples are subdivided into textural domains that each reflect a specific degassing process and are summarised in Section 4.1 and Figure 2, with the underlying rationale discussed below. The collected samples represent surface and sub-surface degassing events. Surface degassing is recorded by in situ vent outcrops or material adhered to bomb surfaces. Sub-surface degassing domains are those that underwent fragmentation followed by varying degrees of melt relaxation, ductile deformation, welding and compaction (e.g. tuffisites, breccias and banded obsidians). These textures are known to be generated within the upper conduit and relate to outgassing (e.g. Stasiuk et al., 1996; Tuffen et al., 2003; Tuffen and Dingwell, 2005; Farquharson et al., 2016; Isgett et al., 2017). Flow textures are not discussed in this study as the rhyolite flow undergoes additional processes at the surface as it cools that are recorded texturally and chemically, e.g. devitrification and secondary boiling, (Schipper et al., 2015; Magnall et al., 2018; Schipper et al., in prep.).

### **3.2 Analytical Methods**

Geochemical analyses were performed on polished thin sections (30-50  $\mu\text{m}$  thick) and one-inch mounts both made from epoxy-impregnated samples. Electron probe microanalysis (EPMA) was conducted on the JEOL JXA-8230 at Victoria University of Wellington. Each spot was analysed twice, once for  $\text{SiO}_2$ ,  $\text{TiO}_2$ ,  $\text{Al}_2\text{O}_3$ ,  $\text{FeO}$ ,  $\text{MnO}$ ,  $\text{MgO}$ ,  $\text{CaO}$ ,  $\text{Na}_2\text{O}$ ,  $\text{K}_2\text{O}$ ,  $\text{Cr}_2\text{O}_3$  and  $\text{P}_2\text{O}_5$ , and secondly for S and Cl. Defocused beam sizes of 10-20  $\mu\text{m}$  were used with working conditions of 15 kV and 8.0 nA for major elements and 15 kV and 6.0 nA for volatile elements. Counting times for major elements were 30 and 15 seconds (peak and background). Sodium loss was avoided by analysing  $\text{Na}_2\text{O}$  first at reduced times of 10 and 5 seconds, with no peak search. Volatiles were measured for 60 and 30 seconds (peak and background).  $\text{Cr}_2\text{O}_3$  and  $\text{P}_2\text{O}_5$  were consistently below detection and are excluded. Iron is measured as total iron  $\text{FeO}_t$ . Primary standards were rhyolite glass VG568 for Si, Al, Na, K, and Cl; basaltic glass VGA99 for Ca, Mg, and Fe; pure synthetic oxides for Ti, Mn, and Cr; Elba Pyrite for S, and Durango apatite for P (Jarosewich et al., 1980). Secondary standards (VG2, VGA99 and VG568) were periodically analysed to assess for drift during the analyses over several days. Relative standard deviations (% RSD) are calculated using these standards:  $\text{SiO}_2$ ,  $\text{Al}_2\text{O}_3$ , and  $\text{MgO}$  (excluding values near detection limit) are <2 % RSD;  $\text{TiO}_2$ ,  $\text{CaO}$ ,  $\text{FeO}_t$ ,  $\text{Na}_2\text{O}$  and  $\text{K}_2\text{O}$  are between 2 and 6 % RSD; % RSD is 7-8 % for Cl and 13-15 % for MnO. S is near detection in samples and has a % RSD <50. Crystals and void spaces were avoided to ensure a pure glass signature on the samples. Samples were further filtered for contamination by excluding data with low totals (due to void space) and anomalously high  $\text{Al}_2\text{O}_3$ ,  $\text{FeO}_t$ ,  $\text{MgO}$  and/or  $\text{CaO}$  (crystals), or Cl or S (resin) concentrations. Concentrations in Appendix A are calculated anhydrous averages for each sample, and reported as oxides except Cl and S.

Laser ablation analyses were conducted using a NewWave 213 nm Nd-YAG laser ablation system coupled to a Thermo Finnigan iCapQ ICP-MS at McGill University, and a RESolution

S155-SE 193 nm Excimer Laser coupled to an Agilent 7500CS ICP-MS at Victoria University of Wellington. Spot sizes of 12-20  $\mu\text{m}$  were used for laser profiles with a restricted element list, whilst large spots of 30-60  $\mu\text{m}$  were used to analyse for a larger range of elements. Spot analyses, >30  $\mu\text{m}$  in diameter, were randomly conducted on a thin section in multiple areas to ensure a representative mean concentration in a wide range of elements. Individual line analyses were conducted running parallel to interfaces obtain data for diffusion profiles (Section 4.2.2). Analyses counting times (<45 seconds) for spot and line profiles were dependent on line length/ spot size and thin section thickness. Each analysis was preceded by a single 70 or 140  $\mu\text{m}$  cleaning pulse and a laser warm-up/background counting period of 30-45 seconds, followed by a <60 second washout period. Energy outputs and frequencies varied with spot size to ensure no melting or fracturing occurred during ablation. Analyses were conducted at 10-20 Hz with a resultant fluence of  $\sim 4\text{-}12 \text{ Jcm}^{-2}$ . Up to 55 elements were analysed including  $^7\text{Li}$ ,  $^{23}\text{Na}$ ,  $^{24}\text{Mg}$ ,  $^{27}\text{Al}$ ,  $^{29}\text{Si}$ ,  $^{31}\text{P}$ ,  $^{39}\text{K}$ ,  $^{44}\text{Ca}$ ,  $^{45}\text{Sc}$ ,  $^{47}\text{Ti}$ ,  $^{51}\text{V}$ ,  $^{52}\text{Cr}$ ,  $^{55}\text{Mn}$ ,  $^{57}\text{Fe}$ ,  $^{59}\text{Co}$ ,  $^{60}\text{Ni}$ ,  $^{63}\text{Cu}$ ,  $^{66}\text{Zn}$ ,  $^{71}\text{Ga}$ ,  $^{75}\text{As}$ ,  $^{85}\text{Rb}$ ,  $^{88}\text{Sr}$ ,  $^{89}\text{Y}$ ,  $^{90}\text{Zr}$ ,  $^{93}\text{Nb}$ ,  $^{95}\text{Mo}$ ,  $^{107}\text{Ag}$ ,  $^{111}\text{Cd}$ ,  $^{115}\text{In}$ ,  $^{118}\text{Sn}$ ,  $^{121}\text{Sb}$ ,  $^{133}\text{Cs}$ ,  $^{137}\text{Ba}$ ,  $^{139}\text{La}$ ,  $^{140}\text{Ce}$ ,  $^{146}\text{Nd}$ ,  $^{147}\text{Sm}$ ,  $^{153}\text{Eu}$ ,  $^{157}\text{Gd}$ ,  $^{163}\text{Dy}$ ,  $^{166}\text{Er}$ ,  $^{172}\text{Yb}$ ,  $^{175}\text{Lu}$ ,  $^{178}\text{Hf}$ ,  $^{182}\text{W}$ ,  $^{205}\text{Tl}$ ,  $^{208}\text{Pb}$ ,  $^{232}\text{Th}$  and  $^{238}\text{U}$ . Na, Mg, Si, K, P, Ca and Fe were measured to assess for crystal contamination, allowing contaminated spot analyses to be easily identified and removed from the dataset. Based on EPMA, Al was found to minimally vary in samples and a median concentration (14.1 wt. %  $\text{Al}_2\text{O}_3$ , interquartile range 14.0-14.3 wt. %  $\text{Al}_2\text{O}_3$ ) is used for internal standardisation. All laser analyses were bracketed by the primary standard NIST610 (Jochum et al., 2011), with BCR-2G repeatedly analysed as a secondary standard to assess for reproducibility and instrument precision. BCR-2G average elemental concentrations, and associated % RSDs, are noted in Appendix A. BCR-2G concentrations were compared to both the preferred GEOREM values (Jochum, 2009) and the median concentration of the wider selection of elements published values on GEOREM (“GeoReM: BCR-2G (published values),”

2015). Daily sessions were levelled using a robust regression calibration line calculated from the USGS standards GSC, GSD and GSE that were analysed at least twice per daily analytical session. Data reduction was undertaken in Iolite (Paton et al., 2011) with offline corrections for internal element standardisation. Further corrections were made to sessions that had systematically unusual BCR-2G concentrations. Errors on individual analyses are calculated via Iolite during processing and depend on the choice of integration window. Concentrations for each sample, Appendix A, are calculated means from all spot analyses conducted on a sample.

## **4. Results: Textural and Chemical Observations**

### **4.1 Domain Petrology**

*Bomb* and *vent* samples have complex and heterogeneous textures thought to preserve fracturing and degassing events melt undergoes as it ascends from depth within the conduit. Below we describe the main classifications of textural domains that constitute these samples. Each domain represents degassing processes within a part of the conduit.

#### **Ash Domains**

Many bombs and bomb fragments found within the vent are partially coated in fine veneers of light pink-orange oxidised ash (Fig. 2). This veneer commonly thickens in concave or uneven areas on bomb surfaces. Ash shards are <10  $\mu\text{m}$  in size, and sub-millimetric laminations are

picked out by variations in grain size. The ash is glassy and largely devoid of microlites. Ash adheres to both non-oxidised and heavily oxidised and altered bomb surfaces.

### **Nozzle Domains**

The vent area within the tephra cone comprises heavily-fractured dome-like lava bodies, many of whose near-planar fracture surfaces are coated with dark-orange to red veneers (Fig. 2). The veneers consist of heavily oxidised and sintered ash material adhered onto planar surfaces, and in certain locations the surface of the lava itself has been altered by oxidation. The lava is variably vesiculated and moderately microcrystalline, with distinct more microlite-rich bands. Fracture orientation is unrelated to the orientations of the bands or vesicles. Microlites are <50  $\mu\text{m}$  in length and are predominantly plagioclase and pyroxene; some devitrification textures are locally present (see also Magnall et al., 2018). Sub-rounded bubbles are also present (see banded obsidian description).

### **Breccias and Tuffisites**

*Bomb* textures at Cordón Caulle are complex. Many bombs from this eruption are breccias, with domains of pumice and angular obsidian separated, but sintered together, by fine-grained ( $\mu\text{m}$ - to mm-sized), variably oxidised ash matrices. Breccias form in the conduit and are then explosively expelled as bombs. Breccias and tuffisites are subdivided into two groups based on the intensity of their oxidation. Oxidised domains display heavy oxidation of clasts or matrix ash, expressed as deep orange to red colours, whilst non-oxidised domains show little or no oxidation of components, and vary from white-grey to light pink-orange in colour. The oxygen fugacity of the environment, and degree of oxidation of samples, will change towards the surface due to increased interaction with oxidising, atmospheric gases or loss of reducing

agents (e.g. hydrogen) (Moriizumi et al., 2009; Furukawa et al., 2010). Thus more oxidised domains are thought to represent degassing closer to the surface, with greater interaction with the atmosphere than their less-oxidised counterparts.

### **Oxidised Breccia Domains**

Oxidised breccias sampled from the vent are defined by their heavily oxidised (orange to red in colour) interstitial ash matrices. The cm-sized clasts comprise dense, banded and, in some cases, highly vesiculated obsidian. Some clasts have densely micro-cracked cores and others contain cristobalite within vesicles. Vesiculated clasts have contorted bubble shapes and evidence of coalescence and fracturing of bubble wall films. Microlite populations in dense clasts are similar to those in nozzle samples. Oxidation affects the outer ~30-200  $\mu\text{m}$  of clast surfaces and bubble walls. Interstitial ash matrices can either be microlite-rich and texturally similar to neighbouring clasts, implying a local source, or glassy and microlite-poor. The matrix material can exhibit alternating laminations of both fine-grained (~10-30  $\mu\text{m}$ ) sub-rounded shards and coarse-grained (<400  $\mu\text{m}$ ) angular shards, similar to tuffisites at this and other volcanic centres (Stasiuk et al., 1996; Tuffen and Dingwell, 2005; Saubin et al., 2016; Paisley et al., in review). Ash matrix shard shapes vary from highly rounded to angular, depending on their size and degree of sintering.

### **Non-Oxidised Breccia and Tuffisite Domains**

Many breccias and tuffisite veins within Cordón Caulle bombs have little or no oxidation of their hosts, clasts, and any interstitial ash or tuffisite material. Vesicle sizes increase towards the centres of larger (>0.5 m) bombs suggesting post-fragmentation inflation. Centimetre- to decimetre-sized clasts are mostly pumiceous, with rare dense obsidian clasts. Individual

pumiceous clasts display spatially heterogeneous bubble sizes with the largest, cm-sized bubbles in the clast interiors, indicating post-fragmentation vesiculation. Clast edges are either rounded or straight, indicating a variable degree of post-fragmentation viscous deformation. Fine-grained ( $\sim 30 \mu\text{m}$ ), well-sorted, sub-rounded glassy ash constitutes the interstitial matrix and sinters the larger clasts together. Ash matrices are largely void of phenocrysts and crystal fragments. Clast foaming and expansion can compact the surrounding matrix material. Tuffisite veins are preserved in some pumiceous and dense obsidian bombs; they commonly have sub-parallel edges; and are  $<3 \text{ cm}$  wide. Tuffisite ash is white to light pink-orange in colour and glassy, with rare microlites. Individual ash shards in veins are rounded to sub-rounded in shape with sizes varying from  $10\text{-}50 \mu\text{m}$ . The degree of sintering varies extensively both between and within tuffisite veins. Laminations within a single vein can display sintering textures spanning from necking and preservation of primary void space (common in coarse-grained  $>30 \mu\text{m}$ -sized ash laminations), to complete compaction and densification of ash (common in fine-grained  $<30 \mu\text{m}$ -sized ash laminations). However, there is not always a clear correlation between ash grain size and degree of sintering. Sintering of neighbouring shards can obscure their original shapes, particularly in strongly-compacted tuffisites, where only the presence of sub-micron-sized crystals delineate the shapes of individual shards (Tuffen and Dingwell, 2005). Vesiculation of shard cores has been observed within tuffisite material, with dense poorly-vesiculated rinds outlining their shapes (as described in Saubin et al. 2016). Individual shards can show evidence for strain localisation and bubble coalescence akin to textures in pumice erupted during earlier stages of activity (Schipper et al., 2013). Phenocrysts are rare in tuffisites but when found are within larger clasts with surrounding glass or as broken crystal fragments. Paisley et al (in review) describe one bomb type, which is largely excluded from this study – metre-scale, homogenous, grey and pumiceous bombs with rare pink-coloured tuffisite veins and dense obsidian clasts. These are not the focus of this study because they



likely represent gas-driven flow of bubbly magma but are integrated into the discussion with reference to Paisley et al. (in review).

## **Banded Obsidian Domains**

Dense banded obsidian is prevalent throughout the suite of bombs at Cordón Caulle. Large metre-scale bombs of banded obsidian are found on the distal ridge noted in Figure 1. Many bombs have adhering tuffisite ash on their surfaces, and contain cm-sized clasts of pumice or oxidised lithics. Domains of obsidian occur within breccia bombs as large cm-sized clasts or as mm-cm sized angular shards within tuffisite veins. Edges of banded obsidian domains are often sharp unless influenced by post-fragmentation vesiculation, e.g. bomb inflation. Banded domains may contain vesiculated bands, with rounded mm- to cm-sized vesicles showing evidence for coalescence. Phenocrysts are rare, and light-coloured glassy bands are largely devoid of crystals whilst darker bands have higher proportions of oxides and pyroxenes <1  $\mu\text{m}$  in size, or ‘nanolites’ as coined by Mujin et al. (2017). Needle-shaped microlites of plagioclase and pyroxene are <50  $\mu\text{m}$  in length, if present. Flow bands are deflected around large crystals, dense and lithic clasts. Banding is also seen within the lava, with breakout textures extensively described by Schipper et al. (2015) and Magnall et al. (2018). Vesicles and voids in the flow are cristobalite-coated, with vesicle collapse preserved by parallel bands of cristobalite (Schipper et al., 2015).

## **4.2. Chemical Analyses**

### **4.2.1 Sample Variation: Majors & trace elements systematics during eruption**

Average major and trace element concentrations for each sample and their associated errors are summarised in Appendix A, with highlights discussed below. Glass concentrations for the 2011-2012 eruptive materials average  $71.8 \pm 0.6$  wt. %  $\text{SiO}_2$ ,  $14.2 \pm 0.2$  wt. %  $\text{Al}_2\text{O}_3$  and  $5.0 \pm 0.2$  wt. %  $\text{Na}_2\text{O}$ . *Bomb*, *vent* and *flow* samples have similar concentrations for each element (Appendix A), which correspond closely to those reported by Castro et al. (2013). No systematic variations in major elements are apparent when the *bomb* and *vent* samples are compared to the early Plinian phase and the concurrent *flow* phase (Castro et al., 2013; Schipper et al., in prep., this study). V2 has higher  $\text{SiO}_2$  and lower concentrations of compatible elements (e.g.  $\text{CaO}$ ,  $\text{MgO}$ ,  $\text{TiO}_2$ ) than other samples, and is more microlite-rich resulting in a more evolved interstitial glass chemistry. Although individual samples plot within error of each other, positive correlations between certain major elements (e.g.  $\text{FeO}^t$  vs.  $\text{TiO}_2$  or  $\text{CaO}$  vs.  $\text{TiO}_2$ ) are apparent, and minor variation in microlite/phenocryst content would account for these trends (Fig. S1). There is no correlation between Cl and  $\text{K}_2\text{O}$  (Fig. S1), with  $\text{K}_2\text{O}$  values averaging  $3.0 \pm 0.2$  wt. % but Cl varying between ~600 and 1900 ppm. Median Cl concentrations for the suite of samples analysed is ~1500 ppm, compared to ~1700-2100 ppm in plagioclase and clinopyroxene-hosted melt inclusions (Castro et al., 2013; Jay et al., 2014). *Bomb* sample Cl concentrations range from ~1350 to ~1870 ppm. *Vent* samples V1 and V2 have lower than average Cl of ~1200 ppm and ~630 ppm (~70 % RSD) respectively. S concentrations are close to the detection limit at 10-20 ppm.

To compare trace element variation between samples, elements have been grouped based on their properties and behaviours in silicic systems. Group 1 elements (Sc, Ti, V, Cr, Mn, Co, Ni and Sr) are primarily compatible in the plagioclase, clinopyroxene and orthopyroxene-

dominated phenocryst assemblage. Group 2 elements (Ba, Ga, La, Ce, Nd, Sm, Eu, Dy, Er, Yb, Lu, Y, Zr, Nb, Hf, Th and U) are the high field strength elements (HFSEs), rare earth elements (REEs) and other incompatible elements. Group 3 elements (Li, Rb, Cs, As, Sb, Mo, W, Cu, Zn, Ag, Cd, In, Sn, Pb, Tl and Bi) are elements known to be volatile and partition into magmatic and hydrothermal fluids and vapours. Group 3 can be subdivided further into 3 sub-categories; alkalis (Li, Rb and Cs), predominantly OH-complexing elements (As, Sb, Mo, W) and predominantly S- and/or Cl-complexing elements (Cu, Zn, Ag, Cd, In, Sn, Pb, Tl and Bi) (e.g. Webster, 1990; Churakov et al., 2000; Wahrenberger et al., 2002; Zajacz et al., 2008; Pokrovski et al., 2013). *Bomb*, *vent* and *flow* samples cluster around a mean concentration for each trace element (Appendix A); plot within error of each other; and are comparable to bulk and glass analyses from the 1922, 1960 and 2011-12 eruptions (Gerlach et al., 1988; Jicha et al., 2007; Castro et al., 2013; Daga et al., 2014). There are no systematic differences between the different components of the hybrid phase of activity (*bomb* vs. *vent* vs. *flow*) in Group 1, Group 2 and most Group 3 elements (Fig. S1). Subtle positive correlations between elements in Group 1 (e.g. Zr vs. Th) and in Group 2 (e.g. Co vs. Mn) are significant at the 95% confidence interval (Fig. S1), although samples remain within error of each other. At the sample scale, Group 3 elements do not show the same systematic, strong correlations (at a 95% confidence interval) with either Group 1 (compatible) or Group 2 (incompatible) elements. Certain elements (Cr, Ni, Cu, Cd, In, Tl and Bi) have large % RSDs (>24 %) due to variability across the sample suite (Appendix A). *Vent* and *flow* samples have greater % RSDs in all elements than *bomb* samples. Tl, Bi and In concentrations are subtly different in the three sample categories (Fig. 3), with *vent* samples having the lowest median concentrations. Median *bomb* and *flow* sample concentrations cluster at ~14 ppm Cu, ~0.45-0.65 ppm Tl, ~0.1-0.15 ppm In and ~0.07 ppm Bi. *Vent* samples cluster at ~10 ppm and 22 ppm Cu but have lower Tl (0.15-0.4 ppm) and In (0.06-0.1 ppm) concentrations. *Vent* samples cluster around ~0.04 ppm Bi except for V2 (~0.12

ppm Bi). These groupings, and the large spread of concentrations, become more apparent when individual analyses are plotted (Fig. 3).

#### **4.2.2 Domain Variation: Trace element and Cl systematics from depth to surface**

Although few systematic variations are observed between samples on a macroscopic scale, there is a large spread in the concentrations of certain elements within samples (as evident from the high % RSDs). Chemical variation correlates strongly with the textural domains within samples described in Section 4.1. Domains within individual samples can be chemically distinct from each other, with significant variations at the interfaces between domains or across textural features.

##### **4.2.2.1 Domain Chemistry Comparison**

Chlorine concentrations and distributions vary for each domain (Fig. 4). Deposited ash domains have a median concentration of ~640 ppm. Oxidised breccia material has a similar median Cl concentration but a significantly larger spread with a range, ~200-2000 ppm (Fig. 4). Oxidised breccia host material has a median concentration of ~1250 ppm but areas can have <500 ppm Cl. Non-oxidised domains have narrower distributions and higher median Cl concentrations than the oxidised domains. Breccias (~1630 ppm) and tuffisites (~1670 ppm) have slightly higher Cl concentrations than their host material (~1510 ppm). Banded obsidian bombs and clasts have median concentration of ~1500 and ~1570 ppm respectively. Certain bands within banded obsidian bombs have Cl concentrations comparable to those recorded in melt inclusions

from this eruption (Fig. 4). No nozzle domains were analysed for Cl. Other elements (e.g. SiO<sub>2</sub>, Al<sub>2</sub>O<sub>3</sub>, TiO<sub>2</sub> and CaO) do not vary extensively with textural type. Ash domains have lower median concentrations of MnO, MgO, FeO<sup>t</sup> and K<sub>2</sub>O, and a higher median Na<sub>2</sub>O concentration than other domains. Domains in *vent* samples have wider total ranges than other domains.

The domain-host ratio defines the ratio of elemental concentrations of a domain, such as a tuffsite or ash matrix, with their respective host, e.g.  $\text{Li}_{\text{Tuffsite}}/\text{Li}_{\text{Host}}$ . Elemental enrichments or depletions relate to sources or processes (see Discussion). Figure 5 summarises the domain-host ratios for many elements from Groups 1, 2 and 3 whilst Table 1 denotes the elements that have a domain-host ratios outside of error of unity. We see no systematic enrichments or depletions in Group 1 or 2 elements within textural domains when compared to their hosts, with the exception of V that is enriched oxidised domains and variable in non-oxidised domains. Group 3 elements show a wider range of variability, particularly within oxidised and ash domains. Alkali elements (Li, Rb, and Cs) are largely depleted in all domains. The predominantly OH-complexing elements (e.g. As, Sb, Mo) show little variation between domains with the exception of Sb that can be depleted. Cu, Zn, Tl, Pb and Bi show the greatest amount of variation. Average Cu concentrations for all domains are within error of one (except V3 ash) but profiles across V1 breccia domain 1 and host highlight how Cu is systematically elevated, but highly variable, in the breccia ash (Fig. 6). Zn, Pb and Tl show depletions in several domains (Fig. 5, Table 1). Bi is enriched in most domains (ratios between 1 and 3 in non-oxidised domains and ~6 to 16 in deposited ash domains) and Tl is enriched in the deposited ash domains (ratios between ~4 and 7).

#### 4.2.2.2 Chemical Heterogeneity within Domains

In addition to the element variation observed between different domains and hosts, variation on the micron-scale occurs within many textural domains that we relate to diffusion in Section 5.3 (Table 2). Table 3 summarises elements showing systematic variations towards domain interfaces and the approximate length scales over which they vary. Figures 7-10 show how select elements vary towards or across interfaces in nozzle (Fig. 7), oxidised (Fig. 8), non-oxidised (Fig. 9), and banded obsidian (Fig. 10) domains. No analyses could be conducted to assess elemental variability across individual ash shards in ash domains due to their micron size. To summarise, in nozzle domains Cu, Tl and Pb show the most systematic variation (Fig. 7), decreasing towards fracture surfaces over a ~500  $\mu\text{m}$ -wide zone. In oxidised domains, Li, Rb and Tl decrease towards a clast interface in V2 which has a dense ~200  $\mu\text{m}$ -wide, chemically distinct rim zone that has overprinted part of these systematic depletions (Table 3, Fig. 8). Fewer profiles are observed in non-oxidised and banded obsidian domains with many examples showing no variation. Alkali elements (Li, Rb  $\pm$  Na) are shown to decrease towards a clast interface (Fig. 9) in a non-oxidised breccia and across bands in obsidian domains (Fig. 10). Supplementary Figures 3-6 compare elements discussed above (e.g. Table 3) to others discussed in Section 4.2.2 that do not vary towards interfaces, for data see Appendix B. Local degassing can induce microlite crystallisation, certain microlite-rich bands have elevated  $\text{TiO}_2$  and depleted Cl concentrations (e.g. Fig S.2).

## **5. Discussion**

### **5.1 Degassing: from eruption onset to decline**

Previous geochemical studies of the 2011-2012 Cordón Caulle eruptive products have largely focused on the pumices from the initial Plinian phase, and tephra and ash from the subsequent 10 days of activity (e.g. Castro et al., 2013; Collini et al., 2013; Daga et al., 2014; Alloway et al., 2015). The tightly constrained magma composition of this and the previous two eruptions (1922, 1960), along with interferometric synthetic aperture radar (InSAR) studies suggest a single, long-lived interconnected magma plumbing system has fed the past three eruptions (Jay et al., 2014; Delgado et al., 2016). Alloway et al. (2015) argue that three co-genetic pockets of magma (defined by differing CaO and Sr concentrations), each undergoing varying degrees of plagioclase fractionation at different pressures, were tapped simultaneously during the paroxysmal phase of the 2011-2012 eruption. We find no chemical evidence to suggest a melt source different to the long-lived, pre-existing reservoir was tapped, or that the melt source evolved significantly, as this eruption progressed. Minor trends in major and trace elements (Fig. S.1) likely result from phenocryst and microlite growth. But compositional differences between samples, which may reflect differing degrees of crystallisation, are typically smaller than the chemical variance within samples. This indicates that most crystal growth occurred in the conduit, likely in the form of microlites that were not subsequently segregated, inducing small-scale, intra-sample glass heterogeneities much larger than inter-sample heterogeneity induced by differentiation.

Previous studies have been unable to constrain the volatile evolution of this eruption as the final erupted products have no systematic water variations and are degassed to near-atmospheric conditions (<0.35 wt. % H<sub>2</sub>O, Schipper et al., 2013; Castro et al., 2014). Our trace element data shows certain volatile elements (In, Tl and Bi) are much lower in concentration in *vent* samples than in the earlier erupted products (*bomb* and *flow*, Fig. 4). As *vent* samples

represent the final, waning phase of activity the hybrid activity arguably did progressively degas certain volatiles from the system during the course of the eruption.

A caveat of this study is sampling bias and eruption dynamics prevent the study of certain components of the eruption. *Vent* samples representing the early hybrid phase were not attainable due to their location in inaccessible parts of the lava flow and/or their burial. The analysed *vent* samples have been collected in situ (or nearby in case of erupted breccias) and represent vent processes, but only those at the end of the eruption. *Bomb* samples far from the vent site are thought to derive from earlier in the eruption sequence (Section 3.1) and smaller *bombs* from the vent are thought to represent the later, less energetic phases of the eruption. This means that our sampling of the eruption sequence is early and deep (*bombs*), followed by later and surficial (*vent* samples). When comparing the elemental variation in different samples (discussed in the following sections) it is hard to definitively distinguish whether the concentration variations in mobile elements reflect changing gas compositions with time during eruption or depth, or the timescales of individual events.

## **5.2 Degassing: from depth to the surface**

Textural domains within samples can record numerous processes during magma ascent in the conduit, and any chemical heterogeneity needs to be carefully associated with specific degassing events that occurred at different times and depths. Interfaces between such domains preserve information about their relative timings and will be discussed in the next section. Many bombs have undergone post-fragmentation vesiculation, as demonstrated by breadcrust textures and increasing vesicle sizes towards bomb centres, but we instead focus on pre-



ejection degassing processes. Low H<sub>2</sub>O concentrations in Cordón Caulle ejecta indicate degassing to near-surface pressures, corresponding to the top tens of metres of the conduit (Schipper et al., 2013; Castro et al., 2014), in contrast with H<sub>2</sub>O-rich bombs from Chaitén that record phases of vertical clast migration over hundreds of metres (Saubin et al., 2016). Low H<sub>2</sub>O concentrations complicates placing quantitative constraints on the depths of successive degassing events. However, we can use textures and knowledge of the eruption evolution to estimate the likely conduit extraction depths of different bomb types and domains.

Surface uplift related to shallow laccolith emplacement (inferred to be ~20-200 m below the surface and <200 m thick) began on 8<sup>th</sup> June alongside vent constriction, Vulcanian blasting and low-intensity plume behaviour (Pistolesi et al., 2015; Castro et al., 2016). The laccolith would therefore have been present, or at least developing, during ejection of all of the studied bombs. Although Vulcanian events can, in some cases, evacuate the top ~2 km of silicic conduits (e.g. Wright et al., 2007) the low H<sub>2</sub>O in Cordón Caulle bombs indicate ejection from tens of metres depth – most likely above the laccolith intrusion or close to its roof. We use bomb textures to aid definition of the relative sources of discrete domain types. For example, a heavily oxidised sample is more likely to have come from a shallower environment than a non-oxidised sample. Similarly, material that has undergone several generations of fractures followed by extensive viscous deformation, prior to bomb expansion, will have likely had a more prolonged in-conduit residence than material preserving only a single generation of brittle fractures (Tuffen and Dingwell, 2005). Additionally, Cl concentrations from different domains can be used as a relative pressure indicator as they are a function of pressure and degree of open-system degassing (Villemant et al., 2008). Cl is largely retained in the melt until magma ascends into the near-surface when it can be readily degassed into an available vapour phase as HCl (Edmonds et al., 2002; Lowenstern et al., 2012). The loss of Cl in some domains helps

us to constrain them and their processes to the near-surface environment whilst it is inferred that Cl-rich samples would have quenched at higher pressures, see below.

### **Chemical Heterogeneity of Domains**

The lack of systematic chemical variation in elements predominantly controlled by fractional crystallisation (e.g. compatible and incompatible elements, Groups 1 & 2) allow us to isolate and focus on chemical heterogeneity induced by degassing (Group 3 elements). The following discussion is broken down into sub-sections that focus on the chemical heterogeneity of specific domains (Fig. 2) and what we can infer about fracturing and degassing processes. Domains are discussed in order from deep to surface domains. Also general elemental variability, as represented by the size of the error bars in Fig. 5, is high in the fine-grained ash domains within breccias and veins. This reflects the analytical detection limits and varied provenance of the ash particles, which derive from both the local host and deeper in the conduit (see below). We cannot definitively state whether heterogeneity in elements such as Cd, In and Ag relate to solely to degassing processes or are a function of their concentrations being close to their limits of detection and thus these elements are not discussed in the following section.

#### **5.2.1 Banded Obsidian Domains**

Banded obsidian textures are interpreted as zones of thoroughly compacted, formerly clastic material that had an initially high permeability prior to sintering and compaction (Tuffen and Dingwell, 2005). Banded obsidian bombs and clast domains are thought to represent relatively deeper fracturing in the system for two main reasons. Firstly, high Cl concentrations in certain

bands of microlite-free glass support the suggestion that banded obsidian bombs are deeper-sourced and less degassed than samples that spend a significant period at the surface. The highest Cl concentrations, <2300 ppm (Fig. 4), are comparable to the Cl concentrations (~1700-2100 ppm) found in melt inclusions in plagioclase and pyroxene crystals (Castro et al., 2013; Jay et al., 2014). Secondly, the extensive folding of thoroughly-sintered bands, removal of ash textures, and alignment of nanolites is consistent with a prolonged post-fracturing period of viscous melt relaxation.

Degassing in banded obsidian domains is largely recorded texturally as the majority of these domains have minimal chemical heterogeneity preserved. It is impossible to confirm whether bands were chemically similar prior to juxtaposition or the bands have chemically homogenised. However, given some variation is recorded (e.g. Fig. 10) it is likely chemical homogenisation has played a role. The exsolution or presence of a volatile phase (composed of major volatiles such as H<sub>2</sub>O) is necessary for the formation of trace volatile depletions. Metal species diffuse towards the melt-gas interface and then partition into the volatile phase (e.g. MacKenzie and Canil, 2008). Chemical variation is largely lost because of the extended time the melt spends in high temperature conditions (above T<sub>g</sub>) after a phase of gas mobility within a permeable fracture pathway. If high permeability is briefly sustained only the fastest diffusing elements (e.g. Li, Table 2) would significantly diffuse through the melt and partition into the gas phase during this timeframe. The subsequent residence of the system at high temperature would be sufficient to facilitate diffusive re-equilibration and remove any initial compositional variation, assuming there is no rapid quenching. Evidence for a protracted period of high-temperature, post-fracturing melt relaxation includes complete removal of initial porosity and extensive ductile deformation of bands. Gardner et al., (2018), for example, show ash can be sintered to dense glass in minutes under favourable conditions. When compositional

heterogeneity is chemically preserved (Section 5.3) the timescale recorded represents every process from initial fracturing and juxtaposition of the two contrasting bands, through their healing, bomb ejection and cooling, as only the last process will quench the glasses and lock in any chemical variation.

Textural evidence of degassing includes degassing-induced microlite crystallisation in concentrated bands and collapsed foam textures that record vesiculation and deflation (Tuffen and Dingwell, 2005; von Aulock et al., 2017). Vesicular, microlite-free bands within banded obsidian clasts were likely less degassed than microlite-rich, vesicle-free bands, allowing preferential bubble nucleation upon ejection. Geochemical signatures of degassing include the large range in Cl concentrations within banded obsidian bombs. Low Cl concentrations are restricted to bands that have undergone degassing-induced microlite crystallisation of oxides, bands also have elevated TiO<sub>2</sub> and MgO (Fig. S.2). Loss of H<sub>2</sub>O raises the liquidus temperature resulting in the crystallisation of oxides. Textures and chemistry therefore point towards gas loss from these bands, presumably when they were highly permeable channels prior to their healing. Rare depletions of Li (and Rb) in dense bands in banded obsidians (Fig. 10) indicate that heterogeneity of rapidly-diffusing trace volatiles can be preserved by quenching. However, there are no clear depletions of slower-diffusing species (e.g. Cs, Tl, Pb, see Table 2) within the same bands, reflecting diffusion-limited degassing (e.g. MacKenzie and Canil, 2008; Gardner et al., 2012), where there is insufficient time for metals to diffuse to a gas-melt boundary.

Banded obsidian clasts within breccias have a more restricted range of Cl concentrations than bombs entirely composed of banded obsidian (Fig. 4). Our interpretation is that fracturing and

entrainment of the obsidian clasts within breccias was constrained to the top ~200 m of the conduit, above the laccolith, but occurred at greater depths than the shallow sub-vent structures (top tens of metres) where flow emplacement begins (Villemant et al., 2008; Castro et al., 2016).

### **5.2.2 Non-Oxidised Breccias & Tuffisites Domains**

Although breccia bombs and tuffisite-hosting bombs are texturally distinct, their origins are arguably similar. Breccias are formed when there is fracturing and fluxing of material on a scale of centimetres to metres within the conduit (e.g. Gonnermann and Manga, 2003). Larger clasts sinter together via a fine-grained melt-rich matrix, before pressure build-up in the system results in fragmentation and bomb ejection. Tuffisite veins form when a fracture propagates through a dense melt-rich plug, with fluxing clastic material in the vein sintering together and eventually sealing the permeable fracture pathway (e.g. Tuffen et al., 2003; Castro et al., 2012; Saubin et al., 2016). Both processes involve a fracturing event generating a permeable pathway for gases, before sealing by sintering and compaction processes. As such, we will not refer to them as two separate processes but rather the same process on two differing scales, as breccias can be considered the clastic fill of tuffisite veins that are larger than the dimensions of the ejected bombs. Breccias and tuffisite veins therefore represent fracturing that occurs throughout the upper conduit at Cerdón Caille. The lack of pervasive oxidation indicates minimal interaction with the atmosphere and therefore derivation from greater depths than the surface vent nozzles, but the modest compaction and healing argue against an origin in the deep conduit. The Cl content of the host of one tuffisite vein (Fig. 4) is intermediate between the Cl-rich banded obsidian bombs and the Cl-poor shallowest breccias and ash domains. The non-

oxidised pumiceous material and clasts that make up the breccias have similar concentrations of Cl to their banded obsidian counterparts, again suggesting that they are being sourced from a similar region in the conduit during their expulsion.

Textural and chemical evidence from these domains aid assessment of the roles of permeable zones as pathways for gas and ash fluxing. Schipper et al. (2013) use a vesiculation model to constrain the onset of permeability via connected bubbles in the ascending magma to a depth of 1-1.5 km. Our breccia clast textures (dense vs. highly vesicular) suggest extensive connectivity of permeable zones that enabled juxtaposition of melts of differing original volatile contents. Volatile-rich deeper melts rapidly vesiculate as H<sub>2</sub>O solubility drops on approach to the surface, with clast expansion compacting the ash matrix of breccias (Fig. 9). The lack of water variations in the residual glasses, however, prevent us from quantitatively constraining the transport distances of clasts within fractures (e.g. Saubin et al., 2016). Tuffisite veins have previously been shown to be pathways for gas fluxing at Cordón Caulle (Paisley et al., in review) and data presented in this study further highlight their role as pathways for gas transport. The matrices of breccias and tuffisites, areas that would have been most permeable to gases, are largely depleted in volatiles (e.g. Pb and Tl), where heterogeneity is preserved (Fig. 5), although Bi enrichment is a notable exception and discussed separately (Section 5.2.6). Paisley et al. (in review) propose that vein depletions may result from metal scavenging from individual shards or tapping of more degassed melt prior to fracturing, and we argue that the former scenario is more likely. We use the characteristic diffusion length of elements (Table 2) to compare the time required for metals to diffuse across a distance equivalent to the shards' radii. Shards are ~30 µm in diameter and only minutes of fluxing would be required for Pb (and Tl) to diffuse across shards and partition into the gas phase. Final species concentrations would reflect their partitioning behaviour under these eruptive conditions and species activities

in the gas phase (Zajacz et al., 2008). Further evidence of the active stripping of elements by a fluxing gas phase is the degassing-induced elemental gradients (in alkalis, Tl and Pb) observed at domain interfaces (Table 3, Section 5.3).

### 5.2.3 Oxidised Breccias Domains

Heavily oxidised domains are thought to represent fracturing in the near-surface environment, consistent with the lower median Cl concentrations of ash shards and clasts (Fig. 4; Villemant et al., 2008). Textures indicate these samples originate from within sub-vents and therefore their chemical heterogeneities represent processes occurring in the top few metres of the conduit during ash jetting and small explosions (Schipper et al., 2013).

Clasts within these breccias are a combination of material from three sources: *deep*, *local* and the lava *flow*. Textural evidence that material is sourced from *depth* includes clasts within breccias that are highly vesicular, with contorted vesicles, likely the result of volatile-rich melt rapidly reaching the surface and vesiculating. Vesicles that intersect bomb rims can be filled with sintered ash adhered to the bombs after ejection, showing that some vesiculation occurred prior to bomb ejection. Certain clasts with collapsed foam textures have later been partially oxidised around their rims, indicating the clast was foamed prior to it reaching the surface environment where it then underwent extensive oxidation around its exterior and into any exposed voids. *Locally*-sourced material includes clasts and ash shards within the matrix which have similar microlite textures to the nozzle material (the host walls of the sub-vent fractures). Previous studies have shown how fractures are capable of transporting both local and deeper-derived material (Saubin et al., 2016). Cristobalite-bearing clasts in breccias are evidence of

lava *flow* material being entrained within the nozzles as cristobalite has only been observed in the rhyolite flow at Cordón Caulle (Schipper et al., 2015). For these clasts to be found in breccias, explosions within the vent must excavate shallow flow material. The mixed provenance of clasts reflects how these fractures are the surface expressions of deeper permeable networks, with incorporation of shallow-derived material. Pressure build-up in the system, due to blocking of nozzles or overpressure at depth, led to the explosive expulsion of these heavily oxidised breccias. There is strong chemical evidence of degassing in the near-surface. Here too, Pb and Tl are depleted in matrix material, more so than the matrix of non-oxidised domains (Fig. 5). One entrained clast within the matrix (Sample V1, Fig. 6), with its distinct Cl, Tl and Pb concentrations, is an example of the juxtaposition of variably degassed melt fragments.

Figure 6 graphically shows why RSDs for *vent* samples are greater than their *bomb* counterparts (see Appendix A). Volatile element RSDs are higher in samples V1-V5 because they comprise of diverse, variably-degassed clast types and domains which have subtly different volatile concentrations, resulting in higher standard deviations. This is most clearly noted in Li, Cu, Rb, Cd, In, Cs, Tl, Pb and Bi where RSDs are >30 % higher than the respective RSDs in *bomb* samples. The RSDs for the remaining Group 1 and Group 2 elements are also higher in *vent* samples: 10-20 %, as opposed to <10 % in *bomb* samples, which reflects microlite growth. *Vent* and *flow* samples have undergone some microlite growth and devitrification. Ablation via laser is a mini-bulk analysis of glass and microlites. When averaging multiple analyses, microlite growth will not affect the accuracy of the calculated mean, as no fractionation between crystals and melt occurred, but it will affect precision as laser pits will have variable proportions of microlites. This is especially apparent at smaller spot sizes of <50  $\mu\text{m}$ , which are comparable to microlite dimensions in these samples. If higher RSDs in volatiles were also



due to microlite growth then Group 3 elements would be expected to show a similar increase in % RSD (from <10 to 10-20 %) but this is not the case. Furthermore, individual breccia clasts can be chemically distinct. Thus we argue the high RSDs of volatile elements in *vent* samples, particularly oxidised breccias (V1-V2), represent the complex degassing histories of their constituent clasts up to and prior to entrainment in the sub-vent areas.

#### **5.2.4 Nozzle Domains**

Although no Cl concentration data were collected for the veneers and nozzle material they are a surface feature sampled in situ within the vent where lava extrusion and venting were occurring. Nozzles are the sub-vent structures that were seen to host regular explosions by Schipper et al. (2013) and are the sources of the oxidised breccias discussed above. Field and textural evidence for the channelling of gases through these features includes extensive oxidation and ash adhering to the surfaces. Ash particles flux through the permeable network of fractures, with some sintering to the walls of the nozzles. Degassing of volatile elements into these features is preserved by elemental gradients of Cu, In, Tl and Pb, and their diffusion is discussed later. Elemental depletions towards surfaces imply that metals are diffusing towards the melt-gas interface and partitioning into the gas phase. This is strong evidence that fractures at Cordon Caulle can actively degas local melt, as shown for Chaitén (Castro et al., 2012; Berlo et al., 2013).

#### **5.2.5 Ash Domains**

The adhesion of ash to bombs occurred at the surface within the vents, as ash domains only occur on the outer surfaces of small ejected bombs, its oxidisation indicating interaction with air (Fig. 2). The low Cl concentrations of ash domains (Fig. 4) also indicates its degassing occurred in a shallow environment. Ash domains are thought to form when ash fluxing through the nozzle transits from a high temperature, highly oxidising, and pressurised environment to a lower temperature and low pressure environment (i.e. air). As individual shards are only microns across and would quench almost instantly in the surface environment, they must adhere to bombs during their ejection. Ash domains can be either dark-red highly sintered veneers or light-pink, less sintered particles. We infer the adhesion of dark-red ash to surfaces (e.g. nozzles) occurs slightly deeper (where it is more oxidising) as light-pink ash is commonly adhered onto red oxidised surfaces but red oxidised ash is not observed adhered to light-pink ash. The lighter pink colour would also suggest oxidation of this ash occurred in a slightly more aerated, surface environment.

The chemical signatures in ash reflect degassing during its upward trajectory through fractures and at the surface. Low ash-host ratios in Li, Rb and Cs might be suspected to reflect alkali depletion in the ash (Fig. 5). For example, V1 ash has absolute concentrations of ~30 ppm Li, ~30-70 ppm Rb and ~2-4 ppm Cs, which are slightly lower than the Cordón Caulle average. However, the host has ~43 ppm Li, ~76 ppm Rb (but <120 ppm in certain clasts) and ~5.5 ppm Cs, which are significantly higher than average concentrations, and so the apparent depletions largely reflects host enrichment. In places Li and Cl variation correlate (e.g. V2 dense rim) and alkalis are known to complex with Cl (e.g. Pokrovski et al., 2013) thus their mobility, and concentrations, could be tied to the loss of Cl from the small shards in the shallow regime.

Depletions in trace metals such as Zn, Sn and Pb within the ash likely represents scavenging of metals by fluxing gas as the ash shards are transported towards the surface. Zinc and Pb would diffuse across fine-grained ash shards (<10  $\mu\text{m}$  across) on the order of a minute. Thallium is a highly volatile element, with its monovalent state allowing it to complex with Cl and S and form oxide or hydroxide species (Churakov et al., 2000; Baker et al., 2009). Changing conditions (temperature and oxidation) will affect the stability of Tl complexes and total concentrations in the gas phase as it goes from a sub-surface vapour to a surface aerosol within the plume. Thallium shows significant enrichment in ash domains, but depletions in the matrix ash in breccias and tuffisites formed in the conduit where it has been rapidly scavenged (Section 5.2.2, Table 1). Ash within plumes interacts with the concurrent gas phase (Moune et al., 2006; Delmelle et al., 2007; Bagnato et al., 2013) providing surfaces for adsorption or resorption of Tl, with only seconds required to diffuse through a <10  $\mu\text{m}$ -sized shard. The comparable dimensions of ash shards and laser spot sizes would normally preclude the distinction between these two processes. However, Tl enrichment in vesicle walls, in direct contact with the sample exterior, in an oxidised breccia bomb (Fig. 8A) is evidence for Tl resorption in a small window of the surface regime. Thus, we argue that ash material has scavenged and resorbed Tl from the plume at the surface. Resorption would not be preserved in Zn and Pb, their lower diffusivities precluding diffusion across this short length scale given the rapid quenching of ash shards. Zinc, Pb and Tl are known to complex with Cl in fluids and vapours (Churakov et al., 2000; Zajacz et al., 2008), and Cl favourably partitions into a vapour phase in the shallow environment (Webster, 1990; Villemant et al., 2008). Thus the shallow degassing of Cl in the system could be aiding the scavenging of certain metals.

In summary, we have strong textural and chemical evidence that magma fracturing and degassing is prevalent throughout the system at Cordón Caulle. Chemical ratios imply that the

gas phase carrying ash shards through fractures actively strips them of their volatiles, with this process more readily preserved in the surface samples where volatiles are stripped from both shards and host material.

### **5.2.6 Bismuth Behaviour at Cordón Caulle**

Bismuth was degassed and depleted as the eruption progressed. At Cordón Caulle any Bi enrichments are constrained within permeable zones where volatiles actively fluxed (e.g. breccia matrices, tuffisite veins and ash domains, Fig. 5). Paisley et al. (in review) also observed this signature and argued it is due to gas fluxing and adsorption of Bi. Given its low diffusivity, Bi would require considerable time to be resorbed into ash shards  $>30\ \mu\text{m}$  across (Table 2), making it an unlikely method of enrichment, but adsorption onto surfaces could occur (Ruggieri et al., 2011). Alternatively, the source material for the ash matrices is Bi-enriched relative to the vein and breccia hosts. Bismuth is a highly volatile element, commonly associated with mafic magmas and found enriched in plumes (Mather et al., 2012; Guo and Audétat, 2017). Thus Bi enrichments could be suggestive of the transfer and incorporation of volatiles from a mafic magma to the silicic magma at depth. Large errors for Bi domain-host ratios (Fig. 5) are due to both local (Bi depleted) and distal (Bi enriched) glass being analysed. Cu and V show more variable behaviours than other elements, including enrichments in these ash and oxidised domains (Figs 5 and 6). Both are associated with mafic melts, although V is not volatile (Mather et al., 2012; Guo and Audétat, 2017). We argue that these enrichments are evidence for the potential interaction of a volatile-rich mafic melt with the silicic melt in the Cordón Caulle system either before or during the eruption. Evidence for mafic interaction at

depth includes vesiculated mafic enclaves observed within the lava flow by Ruprecht and Winslow (2017).

### 5.3 Timescales of Degassing Events

Element gradients develop when two melts of differing concentrations are juxtaposed against each other, with elements diffusing from high to low concentrations as defined by Fick's law of diffusion (Fick, 1855). Trace element and H<sub>2</sub>O profiles forming at the margins of tuffsite veins have been previously used to assess their diffusive lifespans (Cabrera et al., 2011; Berlo et al., 2013; Castro et al., 2014). To constrain the timescales of processes related to element gradients in Section 4.2.2.2 we fit diffusion models to multiple trace element profiles with solutions of the 1D diffusion equation:

$$\frac{\partial c}{\partial t} = D \frac{\partial^2 c}{\partial x^2} \quad (1)$$

where C is the concentration of element X (ppm), t is time (s), x is position (m) and D is the diffusion coefficient of element X (m<sup>2</sup>s<sup>-1</sup>). Diffusion coefficients are a function of temperature (T) and composition (Zhang et al., 2010); which is assumed to be 895 °C for the 2011-12 Cordón Caulle magma (Castro et al., 2013). The order of the calculated diffusion coefficients is D<sub>Na</sub>>D<sub>Li</sub>>D<sub>Tl</sub>>D<sub>Pb</sub>>D<sub>Rb</sub> (Table 2 and references therein). Equation (1) was solved using an explicit finite-difference model for all profiles (Crank, 1975). The model assumes element X is diffusing in a semi-infinite media. For profiles towards fracture interfaces a pre-fracture melt concentration is assumed to be equal to the median, far field concentration. The boundary concentration of element X is assumed to be in equilibrium with the gas phase and constant throughout. For Fig. 10 conditions are different, two semi-infinite media are assumed to come in contact with each other and then diffusion commences. Accordingly, the initial boundary

concentrations within each media are equal to their respective initial far field concentrations but, unlike profiles towards fractures, the boundary concentrations are not constant throughout. We assume no modification occurred to the profiles after quenching of the melts therefore the timings calculated represent one diffusing event that encompasses all processes from fracturing, degassing and sintering, through to bomb ejection and cooling/quenching. Given analytical uncertainties and the uncertainties of the calculated diffusion coefficients for these trace elements, the modelled timescales should be considered order of magnitude estimations for the timing of events. Diffusion profiles are most commonly found neighbouring fracture surfaces in breccia or nozzle samples. Although chemical variability is found in banded obsidian (see Fig. S2, Fig. 10), and is associated with each band being chemically distinct, only one clear chemical gradient was analysed, constraining the timing of diffusion between two bands. Only certain Group 3 elements were found to preserve diffusion gradients, these are Li, Na, Rb and Cs (the alkalis) and Cu, Tl and Pb. Cl, a ligand, was also found to form a short diffusion gradient in V2 (rim). Four examples are considered here, and summarised in Table 3, highlighting the timescales of different events within the conduit (from depth to the surface) that relate to specific textural domains.

First, calculated diffusion gradients on the order of seconds (Li) and minutes (Rb) observed between two neighbouring bands in a small banded obsidian bomb (Fig. 10) suggest degassing, particle sintering and compaction occurred within these short timescales, in line with experimental studies (Wadsworth et al., 2016; Gardner et al., 2018). These bands quenched very quickly after their juxtaposition, preventing the complete homogenisation of these mobile elements. Rb diffusion is calculated to be slower than that of Pb or Tl (Table 2; Berlo et al., 2014) but these elements have no preserved variation across these bands. This suggests there was minimal initial difference in the concentration of these elements between the two bands.

Second, gradients of Li and Na observed at the edge of a banded obsidian glass shard, within a non-oxidised pumice breccia (Fig. 9), suggests the interstitial ash (and clast edges) underwent only minutes of degassing after a fracturing event, prior to the expulsion of the breccia in a subsequent explosive event. These timescales are comparable to those of sintering for the matrix ash shards given their size ( $\sim 30 \mu\text{m}$  across) and the eruptive conditions (Giordano et al., 2008; Castro et al., 2013; Vasseur et al., 2013).

Third, the chemical and textural heterogeneity in V2 constrain the timing of multiple fracturing and degassing events this bomb underwent. At first the micro-crystalline material, likely a nozzle host, underwent gas fluxing for hours to days as calculated by Tl (1-5 hours) and Rb (14-60 hours) diffusion (Fig. 8B). Far-field Li concentrations for this clast ( $\sim 18.5$  ppm) are lower than the average for this sample ( $\sim 30$  ppm) and average for Cordón Caulle ( $\sim 36$  ppm). Li diffuses faster than Rb or Tl (Table 2) thus this first event likely resulted in the depletion of Li from this material. Fluxing ceased either due to cooling, and negligible elemental diffusion, or plugging of the nozzle. Calculated Li diffusion (seconds) records a second short-lived event, possibly related to the ending of gas fluxing, forming the small Li diffusion profile prior to quenching (Fig. 8B). A new sub-vent forms and gas streaming and heating occurs, preserved as the dense, oxidised clast rim. Elevated Li, Rb, Tl, Cs and Pb (relative to clast core concentrations) suggests chemical re-equilibration with a fluxing gas phase and metal resorption within the narrow zone of reheated material. The narrow width of this rim suggests the process was short-lived and an explosive event forms the micro-crystalline clast that preserves two periods of gas fluxing. This clast falls back into a new nozzle structure and is rapidly sintered to other clasts and re-ejected as the oxidised breccia bomb V2. The sintering

of the ash matrix must have been fast as no clear diffusion profiles are recorded in the dense rim towards the clast interface or towards the depleted clast core. This clast exemplifies how repeating fracturing and degassing can progressively deplete melts and be recorded by elements that diffuse at different rates and have differing affinities for a gas phase.

Finally, Cu, Tl and Pb gradients are preserved away from fracture surfaces in nozzles where gas streaming occurred at the surface. Lead and Tl diffusion imply nozzles experience gas fluxing on the order of several hours (Fig. 7). Schipper et al. (2013) observed individual ash jetting events occurring over timescales of seconds to tens of seconds during hybrid activity in January of 2012. However, sub-vents were long-lived, stable surface structures and repeated explosions were observed from the same locations over timescales of hours (Schipper et al., 2013). Therefore, the hours-to-days timescales inferred from Pb, Tl and Rb heterogeneity in recycled nozzle material (clasts) and in situ sampled nozzles relate to the integration of numerous, ash jetting events from a single nozzle structure, rather than one discrete individual event. Indeed, multiple ash jetting events would be expected to occur from any nozzle during its lifetime, prior to its rafting away from the locus of ash and gas venting, and cessation of elemental diffusion due to cooling. Our data are consistent with a persistent, more stable late vent structure that was connected with an extensive near-surface permeable network, allowing for protracted periods of outgassing.

There is one caveat related to sampling limitations with respect to early vent material: it is not possible to definitively distinguish whether timescales of degassing increase as magma approaches the surface, or whether apparent longer timescales later in the eruption relate to a better developed network of fractures that allow for more continuous gas fluxing. However,



we hypothesise the latter is more likely as observations from this eruption show explosions progressively decreased in size with time (Silva Parejas et al., 2012; Schipper et al., 2013). Pathways within the upper conduit being open for longer would facilitate this as extended periods of outgassing reduce overpressure within the system, thereby reducing the energy of explosions.

#### **5.4 Summary: Fracturing Processes at Cordón Caulle**

Figure 11 summarises the changing degassing processes with depth in the conduit and eruption duration, as well as the constrained timescales of certain degassing processes. Chemical and textural variation within the studied eruptive products are strongly linked and largely attributed to degassing-related processes. Alkali elements (Li, Rb, Cs) and certain metals (Cu, Tl, Pb, Bi) show the most systematic variability. Juxtaposing dense and pumiceous clasts in earlier-erupted breccia samples suggest extensive connectivity through the conduit during the early phases of the eruption, in line with the proposal that interconnected vesicles provided transient permeable degassing pathways in the upper ~1-1.5 km of the conduit (Schipper et al. (2013)). Timescales for fracturing, degassing and compaction of melt during the earlier explosive phases are short, on the order of minutes. These timescales indicate rapid and efficient degassing and sintering of melt prior to sudden bomb ejection and rapid quenching that preserves compositional heterogeneity. The short duration of these degassing events prevents their preservation in slower diffusing elements (e.g. Tl, Pb), with element variability largely confined to faster-diffusing alkali elements (e.g. Li). Matrix ash shards <30 µm across show depletions in elements such as Tl and Pb. The observation of repetitive Vulcanian explosions excavating the conduit during prolonged explosive activity fits with model predictions for

regular pressure build-up and explosive events due to the high permeability threshold of the Cordón Caulle melt (Farquharson et al. 2017). These conditions would also inhibit volatile exchange of fluxing gases with melt and prohibit the preservation of element enrichments that are seen in tuffisites in other systems (Berlo et al., 2013; Paisley et al., in review). Bomb excavation from this earlier phase (beginning 8<sup>th</sup> June and continuing into the hybrid activity phase beginning June 14<sup>th</sup>) was sufficiently deep enough to excavate material that had not undergone extensive oxidation by interactions with air, especially when compared to nozzle-sourced ejecta. Low H<sub>2</sub>O concentrations indicate that *bombs* were probably sourced from above the level of laccolith emplaced 20-200 m below the surface (Silva Parejas et al., 2012; Schipper et al., 2013; Pistolesi et al., 2015; Castro et al., 2016).

The chemistry and textures of samples from later phases of the eruption (both *bomb* and *vent* samples) record an evolution in degassing systematics. *Vent* samples are more degassed than earlier *bombs* or *flow* material (highlighted by their lower In, Tl, and Bi concentrations, Fig. 3). Breccias from the near-surface environment chemically and texturally preserve several fracturing and degassing events. Individual clasts have oxidised textures indicative of extensive, protracted interaction with the atmosphere that was not confined to the final sintering event prior to bomb ejection. Such samples are likely sourced from the top metres of the conduit where there is ample scope for atmospheric interactions. Gradients in multiple elements (Li, Rb, Cu, Tl, Pb) towards fracture interfaces (in breccia clasts and nozzles) indicate that degassing events later in the eruption and nearer the surface were longer in duration (~hours). This implies the upper conduit and vent structure was more stable later in the eruption, with sub-vents stable over hours to days (Schipper et al., 2013). Our chemical observations do not reflect a single ash jetting event from a sub-vent but instead represent the integration of repeated venting over the total nozzle lifespan.

Tuffisite and breccia ash represent the most permeable pathways for gases in the conduit, in the form of initially-open fracture pathways. Systematic depletions in metals (e.g. Zn, Tl, Pb) relative to their hosts imply metal scavenging from shards by the gas phase all the way from depth to the surface, potentially aided by shallow system Cl degassing (Churakov et al., 2000; Villemant et al., 2008; Zajacz et al., 2008). Only once the ash and gases reach the surface environment do systematic Tl enrichments develop. This suggests an abrupt change in the gas capacity of Tl, which drove rapid Tl resorption into the available silicate melt (the ash particles). Bi enrichments throughout permeable zones could reflect volatile input from more mafic magmas (Guo and Audétat, 2017). It is unresolved whether Bi is adsorbed onto the edges of shards within veins, or is entering the rhyolite melt at depth.

## **6. Conclusions**

Our study highlights how trace metals can record degassing of ascending silicic magma, and how chemical and textural heterogeneity in silicic eruptive products can be strongly correlated. The low H<sub>2</sub>O contents in the 2011-12 Cordón Caulle erupted products have previously limited our understanding of its degassing systematics (Castro et al., 2014). However, by combining chemical species that diffuse slower than H<sub>2</sub>O, we have been able to: (1) link chemical and textural heterogeneity to highlight pathways for preferential gas fluxing; (2) constrain timescales of the syn-eruptive degassing processes that form these complex textures; and (3) link these to observations of eruptive behaviour. Results shed new light on the complexity of conduit degassing processes during explosive and hybrid rhyolitic activity. Our study reinforces the value of trace elements as tracers of degassing, particularly in systems where

more commonly-used species (H<sub>2</sub>O, CO<sub>2</sub>, halogens) are heavily depleted. Such an approach can be applied to other volcanic complexes to investigate sub-surface degassing in progressively brecciated and heterogeneous conduits.

## **7. Acknowledgements**

We thank Alex Corgne, Nicolas Vergara Pontigo and Felipe Ignacio P. Gallardo for assistance in the field; Anna Jung and Vincent van Hinsberg for constructive analytical and instrument assistance at McGill; and Bruce Charlier, Luisa Ashworth, and Elliot Swallow for advice at Victoria University of Wellington. RP was supported by travel and research grants from the Mineralogical Association of Canada, the Geological Society of America, McGill University and the Society of Economic Geologists. This work is supported by an NSERC Discovery Grant to KB. HT is supported by a Royal Society University Research Fellowship and thanks LU Facilities staff for assistance. CIS is supported by a Victoria University of Wellington Research Fund.

## 8. References

- Alloway, B.V., Pearce, N.J.G., Villarosa, G., Outes, V., Moreno, P.I., 2015. Multiple melt bodies fed the AD 2011 eruption of Puyehue-Cordón Caulle, Chile. *Sci. Rep.* 5, 17589. <https://doi.org/10.1038/srep17589>
- Bagnato, E., Aiuppa, A., Bertagnini, A., Bonadonna, C., Cioni, R., Pistolesi, M., Pedone, M., Hoskuldsson, A., 2013. Scavenging of sulphur, halogens and trace metals by volcanic ash: The 2010 Eyjafjallajökull eruption. *Geochim. Cosmochim. Acta* 103, 138–160. <https://doi.org/10.1016/j.gca.2012.10.048>
- Bai, T.B., van Groos, A.F.K., 1994. Diffusion of chlorine in granitic melts. *Geochim. Cosmochim. Acta* 58, 113–123. [https://doi.org/10.1016/0016-7037\(94\)90450-2](https://doi.org/10.1016/0016-7037(94)90450-2)
- Baker, R.G.A., Rehkämper, M., Hinkley, T.K., Nielsen, S.G., Toutain, J.P., 2009. Investigation of thallium fluxes from subaerial volcanism—Implications for the present and past mass balance of thallium in the oceans. *Geochim. Cosmochim. Acta* 73, 6340–6359. <https://doi.org/10.1016/j.gca.2009.07.014>
- Bechtold, B., 2016. Violin Plots for Matlab [WWW Document]. GitHub. URL <https://github.com/bastibe/Violinplot-Matlab> (accessed 12.14.18).
- Berlo, K., Brooker, R.A., Wilke, M., 2014. Diffusion coefficients for Tl, Pb, Cd, In, Zn, Bi, As, Mo and Sb in hydrous rhyolite at 100-200 MPa, in: EGU2014-1679. Presented at the EGU General Assembly 2014, Vienna, Austria.
- Berlo, K., Tuffen, H., Smith, V., Castro, J.M., Pyle, D.M., Mather, T.A., Geraki, K., 2013. Element variations in rhyolitic magma resulting from gas transport. *Geochim. Cosmochim. Acta* 121, 436–451. <https://doi.org/10.1016/j.gca.2013.07.032>
- Bertin, D., Lara, L.E., Basualto, D., Amigo, Á., Cardona, C., Franco, L., Gil, F., Lazo, J., 2015. High effusion rates of the Cordón Caulle 2011-2012 eruption (Southern Andes) and

- their relation with the quasi-harmonic tremor: effusion rates and quasi-harmonic tremor. *Geophys. Res. Lett.* 42, 7054–7063. <https://doi.org/10.1002/2015GL064624>
- Cabrera, A., Weinberg, R.F., Wright, H.M.N., Zlotnik, S., Cas, R.A.F., 2011. Melt fracturing and healing: A mechanism for degassing and origin of silicic obsidian. *Geology* 39, 67–70. <https://doi.org/10.1130/G31355.1>
- Cashman, K.V., Sparks, R.S.J., 2013. How volcanoes work: A 25 year perspective. *Geol. Soc. Am. Bull.* 125, 664–690. <https://doi.org/10.1130/B30720.1>
- Castro, J.M., Bindeman, I.N., Tuffen, H., Ian Schipper, C., 2014. Explosive origin of silicic lava: Textural and  $\delta D-H_2O$  evidence for pyroclastic degassing during rhyolite effusion. *Earth Planet. Sci. Lett.* 405, 52–61. <https://doi.org/10.1016/j.epsl.2014.08.012>
- Castro, J.M., Cordonnier, B., Schipper, C.I., Tuffen, H., Baumann, T.S., Feisel, Y., 2016. Rapid laccolith intrusion driven by explosive volcanic eruption. *Nat. Commun.* 7, 13585. <https://doi.org/10.1038/ncomms13585>
- Castro, J.M., Cordonnier, B., Tuffen, H., Tobin, M.J., Puskar, L., Martin, M.C., Bechtel, H.A., 2012. The role of melt-fracture degassing in defusing explosive rhyolite eruptions at volcán Chaitén. *Earth Planet. Sci. Lett.* 333–334, 63–69. <https://doi.org/10.1016/j.epsl.2012.04.024>
- Castro, J.M., Schipper, C.I., Mueller, S.P., Miltzer, A.S., Amigo, A., Parejas, C.S., Jacob, D., 2013. Storage and eruption of near-liquidus rhyolite magma at Cordón Caulle, Chile. *Bull. Volcanol.* 75:702. <https://doi.org/10.1007/s00445-013-0702-9>
- Churakov, S.V., Tkachenko, S.I., Korzhinskii, M.A., Bocharnikov, R.E., Shmulovich, K.I., 2000. Evolution of Composition of High-Temperature Fumarolic Gases from Kudryavy Volcano, Iturup, Kuril Islands: the Thermodynamic Modeling. *Geochem. Int.* 38, 436–451.

- Collini, E., Osores, M.S., Folch, A., Viramonte, J.G., Villarosa, G., Salmuni, G., 2013. Volcanic ash forecast during the June 2011 Cordón Caulle eruption. *Nat. Hazards* 66, 389–412. <https://doi.org/10.1007/s11069-012-0492-y>
- Crank, J., 1975. *The mathematics of diffusion*, 2d ed. ed. Clarendon Press, Oxford.
- Daga, R., Ribeiro Guevara, S., Poire, D.G., Arribére, M., 2014. Characterization of tephra dispersed by the recent eruptions of volcanoes Calbuco (1961), Chaitén (2008) and Cordón Caulle Complex (1960 and 2011), in Northern Patagonia. *J. South Am. Earth Sci.* 49, 1–14. <https://doi.org/10.1016/j.jsames.2013.10.006>
- Delgado, F., Pritchard, M.E., Basualto, D., Lazo, J., Córdova, L., Lara, L.E., 2016. Rapid reinflation following the 2011-2012 rhyodacite eruption at Cordón Caulle volcano (Southern Andes) imaged by InSAR: Evidence for magma reservoir refill: Inflation After a Silicic Eruption. *Geophys. Res. Lett.* 43, 9552–9562. <https://doi.org/10.1002/2016GL070066>
- Delmelle, P., Lambert, M., Dufrêne, Y., Gerin, P., Óskarsson, N., 2007. Gas/aerosol–ash interaction in volcanic plumes: New insights from surface analyses of fine ash particles. *Earth Planet. Sci. Lett.* 259, 159–170. <https://doi.org/10.1016/j.epsl.2007.04.052>
- Digital Globe, 2015. WorldView-2 Pan\_MS1\_MS2 scene 103001003D539F00, 27/02/2015: Accessed from Google Earth.
- Edmonds, M., Pyle, D., Oppenheimer, C., 2002. HCl emissions at Soufrière Hills Volcano, Montserrat, West Indies, during a second phase of dome building: November 1999 to October 2000. *Bull. Volcanol.* 64, 21–30. <https://doi.org/10.1007/s00445-001-0175-0>
- Farquharson, J.I., Heap, M.J., Lavallée, Y., Varley, N.R., Baud, P., 2016. Evidence for the development of permeability anisotropy in lava domes and volcanic conduits. *J. Volcanol. Geotherm. Res.* 323, 163–185. <https://doi.org/10.1016/j.jvolgeores.2016.05.007>

- Farquharson, J.I., Wadsworth, F.B., Heap, M.J., Baud, P., 2017. Time-dependent permeability evolution in compacting volcanic fracture systems and implications for gas overpressure. *J. Volcanol. Geotherm. Res.* 339, 81–97. <https://doi.org/10.1016/j.jvolgeores.2017.04.025>
- Fick, A., 1855. Ueber Diffusion. *Ann. Phys.* 170, 59–86. <https://doi.org/10.1002/andp.18551700105>
- Furukawa, K., Uno, K., Miyagi, I., 2010. Mechanisms of oxidation and degassing in the Takanoobane rhyolite lava of Aso Volcano, Japan. *J. Volcanol. Geotherm. Res.* 198, 348–354. <https://doi.org/10.1016/j.jvolgeores.2010.09.015>
- Gardner, J.E., Befus, K.S., Watkins, J., Hesse, M., Miller, N., 2012. Compositional gradients surrounding spherulites in obsidian and their relationship to spherulite growth and lava cooling. *Bull. Volcanol.* 74, 1865–1879. <https://doi.org/10.1007/s00445-012-0642-9>
- Gardner, J.E., Wadsworth, F.B., Llewellyn, E.W., Watkins, J.M., Coumans, J.P., 2018. Experimental sintering of ash at conduit conditions and implications for the longevity of tuffsites. *Bull. Volcanol.* 80:23. <https://doi.org/10.1007/s00445-018-1202-8>
- GeoReM: BCR-2G (published values) [WWW Document], 2015. URL [http://georem.mpch-mainz.gwdg.de/sample\\_query.asp](http://georem.mpch-mainz.gwdg.de/sample_query.asp) (accessed 9.15.15).
- Gerlach, D.C., Frey, F.A., Moreno, H., 1988. Recent Volcanism in the Puyehue-Cordon Caulle Region, Southern Andes, Chile (40.5°S): Petrogenesis of Evolved Lavas. *J. Petrol.* 29, 333–382.
- Giordano, D., Russell, J.K., Dingwell, D.B., 2008. Viscosity of magmatic liquids: A model. *Earth Planet. Sci. Lett.* 271, 123–134. <https://doi.org/10.1016/j.epsl.2008.03.038>
- Gonnermann, H.M., Manga, M., 2003. Explosive volcanism may not be an inevitable consequence of magma fragmentation. *Nature* 426, 432–435. <https://doi.org/10.1038/nature02138>



- Guo, H., Audétat, A., 2017. Transfer of volatiles and metals from mafic to felsic magmas in composite magma chambers: An experimental study. *Geochim. Cosmochim. Acta* 198, 360–378. <https://doi.org/10.1016/j.gca.2016.11.029>
- Heap, M.J., Farquharson, J.I., Wadsworth, F.B., Kolzenburg, S., Russell, J.K., 2015. Timescales for permeability reduction and strength recovery in densifying magma. *Earth Planet. Sci. Lett.* 429, 223–233. <https://doi.org/10.1016/j.epsl.2015.07.053>
- Heiken, G., Wohletz, K., Eichelberger, J., 1988. Fracture fillings and intrusive pyroclasts, Inyo Domes, California. *J. Geophys. Res. Solid Earth* 93, 4335–4350. <https://doi.org/10.1029/JB093iB05p04335>
- Hinkley, T.K., Le Cloarec, M.-F., Lambert, G., 1994. Fractionation of families of major, minor, and trace metals across the melt-vapor interface in volcanic exhalations. *Geochim. Cosmochim. Acta* 58, 3255–3263. [https://doi.org/10.1016/0016-7037\(94\)90053-1](https://doi.org/10.1016/0016-7037(94)90053-1)
- Isgett, S.J., Houghton, B.F., Fagents, S.A., Biass, S., Burgisser, A., Arbaret, L., 2017. Eruptive and shallow conduit dynamics during Vulcanian explosions: insights from the Episode IV block field of the 1912 eruption of Novarupta, Alaska. *Bull. Volcanol.* 79:58. <https://doi.org/10.1007/s00445-017-1138-4>
- Jambon, A., 1982. Tracer diffusion in granitic melts: Experimental results for Na, K, Rb, Cs, Ca, Sr, Ba, Ce, Eu to 1300°C and a model of calculation. *J. Geophys. Res. Solid Earth* 87, 10797–10810. <https://doi.org/10.1029/JB087iB13p10797>
- Jarosewich, E., Nelen, J.A., Norberg, J.A., 1980. Reference Samples for Electron Microprobe Analysis\*. *Geostand. Geoanalytical Res.* 4, 43–47. <https://doi.org/10.1111/j.1751-908X.1980.tb00273.x>
- Jay, J., Costa, F., Pritchard, M., Lara, L., Singer, B., Herrin, J., 2014. Locating magma reservoirs using InSAR and petrology before and during the 2011–2012 Cordón Caulle

- silicic eruption. *Earth Planet. Sci. Lett.* 395, 254–266.  
<https://doi.org/10.1016/j.epsl.2014.03.046>
- Jicha, B.R., Singer, B.S., Beard, B.L., Johnson, C.M., Moreno-Roa, H., Naranjo, J.A., 2007. Rapid magma ascent and generation of <sup>230</sup>Th excesses in the lower crust at Puyehue–Cordón Caulle, Southern Volcanic Zone, Chile. *Earth Planet. Sci. Lett.* 255, 229–242.  
<https://doi.org/10.1016/j.epsl.2006.12.017>
- Jochum, K.P., 2009. BCR-2G: GeoReM preferred values (1/2009) [WWW Document]. GeoREM. URL [http://georem.mpch-mainz.gwdg.de/sample\\_query\\_pref.asp](http://georem.mpch-mainz.gwdg.de/sample_query_pref.asp) (accessed 11.2.18).
- Jochum, K.P., Weis, U., Stoll, B., Kuzmin, D., Yang, Q., Raczek, I., Jacob, D.E., Stracke, A., Birbaum, K., Frick, D.A., Günther, D., Enzweiler, J., 2011. Determination of Reference Values for NIST SRM 610–617 Glasses Following ISO Guidelines. *Geostand. Geoanalytical Res.* 35, 397–429. <https://doi.org/10.1111/j.1751-908X.2011.00120.x>
- Kendrick, J.E., Lavallée, Y., Varley, N.R., Wadsworth, F.B., Lamb, O.D., Vasseur, J., 2016. Blowing Off Steam: Tuffisite Formation As a Regulator for Lava Dome Eruptions. *Front. Earth Sci.* 4:41. <https://doi.org/10.3389/feart.2016.00041>
- Kolzenburg, S., Heap, M.J., Lavallée, Y., Russell, J.K., Meredith, P.G., Dingwell, D.B., 2012. Strength and permeability recovery of tuffisite-bearing andesite. *Solid Earth* 3, 191–198. <https://doi.org/10.5194/se-3-191-2012>
- Kolzenburg, S., Russell, J.K., 2014. Welding of pyroclastic conduit infill: A mechanism for cyclical explosive eruptions. *J. Geophys. Res. Solid Earth* 119, 5305–5323. <https://doi.org/10.1002/2013JB010931>
- Lara, L.E., Lavenu, A., Cembrano, J., Rodríguez, C., 2006. Structural controls of volcanism in transversal chains: Resheared faults and neotectonics in the Cordón Caulle–Puyehue

- area (40.5°S), Southern Andes. *J. Volcanol. Geotherm. Res.* 158, 70–86.  
<https://doi.org/10.1016/j.jvolgeores.2006.04.017>
- Lara, L.E., Naranjo, J.A., Moreno, H., 2004. Rhyodacitic fissure eruption in Southern Andes (Cordón Caulle; 40.5°S) after the 1960 (Mw:9.5) Chilean earthquake: a structural interpretation. *J. Volcanol. Geotherm. Res.* 138, 127–138.  
<https://doi.org/10.1016/j.jvolgeores.2004.06.009>
- Lowenstern, J.B., Bleick, H., Vazquez, J.A., Castro, J.M., Larson, P.B., 2012. Degassing of Cl, F, Li, and Be during extrusion and crystallization of the rhyolite dome at Volcán Chaitén, Chile during 2008 and 2009. *Bull. Volcanol.* 74, 2303–2319.  
<https://doi.org/10.1007/s00445-012-0663-4>
- MacKenzie, J.M., Canil, D., 2008. Volatile heavy metal mobility in silicate liquids: Implications for volcanic degassing and eruption prediction. *Earth Planet. Sci. Lett.* 269, 488–496. <https://doi.org/10.1016/j.epsl.2008.03.005>
- Magnall, N., James, M.R., Tuffen, H., Vye-Brown, C., 2017. Emplacing a Cooling-Limited Rhyolite Lava Flow: Similarities with Basaltic Lava Flows. *Front. Earth Sci.* 5:44.  
<https://doi.org/10.3389/feart.2017.00044>
- Magnall, N., James, M.R., Tuffen, H., Vye-Brown, C., Schipper, C.I., Castro, J.M., Davies, A.G., 2018. The origin and evolution of breakouts in a cooling-limited rhyolite lava flow. *Geol. Soc. Am. Bull.*
- Mather, T.A., Witt, M.L.I., Pyle, D.M., Quayle, B.M., Aiuppa, A., Bagnato, E., Martin, R.S., Sims, K.W.W., Edmonds, M., Sutton, A.J., Ilyinskaya, E., 2012. Halogens and trace metal emissions from the ongoing 2008 summit eruption of Kīlauea volcano, Hawai‘i. *Geochim. Cosmochim. Acta* 83, 292–323. <https://doi.org/10.1016/j.gca.2011.11.029>

- Moriizumi, M., Nakashima, S., Okumura, S., Yamanoi, Y., 2009. Color-change processes of a plinian pumice and experimental constraints of color-change kinetics in air of an obsidian. *Bull. Volcanol.* 71, 1–13. <https://doi.org/10.1007/s00445-008-0202-5>
- Moune, S., Gauthier, P.-J., Gislason, S.R., Sigmarsson, O., 2006. Trace element degassing and enrichment in the eruptive plume of the 2000 eruption of Hekla volcano, Iceland. *Geochim. Cosmochim. Acta* 70, 461–479. <https://doi.org/10.1016/j.gca.2005.09.011>
- Mujin, M., Nakamura, M., Miyake, A., 2017. Eruption style and crystal size distributions: Crystallization of groundmass nanolites in the 2011 Shinmoedake eruption. *Am. Mineral.* 102, 2367–2380. <https://doi.org/10.2138/am-2017-6052CCBYNCND>
- Pallister, J.S., Diefenbach, A.K., Burton, W.C., Muñoz, J., Griswold, J.P., Lara, L.E., Lowenstern, J.B., Valenzuela, C.E., 2013. The Chaitén rhyolite lava dome: Eruption sequence, lava dome volumes, rapid effusion rates and source of the rhyolite magma. *Andean Geol.* 40, 277–294. <https://doi.org/10.5027/andgeoV40n2-a06>
- Paton, C., Hellstrom, J., Paul, B., Woodhead, J., Hergt, J., 2011. Iolite: Freeware for the visualisation and processing of mass spectrometric data. *J. Anal. At. Spectrom.* 26, 2508–2518. <https://doi.org/10.1039/c1ja10172b>
- Pistolesi, M., Cioni, R., Bonadonna, C., Elissondo, M., Baumann, V., Bertagnini, A., Chiari, L., Gonzales, R., Rosi, M., Francalanci, L., 2015. Complex dynamics of small-moderate volcanic events: the example of the 2011 rhyolitic Cordón Caulle eruption, Chile. *Bull. Volcanol.* 77:3. <https://doi.org/10.1007/s00445-014-0898-3>
- Plail, M., Edmonds, M., Humphreys, M.C.S., Barclay, J., Herd, R.A., 2014. Geochemical evidence for relict degassing pathways preserved in andesite. *Earth Planet. Sci. Lett.* 386, 21–33. <https://doi.org/10.1016/j.epsl.2013.10.044>

- Pokrovski, G.S., Borisova, A.Y., Bychkov, A.Y., 2013. Speciation and Transport of Metals and Metalloids in Geological Vapors. *Rev. Mineral. Geochem.* 76, 165–218. <https://doi.org/10.2138/rmg.2013.76.6>
- Ruggieri, F., Fernández-Turiel, J.-L., Saavedra, J., Gimeno, D., Polanco, E., Naranjo, J.A., 2011. Environmental geochemistry of recent volcanic ashes from the Southern Andes. *Environ. Chem.* 8, 236–247. <https://doi.org/10.1071/EN10097>
- Ruprecht, P., Winslow, H., 2017. Short-circuiting magma differentiation from basalt straight to rhyolite?, in: V11C-1082. Presented at the AGU Fall Meeting, New Orleans, USA.
- Saubin, E., Tuffen, H., Gurioli, L., Owen, J., Castro, J.M., Berlo, K., McGowan, E.M., Schipper, C.I., Wehbe, K., 2016. Conduit Dynamics in Transitional Rhyolitic Activity Recorded by Tuffisite Vein Textures from the 2008–2009 Chaitén Eruption. *Front. Earth Sci.* 4:59. <https://doi.org/10.3389/feart.2016.00059>
- Schipper, C.I., Castro, J.M., Tuffen, H., James, M.R., How, P., 2013. Shallow vent architecture during hybrid explosive–effusive activity at Cordón Caulle (Chile, 2011–12): Evidence from direct observations and pyroclast textures. *J. Volcanol. Geotherm. Res.* 262, 25–37. <https://doi.org/10.1016/j.jvolgeores.2013.06.005>
- Schipper, C.I., Castro, J.M., Tuffen, H., Wadsworth, F.B., Chappell, D., Pantoja, A.E., Simpson, M.P., Le Ru, E.C., 2015. Cristobalite in the 2011–2012 Cordón Caulle eruption (Chile). *Bull. Volcanol.* 77:34. <https://doi.org/10.1007/s00445-015-0925-z>
- Silva Parejas, C., Lara, L.E., Bertin, D., Amigo, A., Orozco, G., 2012. The 2011-2012 eruption of Cordón Caulle volcano (Southern Andes): Evolution, crisis management and current hazards, in: EGU2012-9382-2. Presented at the EGU General Assembly, Vienna, Austria.
- Singer, B.S., Jicha, B.R., Harper, M.A., Naranjo, J.A., Lara, L.E., Moreno-Roa, H., 2008. Eruptive history, geochronology, and magmatic evolution of the Puyehue-Cordon

- Caulle volcanic complex, Chile. *Geol. Soc. Am. Bull.* 120, 599–618.  
<https://doi.org/10.1130/B26276.1>
- Stasiuk, M.V., Barclay, J., Carroll, M.R., Jaupart, C., Ratté, J.C., Sparks, R.S.J., Tait, S.R., 1996. Degassing during magma ascent in the Mule Creek vent (USA). *Bull. Volcanol.* 58, 117–130. <https://doi.org/10.1007/s004450050130>
- Tuffen, H., Dingwell, D., 2005. Fault textures in volcanic conduits: evidence for seismic trigger mechanisms during silicic eruptions. *Bull. Volcanol.* 67, 370–387.  
<https://doi.org/10.1007/s00445-004-0383-5>
- Tuffen, H., Dingwell, D.B., Pinkerton, H., 2003. Repeated fracture and healing of silicic magma generate flow banding and earthquakes? *Geology* 31, 1089–1092.  
<https://doi.org/10.1130/G19777.1>
- Tuffen, H., James, M.R., Castro, J.M., Schipper, C.I., 2013. Exceptional mobility of an advancing rhyolitic obsidian flow at Cordón Caulle volcano in Chile. *Nat. Commun.* 4, 2709. <https://doi.org/10.1038/ncomms3709>
- Vasseur, J., Wadsworth, F.B., Lavallée, Y., Hess, K.-U., Dingwell, D.B., 2013. Volcanic sintering: Timescales of viscous densification and strength recovery. *Geophys. Res. Lett.* 40, 5658–5664. <https://doi.org/10.1002/2013GL058105>
- Villemant, B., Mouatt, J., Michel, A., 2008. Andesitic magma degassing investigated through H<sub>2</sub>O vapour–melt partitioning of halogens at Soufrière Hills Volcano, Montserrat (Lesser Antilles). *Earth Planet. Sci. Lett.* 269, 212–229.  
<https://doi.org/10.1016/j.epsl.2008.02.014>
- von Aulock, F.W., Kennedy, B.M., Maksimenko, A., Wadsworth, F.B., Lavallée, Y., 2017. Outgassing from Open and Closed Magma Foams. *Front. Earth Sci.* 5:46.  
<https://doi.org/10.3389/feart.2017.00046>

- Wadsworth, F.B., Vasseur, J., Scheu, B., Kendrick, J.E., Lavallée, Y., Dingwell, D.B., 2016. Universal scaling of fluid permeability during volcanic welding and sediment diagenesis. *Geology* 44, 219–222. <https://doi.org/10.1130/G37559.1>
- Wahrenberger, C., Seward, T.M., Dietrich, V., 2002. Volatile trace-element transport in high-temperature gases from Kudriavy volcano (Itrup, Kurile Islands, Russia), in: *The Water-Rock Interactions, Ore Deposits, and Environmental Geochemistry: A Tribute to David A. Crerar*, Geochemical Society, Special Publications. pp. 307–327.
- Watkins, J.M., Gardner, J.E., Befus, K.S., 2017. Nonequilibrium degassing, regassing, and vapor fluxing in magmatic feeder systems. *Geology* 45, 183–186. <https://doi.org/10.1130/G38501.1>
- Webster, J.D., 1990. Partitioning of F between H<sub>2</sub>O and CO<sub>2</sub> fluids and topaz rhyolite melt. *Contrib. Mineral. Petrol.* 104, 424–438. <https://doi.org/10.1007/BF01575620>
- Williams-Jones, A.E., Migdisov, A.A., Archibald, S.M., Xiao, Z., 2002. Vapor-transport of ore metals, in: *The Water-Rock Interactions, Ore Deposits, and Environmental Geochemistry: A Tribute to David A. Crerar*, Geochemical Society, Special Publications. pp. 279–305.
- Wright, H.M.N., Cashman, K.V., Rosi, M., Cioni, R., 2007. Breadcrust bombs as indicators of Vulcanian eruption dynamics at Guagua Pichincha volcano, Ecuador. *Bull. Volcanol.* 69, 281–300. <https://doi.org/10.1007/s00445-006-0073-6>
- Zajacz, Z., Halter, W.E., Pettke, T., Guillong, M., 2008. Determination of fluid/melt partition coefficients by LA-ICPMS analysis of co-existing fluid and silicate melt inclusions: Controls on element partitioning. *Geochim. Cosmochim. Acta* 72, 2169–2197. <https://doi.org/10.1016/j.gca.2008.01.034>
- Zhang, Y., Ni, H., 2010. Diffusion of H, C, and O Components in Silicate Melts. *Rev. Mineral. Geochem.* 72, 171–225. <https://doi.org/10.2138/rmg.2010.72.5>

Zhang, Y., Ni, H., Chen, Y., 2010. Diffusion Data in Silicate Melts. *Rev. Mineral. Geochem.* 72, 311–408. <https://doi.org/10.2138/rmg.2010.72.8>



## 9. Tables and Figures

Figure 1:

(A) Schematic timeline of eruption. Samples collected represent the explosive (*bombs*) and effusive (*flow*) components of the eruption and *vent* degassing processes. Arrows indicate inflation associated with laccolith emplacement (Castro et al., 2016). (B) Annotated Google Earth image of 2011-2012 Cordón Caulle flow, SVZ, Chile (Digital Globe, 2015). Boxes (red) highlight sample collection localities. *Bombs* and *flow* material collected far from the vent represent earlier explosive and effusive activity. *Inset*: location of PCCVC in context of the SVZ in Chile.

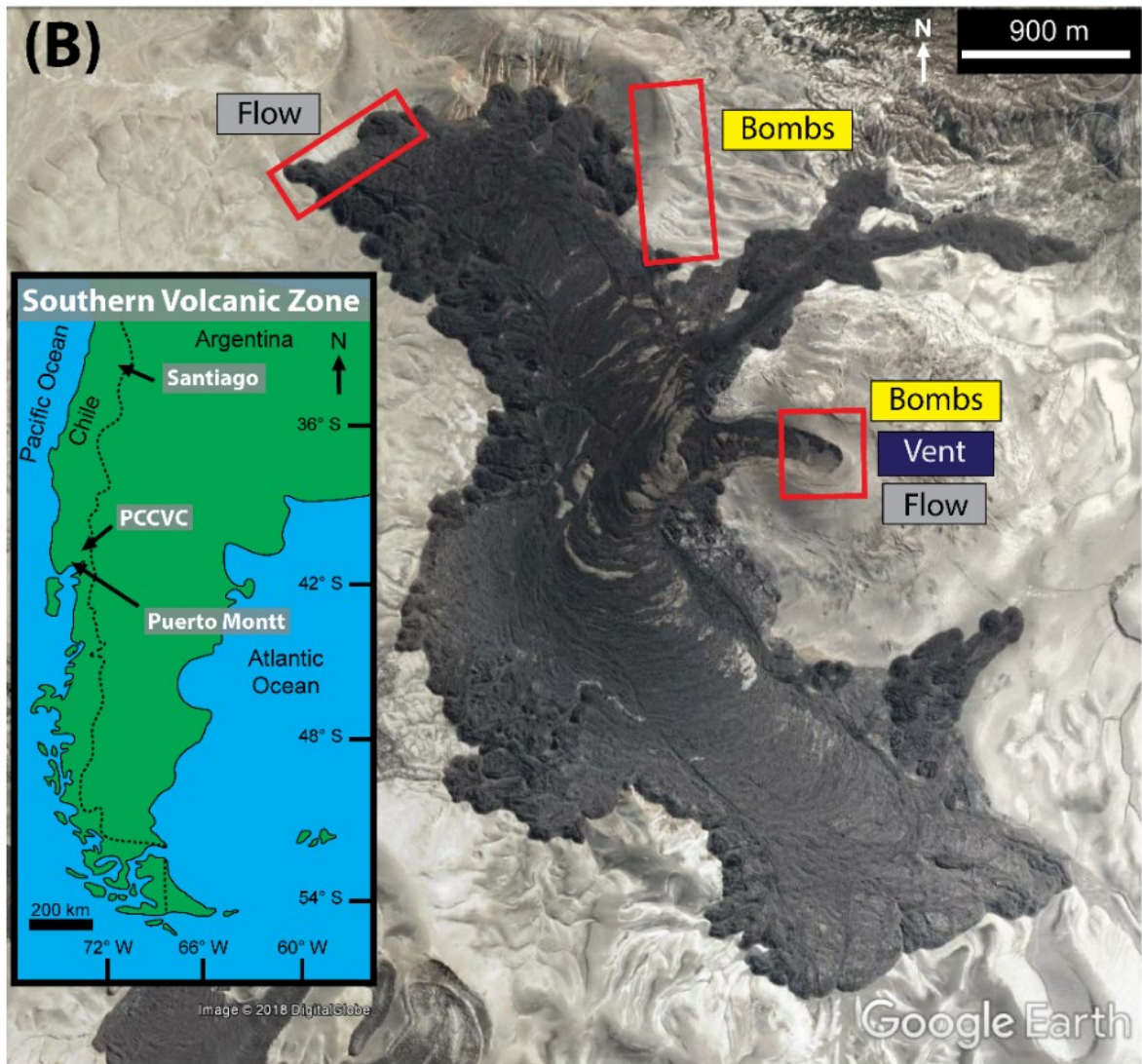
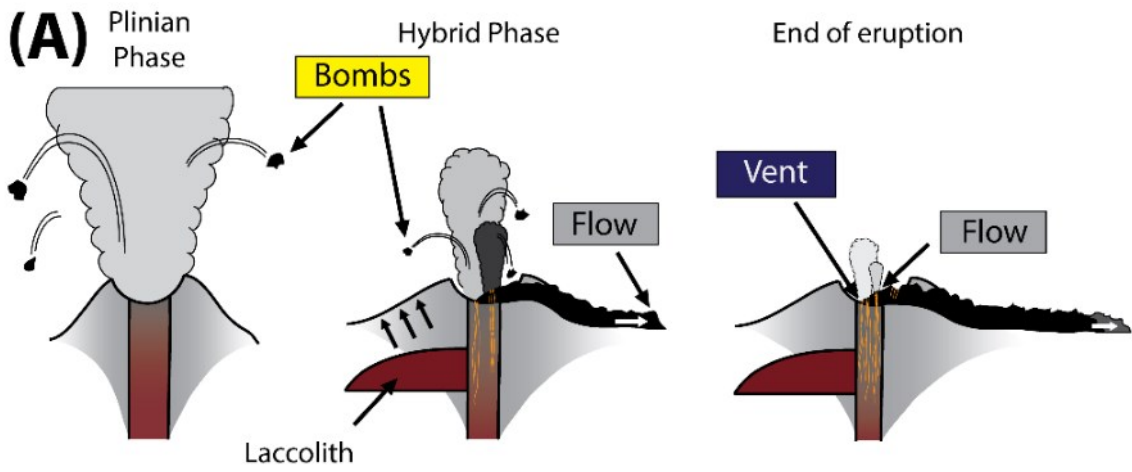


Figure 2:

Schematic overview of the conduit and the relative depths of degassing that are preserved by different domains. Red arrows point to textures that characterise domain types.

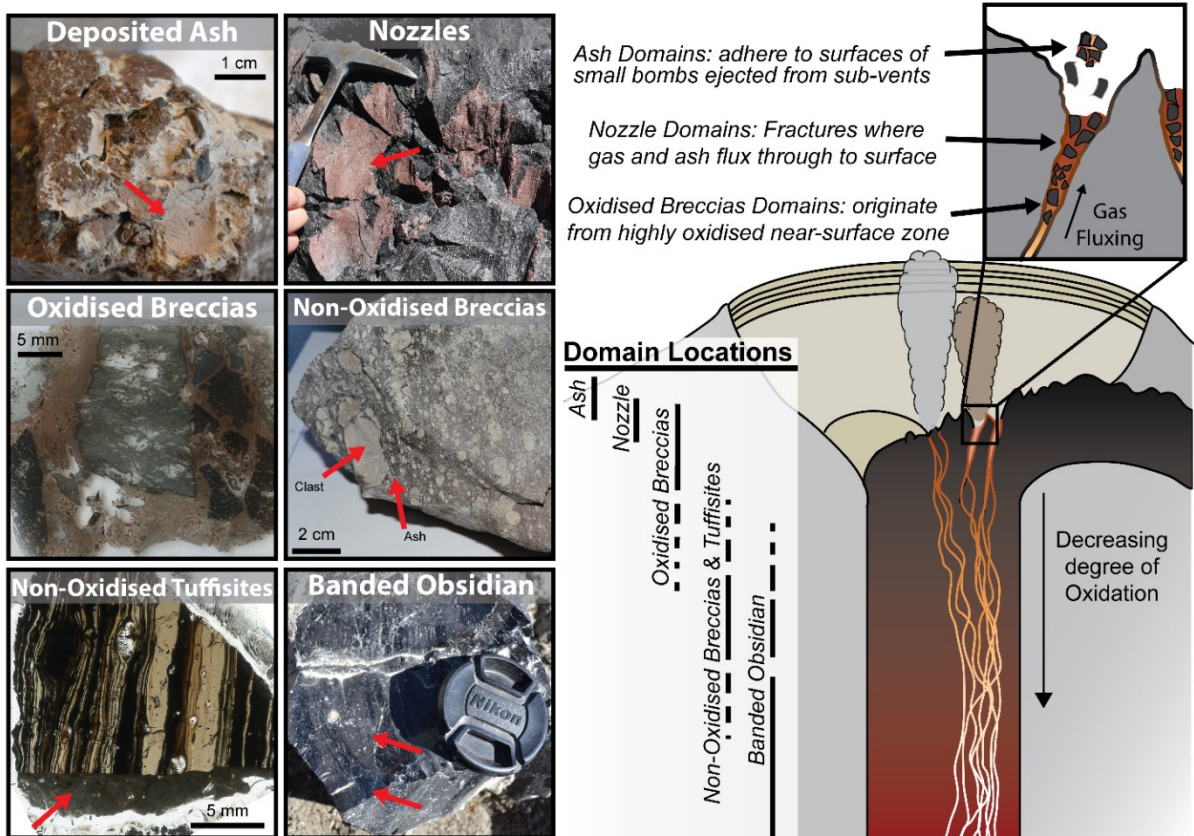


Figure 3:

Comparison of median Tl, In and Bi concentrations of *bomb*, *flow* and *vent* samples from the 2011-2012 eruption (A and B). Error bars extend to the 25<sup>th</sup> (minimum) and 75<sup>th</sup> (maximum) percentiles. (C) and (D) show individual analyses from *bomb* (circles), *flow* (squares) and *vent* (triangle) samples. All three elements are highly volatile. *Vent* samples have lower In, Tl and Bi concentrations than *bomb* and *flow* samples suggestive of the progressive loss of volatiles from the system with eruption duration.

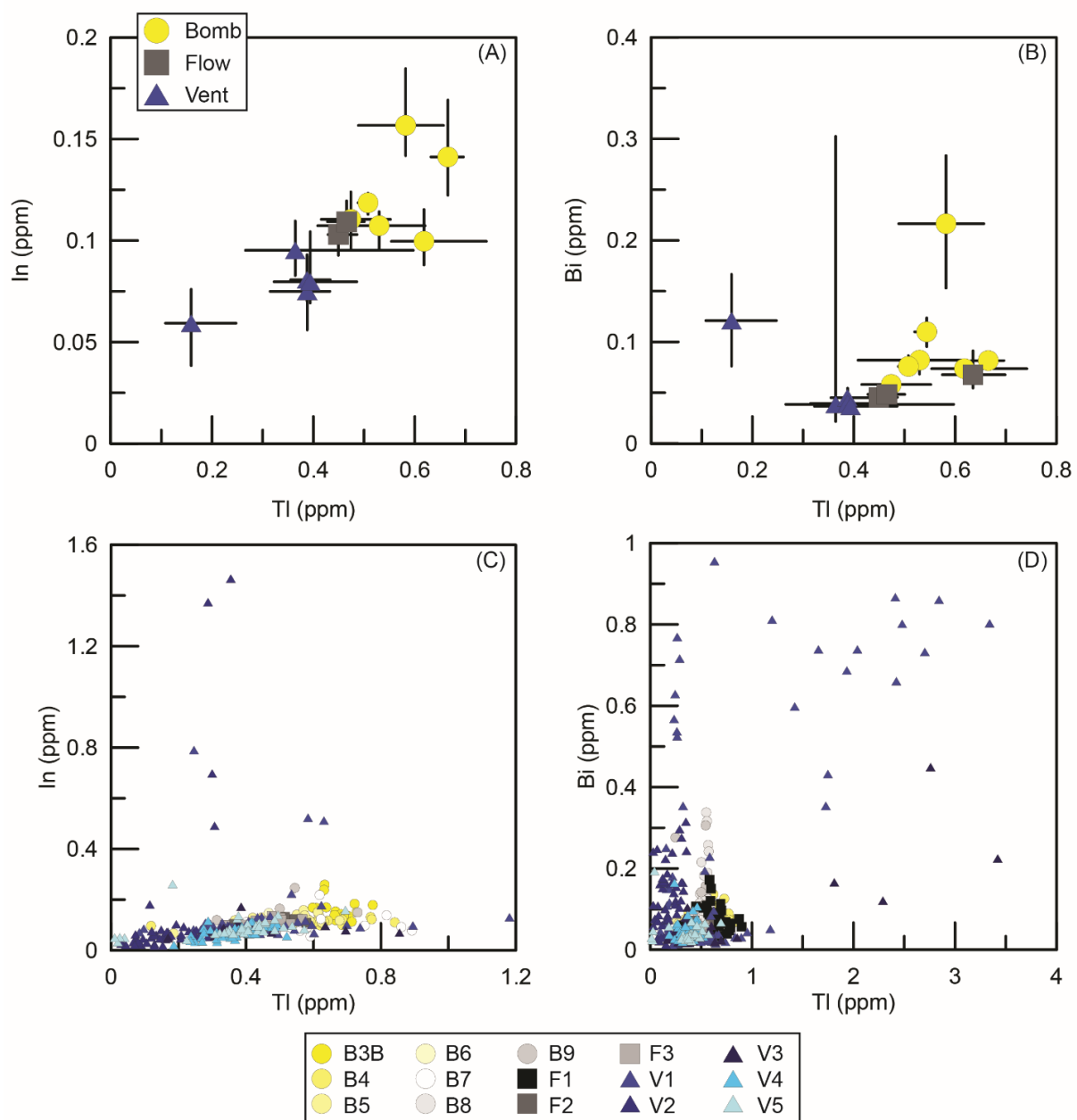


Figure 4:

Violin plot highlighting median Cl concentrations for each textural domain (white circles) with their associated interquartile ranges (grey boxes), total ranges (black lines) and distribution of individual analyses (shaded areas and circles) (Bechtold, 2016). Domains are from *vent* (blue) and *bomb* (yellow) samples. Shaded box represents range of Cl concentrations in melt inclusions (Castro et al., 2013; Jay et al., 2014).

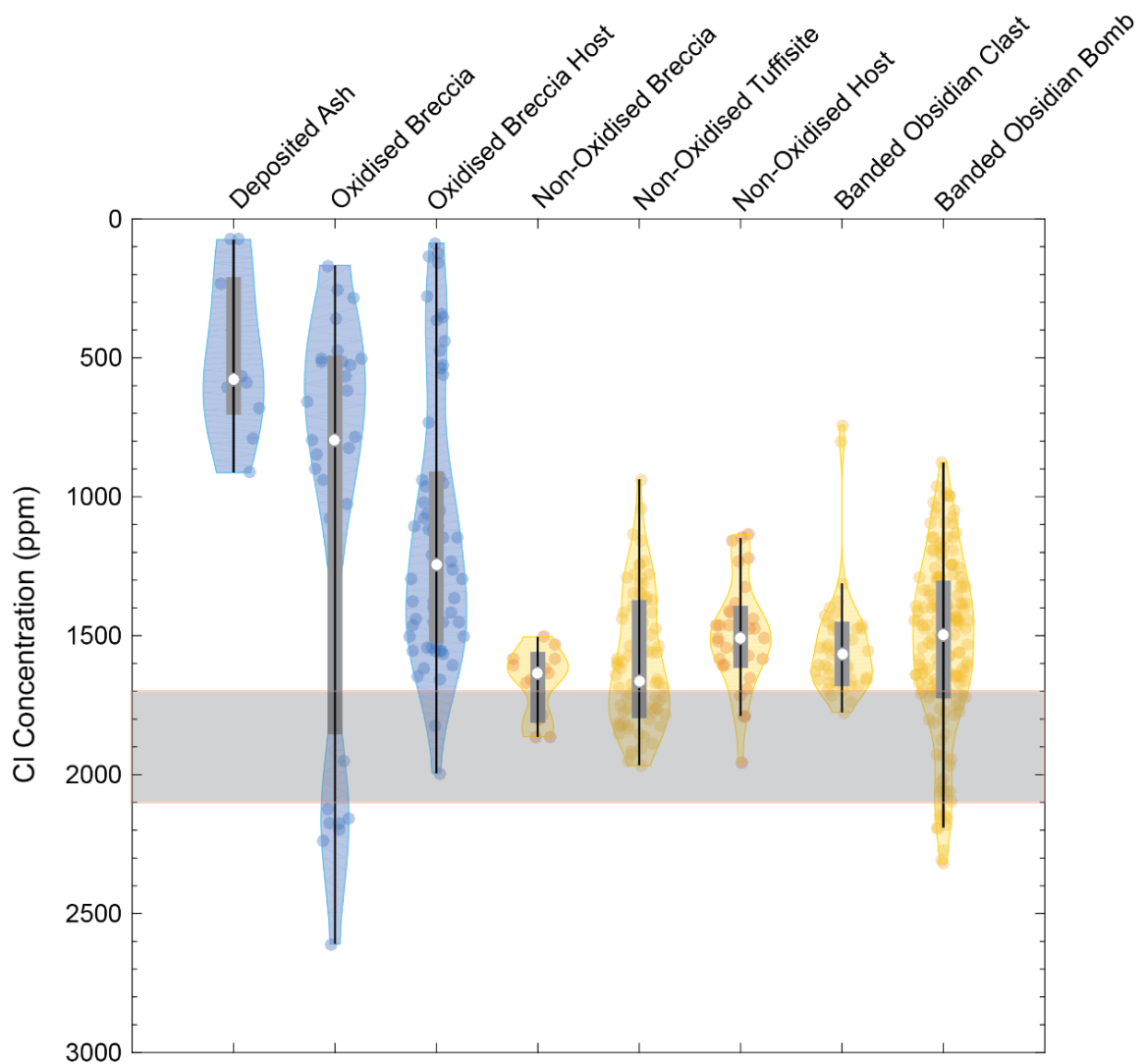


Figure 5:

Domain-host ratios for select elements. Average concentrations for textural domains are normalised to their respective average host concentrations. Errors are 1 standard deviation. Domains are from *vent* (triangles) and *bomb* (circles) samples. Note use of log scale for ash and oxidised domains to account for high Bi ratios. Missing symbols mean element was not analysed for in that domain.

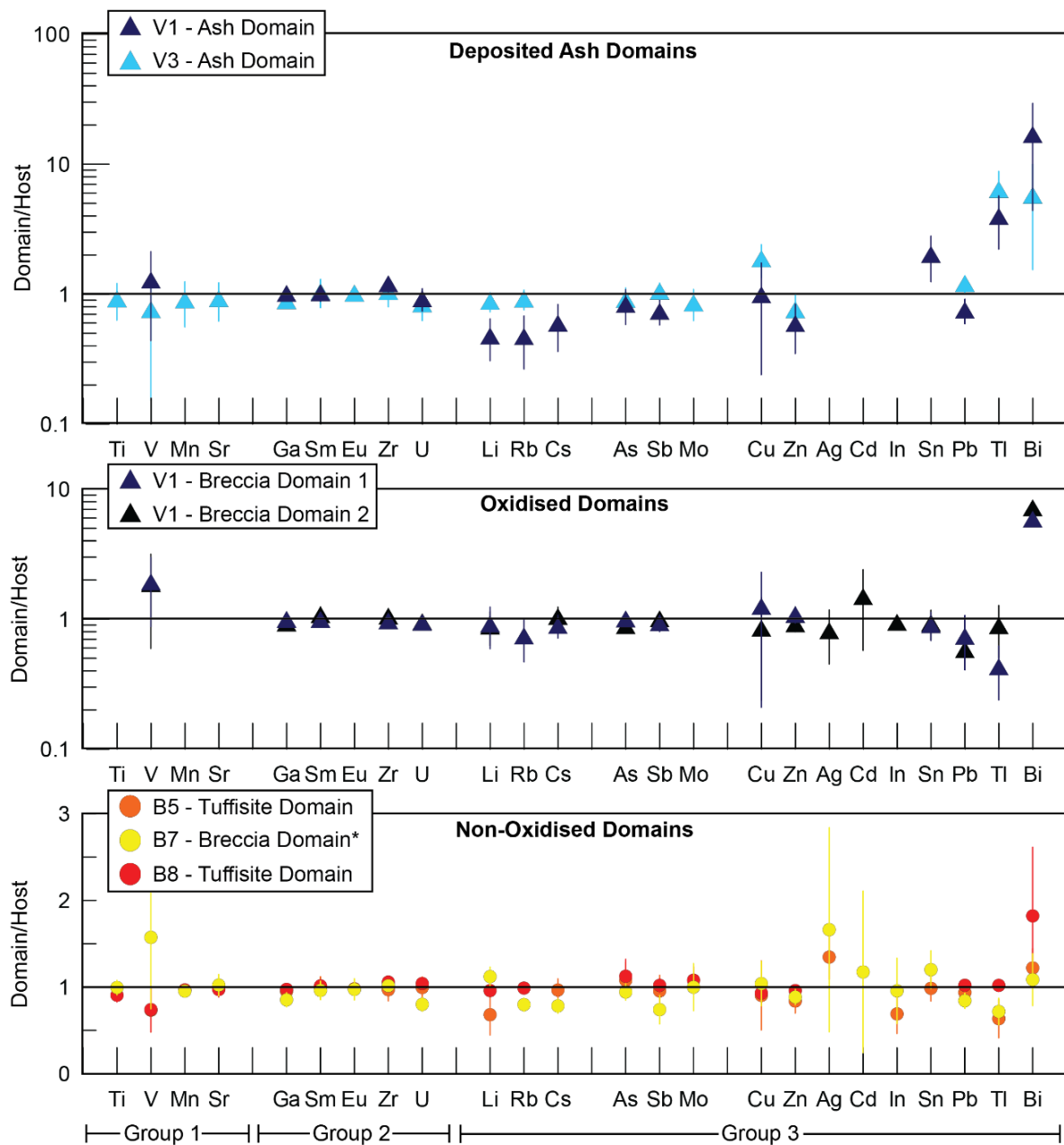




Table 1:

Summary of elements that have domain-host ratios outside of unity. Elements are either enriched (En.) or depleted (Dep.) in domains. Group three is subdivided into alkalis, OH<sup>-</sup> complexing metals (OH<sup>-</sup>) and S & Cl complexing metals (S, Cl). Alkali elements (Li, Rb, Cs) and certain Cl and S complexing elements (Zn, Pb, Tl, Bi) show the most variability. Element depletions in domains are common, although enrichments can be preserved (e.g. Bi).

	Sample ID	Domain Description	Group 1		Group 2		Alkalis		Group 3		S, Cl	Sample Comment
			En.	Dep.	En.	Dep.	En.	Dep.	En.	Dep.		
Deposited Ash	V1	Heavily Oxidised					Li Rb Cs		Sb	Tl Bi	Zn Sn Pb	No Ag, Cd, In data available
	V3	Moderately Oxidised					Li Rb Cs			Cu Pb Tl Bi	Zn	
Oxidised	V1 Domain 1	Breccia Ash	V				Rb			Bi	Pb Tl	
	V1 Domain 2	Breccia Ash	V				Rb			Bi	Pb	Variable Tl concentrations
Non-Oxidised	B5	Tuffisite		V			Li			Bi	Zn Pb Tl	
	B7	Breccia Ash	V				Li Rb Cs		Sb		Zn Sn Pb Tl	Ash compared to a dense obsidian clast in breccia
	B8	Tuffisite		V						Bi	Zn	
Element Comments							Cs is less variable than both Li and Rb				Cu highly variable within domains	

Figure 6:

Trace element profiles across an oxidised breccia matrix between two clasts from a *vent* sample (V1 Domain 1). Matrix ash is largely depleted in volatiles (e.g. Cl, Pb and Tl) compared to its host, Bi and Cu are exceptions. Clasts entrained within the matrix can have distinct compositions to both the host and ash matrix. Bi is below detection limits within parts of the ash (~150-200  $\mu\text{m}$ ) and the entrained clast. Laser analyses did not extend into the host (>900  $\mu\text{m}$ ).



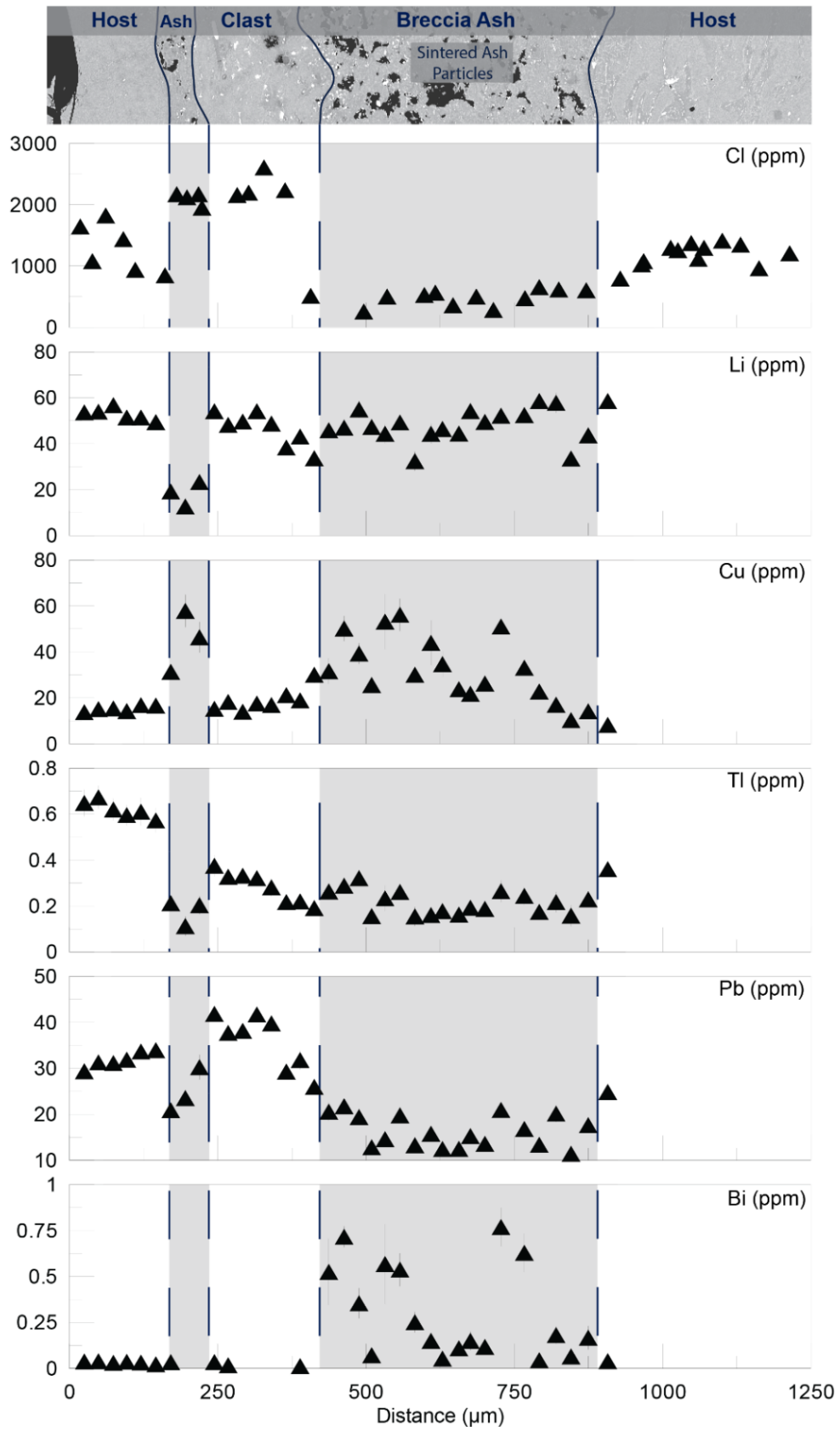


Table 2:

Summary of diffusion coefficients ( $D$ ,  $\text{m}^2/\text{s}^{-1}$ ) calculated at an eruptive temperature of  $895\text{ }^\circ\text{C}$  (Castro et al., 2013) and their references. The characteristic length scale of diffusion equation,  $x \sim \sqrt{Dt}$  - where  $x$  is distance (m) and  $t$  is time (s), is used to compare the time required for elements to diffuse over a known distance given the calculated  $D$  values. Order of diffusivity of elements used in Section 5.3:  $D_{\text{Na}} > D_{\text{Li}} > D_{\text{Tl}} > D_{\text{Pb}} > D_{\text{Rb}}$ .

Element	D ( $\text{m}^2/\text{s}$ )	Time for elements to diffuse			Reference
		5 $\mu\text{m}$ (s)	15 $\mu\text{m}$ (mins)	25 $\mu\text{m}$ (mins)	
Na	2.15E-10	0.1	0.02	0.05	(Zhang et al., 2010)
Li	1.82E-10	0.1	0.02	0.06	(Jambon, 1982)
Tl	3.81E-12	7	1.0	3	(Berlo et al., 2014)
Pb	8.25E-13	30	5	13	(Berlo et al., 2014)
Rb	4.12E-13	61	9	25	(Jambon, 1982)
Cl	4.09E-13	61	9	25	(Bai and van Groos, 1994)
In	3.67E-13	68	10	28	(Berlo et al., 2014)
Zn	2.87E-13	87	13	36	(Berlo et al., 2014)
Bi	6.89E-14	363	54	151	(Berlo et al., 2014)
Cs	4.12E-15	6071	911	2529	(Jambon, 1982)

Table 3:

Summary of the length scales of element variability preserved at certain domain interfaces and the calculated timescales, in brackets, of the related degassing processes. Alkali element gradients are found in multiple domains whilst slower diffusing elements (e.g. Tl, Pb) only have preserved gradients in more surficial domains.

	<b>Nozzle Domains</b>	<b>Oxidised Domains</b>		<b>Non-Oxidised Domain</b>	<b>Banded Obsidian Domain</b>
<b>Samples</b>	V4, V5	V1	V2	B7	B12
<b>Interface description</b>	Planar Fracture Surface	Bubble-Glass	Ash-Dense Clast	Ash-Dense Clast	Juxtaposing glassy and crystal-rich bands
<b>Figures</b>	Fig. 7 Fig. S3	Fig. 8A	Fig. 8B Fig. S4	Fig. 9 Fig. S5	Fig. 10 Fig. S6
<b>Length scales of element variability in <math>\mu\text{m}</math> (calculated timescales)</b>	<b>Li</b>	250	200 (5-30 s)	100 (15-45 s)	100 (<2 s)
	<b>Na</b>			200 (1-3 mins)	
	<b>Rb</b>		500 (14-60 hr)		100 (5-30 mins)
	<b>Cs</b>		<50		
	<b>Cu<sup>1</sup></b>	<500			
	<b>Tl</b>	300 (1-4 hr)	<50	500 (1-5 hr)	
	<b>Pb</b>	<150 (0.5-1 hr)			
	<b>In</b>	500		200	
	<b>Comments</b>	Only V4 has In variation. Li gradients are inconclusive and not discussed further with respect to nozzles.	Profile between one ash-filled bubble and one open bubble	Clast has dense ~200 $\mu\text{m}$ -wide rim elevated in Li, K, Rb, Cs, Pb, Tl and Cl, and depleted in In and Bi, relative to plateau core concentrations.	Clast is banded but profile does not extend into a texturally different band.

<sup>1</sup>The lack of adequate diffusion coefficients for Cu prevent it from being used to estimate timescales.

Figure 7:

Pb and Tl elemental gradients away from a fracture surface in a nozzle (Sample V5) indicate the diffusion of volatile elements towards the fracture interface and partitioning into the fluxing vapour phase. Dashed lines are bounding timescales, calculated via an explicit finite-difference model, and constrain the timescale of gas fluxing between opening of pathway and cessation of gas fluxing. Error bars are two internal standard error.

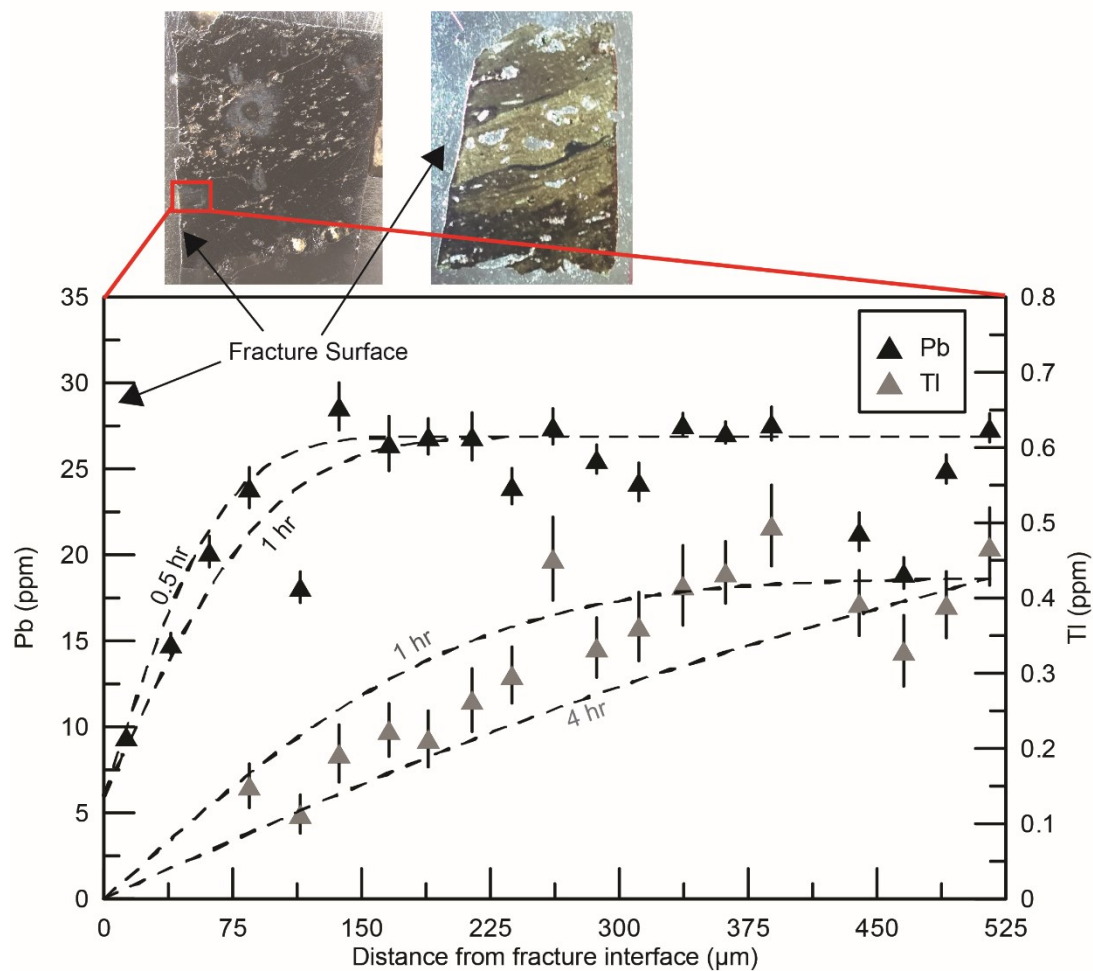


Figure 8:

Elemental variations in oxidised, near-surface samples. (A) Cs and Tl concentrations are elevated at void-host interfaces in a vesiculated clast (Sample V1) due to potential late-stage resorption. (B) Observed Li, Rb and Tl element variations away from a matrix-clast interface in a dense clast (Sample V2) preserve the previous diffusion elements towards an open fracture induced by gas fluxing. Clast rim is chemically distinct from core. Dashed lines are bounding timescales, calculated via an explicit finite-difference model, and constrain the timescale between initiation and cessation of gas fluxing. Error bars are two internal standard error.

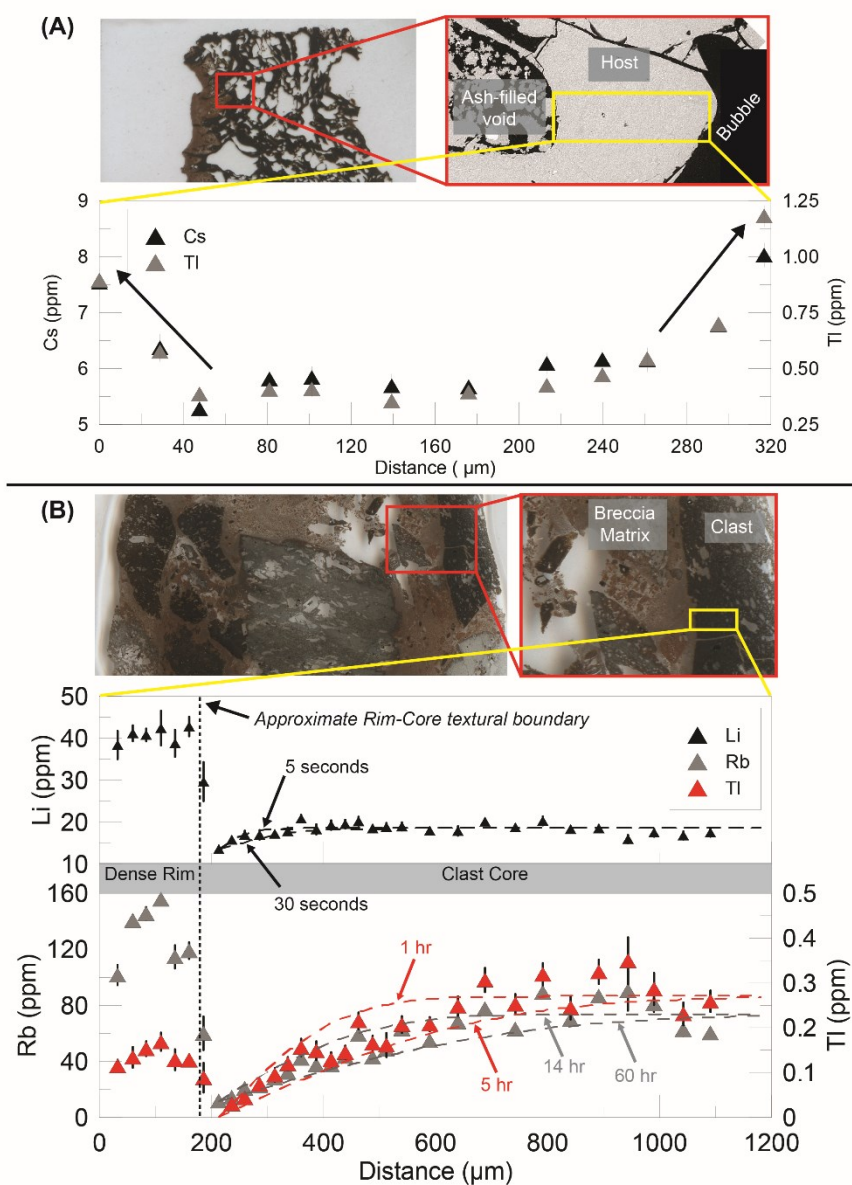


Figure 9:

Li and Na elemental variation in a banded obsidian clast away from the matrix-clast interface in a non-oxidised pumice breccia (Sample B7) preserve the diffusion of alkalis into the gas phase fluxing (and carrying clasts) towards the surface. Dashed lines are bounding timescales, calculated via an explicit finite-difference model, and constrain the timescale between the fragmentation event that opened gas channel and cessation of gas fluxing due to sintering of matrix ash and secondary fragmentation event ejecting pumice breccia from the conduit. Error bars are two internal standard error.

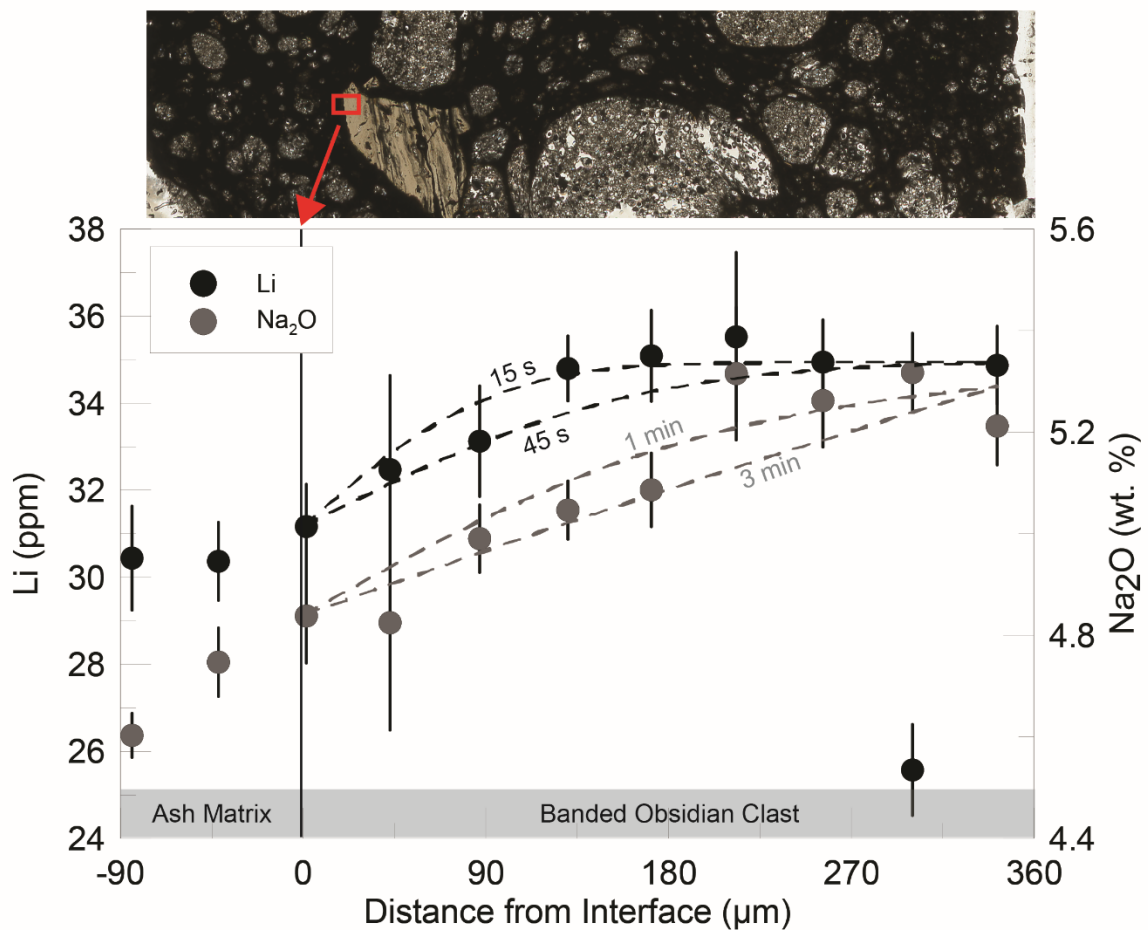


Figure 10:

Li and Rb elemental variation across juxtaposing bands in a banded obsidian bomb (Sample B12) preserve the diffusion of alkalis between a high concentration and low concentration band. Dashed lines are bounding timescales, calculated via an explicit finite-difference model, and constrain the timescale between the two bands being juxtaposed and the bomb ejection and quenching event. Error bars are two internal standard error.

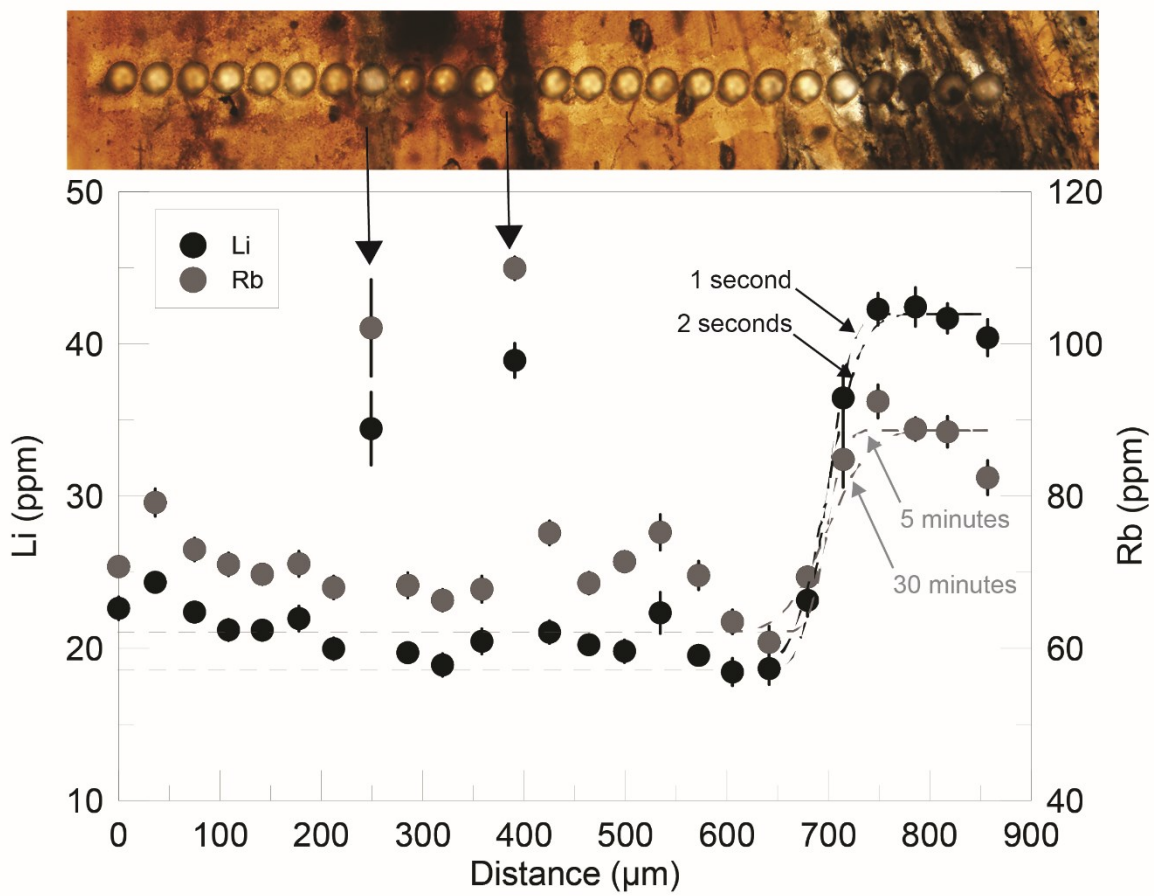
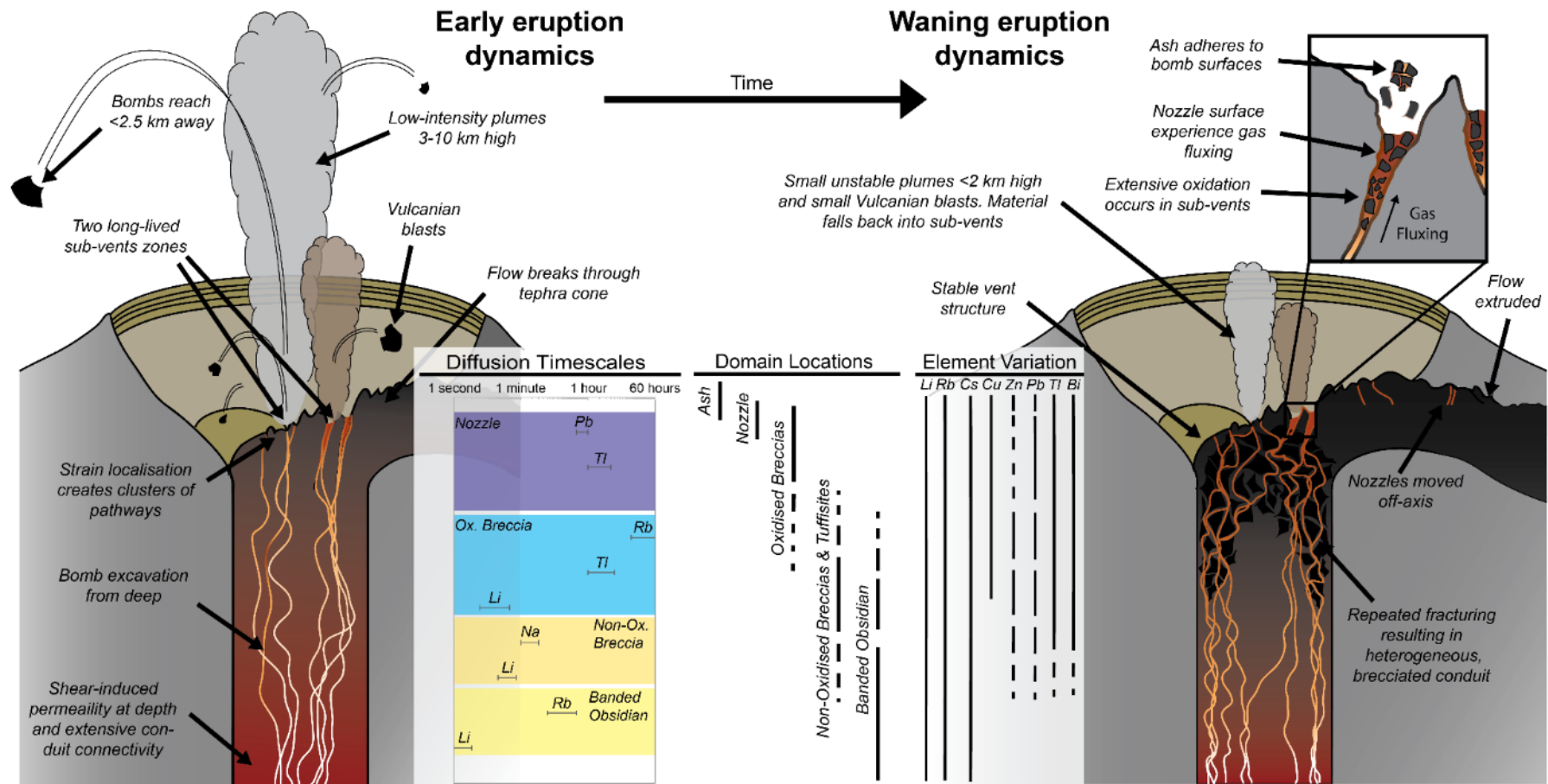


Figure 11:

Summary figure highlighting how our chemical interpretations of the degassing processes throughout the eruption relate to observations summarised in Section 2. Early in the eruption degassing events are short-lived, and preserved largely by alkali elements, as large, repeating explosions excavate non-oxidised breccia and tuffsite-hosting bombs. Later in the eruption a more heterogeneous but stable vent structure allows for hours of gas fluxing from nozzles. Explosions eject oxidised breccias that chemically preserve many previous sub-surface fragmentation and degassing events. Longer periods of gas fluxing in the near-surface environment are preserved by a wider suite of metals (including Pb and Tl). Conduit is schematic and not to scale and represents the system above the emplaced laccolith described by Castro et al. (2016).





## 10. Supplementary Figures

Figure S.1:

FeO<sup>t</sup> (A) and CaO (B) vs. TiO<sub>2</sub> highlighting minor positive correlations between certain major elements. (C) No correlation between K<sub>2</sub>O vs Cl is observed, Cl concentrations are highly variable whilst K<sub>2</sub>O concentrations are approximately constant. Positive correlations are observed between certain Group 1 elements, e.g. Th vs Zr (D) and between Group 2 elements, e.g. Co vs Mn (E). Error bars are 1 standard deviation.

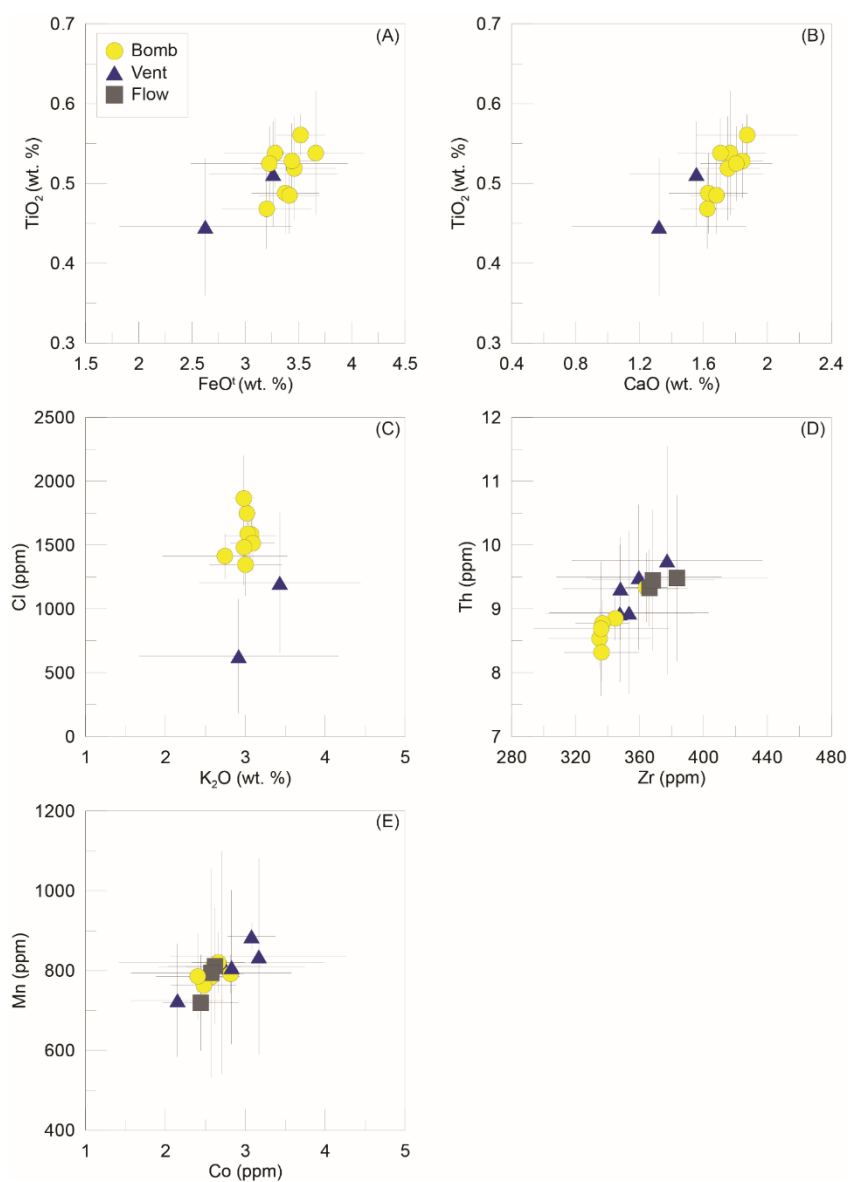


Figure S.2:

Profile of  $\text{TiO}_2$  and Cl concentrations obtained via EMP across a banded obsidian domain (Sample B4).

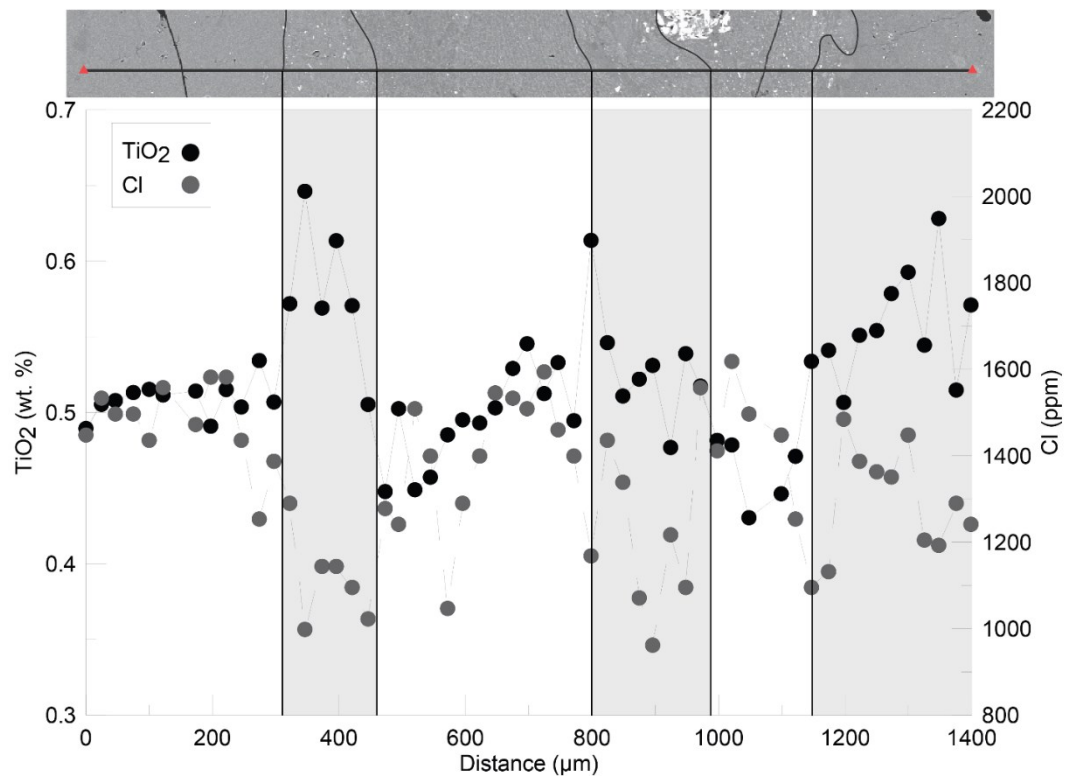


Figure S.3:

Comparison of variation in Group 1 (e.g. V, diamonds), Group 2 (e.g. Ga, Sm, squares) and Group 3 alkalis (e.g. Li, Rb, Cs, circles) and Group 3 metals (e.g. Cu, Tl, Pb, Bi, triangles) elements away from a fracture surface in a nozzle (Sample V5), corresponding timescales estimated via diffusion of Pb and Tl are shown in Fig. 7.

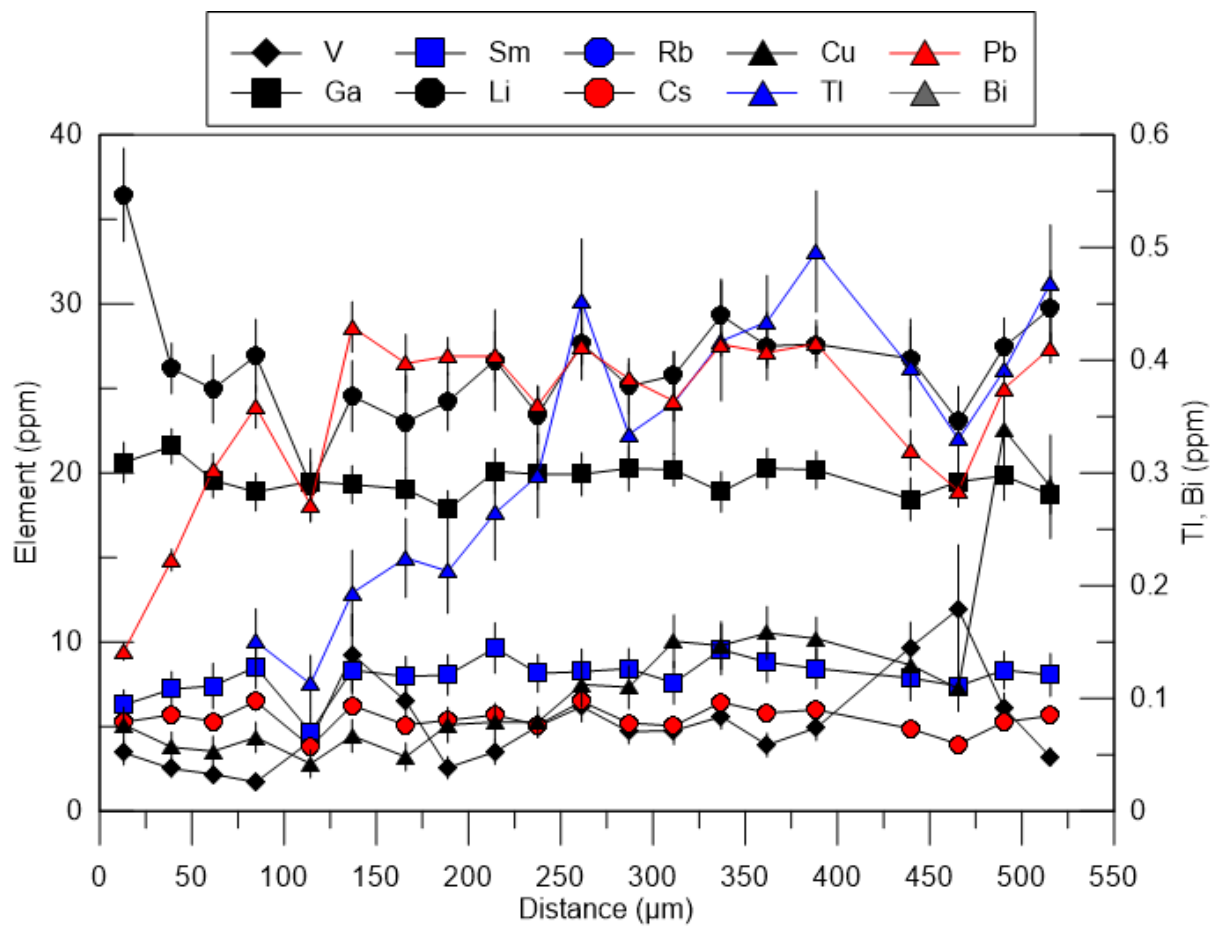


Figure S.4:

Comparison of variation in Group 1 (diamonds), Group 2 (squares) and Group 3 (circles and triangles) elements away from a matrix-clast interface in a dense clast (Sample V2), corresponding timescales estimated via diffusion of Li, Rb and Tl are shown in Fig. 8B.

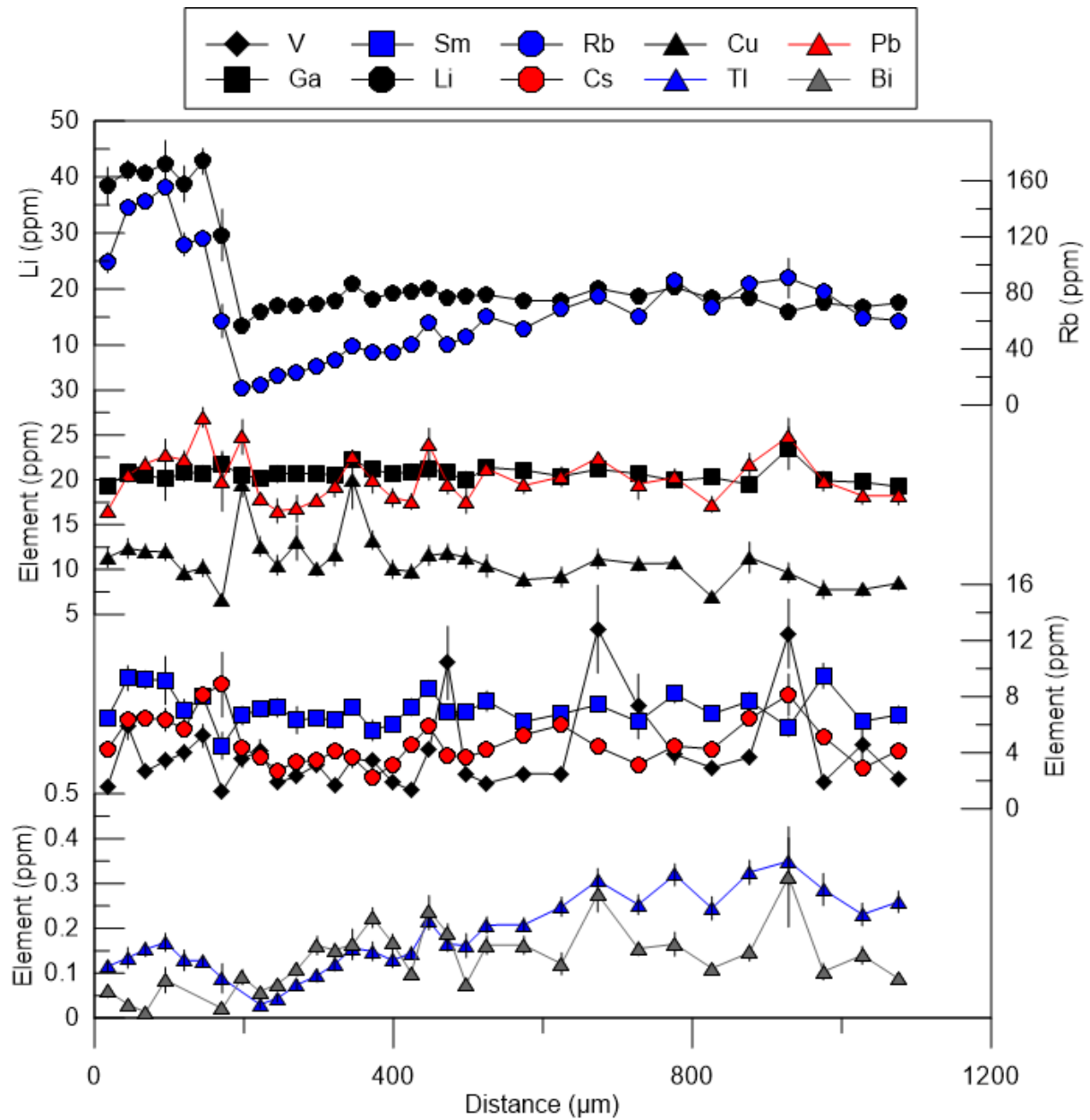


Figure S.5:

Comparison of variation in Group 1 (diamonds), Group 2 (squares) and Group 3 (circles and triangles) elements in a banded obsidian clast away from the matrix-clast interface in a non-oxidised pumice breccia (Sample B7), corresponding timescales estimated via diffusion of Li and Na are shown in Fig. 9.

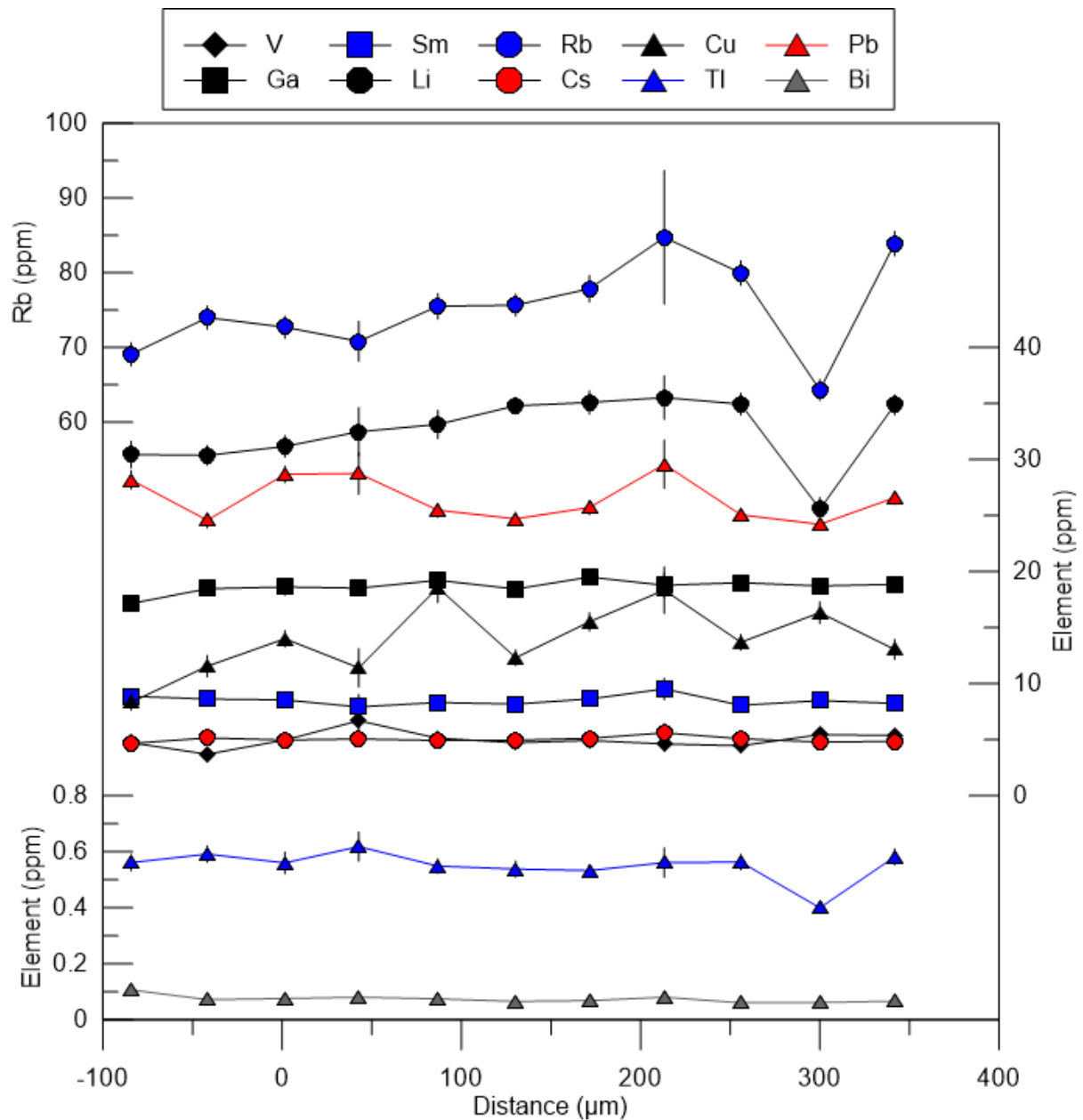
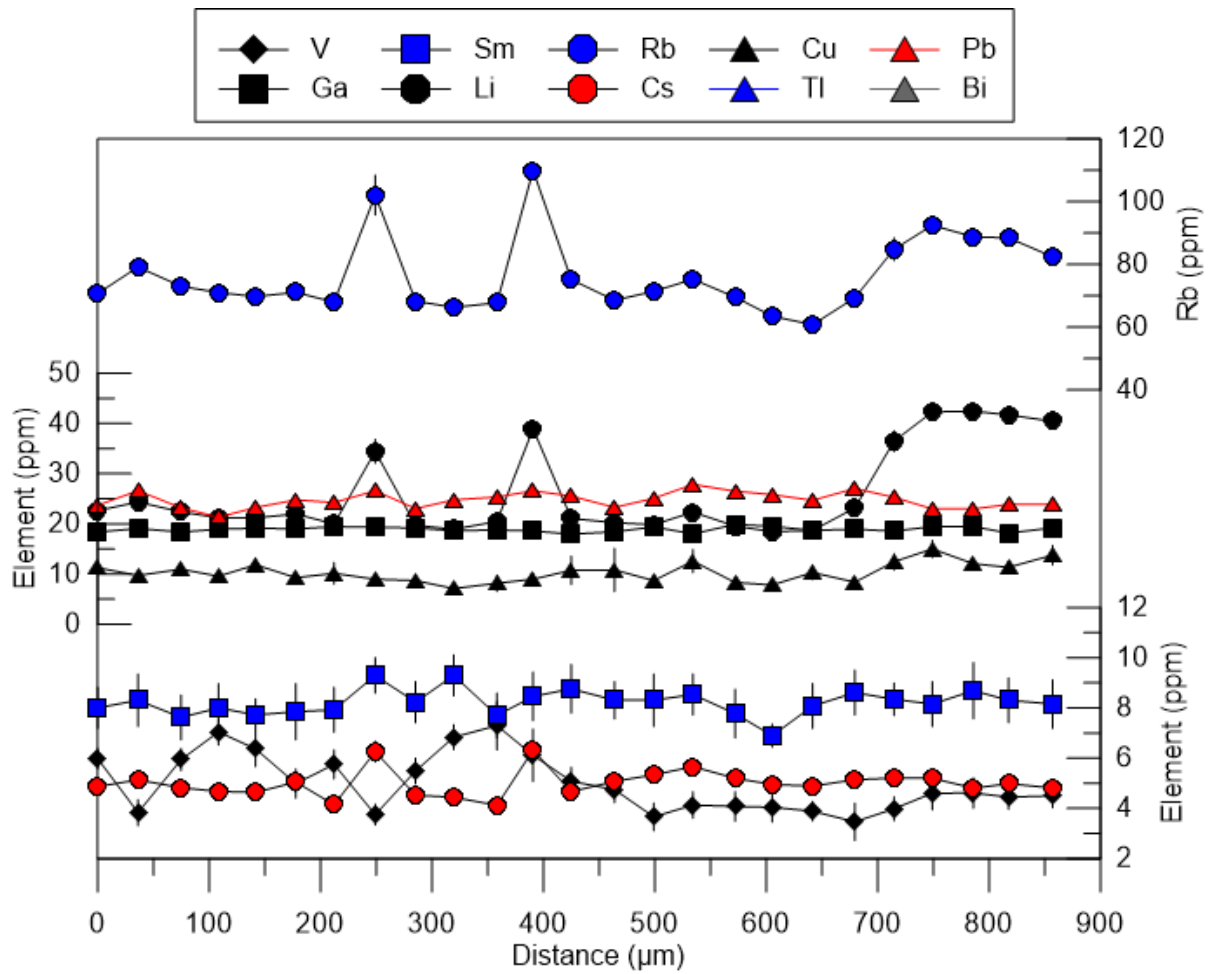


Figure S.6:

Comparison of variation in Group 1 (diamonds), Group 2 (squares) and Group 3 (circles and triangles) elements across juxtaposing bands in a banded obsidian bomb (Sample B12), corresponding timescales estimated via diffusion of Li and Rb are shown in Fig. 10.



## 11. Appendices

### Appendix A: Data Table for Major and Trace Elements

Calculated means for major and trace elements of all samples plus brief sample descriptions and classifications. Means are calculated averages of multiple analyses via EPMA (majors) and LA-ICP-MS (traces). Errors are given as 1 standard deviation and % RSDs. Major elements are in wt. % and trace elements, S and Cl are in ppm. n.a. indicates where an element was not analysed for a sample, the respective error is left blank. n1 is the number of EPMA analyses per sample, n2 is the number of LA-ICP-MS analyses per sample. BCR-2 average and errors presented in the main table, EPMA secondary standard averages and errors presented in separate tables.



Table A.1: Data table of sample descriptions and calculated averages for major and trace elements.

Sample ID	Sample Category	Sample Description	SiO <sub>2</sub>	TiO <sub>2</sub>	Al <sub>2</sub> O <sub>3</sub>	FeO <sup>t</sup>	MnO	MgO	CaO	Na <sub>2</sub> O	K <sub>2</sub> O	S	Cl	n1
B1	Bomb	Non-Oxidised, grey breadcrust bomb with pumice and obsidian domains	71.9	0.49	14.2	3.4	0.10	0.39	1.6	4.8	3.1	16	1574	33
B2	Bomb	Non-Oxidised, grey pumice bomb with dense obsidian shards	72.1	0.47	14.2	3.2	0.10	0.38	1.6	4.8	3.1	14	1584	37
B3A	Bomb	Banded Obsidian Bomb with white oxidised material adhered to edge	71.7	0.49	14.2	3.4	0.10	0.40	1.7	4.9	3.0	17	1750	72
B3B	Bomb	Banded Obsidian Bomb with red, lithic material clast	71.6	0.52	14.3	3.5	0.10	0.44	1.8	4.8	3.0	21	1867	36
B4	Bomb	Banded Obsidian Bomb (collapsed and compacted foam)	71.4	0.54	14.2	3.7	0.11	0.45	1.8	4.9	3.0	17	1347	100
B5	Bomb	Partially collapsed foam with tuffisite vein (mild oxidation of vein material)	71.6	0.56	14.3	3.5	0.10	0.44	1.9	4.9	2.7	17	1414	60
B6	Bomb	Non-oxidised pumice breccia with dense and pumice clasts	n.a.	n.a.	n.a.	n.a.	n.a.	n.a.	n.a.	n.a.	n.a.	n.a.	n.a.	
B7	Bomb	Non-oxidised pumice breccia with reticulite and dense clasts	n.a.	n.a.	n.a.	n.a.	n.a.	n.a.	n.a.	n.a.	n.a.	n.a.	n.a.	
B8	Bomb	Banded Obsidian Bomb with non-oxidised tuffisite material on bomb edge	n.a.	n.a.	n.a.	n.a.	n.a.	n.a.	n.a.	n.a.	n.a.	n.a.	n.a.	
B9	Bomb	Breccia bomb with dense and pumice clasts in dull red-grey matrix	71.4	0.53	14.3	3.4	0.10	0.47	1.8	5.0	3.0	19	1590	10
B10	Bomb	Banded Obsidian Bomb with black and dark-grey glassy bands	71.4	0.54	14.3	3.3	0.11	0.41	1.7	5.1	3.1	19	1515	17
B11	Bomb	Pumiceous Bomb with obsidian rind and subtle (grey-beige) interior banding	71.6	0.52	14.3	3.2	0.10	0.41	1.8	5.1	3.0	13	1482	16
B12	Bomb	Dense, dark grey and black banded sample	n.a.	n.a.	n.a.	n.a.	n.a.	n.a.	n.a.	n.a.	n.a.	n.a.	n.a.	
F1	Flow	Breakout from northern branch of rhyolite flow	n.a.	n.a.	n.a.	n.a.	n.a.	n.a.	n.a.	n.a.	n.a.	n.a.	n.a.	
F2	Flow	Breakout from northern branch of rhyolite flow	n.a.	n.a.	n.a.	n.a.	n.a.	n.a.	n.a.	n.a.	n.a.	n.a.	n.a.	
F3	Flow	Rhyolite flow from vent	n.a.	n.a.	n.a.	n.a.	n.a.	n.a.	n.a.	n.a.	n.a.	n.a.	n.a.	
V1	Vent	Breccia of dense and vesiculated clasts (Oxidised ash domains in breccia and deposited ash domains)	71.3	0.51	14.2	3.3	0.09	0.34	1.6	5.2	3.4	11	1206	72
V2	Vent	Breccia of dense clasts and flow material (Heavily oxidised ash material in breccia)	73.5	0.45	13.6	2.6	0.07	0.23	1.3	5.3	2.9	6	631	30
V3	Vent	Nozzle with oxidised surface	n.a.	n.a.	n.a.	n.a.	n.a.	n.a.	n.a.	n.a.	n.a.	n.a.	n.a.	
V4	Vent	Nozzle with light-pink ash adhered to surface	n.a.	n.a.	n.a.	n.a.	n.a.	n.a.	n.a.	n.a.	n.a.	n.a.	n.a.	
V5	Vent	Nozzle with oxidised surface	n.a.	n.a.	n.a.	n.a.	n.a.	n.a.	n.a.	n.a.	n.a.	n.a.	n.a.	
		Cordon Caulle Average	71.8	0.51	14.2	3.3	0.10	0.40	1.7	5.0	3.0	17	1451	
		Cordon Caulle Standard Deviation	0.6	0.03	0.2	0.3	0.01	0.06	0.2	0.2	0.2	8	326	
		Cordon Caulle % RSD	1%	7%	1%	8%	12%	16%	9%	3%	5%	49%	22%	
		BCR Average	n.a.	n.a.	n.a.	n.a.	n.a.	n.a.	n.a.	n.a.	n.a.	n.a.	n.a.	
		BCR Standard Deviation												
		BCR % RSD												

Element Group No	3	1	1	1	1	3	3	2	3	3	2	2	2	2	3	3	3	3	3
Analysed Mass	7	51	52	59	60	63	66	71	75	85	88	89	90	93	95	107	111	115	118
Sample ID	Li	V	Cr	Co	Ni	Cu	Zn	Ga	As	Rb	Sr	Y	Zr	Nb	Mo	Ag	Cd	In	Sn
B1	n.a.	n.a.	n.a.	n.a.	n.a.	n.a.	n.a.	n.a.	n.a.	n.a.	n.a.	n.a.	n.a.	n.a.	n.a.	n.a.	n.a.	n.a.	n.a.
B2	n.a.	n.a.	n.a.	n.a.	n.a.	n.a.	n.a.	n.a.	n.a.	n.a.	n.a.	n.a.	n.a.	n.a.	n.a.	n.a.	n.a.	n.a.	n.a.
B3A	n.a.	n.a.	n.a.	n.a.	n.a.	n.a.	n.a.	n.a.	n.a.	n.a.	n.a.	n.a.	n.a.	n.a.	n.a.	n.a.	n.a.	n.a.	n.a.
B3B	44.8	5.6	n.a.	n.a.	n.a.	13.0	85.1	20.4	19.7	81.3	n.a.	n.a.	344	n.a.	n.a.	0.11	0.66	0.15	2.97
B4	35.2	5.5	2.31	2.66	0.38	13.9	85.8	19.7	18.5	78.7	126	49.2	335	10.4	2.69	0.11	0.24	0.11	3.28
B5	36.0	5.5	2.08	2.81	0.41	15.0	87.6	20.0	18.2	78.6	122	50.3	336	10.6	2.60	0.12	0.27	0.11	3.23
B6	37.3	4.5	3.46	2.57	0.45	15.5	86.9	18.9	16.5	76.7	123	50.6	345	10.8	2.63	0.09	0.25	0.12	3.33
B7	29.9	4.0	3.78	2.48	0.52	14.1	86.8	20.0	16.1	84.1	112	50.9	364	11.1	2.40	0.09	0.14	0.10	2.76
B8	32.2	5.3	n.a.	2.59	n.a.	15.9	87.0	19.7	14.2	75.4	122	49.5	337	10.3	2.62	n.a.	n.a.	n.a.	n.a.
B9	n.a.	n.a.	n.a.	n.a.	n.a.	n.a.	n.a.	n.a.	n.a.	n.a.	n.a.	n.a.	n.a.	n.a.	n.a.	n.a.	n.a.	n.a.	n.a.
B10	n.a.	n.a.	n.a.	n.a.	n.a.	n.a.	n.a.	n.a.	n.a.	n.a.	n.a.	n.a.	n.a.	n.a.	n.a.	n.a.	n.a.	n.a.	n.a.
B11	n.a.	n.a.	n.a.	n.a.	n.a.	n.a.	n.a.	n.a.	n.a.	n.a.	n.a.	n.a.	n.a.	n.a.	n.a.	n.a.	n.a.	n.a.	n.a.
B12	29.3	5.1	8.07	2.40	n.a.	11.8	78.8	18.9	n.a.	73.7	139	49.2	336	9.9	2.79	n.a.	3.06	0.17	3.05
F1	36.4	5.4	n.a.	2.62	n.a.	10.4	87.6	20.8	17.3	100.1	122	53.3	366	11.2	2.71	n.a.	n.a.	n.a.	n.a.
F2	37.7	4.3	3.06	2.57	0.28	10.0	79.5	18.1	15.8	77.6	120	54.0	368	11.0	2.60	0.09	0.10	0.10	3.20
F3	40.1	5.1	3.16	2.44	0.39	16.7	81.7	19.7	24.7	77.8	113	56.8	383	11.0	2.64	0.12	0.12	0.11	3.24
V1	42.9	8.8	1.50	3.08	0.55	24.3	92.0	21.3	19.6	76.4	113	58.3	348	11.8	3.01	0.15	0.21	0.13	4.07
V2	29.4	4.3	3.50	2.83	0.57	12.7	85.0	21.3	19.9	74.8	102	58.0	377	12.4	3.18	0.14	0.18	0.14	3.44
V3	34.4	4.7	2.95	2.70	0.39	20.2	89.1	19.5	16.5	77.2	113	51.8	353	10.9	2.58	0.13	0.11	0.08	3.46
V4	39.3	4.2	2.88	2.15	0.34	10.7	90.5	20.7	18.2	80.1	119	50.5	348	10.6	2.55	0.10	0.13	0.07	3.57
V5	31.0	5.7	3.71	3.17	0.69	8.1	91.5	20.0	15.7	83.9	112	54.7	360	11.7	2.57	0.09	0.16	0.09	3.26
Cordon Caulle Average	36	5	3.4	2.6	0.5	14	86	19.9	18	80	118	53	353	11.0	2.7	0.11	0.4	0.11	3.3
Cordon Caulle Standard Deviation	5	1	2	0.3	0.1	4	4	0.9	3	6	9	3	16	0.7	0.2	0.02	0.8	0.03	0.3
Cordon Caulle % RSD	13%	22%	48%	10%	26%	29%	5%	4%	14%	8%	7%	6%	4%	6%	7%	19%	184%	24%	10%
BCR Average	10	451	18.5	37.5	12.5	19	155	21.7	0.8	46	338	33	180	11.6	261	0.9	0.2	0.10	2.1
BCR Standard Deviation	2	29	4	2.5	1.3	2	16	1.6	0.2	4	13	2	7	0.5	19	0.2	0.1	0.01	1.3
BCR % RSD	15%	7%	19%	7%	11%	8%	11%	7%	27%	8%	4%	5%	4%	5%	7%	27%	33%	14%	62%

Element Group No	3	3	2	2	2	2	2	2	2	2	2	2	2	2	3	3	3	3	2	2	
Analysed Mass	121	133	137	139	140	146	147	153	157	163	166	172	175	178	182	205	208	209	232	238	
Sample ID	Sb	Cs	Ba	La	Ce	Nd	Sm	Eu	Gd	Dy	Er	Yb	Lu	Hf	W	Tl	Pb	Bi	Th	U	n2
B1	n.a.	n.a.	n.a.	n.a.	n.a.	n.a.	n.a.	n.a.	n.a.	n.a.	n.a.	n.a.	n.a.	n.a.	n.a.	n.a.	n.a.	n.a.	n.a.	n.a.	n.a.
B2	n.a.	n.a.	n.a.	n.a.	n.a.	n.a.	n.a.	n.a.	n.a.	n.a.	n.a.	n.a.	n.a.	n.a.	n.a.	n.a.	n.a.	n.a.	n.a.	n.a.	n.a.
B3A	n.a.	n.a.	n.a.	n.a.	n.a.	n.a.	n.a.	n.a.	n.a.	n.a.	n.a.	n.a.	n.a.	n.a.	n.a.	n.a.	n.a.	n.a.	n.a.	n.a.	n.a.
B3B	1.02	5.28	n.a.	n.a.	n.a.	n.a.	8.03	n.a.	n.a.	n.a.	n.a.	n.a.	n.a.	9.09	n.a.	0.66	24.4	0.08	n.a.	2.53	18
B4	1.04	4.97	664	28.9	65.2	34.0	7.69	1.49	7.78	8.43	5.39	5.91	0.92	8.81	1.53	0.52	25.9	0.08	8.54	2.59	43
B5	0.97	5.21	639	28.7	63.0	33.0	7.82	1.48	7.72	8.50	5.47	5.89	0.95	8.80	1.45	0.47	25.1	0.06	8.32	2.50	44
B6	0.95	5.05	684	30.2	68.3	35.1	8.35	1.52	7.43	8.81	5.68	5.95	0.97	9.10	1.54	0.50	25.7	0.08	8.85	2.68	17
B7	1.16	5.62	703	31.0	69.5	35.7	8.57	1.52	7.28	9.20	5.81	6.26	0.99	9.62	1.47	0.64	27.7	0.08	9.34	2.73	55
B8	0.97	n.a.	670	29.1	66.4	35.0	7.95	1.46	7.44	8.55	5.57	5.90	0.94	9.00	1.64	0.54	26.0	0.12	8.77	2.52	58
B9	n.a.	n.a.	n.a.	n.a.	n.a.	n.a.	n.a.	n.a.	n.a.	n.a.	n.a.	n.a.	n.a.	n.a.	n.a.	n.a.	n.a.	n.a.	n.a.	n.a.	n.a.
B10	n.a.	n.a.	n.a.	n.a.	n.a.	n.a.	n.a.	n.a.	n.a.	n.a.	n.a.	n.a.	n.a.	n.a.	n.a.	n.a.	n.a.	n.a.	n.a.	n.a.	n.a.
B11	n.a.	n.a.	n.a.	n.a.	n.a.	n.a.	n.a.	n.a.	n.a.	n.a.	n.a.	n.a.	n.a.	n.a.	n.a.	n.a.	n.a.	n.a.	n.a.	n.a.	n.a.
B12	1.02	4.91	744	30.6	68.5	35.4	8.22	1.55	7.85	8.55	n.a.	6.05	n.a.	8.55	n.a.	0.54	23.3	0.22	8.69	2.55	72
F1	1.07	n.a.	680	31.2	71.6	37.0	8.35	1.48	7.75	9.01	5.78	6.26	1.00	9.64	1.68	0.64	28.6	0.08	9.33	2.78	33
F2	0.95	5.11	689	31.9	70.4	37.1	8.89	1.52	8.31	9.35	6.18	6.40	1.06	9.58	1.50	0.45	25.0	0.05	9.45	2.68	16
F3	1.08	5.32	641	30.8	63.9	36.7	8.47	1.40	8.45	9.76	6.23	6.61	1.08	10.20	1.51	0.45	26.0	0.05	9.49	2.68	14
V1	0.98	5.47	662	30.1	68.9	36.6	8.29	1.45	8.61	9.81	6.40	6.19	1.11	8.98	1.64	0.60	26.6	0.21	9.32	2.63	108
V2	1.08	5.34	650	31.9	72.4	38.3	7.68	1.33	8.88	9.83	6.45	6.70	1.11	9.96	1.92	0.17	23.1	0.13	9.76	2.82	47
V3	1.00	5.14	666	30.1	68.0	35.6	8.19	1.44	7.62	8.91	5.75	6.13	0.97	9.25	1.57	0.56	27.0	0.06	8.94	2.64	55
V4	1.01	5.39	683	30.2	67.4	35.0	8.18	1.48	7.50	8.69	5.71	6.04	0.97	9.16	1.54	0.38	27.1	0.05	8.93	2.71	55
V5	1.16	5.52	679	31.5	72.4	37.4	8.85	1.51	7.54	9.57	6.16	6.34	1.03	9.45	1.53	0.39	26.2	0.04	9.50	2.67	96
Cordon Caulle Average	1.0	5.3	675	30	68	36	8.2	1.5	7.9	9.1	5.9	6.2	1.0	9.3	1.6	0.5	26	0.1	9.1	2.6	
Cordon Caulle Standard Deviation	0.1	0.2	27	1.0	3	1	0.4	0.1	0.5	0.5	0.4	0.3	0.1	0.5	0.1	0.1	2	0.1	0.4	0.1	
Cordon Caulle % RSD	7%	4%	4%	3%	4%	4%	4%	4%	6%	6%	6%	4%	6%	5%	8%	25%	6%	62%	5%	4%	
BCR Average	0.4	1.2	669	25	52	28	6.4	1.9	8.4	6.2	3.6	3.2	0.5	4.7	0.5	0.2	11	0.08	5.8	1.7	
BCR Standard Deviation	0.1	0.1	23	1	3	1	0.5	0.1	2.0	0.4	0.4	0.3	0.1	0.3	0.1	0.1	1	0.02	0.5	0.2	
BCR % RSD	16%	10%	3%	5%	5%	5%	7%	7%	24%	6%	11%	9%	14%	6%	20%	21%	8%	31%	9%	10%	

Table A.2: Data table of sample errors (1 Standard Deviation).

Sample ID	Sample Category	Sample Description	SiO <sub>2</sub>	TiO <sub>2</sub>	Al <sub>2</sub> O <sub>3</sub>	FeO <sup>t</sup>	MnO	MgO	CaO	Na <sub>2</sub> O	K <sub>2</sub> O	S	Cl	n1
B1	Bomb	Non-Oxidised, grey breadcrust bomb with pumice and obsidian domains	0.6	0.05	0.2	0.32	0.03	0.07	0.25	0.22	0.32	18	237	33
B2	Bomb	Non-Oxidised, grey pumice bomb with dense obsidian shards	0.69	0.05	0.12	0.42	0.02	0.07	0.17	0.15	0.10	15	129	37
B3A	Bomb	Banded Obsidian Bomb with white oxidised material adhered to edge	0.53	0.05	0.14	0.29	0.02	0.06	0.16	0.15	0.10	16	90	72
B3B	Bomb	Banded Obsidian Bomb with red, lithic material clast	0.74	0.06	0.18	0.39	0.03	0.09	0.20	0.13	0.13	30	335	36
B4	Bomb	Banded Obsidian Bomb (collapsed and compacted foam)	0.68	0.08	0.26	0.45	0.02	0.08	0.23	0.37	0.45	13	246	100
B5	Bomb	Partially collapsed foam with tuffisite vein (mild oxidation of vein material)	0.55	0.03	0.21	0.23	0.02	0.06	0.32	0.58	0.78	11	177	60
B6	Bomb	Non-oxidised pumice breccia with dense and pumice clasts												
B7	Bomb	Non-oxidised pumice breccia with reticulite and dense clasts												
B8	Bomb	Banded Obsidian Bomb with non-oxidised tuffisite material on bomb edge												
B9	Bomb	Breccia bomb with dense and pumice clasts in dull red-grey matrix	0.49	0.05	0.11	0.21	0.01	0.04	0.13	0.12	0.07	14	107	10
B10	Bomb	Banded Obsidian Bomb with black and dark-grey glassy bands	0.78	0.04	0.22	0.48	0.02	0.10	0.27	0.29	0.27	18	220	17
B11	Bomb	Pumiceous Bomb with obsidian rind and subtle (grey-beige) interior banding	0.57	0.05	0.21	0.74	0.04	0.11	0.23	0.13	0.10	11	297	16
B12	Bomb	Dense, dark grey and black banded sample												
F1	Flow	Breakout from northern branch of rhyolite flow												
F2	Flow	Breakout from northern branch of rhyolite flow												
F3	Flow	Rhyolite flow from vent												
V1	Vent	Breccia of dense and vesiculated clasts (Oxidised ash domains in breccia and deposited ash domains)	0.78	0.07	0.37	0.60	0.03	0.12	0.42	0.63	1.01	10	553	72
V2	Vent	Breccia of dense clasts and flow material (Heavily oxidised ash material in breccia)	1.81	0.09	1.15	0.81	0.05	0.26	0.54	0.61	1.25	8	448	30
V3	Vent	Nozzle with oxidised surface												
V4	Vent	Nozzle with light-pink ash adhered to surface												
V5	Vent	Nozzle with oxidised surface												

Sample ID	Li	V	Cr	Co	Ni	Cu	Zn	Ga	As	Rb	Sr	Y	Zr	Nb	Mo	Ag	Cd	In	Sn
B1																			
B2																			
B3A																			
B3B	1.95	3.91				3.72	3.70	0.76	1.32	4.28			11.22			0.02	0.23	0.04	0.15
B4	10.32	1.44	0.89	0.33	0.20	4.39	14.19	2.10	3.84	12.06	11.80	2.80	32.21	0.97	0.29	0.02	0.13	0.02	0.38
B5	7.25	1.11	0.35	0.16	0.09	3.37	10.91	1.10	2.38	5.56	10.45	2.14	23.30	0.46	0.21	0.02	0.10	0.02	0.29
B6	0.97	0.33	0.65	0.29	0.21	3.74	3.71	0.55	0.93	2.17	1.93	1.29	10.21	0.40	0.30	0.03	0.08	0.02	0.13
B7	2.69	1.63	1.07	0.41	0.49	2.83	8.40	1.91	1.23	9.74	11.18	2.14	13.14	0.89	0.54	0.05	0.08	0.03	0.47
B8	1.97	1.37		0.34		2.26	3.47	0.66	2.22	2.76	7.97	2.07	16.85	0.39	0.29				
B9																			
B10																			
B11																			
B12	9.74	2.39	4.27	0.52		4.04	10.69	1.04		19.24	42.73	6.01	42.23	1.22	0.56			0.05	0.47
F1	6.88	1.62		0.58		2.42	10.87	0.80	1.87	24.43	7.92	3.19	23.80	0.68	0.35				
F2	3.63	2.26	0.92	1.00	0.17	1.08	16.65	1.25	2.23	8.04	13.44	6.06	38.28	1.00	0.44	0.04	0.05	0.02	0.44
F3	4.97	1.88	0.62	0.47	0.11	2.23	14.53	0.93	6.81	11.69	31.36	8.46	57.05	1.63	0.44	0.02	0.03	0.02	0.45
V1	13.84	5.26	0.17	0.30	0.08	12.59	18.52	1.40	2.64	28.25	15.77	4.35	36.26	0.38	0.17	0.04	0.14	0.13	1.66
V2	16.21	2.96	0.74	0.91	0.22	4.07	21.64	1.35	4.99	41.98	32.95	10.66	59.69	1.89	0.69	0.03	0.11	0.30	0.87
V3	4.94	3.48	1.04	1.29	0.23	6.09	21.71	1.13	2.39	10.52	28.13	8.68	49.76	1.50	0.47	0.06	0.05	0.02	0.50
V4	5.89	1.33	0.62	0.58	0.15	2.32	16.07	1.41	3.05	12.97	24.39	6.24	46.38	1.24	0.40	0.02	0.05	0.02	0.53
V5	6.78	4.20	0.82	1.10	0.83	3.36	25.76	1.60	2.57	11.47	23.66	5.43	51.54	1.38	0.81	0.02	0.07	0.04	0.58

Sample ID	Sb	Cs	Ba	La	Ce	Nd	Sm	Eu	Gd	Dy	Er	Yb	Lu	Hf	W	Tl	Pb	Bi	Th	U	n2	
B1																						
B2																						
B3A																						
B3B	0.08	0.26					0.44							0.35		0.05	1.56	0.01		0.13	18	
B4	0.17	0.87	39.13	1.51	4.85	1.54	0.47	0.11	0.58	0.55	0.48	0.50	0.10	0.80	0.24	0.15	4.05	0.02	0.47	0.36	43	
B5	0.10	0.42	22.02	1.79	2.94	1.37	0.57	0.07	0.41	0.50	0.30	0.57	0.06	0.75	0.11	0.11	2.54	0.01	0.44	0.20	44	
B6	0.06	0.20	13.21	0.75	2.12	1.13	0.37	0.08	0.46	0.36	0.24	0.23	0.05	0.33	0.10	0.02	0.84	0.01	0.34	0.16	17	
B7	0.26	0.71	30.88	1.34	3.69	1.77	0.85	0.16	0.56	0.75	0.49	0.54	0.09	0.58	0.23	0.13	2.73	0.01	0.54	0.31	55	
B8	0.05		19.77	1.10	1.73	0.95	0.31	0.08	0.33	0.35	0.21	0.34	0.05	0.51	0.16	0.03	0.83	0.05	0.37	0.09	58	
B9																						
B10																						
B11																						
B12	0.22	0.85	67.55	3.75	8.34	4.42	0.95	0.23	0.82	1.15		0.69		1.06		0.14	4.59	0.08	1.05	0.28	72	
F1	0.11		27.43	1.76	5.05	2.33	0.61	0.09	0.48	0.59	0.39	0.46	0.07	0.63	0.15	0.13	2.08	0.03	0.60	0.26	33	
F2	0.18	0.55	29.80	2.95	7.14	4.19	1.15	0.13	1.02	1.05	0.72	0.78	0.11	1.19	0.23	0.07	3.57	0.01	1.10	0.32	16	
F3	0.15	0.83	15.38	3.92	8.43	5.24	1.22	0.13	1.17	1.44	0.91	0.90	0.15	1.51	0.22	0.07	3.22	0.01	1.29	0.38	14	
V1	0.14	1.15	17.83	1.97	2.46	2.02	0.79	0.15	0.62	0.72	0.43	0.57	0.08	0.93	0.07	0.64	7.35	0.29	0.81	0.26	108	
V2	0.23	2.50	60.99	4.56	10.39	5.94	1.55	0.28	1.52	1.83	1.18	1.28	0.21	1.71	0.32	0.09	6.59	0.08	1.78	0.59	47	
V3	0.14	0.82	40.65	4.00	8.87	5.12	1.31	0.14	1.11	1.57	1.03	1.01	0.17	1.32	0.24	0.60	3.43	0.06	1.28	0.39	55	
V4	0.15	0.92	26.89	2.86	6.99	3.81	1.01	0.11	0.83	1.14	0.73	0.73	0.13	1.27	0.19	0.08	3.99	0.02	1.08	0.40	55	
V5	0.22	0.96	34.06	4.47	7.52	4.00	1.55	0.19	0.77	1.20	0.77	1.10	0.14	1.52	0.25	0.15	5.42	0.03	1.14	0.41	96	

Table A.3: Data table of sample % Relative Standard Deviations.

Sample ID	Sample Category	Sample Description	SiO <sub>2</sub>	TiO <sub>2</sub>	Al <sub>2</sub> O <sub>3</sub>	FeO <sup>t</sup>	MnO	MgO	CaO	Na <sub>2</sub> O	K <sub>2</sub> O	S	Cl	n1
B1	Bomb	Non-Oxidised, grey breadcrust bomb with pumice and obsidian domains	1%	10%	1%	9%	27%	19%	15%	5%	10%	110%	15%	33
B2	Bomb	Non-Oxidised, grey pumice bomb with dense obsidian shards	1%	11%	1%	13%	24%	19%	10%	3%	3%	108%	8%	37
B3A	Bomb	Banded Obsidian Bomb with white oxidised material adhered to edge	1%	10%	1%	8%	22%	15%	10%	3%	3%	92%	5%	72
B3B	Bomb	Banded Obsidian Bomb with red, lithic material clast	1%	13%	1%	11%	28%	21%	11%	3%	4%	75%	18%	36
B4	Bomb	Banded Obsidian Bomb (collapsed and compacted foam)	1%	14%	2%	12%	22%	18%	13%	7%	15%	81%	18%	100
B5	Bomb	Partially collapsed foam with tuffisite vein (mild oxidation of vein material)	1%	5%	1%	6%	22%	14%	17%	12%	29%	67%	13%	60
B6	Bomb	Non-oxidised pumice breccia with dense and pumice clasts												
B7	Bomb	Non-oxidised pumice breccia with reticulite and dense clasts												
B8	Bomb	Banded Obsidian Bomb with non-oxidised tuffisite material on bomb edge												
B9	Bomb	Breccia bomb with dense and pumice clasts in dull red-grey matrix	1%	9%	1%	6%	14%	9%	7%	2%	2%	72%	7%	10
B10	Bomb	Banded Obsidian Bomb with black and dark-grey glassy bands	1%	8%	2%	15%	23%	24%	16%	6%	9%	94%	15%	17
B11	Bomb	Pumiceous Bomb with obsidian rind and subtle (grey-beige) interior banding	1%	9%	1%	23%	35%	27%	13%	3%	3%	82%	20%	16
B12	Bomb	Dense, dark grey and black banded sample												
F1	Flow	Breakout from northern branch of rhyolite flow												
F2	Flow	Breakout from northern branch of rhyolite flow												
F3	Flow	Rhyolite flow from vent												
V1	Vent	Breccia of dense and vesiculated clasts (Oxidised ash domains in breccia and deposited ash domains)	1%	13%	3%	18%	35%	36%	27%	12%	29%	93%	46%	72
V2	Vent	Breccia of dense clasts and flow material (Heavily oxidised ash material in breccia)	2%	19%	8%	31%	74%	113%	41%	12%	43%	136%	71%	30
V3	Vent	Nozzle with oxidised surface												
V4	Vent	Nozzle with light-pink ash adhered to surface												
V5	Vent	Nozzle with oxidised surface												

Sample ID	Li	V	Cr	Co	Ni	Cu	Zn	Ga	As	Rb	Sr	Y	Zr	Nb	Mo	Ag	Cd	In	Sn
B1																			
B2																			
B3A																			
B3B	4%	70%				29%	4%	4%	7%	5%			3%			16%	35%	27%	5%
B4	29%	26%	38%	12%	53%	32%	17%	11%	21%	15%	9%	6%	10%	9%	11%	16%	55%	15%	11%
B5	20%	20%	17%	6%	21%	23%	12%	6%	13%	7%	9%	4%	7%	4%	8%	20%	38%	22%	9%
B6	3%	7%	19%	11%	48%	24%	4%	3%	6%	3%	2%	3%	3%	4%	12%	32%	31%	13%	4%
B7	9%	41%	28%	16%	93%	20%	10%	10%	8%	12%	10%	4%	4%	8%	22%	55%	55%	30%	17%
B8	6%	26%		13%		14%	4%	3%	16%	4%	7%	4%	5%	4%	11%				
B9																			
B10																			
B11																			
B12	33%	47%	53%	22%		34%	14%	6%		26%	31%	12%	13%	12%	20%			32%	15%
F1	19%	30%		22%		23%	12%	4%	11%	24%	6%	6%	6%	6%	13%				
F2	10%	53%	30%	39%	61%	11%	21%	7%	14%	10%	11%	11%	10%	9%	17%	41%	52%	15%	14%
F3	12%	37%	20%	19%	27%	13%	18%	5%	28%	15%	28%	15%	15%	15%	17%	19%	28%	14%	14%
V1	32%	60%	11%	10%	15%	52%	20%	7%	13%	37%	14%	7%	10%	3%	6%	30%	64%	100%	41%
V2	55%	69%	21%	32%	39%	32%	25%	6%	25%	56%	32%	18%	16%	15%	22%	21%	62%	216%	25%
V3	14%	75%	35%	48%	59%	30%	24%	6%	14%	14%	25%	17%	14%	14%	18%	48%	48%	28%	14%
V4	15%	32%	22%	27%	45%	22%	18%	7%	17%	16%	20%	12%	13%	12%	16%	25%	36%	31%	15%
V5	22%	73%	22%	35%	120%	42%	28%	8%	16%	14%	21%	10%	14%	12%	32%	24%	43%	44%	18%



Sample ID	Sb	Cs	Ba	La	Ce	Nd	Sm	Eu	Gd	Dy	Er	Yb	Lu	Hf	W	Tl	Pb	Bi	Th	U	n2	
B1																						
B2																						
B3A																						
B3B	8%	5%					6%							4%		8%	6%	9%		5%		18
B4	16%	18%	6%	5%	7%	5%	6%	7%	7%	7%	9%	8%	11%	9%	15%	28%	16%	24%	5%	14%		43
B5	11%	8%	3%	6%	5%	4%	7%	5%	5%	6%	6%	10%	6%	9%	8%	24%	10%	18%	5%	8%		44
B6	7%	4%	2%	2%	3%	3%	4%	5%	6%	4%	4%	4%	6%	4%	7%	5%	3%	13%	4%	6%		17
B7	23%	13%	4%	4%	5%	5%	10%	10%	8%	8%	8%	9%	9%	6%	16%	20%	10%	19%	6%	11%		55
B8	5%		3%	4%	3%	3%	4%	6%	4%	4%	4%	6%	5%	6%	10%	5%	3%	43%	4%	4%		58
B9																						
B10																						
B11																						
B12	22%	17%	9%	12%	12%	12%	12%	15%	10%	13%		11%		12%		26%	20%	38%	12%	11%		72
F1	10%		4%	6%	7%	6%	7%	6%	6%	7%	7%	7%	7%	7%	9%	20%	7%	44%	6%	9%		33
F2	19%	11%	4%	9%	10%	11%	13%	9%	12%	11%	12%	12%	10%	12%	15%	15%	14%	27%	12%	12%		16
F3	14%	16%	2%	13%	13%	14%	14%	9%	14%	15%	15%	14%	13%	15%	15%	16%	12%	17%	14%	14%		14
V1	14%	21%	3%	7%	4%	6%	10%	10%	7%	7%	7%	9%	7%	10%	5%	106%	28%	137%	9%	10%		108
V2	21%	47%	9%	14%	14%	16%	20%	21%	17%	19%	18%	19%	18%	17%	16%	53%	29%	58%	18%	21%		47
V3	14%	16%	6%	13%	13%	14%	16%	10%	15%	18%	18%	16%	18%	14%	15%	107%	13%	115%	14%	15%		55
V4	15%	17%	4%	9%	10%	11%	12%	7%	11%	13%	13%	12%	13%	14%	13%	21%	15%	53%	12%	15%		55
V5	19%	17%	5%	14%	10%	11%	18%	13%	10%	13%	12%	17%	14%	16%	16%	38%	21%	68%	12%	15%		96

Table A.4: Calculated averages of secondary standards used for EPMA. n denotes number of analyses of standard.

	SiO <sub>2</sub>	TiO <sub>2</sub>	Al <sub>2</sub> O <sub>3</sub>	FeO <sup>t</sup>	MnO	MgO	CaO	Na <sub>2</sub> O	K <sub>2</sub> O	Cr <sub>2</sub> O <sub>3</sub>	P <sub>2</sub> O <sub>5</sub>	S	Cl	n
<b>VG2 Av</b>	49.24	1.81	13.39	11.58	0.21	6.66	11.01	2.58	0.20	0.02	0.09	1233	382	24
<b>1 St Dev</b>	0.28	0.04	0.12	0.56	0.03	0.08	0.10	0.14	0.01	0.02	0.03	461	29	
<b>% RSD</b>	1%	2%	1%	5%	15%	1%	1%	6%	5%	91%	32%	37%	8%	
<b>VGA99 Av</b>	50.51	4.00	12.28	13.32	0.20	4.90	9.18	2.62	0.85	0.01	0.31	116	223	55
<b>1 St Dev</b>	0.50	0.05	0.15	0.65	0.03	0.06	0.10	0.11	0.02	0.02	0.03	52	19	
<b>% RSD</b>	1%	1%	1%	5%	13%	1%	1%	4%	3%	131%	9%	45%	8%	
<b>VG568 Av</b>	76.64	0.07	12.08	1.12	0.02	0.03	0.44	3.63	4.95	0.01	0.00	9	1000	55
<b>1 St Dev</b>	0.35	0.01	0.09	0.09	0.02	0.01	0.02	0.22	0.10	0.01	0.00	10	58	
<b>% RSD</b>	0.5%	17%	1%	8%	68%	39%	4%	6%	2%	169%		101%	6%	

## **Appendix B: Data Table for Trace Element Diffusion Profiles**

Trace element data for profiles presented in Figures 7-10 and Supplementary Figures 3-6. Internal Standard Errors (2SE) are given for each spot/line analysis. A blank column denotes an element not analysed for that specific profile, <d.l. indicates analysis was below the detection limit. All data and errors are in ppm.

Table B.1: Figure 7 Profile Concentrations (ppm).

Distance	Group One		Group Two					Group Three													
	V	Mn	Ga	Zr	Sm	U	Li	Rb	Cs	As	Mo	Sb	Cu	Zn	Ag	Cd	In	Sn	Tl	Pb	Bi
13.02	3.45		20.62	345.32	6.28	2.54	36.45		5.26	13.19	0.88	1.11	5.10	85.84	<d.l.	<d.l.	<d.l.	<d.l.	<d.l.	9.44	<d.l.
38.95	2.51		21.57	331.19	7.21	2.42	26.18		5.70	14.73	1.01	1.03	3.79	56.35	<d.l.	<d.l.	<d.l.	3.27	<d.l.	14.85	<d.l.
61.39	2.19		19.57	327.66	7.40	2.59	24.97		5.32	13.82	2.24	1.19	3.54	81.18	<d.l.	<d.l.	<d.l.	2.92	<d.l.	20.19	<d.l.
84.64	1.71		18.88	366.52	8.52	2.75	26.92		6.48	16.63	2.06	1.30	4.36	70.34	<d.l.	<d.l.	<d.l.	2.41	0.15	23.92	<d.l.
114.31	4.15		19.49	242.87	4.68	1.67	19.25		3.82	9.82	1.70	1.12	2.80	69.07	<d.l.	<d.l.	<d.l.	<d.l.	0.11	18.12	<d.l.
136.88	9.27		19.31	357.69	8.34	2.77	24.54		6.26	14.80	2.74	1.18	4.44	110.59	<d.l.	<d.l.	<d.l.	2.70	0.19	28.63	<d.l.
165.93	6.51		19.05	302.93	7.96	2.21	23.01		5.09	14.59	0.96	0.89	3.21	102.32	0.11	<d.l.	0.04	3.02	0.22	26.48	<d.l.
188.79	2.57		17.83	353.27	8.06	2.71	24.23		5.38	14.87	1.22	1.17	5.10	76.74	<d.l.	<d.l.	<d.l.	3.50	0.21	26.89	<d.l.
214.29	3.51		20.09	364.75	9.65	2.69	26.66		5.69	13.26	1.87	1.15	5.27	84.26	<d.l.	<d.l.	<d.l.	3.30	0.26	26.89	<d.l.
237.52	5.02		19.92	325.01	8.15	2.33	23.43		5.10	12.21	2.29	0.99	5.27	76.96	<d.l.	<d.l.	<d.l.	2.41	0.30	24.00	<d.l.
261.35	6.18		19.92	395.66	8.24	2.69	27.66		6.48	16.21	2.74	1.19	7.49	97.96	<d.l.	<d.l.	0.08	2.41	0.45	27.47	<d.l.
286.82	4.70		20.27	349.74	8.43	2.54	25.13		5.21	13.47	1.30	1.32	7.33	80.12	<d.l.	<d.l.	<d.l.	2.00	0.33	25.57	<d.l.
311.34	4.76		20.18	340.91	7.59	2.46	25.76		5.04	13.19	2.24	1.06	10.04	92.91	<d.l.	<d.l.	<d.l.	<d.l.	0.36	24.25	<d.l.
337.00	5.59		18.88	399.19	9.56	2.86	29.30		6.45	17.33	3.24	1.24	9.79	101.79	<d.l.	<d.l.	<d.l.	3.21	0.42	27.60	<d.l.
361.82	3.92		20.27	378.88	8.81	2.78	27.51		5.81	15.99	2.58	1.19	10.54	80.50	<d.l.	<d.l.	<d.l.	3.02	0.43	27.12	<d.l.
388.60	4.93		20.18	379.76	8.43	2.71	27.61		6.00	17.19	3.16	1.31	10.21	83.28	<d.l.	<d.l.	<d.l.	3.75	0.50	27.64	<d.l.
439.61	9.69		18.44	336.49	7.87	2.33	26.77		4.88	12.63	1.40	0.75	8.64	109.84	<d.l.	<d.l.	<d.l.	2.96	0.39	21.35	<d.l.
465.55	11.94		19.49	271.13	7.40	1.90	23.06		3.96	11.79	2.58	1.09	7.24	103.82	<d.l.	<d.l.	<d.l.	3.08	0.33	18.95	<d.l.
490.33	6.10		19.83	363.87	8.34	2.57	27.45		5.27	12.21	1.45	1.32	22.55	96.30	<d.l.	<d.l.	<d.l.	<d.l.	0.39	24.99	<d.l.
515.54	3.21		18.70	390.36	8.06	2.68	29.73		5.64	13.40	1.81	1.29	19.18	76.36	<d.l.	<d.l.	<d.l.	2.51	0.47	27.39	<d.l.

Table B.2: Figure 7 Profile Internal Standard Errors (2SE) in ppm.

Distance	Internal Standard Errors (2SE)																				
	V	Mn	Ga	Zr	Sm	U	Li	Rb	Cs	As	Mo	Sb	Cu	Zn	Ag	Cd	In	Sn	Tl	Pb	Bi
13.02	0.72		1.19	13.43	0.90	0.16	2.76		0.37	2.16	0.44	0.20	1.04	6.57	0.13	0.82	0.05	1.72	0.03	0.51	0.05
38.95	0.52		1.04	13.43	1.04	0.13	1.49		0.37	2.54	0.44	0.20	0.90	4.33	0.16	0.82	0.06	1.64	0.03	0.65	0.05
61.39	0.53		1.04	12.69	1.34	0.20	2.01		0.29	1.64	0.75	0.19	0.90	5.90	0.12	0.69	0.06	1.79	0.03	0.97	0.05
84.64	0.44		1.12	16.42	1.27	0.24	2.16		0.54	2.54	0.66	0.23	0.90	4.70	0.14	0.90	0.05	1.34	0.03	1.27	0.05
114.31	0.63		1.19	14.18	1.12	0.13	2.16		0.36	2.54	0.54	0.22	0.82	7.09	0.19	0.90	0.06	1.72	0.03	0.97	0.05
136.88	2.39		1.12	12.69	1.27	0.19	2.09		0.42	2.09	0.82	0.20	0.97	11.19	0.13	0.82	0.04	2.09	0.04	1.49	0.04
165.93	1.04		1.19	23.88	1.19	0.19	2.76		0.49	2.69	0.46	0.17	0.82	10.45	0.13	0.71	0.04	1.57	0.04	1.72	0.04
188.79	0.66		1.12	10.45	1.19	0.13	1.72		0.31	2.31	0.43	0.25	1.04	5.67	0.13	0.97	0.07	2.24	0.04	1.12	0.05
214.29	0.75		1.34	25.37	1.49	0.19	2.98		0.51	1.72	0.73	0.20	1.12	8.95	0.12	0.54	0.05	1.72	0.04	1.49	0.05
237.52	0.66		0.90	14.92	1.12	0.19	1.72		0.37	1.79	0.72	0.16	0.90	6.72	0.13	0.55	0.05	1.42	0.04	1.12	0.04
261.35	0.90		1.27	10.45	1.34	0.18	2.16		0.37	2.31	0.75	0.24	1.34	6.19	0.21	1.34	0.06	2.39	0.06	1.12	0.06
286.82	0.72		1.34	8.95	1.19	0.15	1.64		0.30	1.94	0.56	0.19	1.27	5.67	0.15	0.61	0.05	1.34	0.04	0.90	0.05
311.34	0.82		0.97	14.18	1.27	0.17	1.42		0.32	2.39	0.72	0.25	1.57	4.48	0.18	0.90	0.06	2.46	0.05	1.19	0.04
337.00	0.75		1.19	10.45	1.49	0.16	2.16		0.35	2.54	0.97	0.19	1.42	6.87	0.13	0.75	0.06	1.64	0.05	0.69	0.05
361.82	0.71		1.19	11.94	1.19	0.13	2.01		0.31	2.54	0.75	0.20	1.57	4.93	0.19	0.90	0.06	2.01	0.04	0.68	0.06
388.60	0.75		1.12	8.95	1.19	0.16	1.42		0.33	2.39	0.75	0.18	1.27	6.57	0.18	0.97	0.06	2.39	0.05	1.04	0.05
439.61	1.49		1.27	15.67	1.34	0.15	1.87		0.31	2.16	0.57	0.19	1.34	11.19	0.14	0.75	0.06	1.87	0.04	1.19	0.04
465.55	3.81		1.42	14.18	1.19	0.15	2.01		0.33	2.16	0.82	0.22	1.34	19.40	0.18	0.97	0.06	2.31	0.05	0.97	0.05
490.33	0.90		1.19	8.95	1.12	0.13	1.72		0.27	2.39	0.56	0.17	4.18	5.22	0.16	0.74	0.06	1.87	0.04	0.90	0.05
515.54	0.55		1.12	12.69	1.27	0.15	2.24		0.35	2.39	0.58	0.22	3.06	5.30	0.15	0.73	0.06	1.87	0.05	0.90	0.04

Table B.3: Figure 8 Profile Concentrations (ppm).

Distance	Group One		Group Two					Group Three													
	V	Mn	Ga	Zr	Sm	U	Li	Rb	Cs	As	Mo	Sb	Cu	Zn	Ag	Cd	In	Sn	Tl	Pb	Bi
17.41	1.59		19.25	305.97	6.45	2.01	38.40	101.63	4.24	13.31		0.69	11.34	55.56	<d.l.	<d.l.	0.18	2.30	0.12	16.55	0.06
44.51	5.90		20.81	433.68	9.32	2.93	41.18	140.63	6.31	20.01		1.13	12.35	100.89	0.16	0.10	0.06	3.45	0.13	20.50	0.03
68.37	2.68		20.55	438.82	9.21	3.06	40.80	145.62	6.47	22.82		1.21	12.04	83.74	<d.l.	<d.l.	0.02	3.10	0.15	21.79	0.01
94.81	3.42		20.07	418.25	9.15	2.84	42.42	155.76	6.36	20.17		1.24	11.97	82.26	<d.l.	<d.l.	0.07	3.35	0.17	22.68	0.08
119.97	3.98		20.81	354.83	6.99	2.57	38.79	114.66	5.69	16.54		0.96	9.63	79.93	<d.l.	<d.l.	0.02	2.64	0.13	22.20	<d.l.
145.13	5.20		20.73	364.26	8.00	2.76	42.81	119.10	8.16	18.85		0.99	10.18	78.30	<d.l.	<d.l.	0.02	3.14	0.13	26.96	<d.l.
170.93	1.26		21.72	188.56	4.49	1.49	29.67	60.06	8.85	11.00		0.54	6.69	44.39	0.08	<d.l.	0.02	2.71	0.09	19.86	0.02
198.02	3.58		20.48	333.40	6.65	2.34	13.60	11.62	4.34	15.96		0.86	19.42	65.89	0.16	<d.l.	0.01	3.25	<d.l.	24.78	0.09
221.24	4.12		20.23	337.69	7.09	2.25	15.84	14.27	3.70	15.87		0.85	12.59	71.24	0.10	0.08	0.03	2.56	0.03	17.83	0.06
244.46	1.85		20.65	364.26	7.20	2.57	17.00	20.67	2.72	16.54		0.87	10.49	64.02	<d.l.	<d.l.	0.02	1.95	0.04	16.55	0.08
270.90	2.33		20.73	329.12	6.32	2.33	17.00	22.78	3.37	14.47		0.78	12.98	64.41	0.14	<d.l.	0.05	2.34	0.07	16.79	0.11
297.99	3.14		20.66	335.97	6.47	2.35	17.25	27.92	3.43	16.54		0.90	10.02	66.74	<d.l.	<d.l.	0.05	2.71	0.09	17.76	0.16
321.21	1.71		20.56	357.40	6.31	2.56	17.85	32.29	4.11	16.04		0.97	11.65	58.13	0.11	<d.l.	0.05	3.31	0.12	19.21	0.15
345.07	3.54		22.21	412.25	7.27	2.88	20.86	42.12	3.64	20.50		1.13	20.05	82.42	0.16	<d.l.	0.06	3.56	0.16	22.58	0.16
372.17	3.43		21.14	342.83	5.59	2.64	18.31	37.36	2.28	11.66		0.70	13.29	73.41	0.12	<d.l.	0.08	2.43	0.15	19.94	0.22
398.61	1.89		20.67	361.68	6.03	2.66	19.32	37.75	3.07	14.55		0.86	10.02	65.73	0.13	<d.l.	0.06	2.56	0.13	18.00	0.17
423.76	1.32		20.89	368.54	7.26	2.50	19.55	43.52	4.58	16.70		1.01	9.79	60.45	<d.l.	<d.l.	0.05	2.97	0.15	17.60	0.10
447.63	4.20		21.14	385.68	8.61	3.30	20.24	59.20	5.88	24.47		1.38	11.58	100.89	<d.l.	<d.l.	0.09	3.93	0.22	23.89	0.24
472.79	10.40		20.81	294.83	6.92	2.07	18.54	42.98	3.82	16.54		0.99	11.81	103.21	0.10	<d.l.	0.07	4.10	0.17	19.53	0.19
497.30	2.46		19.91	359.97	6.91	2.36	18.85	48.67	3.64	17.44		0.93	11.34	68.52	0.15	<d.l.	0.04	2.79	0.16	17.51	0.08
525.03	1.82		21.39	401.11	7.68	2.95	19.01	63.33	4.18	19.59		1.12	10.41	70.08	0.13	0.11	0.05	3.53	0.21	21.24	0.16
574.70	2.50		21.08	343.69	6.22	2.03	18.00	54.75	5.28	17.53		1.08	8.86	70.54	<d.l.	<d.l.	0.06	3.28	0.21	19.37	0.16
625.01	2.48		20.40	365.11	6.77	2.63	17.93	68.33	5.96	16.62		1.02	9.17	61.07	0.15	0.06	0.06	2.50	0.25	20.34	0.12
673.38	12.81		21.16	443.11	7.41	3.06	20.14	77.53	4.41	21.91		1.33	11.19	131.15	<d.l.	<d.l.	0.07	5.53	0.31	22.46	0.28
727.56	7.30		20.69	386.54	6.22	2.45	18.78	63.10	3.16	18.11		1.03	10.64	100.89	<d.l.	<d.l.	0.08	3.34	0.25	19.53	0.15
776.58	3.88		19.91	447.39	8.18	3.13	20.32	89.31	4.47	21.74		1.32	10.71	78.38	0.13	0.08	0.06	3.97	0.32	20.26	0.16
826.25	2.92		20.26	350.54	6.76	2.31	18.37	69.89	4.26	15.87		0.96	6.95	75.35	<d.l.	<d.l.	0.07	3.57	0.24	17.27	0.11
876.56	3.69		19.49	432.82	7.68	2.87	18.54	86.50	6.42	22.32		1.16	11.34	85.52	0.14	<d.l.	0.09	4.31	0.32	21.71	0.15
928.80	12.50		23.52	424.25	5.81	2.98	15.99	90.48	8.13	14.63		0.92	9.63	98.56	<d.l.	<d.l.	0.09	5.31	0.35	24.86	0.31
975.24	1.89		19.91	431.11	9.49	3.17	17.54	81.20	5.14	18.60		0.99	7.77	70.93	<d.l.	<d.l.	0.05	3.00	0.29	19.86	0.10
1027.48	4.58		19.74	313.69	6.22	2.09	16.84	62.63	2.87	13.64		0.81	7.76	93.13	<d.l.	0.13	0.08	2.57	0.23	18.24	0.14
1075.86	2.12		19.25	399.40	6.71	2.51	17.54	60.37	4.16	16.37		0.92	8.47	60.84	0.10	<d.l.	0.05	2.88	0.26	18.24	0.09

Table B.4: Figure 8 Profile Internal Standard Errors (2SE) in ppm.

Distance	Internal Standard Errors (2SE)																				
	V	Mn	Ga	Zr	Sm	U	Li	Rb	Cs	As	Mo	Sb	Cu	Zn	Ag	Cd	In	Sn	Tl	Pb	Bi
17.41	0.19		0.82	16.42	0.37	0.13	3.36	7.16	0.31	1.19		0.06	1.12	4.03	0.04	0.03	0.04	0.19	0.01	0.75	0.01
44.51	0.97		0.97	14.18	0.90	0.16	1.87	3.81	0.26	1.72		0.08	1.12	8.95	0.07	0.07	0.02	0.19	0.02	0.75	0.01
68.37	0.30		0.66	10.45	0.64	0.13	1.49	4.55	0.29	1.04		0.10	0.82	2.16	0.05	0.06	0.01	0.13	0.02	0.82	0.004
94.81	0.60		2.39	13.43	1.72	0.31	4.10	2.98	0.82	4.63		0.22	0.97	9.70	0.05	0.19	0.04	0.54	0.02	1.87	0.03
119.97	0.63		0.97	17.91	0.82	0.16	3.21	8.21	0.46	2.09		0.14	0.90	8.21	0.07	0.07	0.01	0.18	0.02	1.04	0.004
145.13	0.82		0.90	11.94	0.48	0.10	2.31	5.90	0.55	0.97		0.08	0.97	4.85	0.07	0.02	0.01	0.22	0.01	1.12	0.003
170.93	0.34		1.19	35.07	0.97	0.30	4.63	11.94	2.31	2.84		0.10	0.60	6.79	0.08	0.10	0.01	0.56	0.03	3.36	0.01
198.02	0.63		0.75	24.63	0.67	0.16	0.82	0.82	0.30	1.94		0.11	1.34	5.90	0.04	0.04	0.01	0.28	0.01	1.94	0.02
221.24	0.82		0.75	13.43	0.55	0.11	0.75	0.75	0.29	0.97		0.08	1.12	4.18	0.04	0.05	0.01	0.15	0.01	0.67	0.01
244.46	0.44		0.97	23.88	0.67	0.26	0.97	1.72	0.28	2.01		0.09	1.12	5.22	0.04	0.06	0.01	0.16	0.01	1.34	0.01
270.90	0.31		0.82	39.55	0.97	0.34	1.12	2.69	0.37	1.94		0.12	1.94	8.21	0.04	0.05	0.01	0.21	0.01	1.49	0.01
297.99	0.41		0.69	16.42	0.45	0.13	0.66	1.34	0.16	1.12		0.09	0.73	7.46	0.04	0.02	0.01	0.19	0.01	0.75	0.02
321.21	0.22		0.82	14.92	0.57	0.16	0.90	1.87	0.28	1.57		0.09	1.27	3.13	0.04	0.05	0.01	0.29	0.01	1.12	0.02
345.07	0.62		0.90	8.21	0.49	0.10	0.90	1.87	0.34	1.27		0.08	3.28	5.37	0.04	0.06	0.01	0.24	0.02	0.67	0.03
372.17	0.33		0.90	24.63	0.74	0.23	1.19	2.69	0.24	1.42		0.07	1.04	5.07	0.05	0.05	0.02	0.21	0.02	1.42	0.02
398.61	0.49		0.74	34.33	0.57	0.31	1.12	3.28	0.33	1.34		0.12	1.04	6.34	0.04	0.03	0.01	0.24	0.02	1.04	0.02
423.76	0.16		0.90	17.16	0.61	0.17	1.04	2.98	0.31	1.27		0.10	0.82	4.55	0.04	0.05	0.01	0.23	0.01	0.90	0.01
447.63	0.36		1.19	23.13	0.56	0.36	1.04	3.51	0.38	1.57		0.17	1.12	8.95	0.07	0.07	0.02	0.19	0.02	1.87	0.03
472.79	2.61		0.90	22.39	0.51	0.18	0.82	3.21	0.31	1.19		0.08	1.04	12.69	0.04	0.04	0.01	0.39	0.02	1.12	0.02
497.30	0.42		1.04	13.43	0.50	0.16	0.97	3.96	0.31	1.57		0.13	1.19	3.43	0.05	0.07	0.01	0.13	0.03	1.27	0.01
525.03	0.25		0.82	20.89	0.72	0.16	0.97	4.18	0.34	1.72		0.10	1.27	4.70	0.05	0.04	0.01	0.26	0.02	0.67	0.02
574.70	0.23		0.71	13.43	0.31	0.13	0.75	2.16	0.19	1.12		0.10	0.82	4.25	0.05	0.03	0.01	0.25	0.02	0.90	0.02
625.01	0.50		0.90	20.89	0.59	0.19	1.12	4.10	0.46	1.27		0.11	1.12	4.03	0.06	0.05	0.01	0.21	0.02	1.12	0.02
673.38	3.13		0.66	20.15	0.51	0.22	0.73	2.46	0.44	1.12		0.13	1.12	19.40	0.05	0.04	0.02	0.57	0.03	0.64	0.04
727.56	2.31		0.68	19.40	0.40	0.15	0.75	3.28	0.36	1.49		0.13	0.82	11.94	0.03	0.05	0.01	0.54	0.02	1.72	0.02
776.58	0.75		0.82	15.67	0.64	0.18	1.04	3.88	0.29	1.42		0.13	0.72	7.46	0.06	0.04	0.01	0.37	0.02	0.97	0.03
826.25	0.37		0.64	17.91	0.45	0.18	0.66	3.88	0.21	0.97		0.09	0.52	2.76	0.05	0.04	0.01	0.23	0.03	0.90	0.01
876.56	0.54		0.90	17.16	0.63	0.19	0.82	3.58	0.34	1.19		0.09	1.72	4.55	0.05	0.04	0.01	0.39	0.03	1.27	0.02
928.80	2.46		2.39	61.19	0.66	0.40	0.97	14.18	1.49	1.72		0.12	1.12	8.95	0.09	0.03	0.02	0.45	0.05	2.01	0.11
975.24	0.31		0.82	27.61	0.90	0.31	0.97	5.90	0.51	1.94		0.13	1.04	5.45	0.07	0.04	0.01	0.32	0.04	1.12	0.02
1027.48	1.34		0.82	26.86	0.43	0.20	0.97	4.48	0.19	1.27		0.09	0.73	14.18	0.04	0.05	0.01	0.30	0.03	0.97	0.02
1075.86	0.20		0.82	15.67	0.63	0.15	0.97	3.28	0.41	1.57		0.09	0.75	4.33	0.05	0.02	0.01	0.22	0.02	1.04	0.01

Table B.5: Figure 9 Profile Concentrations (ppm).

Distance	Group One		Group Two					Group Three													
	V	Mn	Ga	Zr	Sm	U	Li	Rb	Cs	As	Mo	Sb	Cu	Zn	Ag	Cd	In	Sn	Tl	Pb	Bi
-84.33	4.73	719.60	17.15	356.75	8.88	2.52	30.44	69.08	4.67	14.67	1.99	0.95	8.34	74.66	0.12	0.10	0.08	3.05	0.56	28.18	0.11
-41.77	3.71	561.97	18.47	385.46	8.62	2.56	30.37	73.99	5.15	15.86	2.00	0.86	11.56	63.28	0.10	0.17	0.06	3.18	0.59	24.58	0.07
1.52	4.97	741.67	18.62	359.02	8.55	2.59	31.17	72.71	4.97	16.01	2.53	0.97	14.01	74.66	0.01	0.12	0.08	3.28	0.56	28.67	0.08
42.73	6.69	788.96	18.52	343.36	7.93	2.73	32.47	70.82	5.06	16.41	2.50	1.16	11.41	81.85	0.03	0.29	0.22	2.89	0.62	28.76	0.08
86.87	5.13	773.19	19.22	358.35	8.32	2.58	33.13	75.51	4.94	16.73	2.81	0.95	18.57	86.55	0.12	0.13	0.11	3.10	0.55	25.47	0.07
130.33	4.73	765.31	18.44	351.28	8.18	2.56	34.80	75.66	4.95	15.78	2.38	0.97	12.31	82.07	0.05	0.06	0.12	3.15	0.54	24.71	0.07
171.42	4.93	783.44	19.51	350.10	8.63	2.52	35.09	77.85	5.12	15.78	2.25	0.93	15.51	85.60	0.06	0.17	0.09	3.24	0.53	25.72	0.07
213.20	4.62	836.25	18.78	366.26	9.53	2.79	35.53	84.74	5.61	16.01	2.35	1.16	18.35	95.44	0.09	0.06	0.11	3.54	0.56	29.57	0.08
255.91	4.46	791.32	19.01	352.96	8.07	2.52	34.94	79.97	5.08	15.93	2.85	0.97	13.69	90.15	0.07	0.12	0.12	3.24	0.56	25.07	0.06
300.01	5.45	773.98	18.72	343.70	8.48	2.45	25.57	64.31	4.79	16.41	2.35	1.06	16.33	87.80	0.03	<d.l.	0.10	3.14	0.40	24.22	0.06
341.72	5.37	779.50	18.87	345.80	8.25	2.41	34.87	83.91	4.85	16.81	2.50	1.05	13.05	90.66	0.07	0.05	0.09	3.22	0.58	26.59	0.07

Table B.6: Figure 9 Profile Errors Internal Standard Errors (2SE) in ppm.

Distance	Internal Standard Errors (2SE)																				
	V	Mn	Ga	Zr	Sm	U	Li	Rb	Cs	As	Mo	Sb	Cu	Zn	Ag	Cd	In	Sn	Tl	Pb	Bi
-84.33	0.48	10.45	0.48	6.04	0.55	0.11	1.19	1.57	0.14	1.42	0.35	0.09	0.70	3.58	0.05	0.13	0.01	0.19	0.03	0.82	0.02
-41.77	0.28	8.95	0.51	6.42	0.46	0.10	0.90	1.57	0.22	0.97	0.50	0.10	0.97	2.31	0.05	0.13	0.01	0.22	0.03	0.69	0.01
1.52	0.49	12.69	0.75	6.57	0.34	0.08	0.97	1.49	0.22	1.27	0.47	0.10	0.74	4.40	0.03	0.19	0.01	0.20	0.04	0.75	0.02
42.73	0.90	26.12	0.56	5.30	1.12	0.13	2.16	2.69	0.46	2.01	1.42	0.22	1.72	4.40	0.07	0.08	0.13	0.22	0.05	1.87	0.01
86.87	0.29	12.69	0.67	4.85	0.37	0.10	1.27	1.72	0.15	0.97	0.42	0.06	1.34	2.91	0.05	0.14	0.01	0.19	0.03	0.63	0.02
130.33	0.32	11.19	0.55	5.90	0.55	0.10	0.75	1.49	0.16	1.04	0.33	0.04	0.70	2.84	0.04	0.15	0.01	0.14	0.03	0.58	0.01
171.42	0.34	14.18	0.64	6.57	0.37	0.09	1.04	1.79	0.11	1.04	0.31	0.06	0.82	3.28	0.03	0.10	0.01	0.15	0.02	0.63	0.01
213.20	0.58	72.39	1.12	23.13	0.97	0.24	1.94	8.95	0.82	0.82	0.37	0.18	2.09	11.19	0.04	0.21	0.03	0.44	0.05	2.16	0.02
255.91	0.30	15.67	0.45	4.70	0.40	0.06	0.97	1.64	0.16	1.04	0.37	0.07	0.70	2.54	0.05	0.11	0.01	0.16	0.03	0.54	0.01
300.01	0.35	10.45	0.60	5.00	0.36	0.08	1.04	1.42	0.15	0.97	0.40	0.08	0.97	3.51	0.04	0.19	0.01	0.12	0.02	0.52	0.01
341.72	0.32	11.19	0.49	6.57	0.43	0.08	0.90	1.64	0.17	0.90	0.44	0.07	0.90	3.21	0.04	0.11	0.01	0.16	0.03	0.60	0.01



Table B.7: Figure 10 Profile Concentrations (ppm).

Distance	Group One			Group Two					Group Three												
	V	Mn	Ga	Zr	Sm	U	Li	Rb	Cs	As	Mo	Sb	Cu	Zn	Ag	Cd	In	Sn	Tl	Pb	Bi
0.00	5.98	825.02	18.38	325.95	8.00	2.15	22.64	70.77	4.87		<d.l.	<d.l.	11.27	80.15		<d.l.	<d.l.	3.32	0.69	23.72	<d.l.
36.12	3.83	749.03	19.06	351.35	8.31	2.26	24.35	79.19	5.14		2.42	1.10	9.72	78.65		<d.l.	<d.l.	2.94	0.54	26.59	0.16
74.87	5.95	816.49	18.38	329.84	7.62	2.25	22.40	73.02	4.82		2.53	<d.l.	10.97	83.41		<d.l.	<d.l.	<d.l.	<d.l.	23.19	<d.l.
108.37	7.04	804.86	18.94	330.07	8.00	2.40	21.22	71.06	4.67		3.01	<d.l.	9.57	87.79		<d.l.	<d.l.	3.58	<d.l.	21.33	<d.l.
141.67	6.37	820.37	19.14	329.84	7.72	2.51	21.21	69.76	4.64		2.89	0.81	11.86	82.57		<d.l.	<d.l.	2.73	0.25	23.26	0.28
177.79	4.99	809.51	19.01	339.30	7.85	2.44	21.97	71.14	5.05		3.08	<d.l.	9.29	83.94		<d.l.	<d.l.	2.94	<d.l.	24.78	<d.l.
212.04	5.75	814.16	19.44	328.92	7.93	2.24	19.99	68.02	4.15		<d.l.	<d.l.	10.16	80.48		<d.l.	<d.l.	2.60	<d.l.	24.25	<d.l.
249.03	3.75	839.75	19.34	366.38	9.30	3.08	34.45	102.13	6.26		3.16	1.27	8.98	79.24		<d.l.	0.16	3.34	0.50	26.58	0.14
285.21	5.49	853.71	19.19	328.16	8.23	2.51	19.73	68.31	4.53		<d.l.	<d.l.	8.69	80.93		<d.l.	<d.l.	<d.l.	<d.l.	23.05	<d.l.
319.46	6.84	849.83	18.64	326.02	9.30	2.90	18.92	66.35	4.44		<d.l.	<d.l.	7.11	83.68		<d.l.	<d.l.	3.02	<d.l.	24.78	<d.l.
358.25	7.29	890.15	18.79	324.80	7.70	2.51	20.48	67.80	4.12		2.80	<d.l.	8.17	91.18		<d.l.	<d.l.	3.28	<d.l.	25.33	<d.l.
390.66	6.12	927.37	18.56	338.53	8.46	2.65	38.93	109.97	6.32		<d.l.	<d.l.	8.98	83.15		<d.l.	<d.l.	2.58	0.66	26.58	<d.l.
424.97	5.08	633.50	17.96	341.74	8.76	2.58	21.07	75.20	4.67		1.91	0.81	10.75	75.19		<d.l.	<d.l.	2.55	0.54	25.53	0.31
463.81	4.74	766.86	18.42	336.47	8.31	2.29	20.25	68.60	5.08		<d.l.	<d.l.	10.82	78.45		<d.l.	<d.l.	<d.l.	<d.l.	23.28	<d.l.
498.94	3.66	800.21	19.39	340.90	8.31	2.78	19.83	71.43	5.33		<d.l.	<d.l.	8.69	79.04		<d.l.	<d.l.	2.85	<d.l.	25.08	<d.l.
534.18	4.13	845.18	18.00	344.79	8.54	2.59	22.34	75.28	5.66		<d.l.	<d.l.	12.59	78.71		<d.l.	<d.l.	3.66	<d.l.	27.86	<d.l.
572.05	4.07	779.27	19.90	338.69	7.77	2.87	19.55	69.61	5.20		1.91	0.93	8.32	88.83		3.06	<d.l.	3.19	0.32	26.51	<d.l.
605.38	4.04	794.78	19.51	339.60	6.90	2.48	18.46	63.52	4.95		3.20	<d.l.	7.82	82.57		<d.l.	<d.l.	2.96	0.59	25.83	<d.l.
641.60	3.89	694.75	18.71	338.92	8.08	2.51	18.68	60.83	4.89		<d.l.	<d.l.	10.31	75.26		<d.l.	<d.l.	<d.l.	<d.l.	24.70	<d.l.
679.41	3.46	721.12	18.95	337.47	8.61	2.69	23.17	69.40	5.14		3.61	<d.l.	8.39	82.57		<d.l.	<d.l.	4.28	<d.l.	27.04	<d.l.
714.59	3.99	741.28	18.54	337.85	8.35	2.55	36.47	84.86	5.21		2.80	0.79	12.44	80.02		<d.l.	0.25	3.74	0.54	25.30	<d.l.
748.96	4.60	769.97	19.46	345.55	8.15	2.69	42.30	92.48	5.20		3.38	<d.l.	15.02	84.78		<d.l.	<d.l.	2.80	<d.l.	22.98	<d.l.
785.89	4.61	868.44	19.46	339.83	8.69	2.76	42.45	88.85	4.81		<d.l.	<d.l.	12.05	79.82		<d.l.	<d.l.	2.66	<d.l.	22.97	<d.l.
817.47	4.45	644.35	18.17	347.54	8.31	2.61	41.70	88.49	4.98		2.74	<d.l.	11.34	75.32		<d.l.	<d.l.	2.94	<d.l.	23.87	<d.l.
857.09	4.50	710.26	19.22	338.31	8.15	2.57	40.43	82.46	4.81		<d.l.	<d.l.	13.77	76.89		<d.l.	<d.l.	2.51	0.58	23.87	<d.l.

Table B.8: Figure 10 Profile Internal Standard Errors (2SE) in ppm.

Distance	Internal Standard Errors (2SE)																				
	V	Mn	Ga	Zr	Sm	U	Li	Rb	Cs	As	Mo	Sb	Cu	Zn	Ag	Cd	In	Sn	Tl	Pb	Bi
0.00	0.41	14.92	0.67	4.70	0.82	0.16	0.75	1.34	0.22		0.97	0.19	0.97	3.96		1.04	0.09	0.65	0.20	0.97	0.10
36.12	0.52	16.42	0.66	4.78	1.04	0.19	0.54	1.79	0.25		1.04	0.23	0.90	3.21		1.64	0.12	0.69	0.16	0.69	0.10
74.87	0.44	30.60	0.46	5.00	0.90	0.23	0.61	1.49	0.27		0.68	0.31	1.04	3.66		1.57	0.13	0.82	0.19	1.04	0.15
108.37	0.52	8.95	0.71	4.10	0.97	0.16	0.69	1.49	0.19		0.82	0.34	0.47	2.61		1.72	0.11	0.69	0.14	0.72	0.13
141.67	0.70	12.69	0.70	3.88	0.64	0.14	0.55	1.12	0.22		0.62	0.44	1.27	2.16		1.42	0.10	0.66	0.12	0.71	0.13
177.79	0.58	14.18	0.65	5.37	1.12	0.19	0.82	1.64	0.22		0.69	0.33	0.46	4.70		1.57	0.06	0.63	0.15	0.82	0.09
212.04	0.57	22.39	0.54	4.78	0.90	0.19	0.71	1.49	0.22		0.75	0.33	2.16	4.25		1.12	0.08	0.67	0.13	1.12	0.11
249.03	0.42	27.61	0.72	3.28	0.71	0.20	2.39	6.34	0.42		0.82	0.37	0.90	4.10		1.79	0.09	0.69	0.16	1.27	0.10
285.21	0.51	29.85	0.74	5.45	0.82	0.20	0.66	1.64	0.27		0.66	0.31	1.12	3.66		1.19	0.10	0.61	0.13	0.51	0.15
319.46	0.50	20.89	0.51	4.25	0.82	0.22	0.74	1.42	0.22		0.68	0.34	0.63	4.85		1.04	0.10	0.47	0.18	0.82	0.12
358.25	0.97	64.92	0.69	3.88	0.90	0.19	0.82	1.72	0.16		0.65	0.35	1.64	7.31		1.27	0.10	0.65	0.15	0.71	0.13
390.66	1.04	42.54	0.90	6.04	0.97	0.21	1.12	1.49	0.26		1.04	0.36	1.12	5.30		1.49	0.10	0.62	0.15	0.97	0.12
424.97	0.56	38.06	0.67	6.12	0.97	0.27	0.75	1.57	0.21		0.82	0.36	2.84	4.55		1.27	0.07	0.54	0.16	1.04	0.18
463.81	0.52	17.91	0.90	5.90	0.75	0.19	0.52	1.42	0.22		0.82	0.29	4.33	2.84		1.34	0.10	0.90	0.15	0.65	0.16
498.94	0.55	24.63	0.60	5.07	1.04	0.16	0.74	1.34	0.28		0.74	0.28	0.97	4.18		1.57	0.09	0.51	0.17	1.04	0.11
534.18	0.53	41.79	0.63	8.95	0.82	0.14	1.34	2.31	0.31		0.90	0.23	2.31	5.67		1.34	0.12	0.82	0.13	0.90	0.14
572.05	0.59	16.42	0.90	5.30	0.97	0.19	0.62	1.87	0.36		0.75	0.31	0.90	3.58		1.94	0.07	0.64	0.15	1.04	0.16
605.38	0.59	15.67	0.60	5.45	0.46	0.21	0.90	1.57	0.22		0.63	0.31	0.69	4.78		1.64	0.09	0.66	0.14	0.67	0.14
641.60	0.39	12.69	0.75	5.07	0.90	0.16	1.04	2.09	0.33		0.68	0.34	1.42	4.40		1.57	0.10	0.75	0.18	1.04	0.12
679.41	0.75	23.88	0.55	6.72	0.90	0.19	1.04	1.34	0.27		0.63	0.34	0.82	5.07		1.72	0.08	0.74	0.14	0.90	0.06
714.59	0.48	24.63	0.40	6.64	0.65	0.20	2.09	3.66	0.22		0.60	0.33	1.64	3.96		1.87	0.13	0.54	0.15	0.97	0.13
748.96	0.66	27.61	0.82	4.78	0.90	0.15	1.04	2.16	0.37		0.82	0.31	1.72	2.84		1.27	0.09	0.74	0.16	0.72	0.16
785.89	0.60	15.67	0.51	4.48	1.12	0.23	1.27	1.49	0.24		0.82	0.33	0.73	4.33		1.42	0.10	0.54	0.13	0.90	0.15
817.47	0.49	26.12	0.60	3.88	0.90	0.23	0.97	2.01	0.22		0.73	0.26	1.19	3.21		1.42	0.10	0.49	0.16	0.75	0.13
857.09	0.48	11.94	0.54	5.45	0.97	0.16	1.19	2.24	0.16		0.90	0.31	1.94	2.98		1.49	0.09	0.60	0.19	0.90	0.13

## **Link to Chapter Three**

The general introduction summarises the current understanding that tuffisites act as pathways for gases to move through silicic melts. Diffusive degassing surrounding fractures is an inefficient process to degas magma on the timescales of an eruption. Therefore, for them to be efficient enablers of degassing they must interact with volatile-rich, permeable and vesicular melts and efficiently extract volatiles. However, there have been a lack of studies that focus on how fracture networks and bubble networks interact in high-silica melts, as a combination of these textures are rarely preserved in natural samples. In Chapter One chemical data suggest a physical process can result in the preferential transport of glass shards through fractures, and both previous chapters highlight how gases flux through these features implying a gas-rich source.

In this final chapter I build on the work of these previous chapters and focus on a single sample that has texturally preserved a fracture propagating through vesicular melt. I investigate the source material for tuffisite matrices and how the fracture exploited the pre-existing porous network on the  $\mu\text{m}$ - $\text{nm}$  scale. In doing so I show that fracture networks appear capable of degassing zones of vesicular melts on a cm-wide scale, much larger scale than zones recorded in dense melts (sub-mm wide), and highlight the importance for this interaction in degassing silicic systems and the transition from explosive to effusive behaviour with time.

## Chapter Three

### **Fracture propagation through vesicular silicic melts and its implications for tuffisite formation and degassing processes**

**Authors:** R. Paisley<sup>1</sup>, K. Berlo<sup>1</sup>, S. Kolzenburg<sup>1</sup>, J. Owen<sup>2</sup>, H. Tuffen<sup>2</sup>

<sup>1</sup>Department of Earth & Planetary Sciences, McGill University, 3450 Rue University, Montreal, Quebec, Canada, H3A 0E8

<sup>2</sup>Lancaster Environment Centre, Lancaster University, Lancaster, UK

*In preparation for Contributions to Mineralogy and Petrology*

#### **Highlights:**

- Fractures exploit pre-existing structures to propagate efficiently through vesicular melts
- Branching fractures isolate and incorporate host material into the clastic tuffisite vein fill preserved in the erupted products from hybrid phase of the 2011-2012 Cordon Caulle eruption
- Repeated fracturing and healing cycles are recorded in these magma outgassing structures
- Tuffisite veins can efficiently outgas cm-scale wide zones of vesicular melt

## **Abstract**

Tuffisites (volcanic hydrofractures propped open with fragmented clastic material) are highly permeable pathways facilitating gas escape throughout the upper conduit of many silicic volcanoes. However, for tuffisites to have a significant role in the degassing of magmatic systems they must be capable of interacting with and extracting gas from vesicular magmas at depth. Studies have previously assessed tuffisite veins intruding into dense material within country rock, domes and shallow conduits, but little attention has been given to tuffisites within vesicular melts. Here we present a detailed textural characterisation of a tuffisite vein and its vesiculated host melt that record multi-stage fragmentation and healing within a volcanic bomb erupted during the hybrid phase of the 2011-2012 Cordón Caulle eruption. Textures highlight how fractures exploit the weak porous network to further their propagation. The heterogeneous nature of the porous network and the resulting local variations in strength promote branching and undulating fracture propagation, rather than localized and spatially restricted clean fracturing. This results in host material being incorporated into the vein as both larger angular clasts and fine matrix ash. Repeated fracturing and sintering of vein material is concurrent with gas escape resulting in the collapse and compaction of the host on a centimetric scale. Aided by the presence of a permeable porous network, these spatial scales far exceed zones/volumes of degassing in dense melts. We show that the interaction between viscous (foam) and brittle (fracture) permeable networks can be preserved in erupted samples. This study strongly supports the notion that tuffisites source their gases from permeable vesicular melts and are capable of degassing large volumes of magma, allowing for pressure release during an eruption.

## 1. Introduction

The ability or inability for magma to outgas volatiles upon ascent directly influences the eruptive behaviour observed at the surface (Edmonds, 2008). In silicic systems, high melt viscosities preclude the segregation and movement of exsolved gas bubbles, leading to closed-system degassing and hazardous, explosive eruptions (Sparks, 1978; Edmonds, 2008). However, the effusion of volatile-poor lava, forming domes and flows, is evidence silicic magmas can undergo extensive, open-system degassing and efficient segregation of volatiles (Eichelberger et al., 1986). The development of highly permeable bubble networks and fractures (e.g. tuffisite veins) is key to efficient, open-system degassing in high-silica magmas (e.g. Eichelberger et al., 1986; Stasiuk et al., 1996; Gonnermann and Manga, 2003; Tuffen et al., 2003; Okumura et al., 2009). Recent observations of hybrid activity, simultaneous explosive and effusive behaviour, during the 2008 Chaitén and 2011-2012 Cerdón Caille eruptions emphasise the role of syn-eruptive fracturing as a degassing mechanism capable of diffusing eruptions (Pallister et al., 2013; Schipper et al., 2013; Castro et al., 2014). Fracturing accounts for both the punctuated explosions observed, and the progressive degassing of the system with time leading to lava dome and rhyolite flow emplacement (Castro et al., 2014). Tuffisite veins are formed via hydrofracture or shear failure of viscous magma and preserve the brittle fracturing and subsequent fluxing of gas and ash through magma or country rock (Heiken et al., 1988; Stasiuk et al., 1996; Tuffen et al., 2003; Kendrick et al., 2016). Although these features are transient in space and time within the conduit, particle-filled fractures can be several orders of magnitude more permeable than their respective host, before sintering and compaction reduces their porosity and permeability to near initial values (Kolzenburg et al., 2012; Heap et al., 2015; Farquharson et al., 2016). Diffusion of volatiles within silicate melts to fracture-gas interfaces is not a fast enough mechanism to degas magma in the conduit, given

the short lifespans of fractures, and thus repeated fracturing and mm-scale brecciation of magma would be necessary for veins to be efficient modes of degassing via diffusive processes (Okumura et al., 2010; Castro et al., 2012b). Therefore, for fractures to be key enablers of degassing they must primarily be pathways for gases to escape from deeper and more permeable, volatile-rich magmas (Castro et al., 2012b). This suggests that within the conduit, at depth, tuffisite veins originate in or intersect volatile-rich, magmatic foams, allowing for gases to rapidly outgas from the foam, via fracture networks.

Tuffisite veins have previously been noted in country rocks (Cloos, 1941; Heiken et al., 1988; Stasiuk et al., 1996), shallow dissected conduits (Stasiuk et al., 1996; Tuffen et al., 2003; Tuffen and Dingwell, 2005; Berlo et al., 2013), crystal-rich andesitic domes (Kolzenburg et al., 2012; Plail et al., 2014; Farquharson et al., 2016; Kendrick et al., 2016), glassy rhyolitic domes (Heiken et al., 1988; Cabrera et al., 2011; Castro et al., 2012b; Berlo et al., 2013; Castro et al., 2014; Cabrera et al., 2015; Saubin et al., 2016); and in basaltic pyroclasts from a subglacial eruption (Owen et al., 2019). Studies focusing on silicic systems have a bias towards tuffisites preserved in dense rock (e.g. country rock, conduit plug or dome material). Thus the role fractures play as gas pathways has been extensively studied but their origins, deeper propagation mechanisms, and interactions with their gas and ash sources remain unclear. Although tuffisite veins have been found preserved in vesiculated volcanic bombs, bomb textures imply vesiculation was primarily the result of post-fragmentation inflation and that the syn eruptive fracturing would have occurred in dense melt (Paisley et al., in review). In this study we texturally characterise a sample from the 2011-2012 eruption of Cordón Caulle whose textures indicate fracture propagation occurred through a vesiculated melt. We summarise how fractures exploit pre-existing porous networks during their propagation and describe the resulting implications for the source material of tuffisites and the degassing of silicic melts.

## 1.1 The 2011-2012 Cordón Caulle Eruption

The Cordón Caulle fissure system is located in the Chilean Southern Volcanic Zone between Puyehue stratovolcano and Cordillera Nevada caldera (Gerlach et al., 1988). The 2011-2012 eruption commenced on June 4<sup>th</sup> with ~27 hours of Plinian activity (<15 km high column) before transitioning into approximately one week of lower-intensity plume behaviour, with plume heights fluctuating between 3 and 10 km (Silva Parejas et al., 2012; Castro et al., 2013). Hybrid activity, concurrent Vulcanian blasting and lava effusion from a single vent, began mid-June alongside the rapid emplacement of a shallow (~20-200 m deep) laccolith (Silva Parejas et al., 2012; Castro et al., 2016). Hybrid activity continued into 2012 from two sub-vents within a single tephra cone displaying activity from Vulcanian activity (ejecting bombs <1 km away) to ejecta-poor gas venting (Schipper et al., 2013). Although the eruption ended in April of 2012, the rhyolite lava flow continued to grow via breakouts into 2013 (Tuffen et al., 2013). The total erupted volume for the eruption is ~1.4 km<sup>3</sup> dense rock equivalent (Tuffen et al., 2013; Pistolesi et al., 2015). Magmatic storage conditions are estimated to be ~2.5-7.5 km deep, 875-920 °C, with a pre-eruption volatile content of ~2.5-4 wt. % H<sub>2</sub>O (Castro et al., 2013; Jay et al., 2014). The erupted products of this eruption are crystal-poor, <5 vol %, with a phenocryst assemblage comprising of plagioclase, orthopyroxene clinopyroxene, magnetite and ilmenite with trace apatite and pyrrhotite (Castro et al., 2013). Volcanic bombs collected from this eruption show evidence for extensive and repetitive fragmentation, gas fluxing, sintering and compaction in the upper-conduit plug (Schipper et al., 2013; Castro et al., 2014; Whattam, 2018; Paisley et al., in review, Paisley et al., in prep).



## 2. Sample Studied

A ~5 x 8 x 8 cm tuffisite-hosting, partially vesicular bomb (Fig. 1A) was sampled from within the tephra cone, <150 m from the vent openings (~40°52'28.80"S, 72°14'86.60"W). It is thought to originate from the latter period of the eruption, based on observations of projectiles being blasted <1 km from the vent during the waning phase of hybrid activity when concurrent pyroclastic emissions and lava effusion were observed from the vent (Schipper et al., 2013; Paisley et al., in prep.). The host is a partially vesiculated obsidian. A zone (<2 cm-wide) of dense (or less vesicular) glass is present on either side of the tuffisite vein (Fig. 1, Fig. 2). The host shows some minor oxidation (red colouration) of bubbles walls. Rare plagioclase crystals are observed in hand specimen. The host is cut by a 1-2 cm-wide tuffisite vein, composed of two texturally distinct sub-veins referred to as vein one (V1) and vein two (V2) (see Section 4, Figs. 3-4). The host-vein interfaces are ~parallel to each other but have irregular boundaries. V1 is not present through the entire hand sample and pinches out (Fig. 1D), it is brown-orange in colour with angular mm-sized clasts that are not immediately clear in hand specimen. V1 shows a variable degree of sintering and oxidation. V2 dissects across the entire hand sample and overlaps considerably with V1 (Fig. 1D). V2 is mainly comprised of highly sintered and oxidised, pink-orange, fine-grained ash.

## 3. Methodology

Two polished thin sections (30-50 µm thick), oriented at ~90° to each other, (Fig. 1B and C) were made from epoxy-impregnated slabs cut from the hand specimen. Overview images of both thin sections were made on a high-resolution digital scanner. Optical images were taken

on a petrological microscope (2.5-50x magnification); back-scatter electron (BSE) images were taken using a field emission scanning electron microscope (SU5000 FE-SEM at McGill University, with 5-15 kV, 30-50 spot intensity, and 70-11,000x magnification), and a JEOL JXA-8230 Superprobe (at Victoria University of Wellington, with 15kV, 8nA, and 50-1,200x magnification). Brightness and contrast settings were conducted online and offline in ImageJ and Adobe Photoshop to threshold samples for quantitative analysis (e.g. porosity estimates) and to highlight certain textural features. Energy-dispersive spectroscopy (EDS) maps for Si, Al, Ti, Ca, Fe, Mg, Mn, Ti, Na, K and O were collected on the FE-SEM using a working distance of 10mm, 15kV and a spot intensity of 50, dwell times were 750-1200  $\mu\text{s}/\text{pixel}$ .

#### **4. Results & Petrology**

Here we use the terms ‘sintering’ and ‘compaction’ in reference to textures that show any degree of these processes. For example, a sintering texture would encompass any texture from point contact between two particles to complete coalescence and healing of melt (Vasseur et al., 2013). Furthermore, for clarity we discuss crystals in three distinct categories: phenocrysts ( $>100 \mu\text{m}$  in size) that are part of the assemblage formed during storage; microlites ( $\sim 5\text{-}100 \mu\text{m}$ ) that grew upon ascent; and nanolites that are sub-micron sized crystals (Mujin et al., 2017). To avoid confusion individual ash particles ( $<50 \mu\text{m}$  in size) that comprise the vein matrix are referred to as ‘shards’ and ‘clasts’ is used in reference to larger ( $>50 \mu\text{m}$  in size), more distinct particles within the vein. The vein is subdivided into two distinct sub-veins (V1 and V2) based on their subtle colouration and sintering differences in hand specimen. Both sub-veins and host material are described in detail below.

## 4.1 Host Material

The host has two visually distinct zones (dense and vesicular) based on observations of the hand specimen (Fig. 1A, Fig. 2). The vesicular zone gradually transitions into the dense zone over a ~2-5 mm width on either side of the central tuffisite vein. Vesicularity within the host is highly variable across the sample. At its most distal points from the vein (vesicular zone), vesicularity is ~20-35 % and proximal to the vein (dense zone) it is ~5-20 %. In areas of the vesicular zone where elongated bubbles are aligned approximately parallel ( $\pm \sim 10^\circ$ ) to the orientation of the tuffisite (Fig. 2B) bubbles show a degree of compaction. Closer to the vein bubbles are less common, but a parallel alignment of the microlites in the glass is apparent in plane polarised images (Fig. 2C). In the dense zone of the host near the V1-host interface, the elongated and deformed bubbles show a different alignment,  $\sim 32^\circ \pm 7^\circ$  relative to the vein (Fig. 2D, E). This alignment is lost with increasing distance from the tuffisite vein (Fig. 2I).

Throughout the sample, bubble sizes vary from  $\sim 10 \mu\text{m}$  to  $>1 \text{ mm}$  and are highly contorted with uneven bubble walls (Fig. 2B). Rounded to sub-rounded bubbles are not readily observed. In places, where bubble walls touch, the melt shows a degree of sintering (Fig. 2B, I). There is extensive evidence for dimpling, bending and breaking of inter-bubble melt films, (IBFs, Castro et al., 2012a) (Fig. 2F, I), as well as pinching out of bubbles where compaction and sintering between touching bubble walls is greatest (Fig. 2B, D-I). There is also evidence of sintering between clasts of material within bubbles, resulting in irregular shaped void spaces (Fig. 2D, F, I). Phenocrysts are rare but microlites and nanolites are observed. Microlites (plagioclase and pyroxenes) show alignment with the tuffisite vein in the dense zone of the host (Fig. 2C). In areas of complete bubble compaction  $<5 \mu\text{m}$ -wide bands of a darker greyscale

value preserve old bubble walls with occasional nanolites (orthopyroxene and magnetite, e.g. Fig. 2H). In addition to sintered ash particles in bubbles, some bubbles are partially filled with angular <5  $\mu\text{m}$ -sized ash shards (Fig. 2D, G, Fig. 5E, Fig. 7D, F).

## 4.2 Vein One (V1)

Vein one is a tuffisite vein composed of largely angular clasts set in a fine-grained ash matrix (Fig. 3). Vein width is variable throughout the sample, with a maximum width of  $\sim 1$  cm. However, the vein pinches out and is overprinted by V2, thus its original width cannot be accurately determined. The top boundary of the vein with the host is undulating (Fig. 3B). The side edge of the tuffisite, where visible, has a ragged appearance, see Section 4.4 (Fig. 1D, Fig. 3A, Fig. 5). In places the vein is overprinted by V2 and only isolated pockets of V1 material remain preserved (Fig. 1D, Fig. 3A, Fig. 7). Porosity is highly variable within V1 ranging from  $\sim 5\%$  at the edge to  $\sim 20\%$  in the interior between larger clasts. Clasts range in size from  $\sim 100$  to  $1000+$   $\mu\text{m}$  (longest axis) and are angular with irregular-shapes or ragged margins (Fig. 3C-D). Texturally these clasts appear similar to the host material with aligned microlites, although vesicles are largely absent in these clasts (Fig. 3). Texturally heterogeneous, mm-sized clasts are present, but rare, within V1 (e.g. Fig 3E-F, H). Clasts preserve dense banding or veining (Fig. 3E), partially compacted vesicles (Fig. 3F); and bands ( $\sim 40$   $\mu\text{m}$  across) of fully welded ash-grains (Fig. 3H) whose edges are defined by orthopyroxene nanolites. Crystals are rare in V1 but when observed are isolated crystal fragments (Fig. 3D) or found within larger clasts (e.g. Fig 3E, G). The matrix of V1 is comprised of glassy shards  $\sim 5$ - $50$   $\mu\text{m}$  across that have undergone extensive sintering and rounding (e.g. Fig. 5D). Where sintering is complete, edges between shards are often only defined by nanolite trails (Fig. 4, Fig. 5). Small matrix glass

shards are concentrated at the edges of the vein, particularly in concave voids within the host at the interface where clasts are absent (Fig. 3C, Fig. 5B). Glass shards can be found sintered to larger angular clasts within the vein's interior (Fig. 3G-H). There are no clear laminations or sorting of matrix ash, by either size or shape, in V1.

### 4.3 Vein Two (V2)

Vein two is ~5-10 mm-wide and comprised of fine- and coarse-grained laminations of variably sintered shards (Fig 4). Vein walls are contact with V1 material (top) and host material (bottom) and run largely parallel to each other throughout the sample (Fig. 1, Fig 4A-B). The contact between V1 and V2 is diffuse and gradational as clasts of varying sizes are found in both sub-veins. The contact between V2 and the host is sharp and clear but ragged in places, deviating from parallel and make stepwise shifts into the host (Section 4.5, Fig. 4B). It is difficult to distinguish the V1-V2 boundary in BSE images but it is clearer in hand specimen where the two veins differ slightly in colour (brown-orange vs. pink-orange) that likely represent differing oxidation of the vein clasts and matrices (Fig. 1, Fig. 4A-B). Large clasts (500+  $\mu\text{m}$ -wide) are rarer in V2, with most angular clasts preserved in a central lamination within the vein (Fig. 4B). Clasts are angular and irregularly shaped, and can be microlite-rich or banded, and thus similar to those found in V1 (Fig. 4C-D). Fine-grained laminations (~5-30  $\mu\text{m}$ -wide shards) are largely sintered with a porosity of <5 % (Fig. 4E). Coarse-grained laminations (~5-50  $\mu\text{m}$ -wide shards) have a higher porosity ~5-10 % (Fig. 4E). Such laminae compact around clasts hosted within them (Fig. 4D). Shards are sub-rounded to rounded in shape but larger shards >30  $\mu\text{m}$  across show a degree of irregularity in shape despite undergoing sintering (Fig. 4F). Shards in both types of laminations show evidence of sintering, where complete sintering has

occurred, shards can only be distinguished by halos of nanolites (Fig. 4F). Rare microlites are observed within ash shards (Fig. 4F).

#### **4.4 Host-V1 Interface**

At the side boundary of V1 there is extensive evidence for the contorted and irregularly shaped host bubbles being partially to completely filled with sintered ash shards (5-50  $\mu\text{m}$  in size) (Fig. 5A-D). Bubbles not immediately connected to those at the boundary (<500  $\mu\text{m}$  away) are sometimes filled with shards (Fig. 5E), whilst others only show a degree of compaction much like those found in more distal parts of the host (Fig. 5E-F). Matrix material has infilled bubbles following their overall alignment resulting in a ragged appearance to the vein edge (Fig. 5B). Small injection style veins into bubbles not along the same alignment are observed (Fig. 5F). In places ash has infilled parallel bubbles resulting in the host material between bubbles becoming isolated when viewed in 2D (Fig. 5G). Bubble (or vein) walls are rarely straight in appearance but often have a rounded morphology representing their pre-fracture shape (Fig. 5H) or are compacted around matrix material in the vein (Fig. 5I-J). Collapsed bubble trails are made apparent by nanolite chains (Fig. 5I). The same nanolites can be found between matrix shards (Fig. 5J). The top boundary of V1 with the host shows a lesser degree of interaction of between bubbles and matrix ash. The vein wall is largely parallel, ash matrix can be found infilling small open voids in places (e.g. Fig. 3C).

#### **4.5 V2-Host Interface**

The V2-Host interface is largely parallel throughout the sample with minimal host entrainment (Fig. 1, Fig. 4). Where there is a step feature (e.g. Fig. 6) there is generally a greater degree of interaction between host vesicles and matrix shards. Shards can be found in vesicles <150  $\mu\text{m}$  from the interface (Fig. 6B). The edges of the host melt that would have previously been bubbles walls are sharp and angular (Fig. 6B). At the base of the step feature large angular clasts of host and transported tuffisite form a layer of poorly sorted and sintered clasts, some of these clasts are lodged in open vesicles (Fig. 6C). Vesicles near these features show a high degree of compaction, nanolite chains are found extending from pinching out bubbles (Fig. 6D) near the vein-host boundary.

#### **4.6 Failed Fractures and Injection veins**

Within the host, angular and irregular-shaped clasts can be observed in zones of higher porosity (e.g. Fig. 7). The clearest of these clast-filled fracture features extend from the tuffisite vein (V1 and V2). Although they are difficult to distinguish in photomicrographs, (Fig. 7A) they are clearer in BSE images because of their differing porosity to both the host and main vein material (Fig. 7B, G). Clast edges are also easier to define in BSE images. Clasts, where vesicular, have similar internal bubble textures to those found in the host material (Fig. 7H). In addition, sintered ash material can be found in host void spaces neighbouring the vein (Fig. 7C). Voids are partially filled with sintered and rounded (<10  $\mu\text{m}$ -sized) shards; angular non-sintered <5  $\mu\text{m}$ -sized shards; and larger angular clasts of host material (Fig. 7D-E). Broken bubbles walls can be found jutting into the void space (yellow arrows, Fig. 7D). Ash material is sintered both onto larger angular shards and the walls of the void space (Fig. 7E-F). Fractures

cut through some shards and bubbles resulting in a jigsaw-style fit of material either side of the crack (e.g. Fig. 7F).

#### **4.7 Element Maps**

Element (EDS) mapping of the host, sintered, and angular vein material indicate the composition of the host does not vary on either side of collapsed bubble textures (Fig. 8, Fig. S.1). Sintered vein shards and host are similar in composition despite the subtle greyscale variations in BSE images between the two. The darker greyscale rinds and sintered ash are lower in Fe, Mg and Ca but none of the other elements analysed appear elevated (Fig. 8). Neither Na nor K show any variation between host and vein material. These results are comparable to Paisley et al. (in prep) who show that the vein and host have similar concentrations for a wide-range of elements with the exceptions being Tl and Pb depletion in the vein, which they suggested was caused by gas fluxing. Elevated Fe, Mg and Ca indicate the presence of orthopyroxene nanolite crystals (Fig. S.2). Plagioclase (high Na, Ca and Al), clinopyroxene (Ca, Mg) and oxides (Fe, Ti) microlites and phenocrysts can be more easily distinguished in the EDS maps than in BSE maps, particularly the broken crystal fragments in vein material (Fig. 8, Fig. S.1). Diffuse halos of lower Al are observed around some plagioclase microlites. Angular ash shards in void spaces have anomalously high Ca, Mg, Na and in rare cases Si (Fig. 8).

### **5. Discussion**



## 5.1 Discerning between syn-eruptive and post-eruptive textural features

Distinguishing fractures formed syn-eruptively (e.g. tuffisites), post-ejection (e.g. expansion/quench fractures due to inflation/cooling) and those added later during sample preparation (e.g. during sample cutting or resin impregnation) is not always straightforward. Examples of sample preparation fractures in this sample are sub-micron wide cracks with sharp edges and a jigsaw-like fit between opposing sides. The presence long cracks is seemingly random throughout the sample, supportive of a sample preparation origin (Figs. 2D, 2F, 3G). Furthermore, smaller cracks are common in areas that are structurally weaker, such as the edges of thin bubble walls or through isolated sintered particles that can be easily broken during preparation (e.g. Fig.7D, 7F). The lack of evidence for post-fragmentation inflation (e.g. breadcrusting) or shrinking (e.g. cooling cracks) in this small hand sample, or ductile morphologies of these cracks, is further evidence for a sample preparation origin of these features.

Apart from these small fractures, other features that could be the result of sample preparation are small angular shards observed in void spaces. These shards are not sintered to themselves or bubbles walls. They are most common in predominantly large, irregularly-shaped and isolated bubbles or in zones of large neighbouring bubbles that are connected in 3D (Fig. 2D, 2G, 7C-F). Figure 2D shows how some bubbles are completely filled whilst others only have ash in concave or sheltered parts of their void spaces with central, empty circular voids. This material could represent primary, syn-eruptive movement of ash particles by a gas phase through a connected void space in the host (Owen et al., 2019). Indeed their non-random deposition would support this assumption. However, we interpret this to be a secondary,

post-eruptive artefact in our sample for several reasons. Firstly, larger ash shards within the same void spaces show rounding and sintering, implying they spent sufficient time above the glass transition temperature ( $T_g$ ) for surface tension driven relaxation and rounding. Given the angular ash shards we observe are smaller than these, they too should be rounded had they been deposited during a similar period. Only if their depositional event occurred later in the life cycle of the sample and below  $T_g$  can their angular texture be preserved. Secondly, the organised distribution of particles can be explained by exposed IBFs creating weaker areas more prone to sample preparation failure. Figures 7D and 7F highlight how IBFs intrude into large coalesced bubble spaces and can be easily broken at their edges. In smaller bubble voids these IBFs are not present and thus there are fewer sources of glass that can be broken to generate ash shards, hence why shards are more common in larger void spaces. The empty, circular void spaces observed are bubbles within the epoxy resin where the sample has not been fully filled. Thirdly, we observe small angular material within cracks formed during sample preparation, thus the ash shards must have formed concurrently with crack formation and not before. In EDS maps these shards appear to have particularly anomalous Na, Ca and Mg (Fig. 8), which we argue are edge effects related to the depth of penetration of the electrons vs. the small size of these shards (Kanaya and Okayama, 1972). Thus we argue that both small fractures and angular shards are not syn-eruptive features but represent unavoidable sample preparation issues common with fragile, vesicular samples.

## **5.2 Pre-existing porous network**

Contrary to the vesicles filled with angular shards, vesicles infilled with sintered ash shards at the host-vein interfaces imply the host was vesicular prior to fracturing and tuffisite formation.

Previous work has largely focused on tuffisites in dense host domains (e.g. Castro et al., 2012b; Berlo et al., 2013; Kendrick et al., 2016; Saubin et al., 2016). Complex sinuous bubble textures, bending of bubble walls, and pinching out of bubbles point to coalescence and partial collapse of the vesicular melt. There is also ample evidence of multiple phases of fracturing and sintering within the host too, such as rounding of material lodged within large bubbles and sintering of touching bubble walls (e.g. Fig. 2D, F, I). Furthermore, there is evidence for zones of large, uneven shaped clasts sitting in zones of higher porosity (Fig. 7A-B, G). The internal textures of these clasts match the general textures of the host (Fig. 7G-H). These clasts resulted from localised fragmentation of the vesicular melt but there was no long-range transportation of clasts (greater than mm-scale in this case), which instead remain in situ and sinter back together (e.g. Fig. 2D-E). It is likely that many fragmentation events are not preserved in areas that have undergone significant sintering and healing, with only sinuous void space remaining.

There is a difficulty in defining the original degree of vesicularity of the host prior to V1 propagation, in particular the degree to which pore spaces were connected. Magmatic foams are considered to have >74 vol. % bubbles whilst a sub-critical foam is defined as having thicker bubble walls that largely prevent coalescence (Proussevitch et al., 1993; Cashman and Mangan, 1994). The host's preserved porosity is significantly lower at <40 % and even bubbles distal from the vein are contorted so there is no preservation of rounded bubbles that would be indicative of a primary texture. Castro et al., (2012a) found that IBFs >8  $\mu\text{m}$  across did not show deformation (dimpling). Many IBFs observed in this host are >8  $\mu\text{m}$  and show evidence of both brittle and viscous deformation. Fractured and broken IBFs in large void spaces (e.g. Fig. 2G) suggest voids became connected or coalesced via fracturing of bubble walls, not only via IBF stretching described by Castro et al., (2012a). The alignment of voids within the host (above the tuffisite vein, e.g. Fig. 2E) was a pre-existing texture as vein material infills into the

host along this configuration (Fig. 4B). Shearing would aid in the deformation and coalescence of bubbles accounting for the elongated, aligned and large bubbles observed in the host (Okumura et al., 2008; Burgisser and Degruyter, 2015). However, this shearing is only preserved in the dense zone above the tuffisite vein, further away the alignment is lost (Fig. 2I) suggesting that the shearing was localised. The bubble alignment corresponding to the V2-host interface is discussed separately in Section 5.4. The sample did not undergo post-ejection vesiculation, as evidenced by the lack of rounded bubbles in both the dense and vesicular parts of the host. Thus the dense zone of melt either side of the vein is dense due to pre-eruption degassing and compaction and not a lack of vesiculating upon ejection.

Prior to tuffisite formation the host was a vesicular, sheared melt, or sub-critical foam, that had undergone cycles of fragmentation, sintering and suturing of clasts back together, akin to pyroclasts found in erupted tephra (Gardner et al., 2017). Shear deformation of the magma, combined with breaking of the bubble walls, enhances the connectivity and permeability of this pre-existing porous network (Okumura et al., 2009). These processes continued after vein formation in addition to compaction so, although we argue the host had a high degree of connectivity of its pore space prior to vein formation, we cannot accurately quantify it. The preserved porosity in the host is thus a minimum estimate of the porosity prior to tuffisite formation and bubble compaction.

The onset of permeability via viscous processes (shear-enhanced bubble coalescence similar to that described above) occurred in the upper 1-1.5 km of the conduit (Schipper et al., 2013). In addition, extensive fracturing and fragmentation occurred within the conduit plug (Whattam, 2018; Paisley et al., in prep.). This sample preserves evidence of both processes and we argue

the small bomb represents a particularly vesicular, but ultimately brecciated and sintered part of the conduit plug. However, this sample is analogous to a highly vesicular melt ascending within the conduit below a volcanic plug and thus can provide great insights into the interaction of fractures with vesicular melts and a combined brittle-ductile degassing of magma at depth.

### **5.3 Fracturing of vesicular melts, tuffisite sources, and timescale estimates**

#### **Evidence of Fracturing**

Figure 4 shows how the pre-existing porous network is exploited by fracturing (associated with V1 formation). Gas and ash shards are injected into void spaces that have lower gas pressures than incoming over-pressured gas from depth, the connected porosity allows for a reduction in the overpressure of the system and therefore simultaneously reduces fragmentation of the localised pre-existing textures and attenuates the pressure wave propagating through the melt (Richard et al., 2013). Fracturing must have occurred between bubble walls in places to allow for the continued propagation of material through the pore network, this is best recorded by the host clasts that become isolated as a result of fragmentation (e.g. Figs. 3C, 4C, 5C, 5G, 7E). Clasts within the vein have uneven edges, both ragged and rounded. The rounded sides are the pre-existing bubble walls whilst the angular sides represent where brittle fragmentation occurred between two neighbouring void spaces. Material intrudes furthest along the alignment of the bubbles, pore space off this alignment can be partially filled with ash but there is no progressive fracturing to continue infilling along that orientation (Fig. 5F). We also note reservoir zones of sintered tuffisite material, defined by Tuffen and Dingwell, (2005), where void space off-shooting from the central vein is filled with ash. These zones are not associated

with the overall alignment of bubbles but are related to V1's propagation through the host and deposition of its clastic material (Fig. 7C-F).

In summary, the vein is not a simple tuffisite but comprised of two clear overlapping sub-veins, the second of which has alternating fine-grained and coarse-grained laminations and overprints the first (e.g. Fig. 1). These textures are evidence that at least one later period of fracturing occurred, forming V2. The fracture underwent transient pressure gradients resulting in the sorting and deposition of matrix ash (Tuffen and Dingwell, 2005). Step features in the vein (Fig. 6) where wide bands of melt between bubble walls are broken through at the host-vein interface suggest this secondary fracturing event was of higher energy, supported by the smaller grain size of the matrix in V2 (Zimanowski et al., 2003) (see Section 5.4).

The porosity of V1 is <20 % and the vein has not undergone complete sintering or compaction relative to the neighbouring host melt that has a porosity of <10 % and has compacted, narrow bubbles. To determine whether the host or V1 would fracture first based on their strength properties, we use the pore-emanating crack model to estimate the unconfined compressive strength ( $\sigma_n$ ) required to fracture each material:

$$\sigma_n = \frac{1.325 K_{IC}}{\Phi^{0.414} \sqrt{\pi a}} \quad (1)$$

where  $\Phi$  is porosity (as a fraction between 0 and 1);  $K_{IC}$  is a critical stress intensity factor and is  $\sim 0.66$  for silicate glasses (Yu et al., 2015); and  $a$  is an estimated pore radius (m) (Zhu et al., 2010). Host material near the vein has an  $\Phi \sim 0.1$  and  $a \sim 25 \mu\text{m}$ , whilst V1 has a  $\Phi \sim 0.15$  and  $a \sim 25 \mu\text{m}$  and therefore a higher compressive strength is required to fracture the host (251 MPa vs. 196 MPa). V1 thus provides a structurally weaker zone that would be easier to fracture. As

tuffisites are often hydro-fractures (Heiken et al., 1988) their failure is in tension, even under compressive regimes, which would require lower overpressures for failure (e.g. Rutter, 1986; Lavallée et al., 2013). The major caveat of this estimation being the host and vein likely underwent further compaction post V2 emplacement, so it is difficult to estimate their previous porosity and pore radii at the time V2 propagated through. Thus, these estimates are conservative but provide quantitative insight into why fracturing occurred through V1. It is not possible to say whether V2 intruded V1 at its edge or through a particular weak zone in the middle of the vein, as much of V1 has been overprinted by V2.

### **Source material for tuffisite clasts and matrices**

Tuffisites have two main sources of their clastic and matrix material, both are linked to fracturing (Saubin et al., 2016; Owen et al., 2019, Paisley et al., in prep.). The first source, particularly for these sub-veins, is local. This includes fracturing and isolation of large areas of host melt to form angular clasts, which preserve bubble and microlite textures from the host. The same observations were made by Saubin et al. (2016) who note dense obsidian host material accounts for ~35% of clasts in a large tuffisite vein found at Chaitén. We argue that much of the matrix material is also local because at vein edges it is apparent how even smaller clasts and matrix material look similar texturally to the host, particularly in photomicrographs (Fig. 3), as well as being compositionally similar (Fig. 8). In experiments by Okumura et al. (2010) ash shards <50  $\mu\text{m}$  in size were formed during brittle deformation of vesicular melts. Much of the matrix material in these veins is <<50  $\mu\text{m}$  and is likely formed by the fracturing of the bubble melt walls as the vesicular host is broken apart by the intruding and overprinting vein. This material is carried through the fracture by gases, becoming a distal source if vein connectivity is on the order of hundreds of metres (e.g. Cloos, 1941; Castro et al., 2014; Saubin

et al., 2016). An alternative local source specific to V2 would be vein material from V1. The re-fracturing of the vein would have resulted in a degree of recycling of material by V2, particularly at the boundary in the finer-grained laminations as material present was fragmented during fracture propagation. Rare clasts of host material found in V2 highlight that it too sourced from the local melt.

The second source of tuffisite material is more distal as clasts are transported through fractures. Texturally complex clasts that preserve sintered ash and dense banding cannot be locally sourced given they are distinct from the host. Instead they preserve old fracturing events, deeper in the conduit, which underwent healing and subsequent fracturing. Transport through the vein juxtaposed them against the vesicular melt host. Clast textures and bubble distributions have been used to assess the connectivity of tuffisite veins (Saubin et al., 2016). Chemically our tuffisite material is compositionally similar to the host (Fig. 8, Paisley et al., in prep), however other studies show how chemically distinct country rock and old dome material can be found within veins indicating fracturing is not confined to the conduit (Saubin et al., 2016; Owen et al., 2019, Paisley et al., in review).

### **Timescale estimates of processes**

Rounding and sintering of matrix shards indicate they were exposed to temperatures above the glass transition temperature ( $T_g$ ) for a period of time subsequent to fracturing. Both their shape and degree of sintering can be used to obtain first-order estimates of healing timescales of each of the sub-veins. Ash shards would have been angular prior to healing and thus calculated timescales must account for both shard rounding and subsequent sintering. We use the characteristic timescale of bubble relaxation ( $\lambda_b$ ), i.e. rounding, from Gardner et al. (2017) to



estimate the timescale of shard relaxation, as the equation can be used a proxy for clast rounding (Owen et al., 2019).

$$\lambda_b = \frac{\eta R}{\sigma} \quad (2)$$

where  $\eta$  is melt viscosity (Pas),  $R$  is particle radius (m) and  $\sigma$  is surface tension ( $\text{Nm}^{-1}$ ). The sintering timescale ( $\tau_s$ ) is described by a similar equation:

$$\tau_s = \frac{R\eta}{\gamma} \quad (3)$$

where  $\gamma$  is the melt-vapour interfacial tension ( $\text{Nm}^{-1}$ ) (Vasseur et al., 2013). A value of  $0.3 \text{ Nm}^{-1}$  is used for both  $\sigma$  and  $\gamma$ , a common estimate for a dry silicic melt (e.g. Gardner and Denis, 2004; Sumner et al., 2005). We use the model of Giordano et al. (2008) to estimate the Cordón Caulle melt viscosity at the eruptive temperature of  $900 \text{ }^\circ\text{C}$  (assumed to be constant) with the bulk chemical composition described by Castro et al. (2013). Melt viscosity is strongly dependent on water concentration and the preserved water concentrations in the erupted products at Cordón Caulle are  $<0.35 \text{ wt. \% H}_2\text{O}$  (Schipper et al., 2013; Castro et al., 2014). Thus, we model melt viscosity ( $\sim 10^{6.5} - 10^{7.5} \text{ Pas}$ ) over a small range of water concentrations (0.1-0.5 wt. %) to estimate timescales of healing of partially to fully degassed melts in the shallow conduit plug. Given the similarities between equations (2) and (3), calculated timescales of particle rounding and sintering, and how they vary with particle radius, are the same and are summarised in Figure 9. First-order estimates for the timescales of healing, i.e. the rounding of particles and subsequent loss of pore space via sintering, are then double the length of time of the processes summarised in Figure 9. We assume that healing time begins after the sample crosses above  $T_g$  and ends with the quenching of the sample. We further assume that compaction timescales are not influenced by changing stresses or gas pressure during sintering.

Fine-grained laminations ( $R < 15 \mu\text{m}$ ) in V2 are fully healed, whilst coarse-grained laminations ( $R < 25 \mu\text{m}$ ) have sub-rounded shards and residual porosity (Fig. 4E). Timescales of healing must be between  $\sim 20$  and  $\sim 32$  minutes (assuming  $\sim 0.25$  wt. %  $\text{H}_2\text{O}$ ) to account for the complete healing of certain laminations but not others (Fig. 9). Clasts in V1 ( $R > 50 \mu\text{m}$ ) are still highly angular suggesting this vein underwent  $< 1$  hour of total healing (including healing time that would occur in parallel with V2). Therefore, the intervening time between V1 and V2 emplacement could not have been more than tens of minutes. These timescale estimates also highlight why large clasts preserve their uneven shapes, as clasts  $> 200 \mu\text{m}$  across require hours of time to round given the low water concentrations (Fig. 9). Healing timescales are comparable to degassing timescales recorded by trace element variation in samples from the same eruption (Paisley et al., in prep.).

#### **5.4 Evidence for gas fluxing**

Tuffisite veins at many volcanic centres texturally and chemically preserve evidence of gas fluxing through their permeable pathways (e.g. Tuffen et al., 2003; Stasiuk et al., 1996; Berlo et al., 2013; Castro et al., 2014). We have evidence in our sample for multiple stages of degassing that we summarise in Figure 10. Stage One is the shearing and fragmentation of a vesicular melt forming a complex but connected network of pore spaces. Stage Two is fracture propagation that results in V1. The pre-existing porous network is exploited but no significant evidence of shearing is found. The transport of distally sourced clasts, which preserve relic fracturing events, is evidence for extensive gas transport through this vein. Compaction of the host around clasts intruded into bubbles at the vein edge is evidence of some degree of

degassing during this stage. Healing and sintering of material in V1 occurred but was not sufficient in length (10s of minutes) to reduce the porosity of V1 to below that of the compacting host and, because it is weaker, V1 is re-fractured during Stage Three and V2 is formed. The alternating laminations of fine- and coarse-grained material are evidence of the fluidised flow through this pathway (Tuffen and Dingwell, 2005). There is extensive evidence for compaction solely related to V2 emplacement and degassing. A crystal at the interface of V2 and the host (Fig. 7A) acts as a compaction indicator and records no evidence of shear (e.g. pressure shadows) but does show compaction of the surrounding melt. This is supported by the parallel bubble orientations with respect to the V2-host interface (Fig. 2B). Vesicles align with V2's orientation through the sample and not with the pre-existing orientation preserved at the V1-host interface. Alignment of microlites with the vein is further evidence for this compaction. The densified zone is ~2 cm wide but the compaction of bubbles extends far beyond into the distal vesicular zone <4 cm away. The width of this zone of compaction far exceeds any diffusively degassed boundary at tuffisites and fractures discussed in the literature where fractures are preserved in dense glasses (<500  $\mu\text{m}$ -wide, Cabrera et al., 2011; Castro et al., 2012b; Berlo et al., 2013) and is evidence this vein depressurised and extracted gas from the porous and connected network over a significant scale. Although it is hard to distinguish how much compaction this melt had undergone prior to V2, the change in the alignment of bubbles, even distally, would suggest that most compaction was related to the V2 formation and subsequent degassing. Stage Four is elemental exchange that occurred concurrently with sintering. The differing greyscale values in BSE images of small matrix ash shards and bubble walls across much of the host (Fig. 8) implies the exchange was concurrent with a time when gases were fluxing through, depositing shards, and exchanging volatiles with bubble walls (host) and transported shards. Otherwise only bubble walls or shards would have differing greyscale values, not both. McIntosh et al. (2014) show how  $\text{H}_2\text{O}$  resorption around bubbles

can be noted by differing BSE values. However, they observe a subtle gradation into the far-field greyscale values whilst our zones are more defined rinds depleted in Mg, Ca and Fe (Fig. 8). Nanolites are present between shards and in zones of pinched out bubbles where sintering has occurred, and thus we argue it is a concurrent process with sintering and gas fluxing. Either elemental diffusion of these elements towards void-melt interfaces results in the nucleation or growth of these Mg-Fe-Ca-rich orthopyroxene crystals at gas-melt interfaces, or they are forming as precipitates from the gas phase as seen in high-temperature fumaroles (e.g. Wahrenberger, 2002). Indeed, these nanolites are widely observed in banded obsidian and brecciated volcanic bombs from this eruption that preserve old gas-fluxing pathways that have since healed (Whattam, 2018; Paisley et al., in prep). A degree of hydration may have occurred at a late stage to contribute to the changing greyscale values but low water concentrations in samples from this eruption and the small width of the rinds prevent us in quantifying this process. Hydration would reduce melt viscosity and reduce the welding and compaction timescale, thus eliminating porosity in the vein.

In summary, we show how tuffisites are capable of degassing highly porous networks by exploiting void spaces and occasionally fracturing between voids. Breaking of bubble walls in foams would lead to rapid outgassing (von Aulock et al., 2017). The extraction of gas and resultant loss of pressure results in compaction of the host material around the vein.

## **6. Conclusions**

Tuffisites have long been shown to be efficient outgassing pathways and contribute to the changing eruptive behaviours observed at silicic centres as eruptions progress (e.g. Castro et

al., 2012b; Berlo et al., 2013). We show that the interaction of fracture and porous networks can result in degassing and compaction of a vesicular melt. Fractures exploit and propagate through pre-existing porous networks and, in the process, generate fine-grained ash and larger clasts that constitute the textural make-up of many types of tuffisites. The re-fracturing of the tuffisite vein highlights how previously propagated veins provide a rheologically weaker zone of material that can be re-exploited. The compaction of a vesicular melt on a cm-scale highlights how tuffisites can extract gas over a long-range when they interact with an already connected pore-space network. This study addresses the fundamental question of where tuffisites source their gases from and reinforces the notion that gas extraction from deeper vesicular and permeable melts, via fracturing, can be key to diffusing explosive behaviour.

## **7. Acknowledgements**

We thank Alex Corgne, Nicolas Vergara Pontigo and Felipe Ignacio P. Gallardo for assistance in the field. RP thanks Ian Schipper for assistance to collect BSE images with the electron microprobe at the Victoria University of Wellington, Wellington, New Zealand. Further thanks to Lang Shi for instrument assistance and Kyle Henderson and Shane Rooyakkers for technical support at McGill. RP was supported by travel and research grants from the Mineralogical Association of Canada, the Geological Society of America, McGill University and the Society of Economic Geologists. This work is supported by an NSERC Discovery Grant to KB. SK acknowledges financial support from a H2020 Marie Skłodowska-Curie fellowship DYNAVOLC – No.795044. JO is the beneficiary of a post-doctoral grant from the AXA Research Fund. HT is supported by a Royal Society University Research Fellowship and thanks Sports Centre and Grounds Staff at Lancaster University for assistance.



## 8. References

- Berlo, K., Tuffen, H., Smith, V., Castro, J.M., Pyle, D.M., Mather, T.A., Geraki, K., 2013. Element variations in rhyolitic magma resulting from gas transport. *Geochim. Cosmochim. Acta* 121, 436–451. <https://doi.org/10.1016/j.gca.2013.07.032>
- Burgisser, A., Degruyter, W., 2015. Magma Ascent and Degassing at Shallow Levels, in: *The Encyclopedia of Volcanoes*. Elsevier, pp. 225–236. <https://doi.org/10.1016/B978-0-12-385938-9.00011-0>
- Cabrera, A., Weinberg, R.F., Wright, H.M.N., 2015. Magma fracturing and degassing associated with obsidian formation: The explosive–effusive transition. *J. Volcanol. Geotherm. Res.* 298, 71–84. <https://doi.org/10.1016/j.jvolgeores.2014.12.014>
- Cabrera, A., Weinberg, R.F., Wright, H.M.N., Zlotnik, S., Cas, R.A.F., 2011. Melt fracturing and healing: A mechanism for degassing and origin of silicic obsidian. *Geology* 39, 67–70. <https://doi.org/10.1130/G31355.1>
- Cashman, K.V., Mangan, M.T., 1994. Physical aspects of magmatic degassing; II, Constraints on vesiculation processes from textural studies of eruptive products. *Rev. Mineral. Geochem.* 30, 447–478.
- Castro, J.M., Bindeman, I.N., Tuffen, H., Ian Schipper, C., 2014. Explosive origin of silicic lava: Textural and  $\delta D-H_2O$  evidence for pyroclastic degassing during rhyolite effusion. *Earth Planet. Sci. Lett.* 405, 52–61. <https://doi.org/10.1016/j.epsl.2014.08.012>
- Castro, J.M., Burgisser, A., Schipper, C.I., Mancini, S., 2012a. Mechanisms of bubble coalescence in silicic magmas. *Bull. Volcanol.* 74, 2339–2352. <https://doi.org/10.1007/s00445-012-0666-1>

- Castro, J.M., Cordonnier, B., Schipper, C.I., Tuffen, H., Baumann, T.S., Feisel, Y., 2016. Rapid laccolith intrusion driven by explosive volcanic eruption. *Nat. Commun.* 7, 13585. <https://doi.org/10.1038/ncomms13585>
- Castro, J.M., Cordonnier, B., Tuffen, H., Tobin, M.J., Puskar, L., Martin, M.C., Bechtel, H.A., 2012b. The role of melt-fracture degassing in defusing explosive rhyolite eruptions at volcán Chaitén. *Earth Planet. Sci. Lett.* 333–334, 63–69. <https://doi.org/10.1016/j.epsl.2012.04.024>
- Castro, J.M., Schipper, C.I., Mueller, S.P., Militzer, A.S., Amigo, A., Parejas, C.S., Jacob, D., 2013. Storage and eruption of near-liquidus rhyolite magma at Cordón Caulle, Chile. *Bull. Volcanol.* 75:702. <https://doi.org/10.1007/s00445-013-0702-9>
- Cloos, H., 1941. Bau und Tätigkeit von Tuffschloten: Untersuchungen an dem Schwäbischen Vulkan. *Geol. Rundsch.* 32, 709–800. <https://doi.org/10.1007/BF01801913>
- Edmonds, M., 2008. New Geochemical Insights into Volcanic Degassing. *Philos. Trans. Math. Phys. Eng. Sci.* 366, 4559–4579.
- Eichelberger, J.C., Carrigan, C.R., Westrich, H.R., Price, R.H., 1986. Non-explosive silicic volcanism. *Nature* 323, 598–602. <https://doi.org/10.1038/323598a0>
- Farquharson, J.I., Heap, M.J., Lavallée, Y., Varley, N.R., Baud, P., 2016. Evidence for the development of permeability anisotropy in lava domes and volcanic conduits. *J. Volcanol. Geotherm. Res.* 323, 163–185. <https://doi.org/10.1016/j.jvolgeores.2016.05.007>
- Gardner, J.E., Denis, M.-H., 2004. Heterogeneous bubble nucleation on Fe-Ti oxide crystals in high-silica rhyolitic melts. *Geochim. Cosmochim. Acta* 68, 3587–3597. <https://doi.org/10.1016/j.gca.2004.02.021>



- Gardner, J.E., Llewellyn, E.W., Watkins, J.M., Befus, K.S., 2017. Formation of obsidian pyroclasts by sintering of ash particles in the volcanic conduit. *Earth Planet. Sci. Lett.* 459, 252–263. <https://doi.org/10.1016/j.epsl.2016.11.037>
- Gerlach, D.C., Frey, F.A., Moreno, H., 1988. Recent Volcanism in the Puyehue-Cordon Caulle Region, Southern Andes, Chile (40.5°S): Petrogenesis of Evolved Lavas. *J. Petrol.* 29, 333–382.
- Giordano, D., Russell, J.K., Dingwell, D.B., 2008. Viscosity of magmatic liquids: A model. *Earth Planet. Sci. Lett.* 271, 123–134. <https://doi.org/10.1016/j.epsl.2008.03.038>
- Gonnermann, H.M., Manga, M., 2003. Explosive volcanism may not be an inevitable consequence of magma fragmentation. *Nature* 426, 432–435. <https://doi.org/10.1038/nature02138>
- Heap, M.J., Farquharson, J.I., Wadsworth, F.B., Kolzenburg, S., Russell, J.K., 2015. Timescales for permeability reduction and strength recovery in densifying magma. *Earth Planet. Sci. Lett.* 429, 223–233. <https://doi.org/10.1016/j.epsl.2015.07.053>
- Heiken, G., Wohletz, K., Eichelberger, J., 1988. Fracture fillings and intrusive pyroclasts, Inyo Domes, California. *J. Geophys. Res. Solid Earth* 93, 4335–4350. <https://doi.org/10.1029/JB093iB05p04335>
- Jay, J., Costa, F., Pritchard, M., Lara, L., Singer, B., Herrin, J., 2014. Locating magma reservoirs using InSAR and petrology before and during the 2011–2012 Cordón Caulle silicic eruption. *Earth Planet. Sci. Lett.* 395, 254–266. <https://doi.org/10.1016/j.epsl.2014.03.046>
- Kanaya, K., Okayama, S., 1972. Penetration and energy-loss theory of electrons in solid targets. *J. Phys. Appl. Phys.* 5, 43–58. <https://doi.org/10.1088/0022-3727/5/1/308>

- Kendrick, J.E., Lavallée, Y., Varley, N.R., Wadsworth, F.B., Lamb, O.D., Vasseur, J., 2016. Blowing Off Steam: Tuffisite Formation As a Regulator for Lava Dome Eruptions. *Front. Earth Sci.* 4:41. <https://doi.org/10.3389/feart.2016.00041>
- Kolzenburg, S., Heap, M.J., Lavallée, Y., Russell, J.K., Meredith, P.G., Dingwell, D.B., 2012. Strength and permeability recovery of tuffisite-bearing andesite. *Solid Earth* 3, 191–198. <https://doi.org/10.5194/se-3-191-2012>
- Lavallée, Y., Benson, P.M., Heap, M.J., Hess, K.-U., Flaws, A., Schillinger, B., Meredith, P.G., Dingwell, D.B., 2013. Reconstructing magma failure and the degassing network of dome-building eruptions. *Geology* 41, 515–518. <https://doi.org/10.1130/G33948.1>
- McIntosh, I.M., Llewellyn, E.W., Humphreys, M.C.S., Nichols, A.R.L., Burgisser, A., Schipper, C.I., Larsen, J.F., 2014. Distribution of dissolved water in magmatic glass records growth and resorption of bubbles. *Earth Planet. Sci. Lett.* 401, 1–11. <https://doi.org/10.1016/j.epsl.2014.05.037>
- Mujin, M., Nakamura, M., Miyake, A., 2017. Eruption style and crystal size distributions: Crystallization of groundmass nanolites in the 2011 Shinmoedake eruption. *Am. Mineral.* 102, 2367–2380. <https://doi.org/10.2138/am-2017-6052CCBYNCND>
- Okumura, S., Nakamura, M., Nakano, T., Uesugi, K., Tsuchiyama, A., 2010. Shear deformation experiments on vesicular rhyolite: Implications for brittle fracturing, degassing, and compaction of magmas in volcanic conduits. *J. Geophys. Res.* 115, B06201. <https://doi.org/10.1029/2009JB006904>
- Okumura, S., Nakamura, M., Takeuchi, S., Tsuchiyama, A., Nakano, T., Uesugi, K., 2009. Magma deformation may induce non-explosive volcanism via degassing through bubble networks. *Earth Planet. Sci. Lett.* 281, 267–274. <https://doi.org/10.1016/j.epsl.2009.02.036>

- Okumura, S., Nakamura, M., Tsuchiyama, A., Nakano, T., Uesugi, K., 2008. Evolution of bubble microstructure in sheared rhyolite: Formation of a channel-like bubble network. *J. Geophys. Res. Solid Earth* 113, B07208. <https://doi.org/10.1029/2007JB005362>
- Owen, J., Shea, T., Tuffen, H., 2019. Basalt, Unveiling Fluid-filled Fractures, Inducing Sediment Intra-void Transport, Ephemeral: Examples from Katla 1918. *J. Volcanol. Geotherm. Res.* 369, 121–144. <https://doi.org/10.1016/j.jvolgeores.2018.11.002>
- Pallister, J.S., Diefenbach, A.K., Burton, W.C., Muñoz, J., Griswold, J.P., Lara, L.E., Lowenstern, J.B., Valenzuela, C.E., 2013. The Chaitén rhyolite lava dome: Eruption sequence, lava dome volumes, rapid effusion rates and source of the rhyolite magma. *Andean Geol.* 40, 277–294. <https://doi.org/10.5027/andgeoV40n2-a06>
- Pistolesi, M., Cioni, R., Bonadonna, C., Elissondo, M., Baumann, V., Bertagnini, A., Chiari, L., Gonzales, R., Rosi, M., Francalanci, L., 2015. Complex dynamics of small-moderate volcanic events: the example of the 2011 rhyolitic Cordón Caulle eruption, Chile. *Bull. Volcanol.* 77:3. <https://doi.org/10.1007/s00445-014-0898-3>
- Plail, M., Edmonds, M., Humphreys, M.C.S., Barclay, J., Herd, R.A., 2014. Geochemical evidence for relict degassing pathways preserved in andesite. *Earth Planet. Sci. Lett.* 386, 21–33. <https://doi.org/10.1016/j.epsl.2013.10.044>
- Proussevitch, A.A., Sahagian, D.L., Kutolin, V.A., 1993. Stability of foams in silicate melts. *J. Volcanol. Geotherm. Res.* 59, 161–178. [https://doi.org/10.1016/0377-0273\(93\)90084-5](https://doi.org/10.1016/0377-0273(93)90084-5)
- Richard, D., Scheu, B., Mueller, S.P., Spieler, O., Dingwell, D.B., 2013. Outgassing: Influence on speed of magma fragmentation. *J. Geophys. Res. Solid Earth* 118, 862–877. <https://doi.org/10.1002/jgrb.50080>
- Rutter, E.H., 1986. On the nomenclature of mode of failure transitions in rocks. *Tectonophysics* 122, 381–387. [https://doi.org/10.1016/0040-1951\(86\)90153-8](https://doi.org/10.1016/0040-1951(86)90153-8)

- Saubin, E., Tuffen, H., Gurioli, L., Owen, J., Castro, J.M., Berlo, K., McGowan, E.M., Schipper, C.I., Wehbe, K., 2016. Conduit Dynamics in Transitional Rhyolitic Activity Recorded by Tuffisite Vein Textures from the 2008–2009 Chaitén Eruption. *Front. Earth Sci.* 4:59. <https://doi.org/10.3389/feart.2016.00059>
- Schipper, C.I., Castro, J.M., Tuffen, H., James, M.R., How, P., 2013. Shallow vent architecture during hybrid explosive–effusive activity at Cordón Caulle (Chile, 2011–12): Evidence from direct observations and pyroclast textures. *J. Volcanol. Geotherm. Res.* 262, 25–37. <https://doi.org/10.1016/j.jvolgeores.2013.06.005>
- Silva Parejas, C., Lara, L.E., Bertin, D., Amigo, A., Orozco, G., 2012. The 2011–2012 eruption of Cordón Caulle volcano (Southern Andes): Evolution, crisis management and current hazards, in: EGU2012-9382-2. Presented at the EGU General Assembly, Vienna, Austria.
- Sparks, R.S.J., 1978. The dynamics of bubble formation and growth in magmas: A review and analysis. *J. Volcanol. Geotherm. Res.* 3, 1–37. [https://doi.org/10.1016/0377-0273\(78\)90002-1](https://doi.org/10.1016/0377-0273(78)90002-1)
- Stasiuk, M.V., Barclay, J., Carroll, M.R., Jaupart, C., Ratté, J.C., Sparks, R.S.J., Tait, S.R., 1996. Degassing during magma ascent in the Mule Creek vent (USA). *Bull. Volcanol.* 58, 117–130. <https://doi.org/10.1007/s004450050130>
- Sumner, J.M., Blake, S., Matela, R.J., Wolff, J.A., 2005. Spatter. *J. Volcanol. Geotherm. Res.* 142, 49–65. <https://doi.org/10.1016/j.jvolgeores.2004.10.013>
- Tuffen, H., Dingwell, D., 2005. Fault textures in volcanic conduits: evidence for seismic trigger mechanisms during silicic eruptions. *Bull. Volcanol.* 67, 370–387. <https://doi.org/10.1007/s00445-004-0383-5>

- Tuffen, H., Dingwell, D.B., Pinkerton, H., 2003. Repeated fracture and healing of silicic magma generate flow banding and earthquakes? *Geology* 31, 1089–1092. <https://doi.org/10.1130/G19777.1>
- Tuffen, H., James, M.R., Castro, J.M., Schipper, C.I., 2013. Exceptional mobility of an advancing rhyolitic obsidian flow at Cordón Caulle volcano in Chile. *Nat. Commun.* 4, 2709. <https://doi.org/10.1038/ncomms3709>
- Vasseur, J., Wadsworth, F.B., Lavallée, Y., Hess, K.-U., Dingwell, D.B., 2013. Volcanic sintering: Timescales of viscous densification and strength recovery. *Geophys. Res. Lett.* 40, 5658–5664. <https://doi.org/10.1002/2013GL058105>
- von Aulock, F.W., Kennedy, B.M., Maksimenko, A., Wadsworth, F.B., Lavallée, Y., 2017. Outgassing from Open and Closed Magma Foams. *Front. Earth Sci.* 5:46. <https://doi.org/10.3389/feart.2017.00046>
- Wahrenberger, C., Seward, T.M., Dietrich, V., 2002. Volatile trace-element transport in high-temperature gases from Kudriavy volcano (Itrup, Kurile Islands, Russia), in: *The Water-Rock Interactions, Ore Deposits, and Environmental Geochemistry: A Tribute to David A. Crerar*, Geochemical Society, Special Publications. pp. 307–327.
- Whattam, J., 2018. Under the surface: Textural analysis of complex, multi-component Vulcanian bombs produced during the hybrid effusive-explosive phase of the 2011-2012 Cordón Caulle eruption, Chile (Thesis). Victoria University of Wellington.
- Yu, Y., Wang, B., Lee, Y.J., Bauchy, M., 2015. Fracture Toughness of Silicate Glasses: Insights from Molecular Dynamics Simulations. *MRS Online Proc. Libr. Arch.* 1757. <https://doi.org/10.1557/opl.2015.50>
- Zhu, W., Baud, P., Wong, T., 2010. Micromechanics of cataclastic pore collapse in limestone. *J. Geophys. Res. Solid Earth* 115, B04405. <https://doi.org/10.1029/2009JB006610>

Zimanowski, B., Wohletz, K., Dellino, P., Büttner, R., 2003. The volcanic ash problem. J. Volcanol. Geotherm. Res. 122, 1–5. [https://doi.org/10.1016/S0377-0273\(02\)00471-7](https://doi.org/10.1016/S0377-0273(02)00471-7)

## 9. Figures

Figure 1:

Tuffisite-hosting volcanic bomb. (A) Overview of hand specimen with two overlapping veins (V1 and V2) surrounded by a dense zone of glass (<2 cm-wide either side of the vein) within a vesicular host. Two thin sections (B) and (C) were prepared. (D) Summary of respective orientation and positions of thin sections within the hand specimen relative to the planar V2-Host interface (orange surface). V1 pinches out over hand specimen scale.

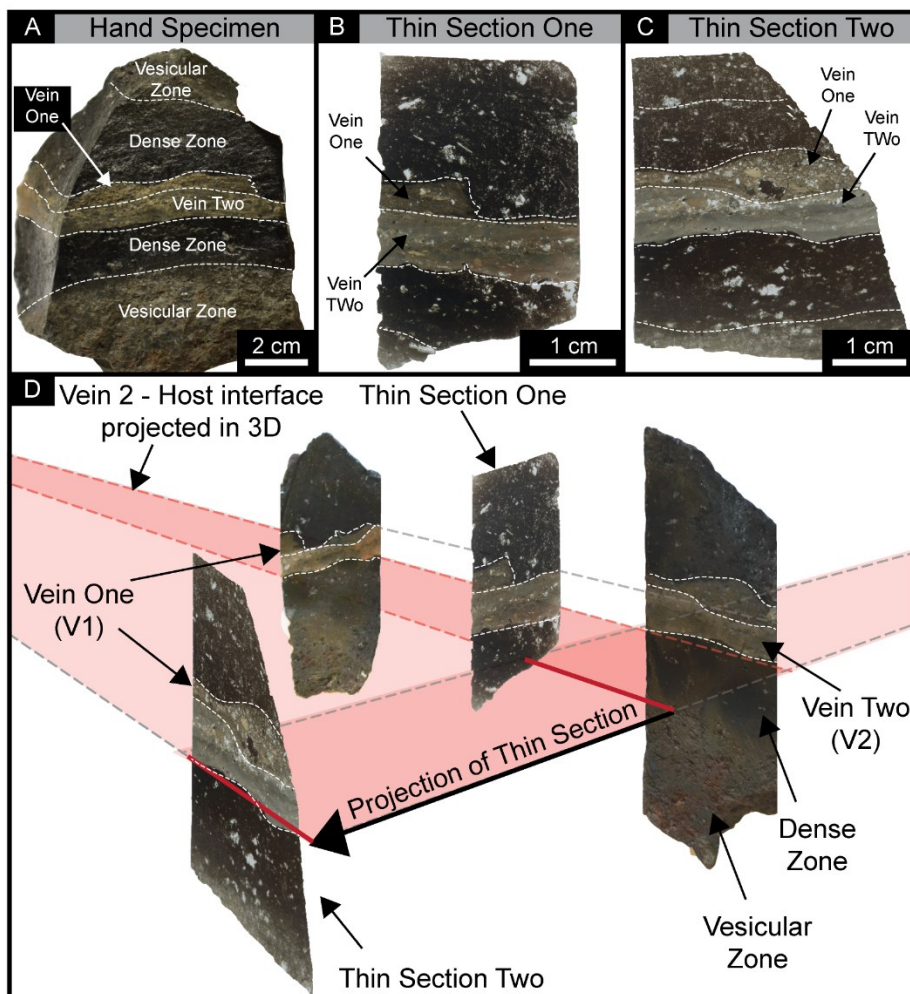


Figure 2:

Images of typical textures in host. Yellow arrows highlight textural features. White arrows indicate sample preparation fractures or particle-filled vesicles. (A) Overview of thin sections one (left) and two (right). (B) Collapsed and aligned bubbles typical in the distal host material below the vein. (C) Photomicrograph of strongly aligned microlites and minimal bubbles in dense host close to the vein. (D) Bubble aligned  $\sim 32^\circ$  to vein orientation close to, and above, vein. Evidence of pinching out and compaction of bubbles. (E) Pinched out and compacted bubbles have similar alignment to vein orientation in the distal portions of the host. (F) Example of bending of bubble walls; pinching out of bubbles; and sintering where two bubble walls come into contact in distal host. (G) Example of fractured bubble walls that have undergone subsequent viscous recovery. (Hi) Sintered trapped ash shard in a compacted bubble in distal host. (Hii) Image with enhanced contrast: dashed yellow lines indicate darker rinds preserving old collapsed bubbles and host microlite (red lines). (I) Stretching, pinching and compaction of bubbles, along with sintering of melt, in distal host with minimal bubble alignment.



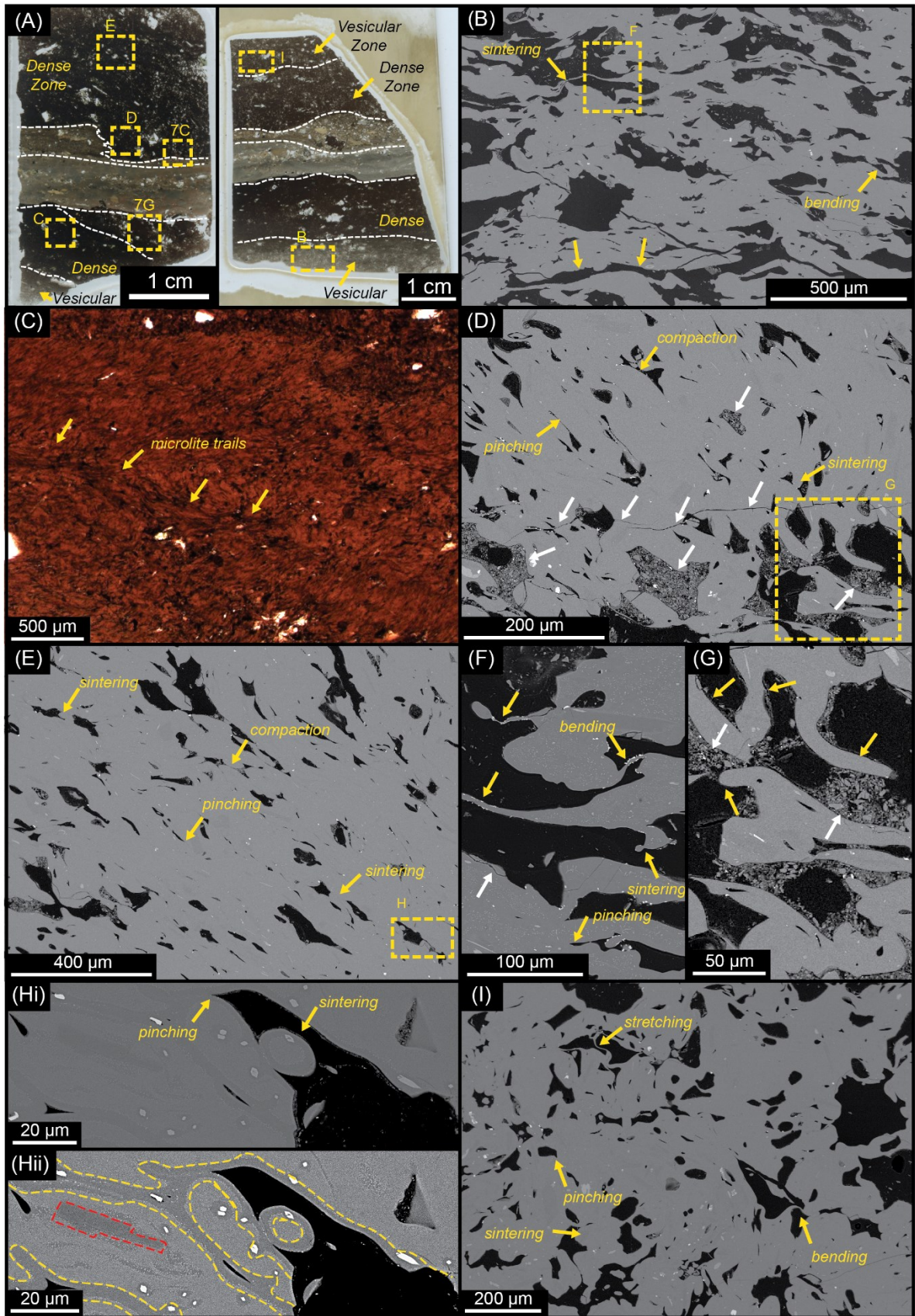


Figure 3:

Images of typical textures in V1. Yellow arrows highlight textural features. Overview of vein in thin sections one (A) and two (B). (C) Photomicrograph of poorly-sorted, angular clasts of host material (dashed yellow lines). Matrix ash infills voids in host at interface (arrows). (D) BSE image of angular clasts in vein with crystals fragments (arrows). (E) Large rectangular banded (arrows) clast set in a matrix of angular clasts (dashed lines). (F) Vesicular clast that has undergone degree of compaction. (G) Complete crystals more commonly found in clasts rather than isolated. Ash matrix shards sinter to larger clasts (arrows). (H) Clast preserves a ~40  $\mu\text{m}$ -wide band of fully-compacted and sintered shards, nanolites record their outlines. Arrows indicate sintering matrix ash to clast.



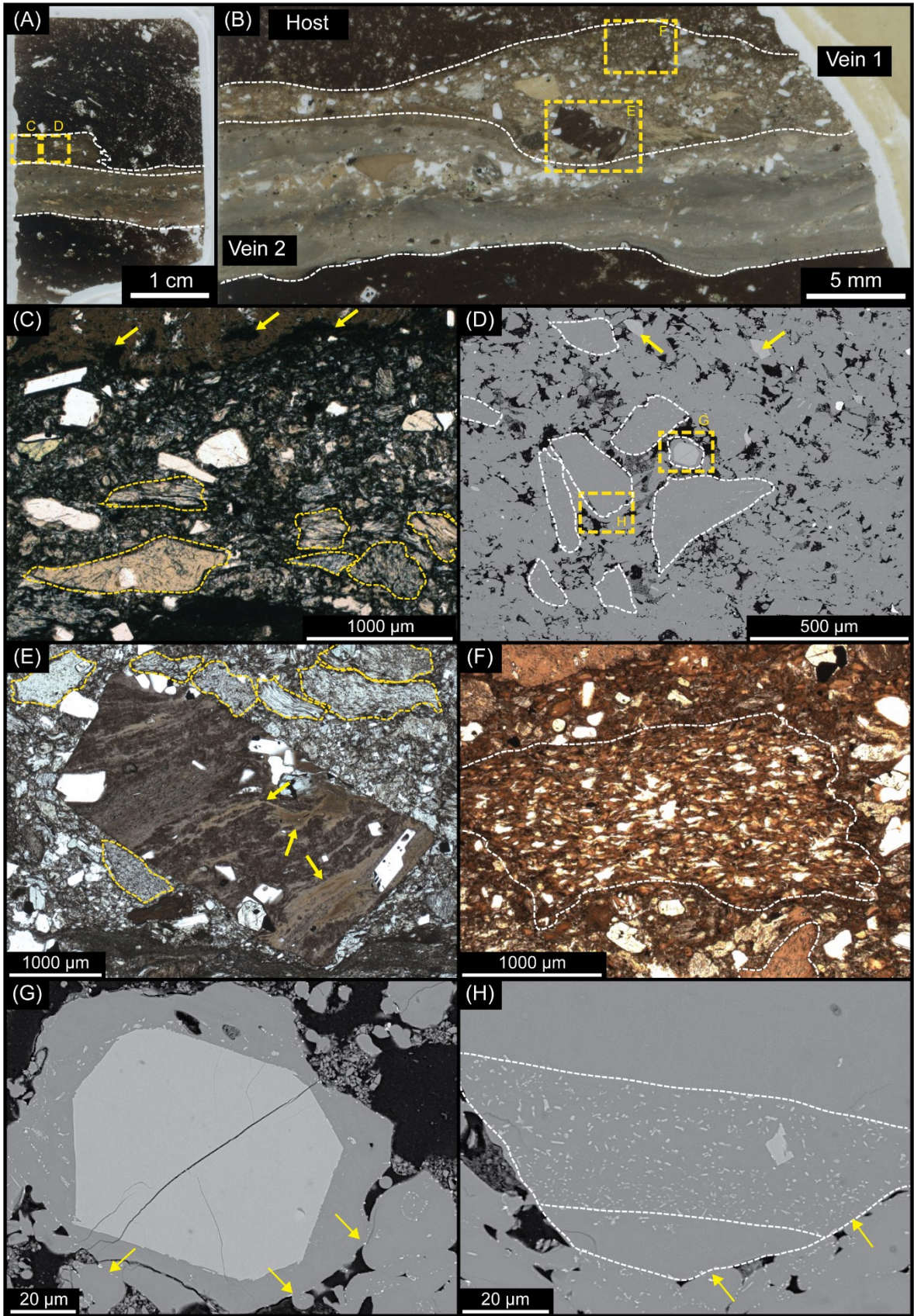


Figure 4:

Images of typical textures in V2. Yellow arrows highlight textural features. Overview of vein in thin sections one (A) and two (B). (B) Concentration of coarse clasts visible in centre of vein. Banding of fine- and coarse-grained ash is noted in rest of vein. (C) Nanolites commonly found on edges of larger, angular clasts as well as matrix shards. Arrows indicate where matrix has filled in void in a clast. (D) Angular clast that preserves old banding (arrows). Ash matrix laminations compact around clast. (E) Fine- and coarse-grained laminations have differing degrees of sintering and porosity. (F) Microlites found in matrix ash shards. Edges of shards made apparent by microlite chains.



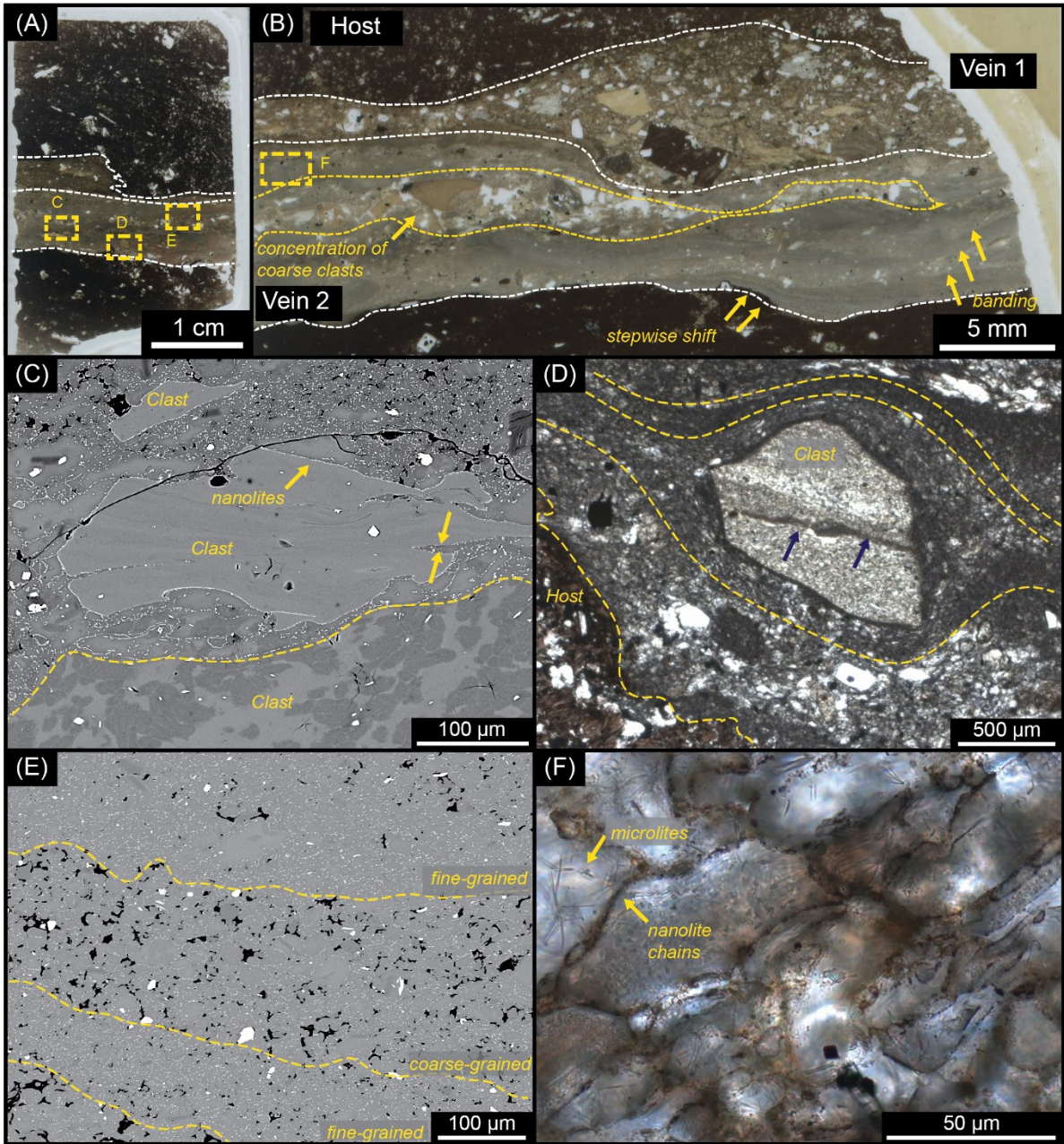


Figure 5:

Textures found at V1-host interface. Overview of vein in thin section one (A). (B) Photomicrograph mosaic of V1-host boundary, vein material becomes finer and harder to distinguish near interface. (C) Photomicrograph of isolated host material in vein and ash material infilling bubbles that are aligned with microlites. (D) Individual ash shards sintered together, boundaries defined by nanolites, ash material infilling host voids (arrows). (E) BSE overview image showing connectivity of bubbles in 3D. Ash matrix fills certain bubbles but not all further from interface. Evidence of compaction of bubbles near interface and infilling along a general alignment. Injection veins partially infill bubbles off main alignment. (F) Partial infilling of bubbles by sintered, rounded ash shards. Neighbouring open bubbles show incomplete connection of bubble network in 3D. (G) Ash matrix infills large, open, parallel-oriented bubbles isolating interstitial host material and incorporating host into vein as clasts. (H) Vein walls are not parallel but rounded. Inset: enhanced contrast image showing subtle greyscale variations between host, matrix material and  $<5\ \mu\text{m}$  of host wall. (I) Bubble walls have compacted around larger tuffisite clasts (yellow dashed lines). (J) Some bubbles completely filled with shards, nanolites found at shard interfaces (arrows).



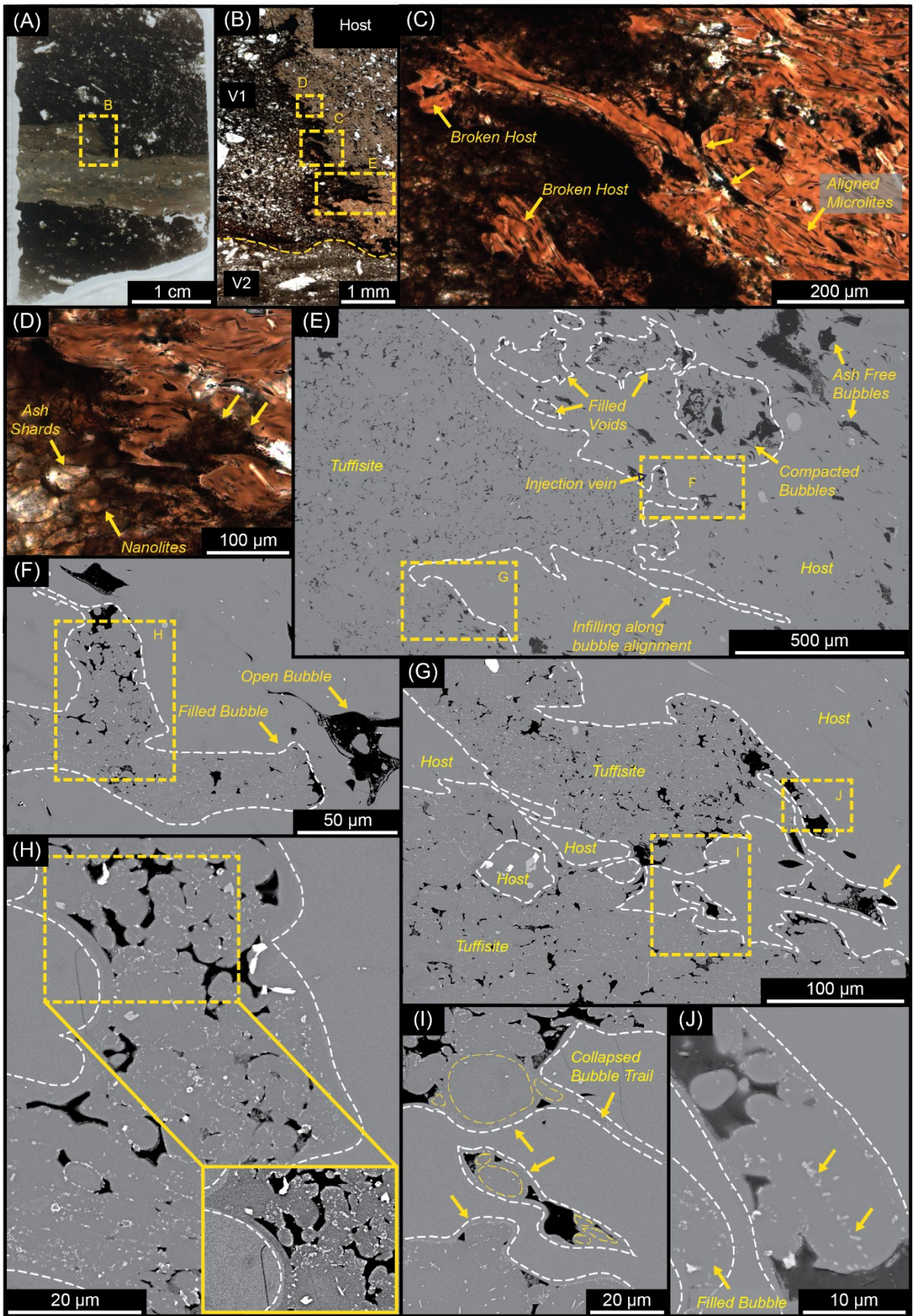




Figure 6:

Textures found at V2-host interface. Overview of vein in thin sections two (A). (B) BSE overview image of stepwise shift. Tuffisite matrix partially infills bubbles <math><150 \mu\text{m}</math> into host material. Bubbles in host heavily compacted and pinched out. (C) Angular, coarsely-grained material (yellow dashed lines) at bottom of step feature. Clasts fill and block bubbles. (D) Nanolite chains extend from pinched out bubbles near V2-host interface.

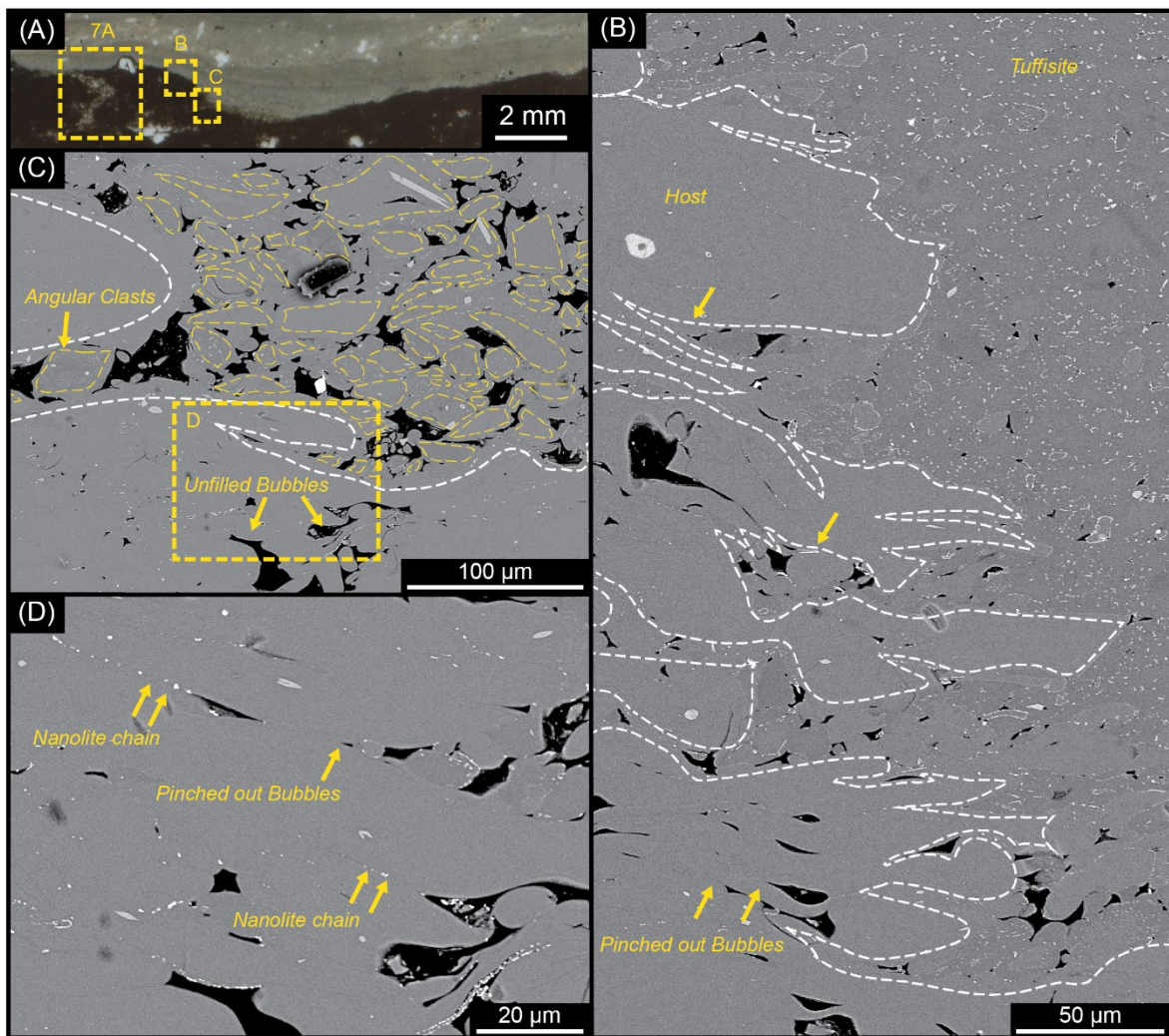




Figure 7:

Examples of injection veins and fracturing into host material. (A) Fracture with angular uneven walls within host material. Arrows indicate compaction of host and vein material around crystal near boundary. (B) Fracture feature made more apparent in BSE image by angular, poorly sorted clasts with higher interstitial porosity than the tuffisite vein or host. (C) Injection vein into vesicular host material whose bubble orientation does not align with tuffisite vein orientation. (D) Void space partially filled with sintered ash and angular clasts. Arrows indicate broken bubble walls at edges of void space. (E) Angular clast of host material with microlites (red dashed lines). Ash material sintered to clast edges. (F) Sintered ash material connected to bubble walls of void. Shard fractured due to sample preparation. Small angular ash material infills parts of void. (G) Vesicular clast found in host material (see Fig. 2A for location). Zone of host comprised of angular clasts. (H) Clasts have vesicle textures similar to host material.

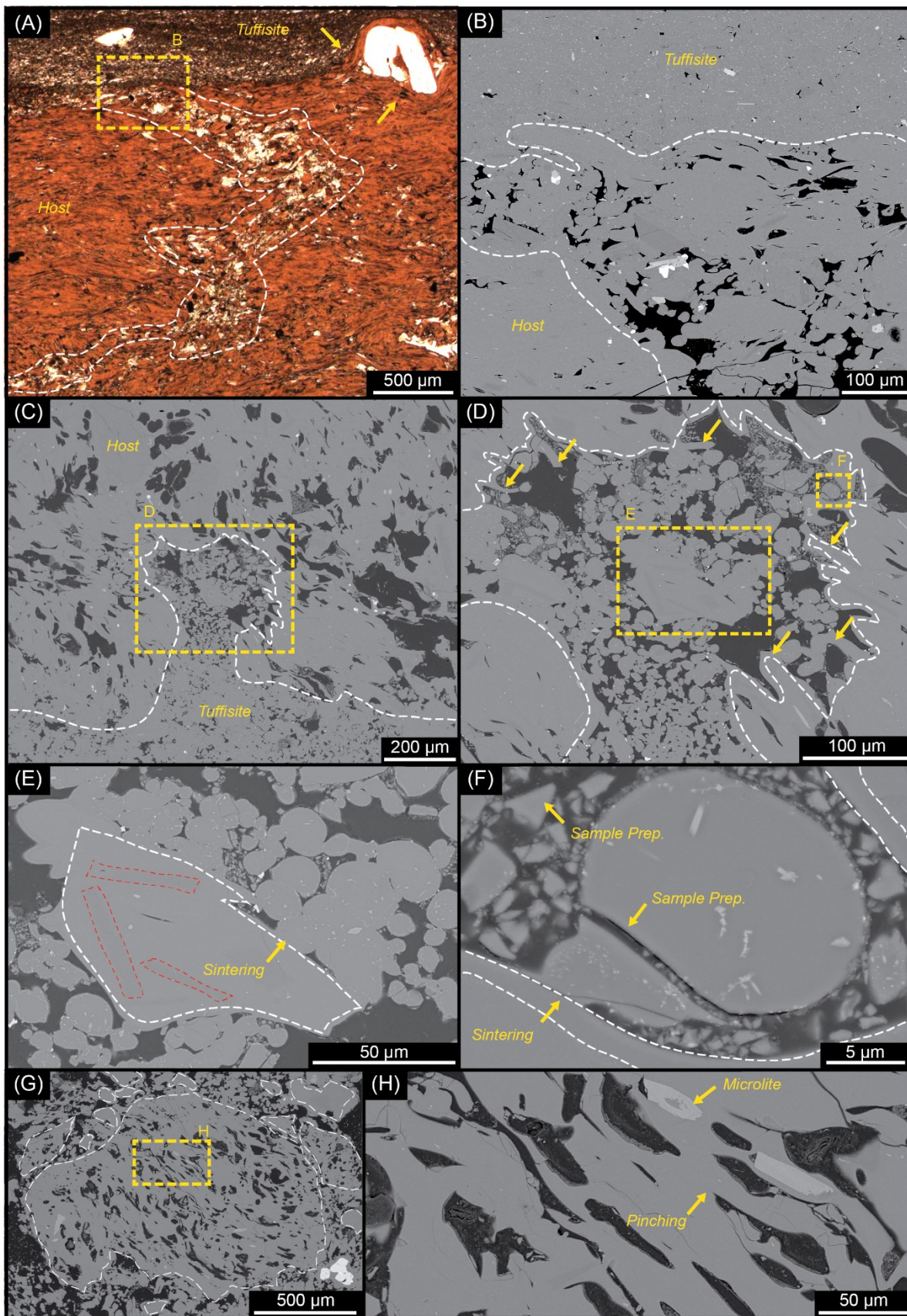




Figure 8:

Annotated compositional maps and BSE image showing sintered ash shards in a small <25  $\mu\text{m}$ -wide, partially-healed vein (dashed white lines). Colours represent relative element abundances with brighter colours representing a higher elemental abundance. Collapsed bubbles and the vein material are surrounded by a <5  $\mu\text{m}$ -wide rind that has lower relative Mg, Ca and Fe abundances. Sintered ash shards are also depleted in Mg, Ca and Fe. Na or K show no depletions in the vein. Microlites of plagioclase (Plag), clinopyroxene (CPX), orthopyroxene (OPX) and oxides in the host and within sintered ash shards are made apparent by their differing chemical composition to the silicic melt. Angular shards fill certain void spaces and have anomalous Na, Ca and Mg abundances.

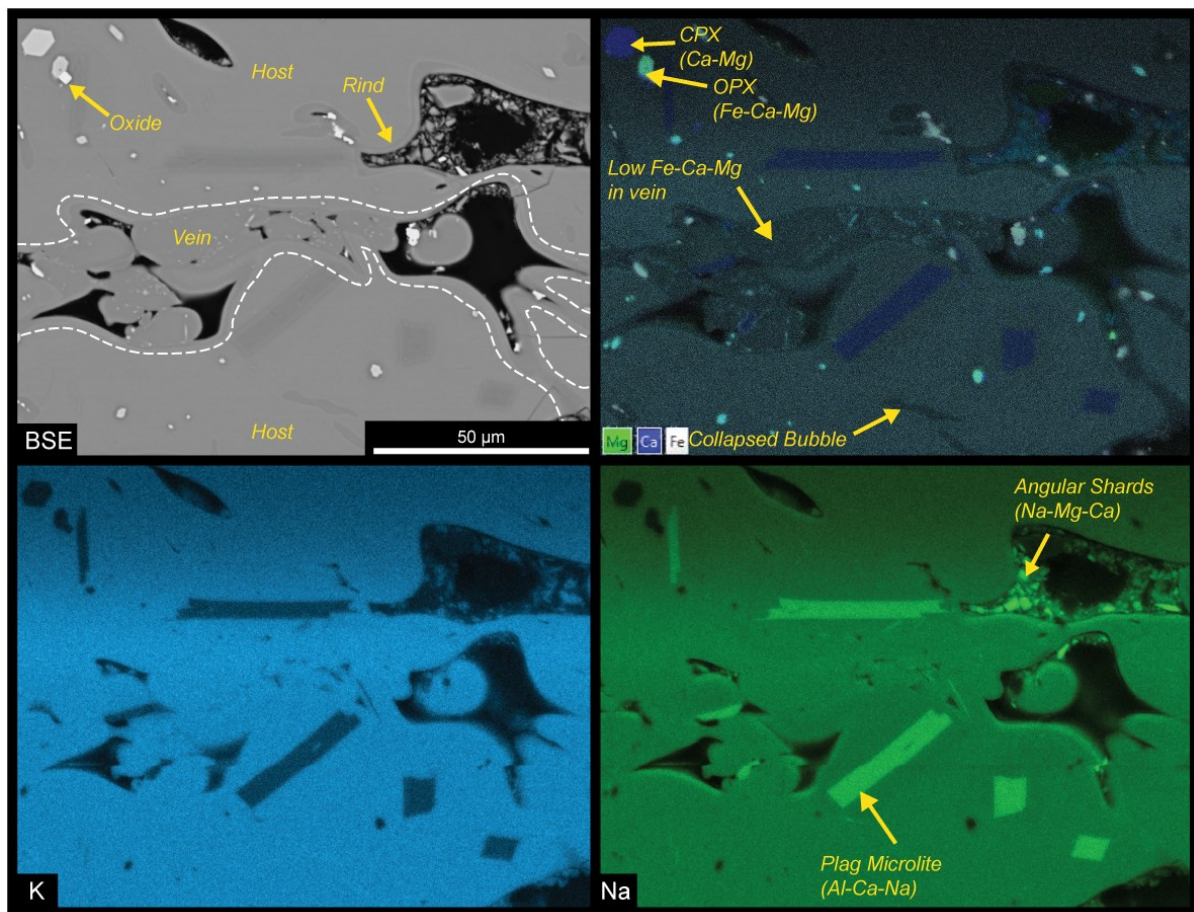


Figure 9:

Calculated timescales of rounding/sintering of particles as a function particle radius and H<sub>2</sub>O concentrations of the melt. The healing time is a combined rounding plus sintering time and is double the values shown here (see text).

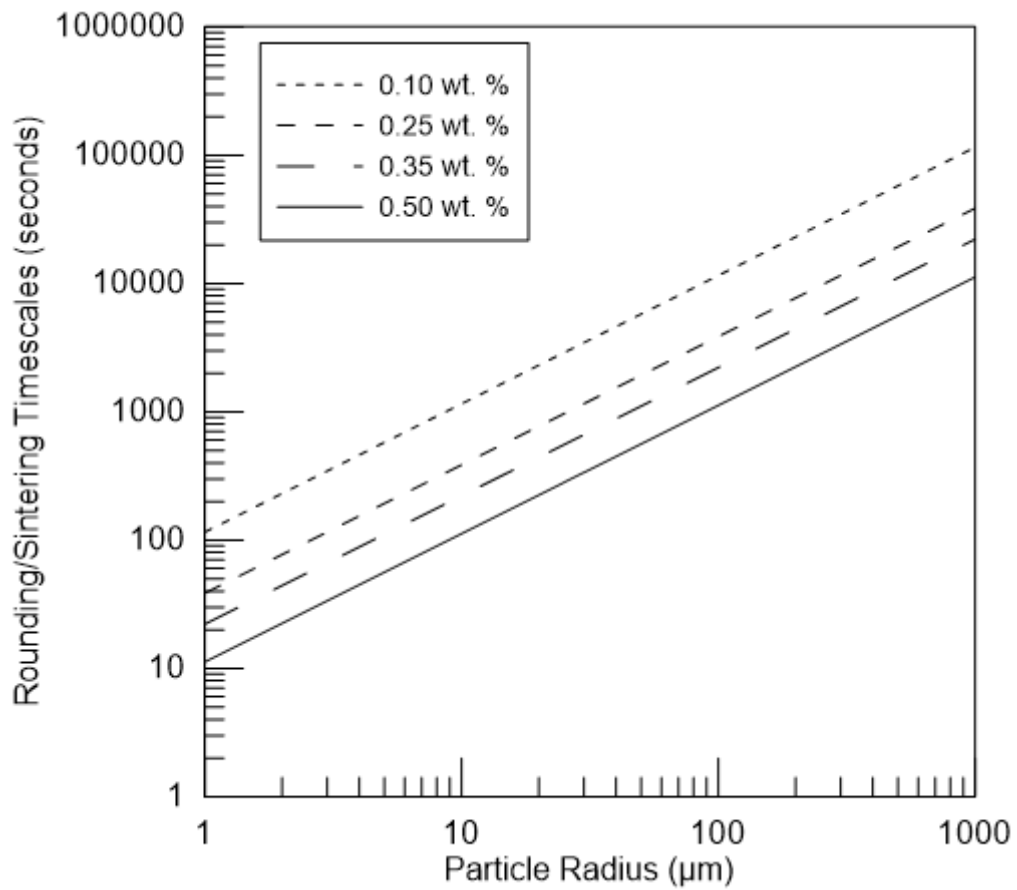
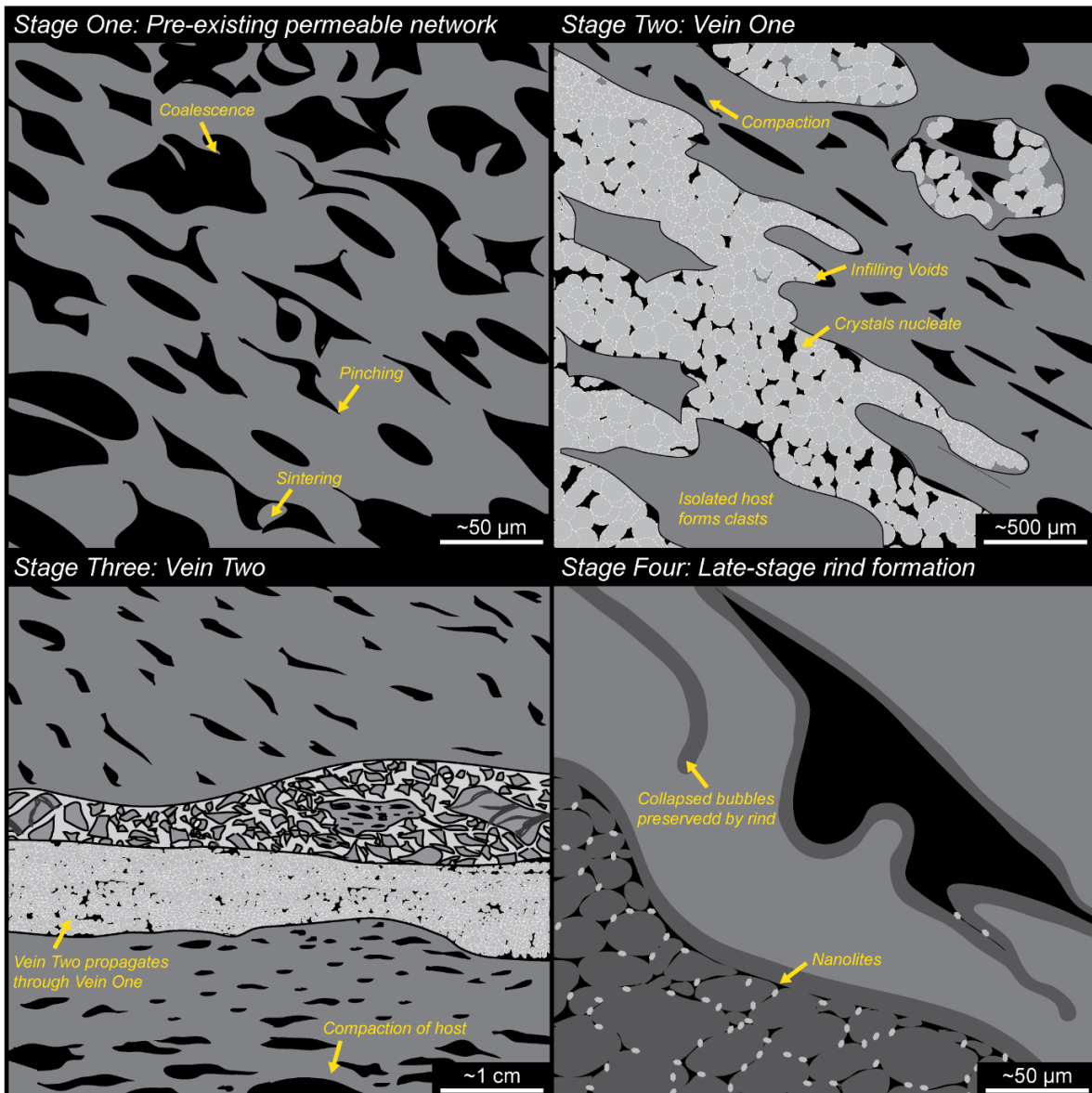


Figure 10:

Schematic summary of the four key stages of fracturing and degassing. Stage One: A pre-existing network of pore spaces is developed via the coalescence of bubbles and fracturing and sintering of melt. Stage Two: Fracturing and injection of ash shards through the pre-existing networks results in the formation of Vein One. Gases exploits the open network of pore spaces and fracturing between bubble walls aids in vein propagation and formation of vein clasts. Stage Three: After a short period of healing (minutes) a secondary fracturing event propagates through the partially healed V1 and results in the deposition of fine- and coarse-grained ash and the formation of V2. V2 undergoes <30 minutes of healing time before the sample was ejected as a bomb and quenched. Stage Four is a period of rind formation via elemental exchange between the gas and melt that likely occurs concurrently with gas fluxing and sintering prior to quenching. The formation of nanolites is tied to this exchange process.



## 10. Supplementary Figures

Figure S.1:

BSE image (top) and corresponding compositional map (bottom) of sintered ash intruding into bubbles within the host. Colours relate to specific elements with brighter colours indicating a higher relative abundance; Fe = red, Ca= green, Mg = blue. Crystal fragments within the vein are hard to decipher in BSE images but are clearer in compositional maps (green and red crystals), along with nanolites (green and blue) in and around sintered shards. Subtle depletions in Mg, Ca and Fe of bubble rinds and smaller ash material in vein are apparent.



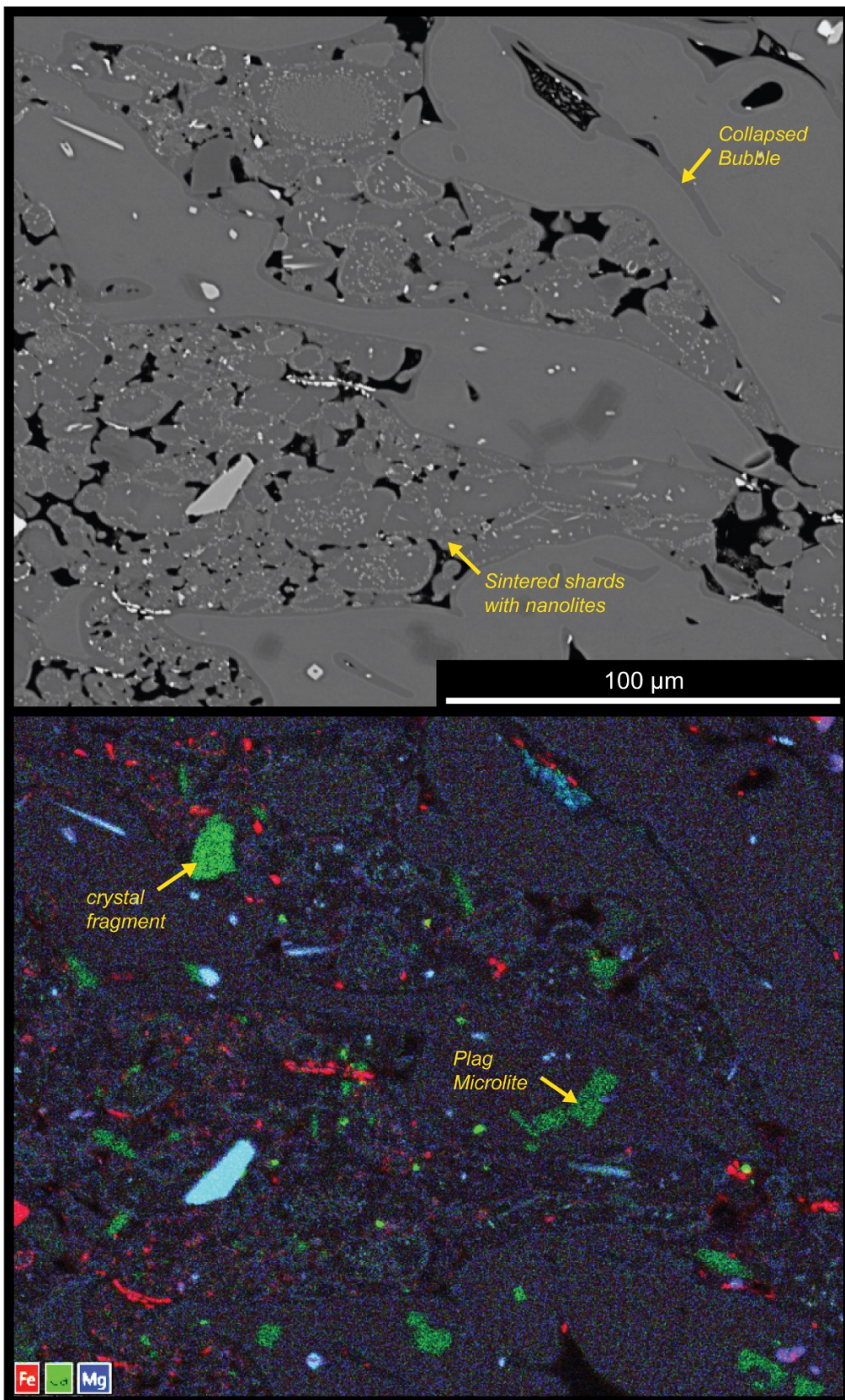
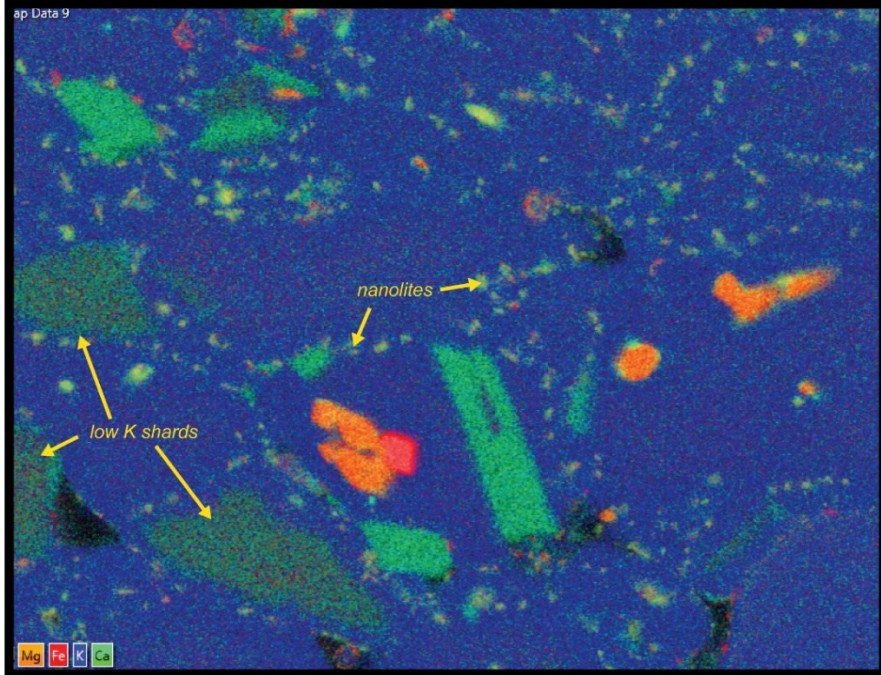
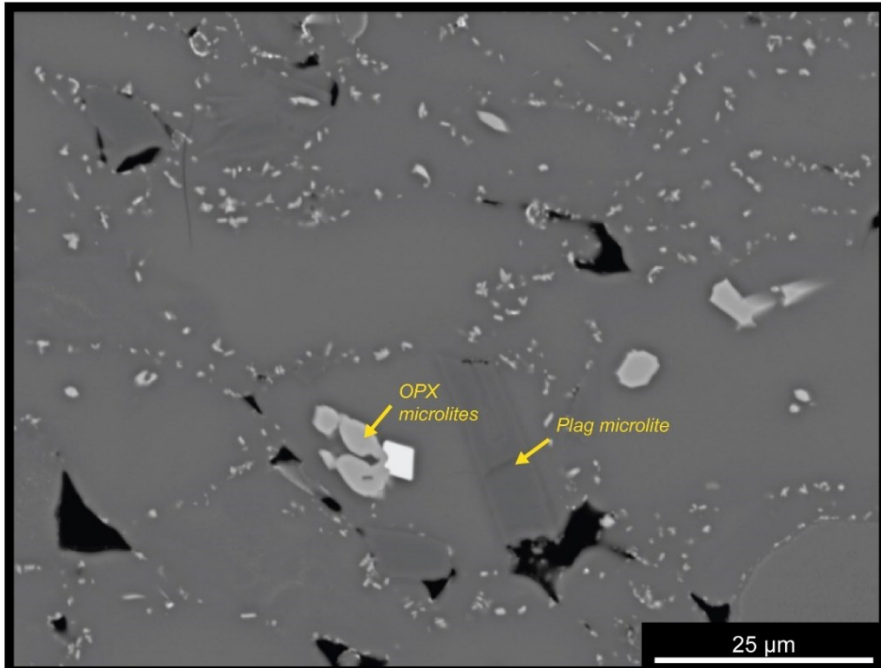




Figure S.2:

BSE image (top) and corresponding compositional map (bottom) of sintered ash within the tuffisite vein. Colours relate to specific elements with brighter colours indicating a higher relative abundance; Mg = orange, Fe = red, K = blue, Ca = green. Nanolites of OPX between sintered shards are elevated in Ca, Mg and Fe. Rare shards with relatively lower K abundances are found within the vein. Microlites can be preserved within the sintered shards.



## General Conclusions

### 1. Major Findings

The recent eruptions at Chaitén and Cordon Caulle demonstrated a need to understand how processes that occur in the volcanic conduit (e.g. fracturing and degassing) facilitate outgassing and influence eruptive behaviour. In this thesis I used textural and chemical techniques that span a wide range of analytical scales (dm-nm) to better constrain these processes. This approach was effective as questions that remained unresolved after one technique could be answered by another method. For example, taking a chemical approach allows for an understanding of where volatile metals are scavenged from or resorbed/adsorbed by silicic melts within the conduit, processes that cannot be constrained texturally. Similarly, assessing fracturing at multiple scales constrained its role in both generating tuffisite material (clasts and matrix) at the micron-scale and creating transient pathways along which material is fluxed to the surface at the dm-scale. Overall, I show fracturing and degassing processes are intimately linked. The key conclusions of this thesis are as follows:

- At a bulk-vein scale trace elements record gas streaming through fractures and the interaction of gases with the transported clasts at both Chaitén and Cordon Caulle. However a degassing signature is not preserved in the  $^{210}\text{Pb}$ - $^{226}\text{Ra}$  isotope record. The disparity between these geochemical signals is due to the brevity of the degassing events (<day) and the relative volumes of degassing magma and tuffisite veins (conduit-wide degassing reservoirs required for typical sized, cm-to-m-wide veins).

- The lack of preserved  $^{210}\text{Pb}$  enrichments in the tuffisite veins is used to place an upper limit on the degree of gas transport by fractures from deeper, gas-rich magmatic foams. For example, the mass ratio between veins and their reservoirs had to be  $<4,500$  (Chapter One, Figure 6) at Chaitén given their approximate lifespans. The isotope model used to constrain this can be applied to future isotope studies at other volcanic centres and highlights the need for longer durations of degassing through veins to result in  $^{210}\text{Pb}$  enrichments.
- Physical processes other than degassing are chemically preserved within tuffisite veins. These include preferential transport of glass over crystals in veins at Cordon Caulle, and the incorporation of non-juvenile material, that has undergone its own degassing and crystallisation history, into veins at Chaitén. This highlights the need to study a wide suite of trace elements and not just volatiles.
- Chemical and textural variability is strongly correlated at Cordon Caulle. Significant metal scavenging by the gas phase occurred within permeable gas fluxing zones and is preserved as depletions in metals in vein and breccia matrices. The extensive and systematic variations of volatile elements (e.g. Li, Rb, Cs, Cu, Zn, Pb, Tl and Bi) highlights how trace elements can be used as an alternate method for assessing degassing in systems that are depleted in  $\text{H}_2\text{O}$  and  $\text{CO}_2$ .
- At Cordon Caulle, deep and early degassing events were on the order of minutes, whilst fluxing near to the surface, in the waning phases of the eruption, occurred for hours at a time. These correlate with observations made of the eruption and is the first study to

be able to put time constraints on sub-surface, syn-eruptive processes during this eruption.

- Fractures will exploit any pre-existing permeable network, such as connected bubbles. During fracturing and vein propagation, host material can become incorporated into the vein as large, angular clasts and matrix ash. The clast textures can preserve previous fracturing and healing events.
- The intersection of permeable and connected void spaces by fractures allows for the efficient outgassing of melt over a cm-scale and will result in compaction and degassing of the source. The intersection of magmatic foams (or vesicular melts) by tuffisite veins is necessary for fractures to be an efficient mechanism for degassing.

In conclusion, this thesis has furthered the understanding of sub-surface processes that can contribute and control rare but hazardous behaviour at silicic volcanic centres. This is a key step to mitigating the impacts of eruptions. In the event of future high-silica eruptions, research presented here allows for a greater understanding of potential volcanic hazards associated with transitional eruptive behaviour and how this behaviour can evolve (e.g. timings of blasting and jetting events, trace volatiles that may that be degassed). A wider theoretical knowledge base, in turn, allows for the improved communication of potential impacts to relevant community groups and better preparations to minimise the risk to the affected populous.

## 2. Contributions to Original Knowledge

The work presented in each of the chapters in this thesis sheds new light on our understanding of degassing via fracturing using different and novel techniques and methods. Chapter One represents the first  $^{210}\text{Pb}$ - $^{226}\text{Ra}$  isotope study on tuffisite veins and on rhyolitic deposits. It is the first study to also do bulk trace element analyses on tuffisites. It highlights how the two types of analyses in combination can be used to understand the complete history of a tuffisite vein and its interaction with surrounding gas, melt and country rock. Chapter Two represents the first study to chemically constrain degassing processes at Cordon Caulle. Prior to this study little had been discussed as studies with a focus on water concentrations by other scientists had not been fruitful. The chapter highlights an alternate approach to assessing degassing processes. Chapter Three addresses a fundamental question of how tuffisites interact with deeper volatile, vesicular magmas. By focusing on the interaction between fracture and bubble networks; two permeable networks that are traditionally focused on in isolation, we better understand the complexities of syn-eruptive fracturing. These chapters all describe models (e.g. isotope disequilibria modelling) and analytical strategies (e.g. combined textural and LA-ICP-MS diffusion profiling) that can be used, and built upon, to further constrain eruption dynamics of other high-silica systems. In summary, each chapter addresses important questions using novel techniques and provides a more cohesive understanding of syn-eruptive processes (e.g. fracturing and degassing) that occur in silicic systems.

All three chapters assess samples from the 2011-2012 Cordon Caulle eruption. This thesis as a whole enhances our understanding of the spatial and temporal evolution of the conduit plug that was confined between a shallow laccolith and a growing rhyolite flow. Early in the eruption

fracturing processes at depth sourced gas and ash from porous and connected networks. Brecciation of magma formed short-lived permeable pathways through the upper conduit channelling gases towards the surface where vent structures allowed for outgassing. Gases carried and juxtaposed material of differing volatile contents, recording the long-range transport of clasts. As the eruption progressed fracture pathways in the extensively brecciated and heterogeneous conduit plug were open for longer, allowing for extended periods of outgassing from stable sub-vents and the progressive depletion of volatiles from the magma, likely contributing to the decline in explosive behaviour. Degassing processes during this eruption largely scavenged metals from zones that underwent gas fluxing, a chemical signature contrary to those preserved in tuffisite veins from the 2008 Chaitén eruption. This observation expands our understanding of how gases interact with the transported clasts and how the depth of the degassing regime influences the preserved trace chemical signatures. The 2011-2012 eruption at Cerdón Caulle was only the second rhyolite eruption scientifically observed in detail, providing an opportunity to greatly improve our understanding of syn-eruptive processes and their influence on eruptive behaviour in high-silica systems. The key conclusions of my thesis address this and show how fracturing and degassing processes evolved, and were preserved, during this silicic eruption.

### **3. Topics for Further Research**

Although considerable research has been undertaken into magma fracturing and degassing in the last decade, many outstanding questions remain. From a textural perspective, there is evidence from the Cordón Caulle eruption that tuffisite textures vary with time during eruption, which could reflect a changing and developing volcanic plug. This would be an exciting avenue of research to explore as currently many tuffisite textures have been noted at different volcanic centres but they have yet to be related to timing of fracturing during different phases of an eruption. Studies with time-constrained ejecta would be useful to address the changing role of fracturing with eruption duration.

From a chemical perspective, further work into the behaviour of trace elements during outgassing of high temperature volcanic gases from rhyolitic eruptions would directly link studies like those described in this thesis to surface emissions. However, it must be noted this information is absent primarily down to lack of rhyolitic eruptions and the hazards associated with sampling. Experimental studies furthering our understanding of the diffusion of trace elements in melts would aid in their use as timescale indicators, allowing for more precise estimates to be made. Advances have been made into trace metal gas-melt partitioning behaviour. Further constraining the changing behaviour of elements with ligands (e.g. Cl, S, and F) would aid degassing studies as volcanic gas compositions vary with volcano. If future studies continue to combine the textural and chemical preservation of fracturing and degassing with permeability and porosity studies, I envision the development of a cohesive, conceptual model of fracturing processes in the upper conduit during volcanic plug formation. This would be analogous to a “conduit is a tuffisite vein” model.



## References

- Berlo, K., Tuffen, H., Smith, V., Castro, J.M., Pyle, D.M., Mather, T.A., Geraki, K., 2013. Element variations in rhyolitic magma resulting from gas transport. *Geochimica et Cosmochimica Acta* 121, 436–451. <https://doi.org/10.1016/j.gca.2013.07.032>
- Berlo, K., Turner, S., 2010.  $^{210}\text{Pb}$ – $^{226}\text{Ra}$  disequilibria in volcanic rocks. *Earth and Planetary Science Letters* 296, 155–164. <https://doi.org/10.1016/j.epsl.2010.05.023>
- Berlo, K., Turner, S., Blundy, J., Black, S., Hawkesworth, C., 2006. Tracing pre-eruptive magma degassing using ( $^{210}\text{Pb}/^{226}\text{Ra}$ ) disequilibria in the volcanic deposits of the 1980–1986 eruption of Mount St. Helens. *Earth and Planetary Science Letters* 249, 337–349. <https://doi.org/10.1016/j.epsl.2006.07.018>
- Brown, S.K., Jenkins, S.F., Sparks, R.S.J., Odbert, H., Auker, M.R., 2017. Volcanic fatalities database: analysis of volcanic threat with distance and victim classification. *Journal of Applied Volcanology* 6, 15. <https://doi.org/10.1186/s13617-017-0067-4>
- Cabrera, A., Weinberg, R.F., Wright, H.M.N., 2015. Magma fracturing and degassing associated with obsidian formation: The explosive–effusive transition. *Journal of Volcanology and Geothermal Research* 298, 71–84. <https://doi.org/10.1016/j.jvolgeores.2014.12.014>
- Cashman, K.V., Sparks, R.S.J., 2013. How volcanoes work: A 25 year perspective. *Geological Society of America Bulletin* 125, 664–690. <https://doi.org/10.1130/B30720.1>
- Cassidy, M., Manga, M., Cashman, K., Bachmann, O., 2018. Controls on explosive-effusive volcanic eruption styles. *Nature Communications* 9, 2839. <https://doi.org/10.1038/s41467-018-05293-3>
- Castro, J.M., Bindeman, I.N., Tuffen, H., Ian Schipper, C., 2014. Explosive origin of silicic lava: Textural and  $\delta\text{D}$ – $\text{H}_2\text{O}$  evidence for pyroclastic degassing during rhyolite effusion.

- Earth and Planetary Science Letters 405, 52–61.  
<https://doi.org/10.1016/j.epsl.2014.08.012>
- Castro, J.M., Cordonnier, B., Tuffen, H., Tobin, M.J., Puskar, L., Martin, M.C., Bechtel, H.A., 2012. The role of melt-fracture degassing in defusing explosive rhyolite eruptions at volcán Chaitén. *Earth and Planetary Science Letters* 333–334, 63–69.  
<https://doi.org/10.1016/j.epsl.2012.04.024>
- Condomines, M., Sigmarsson, O., Gauthier, P.J., 2010. A simple model of  $^{222}\text{Rn}$  accumulation leading to  $^{210}\text{Pb}$  excesses in volcanic rocks. *Earth and Planetary Science Letters* 293, 331–338. <https://doi.org/10.1016/j.epsl.2010.02.048>
- Cunningham, H.S., Turner, S.P., Patia, H., Wysoczanski, R., Nichols, A.R.L., Eggins, S., Dosseto, A., 2009. ( $^{210}\text{Pb}/^{226}\text{Ra}$ ) variations during the 1994–2001 intracaldera volcanism at Rabaul Caldera. *Journal of Volcanology and Geothermal Research* 184, 416–426. <https://doi.org/10.1016/j.jvolgeores.2009.04.018>
- Edmonds, M., 2008. New Geochemical Insights into Volcanic Degassing. *Philosophical Transactions: Mathematical, Physical and Engineering Sciences* 366, 4559–4579.
- Eichelberger, J.C., 1995. Silicic Volcanism: Ascent of Viscous Magmas from Crustal Reservoirs. *Annu. Rev. Earth Planet. Sci.* 23, 41–63.  
<https://doi.org/10.1146/annurev.ea.23.050195.000353>
- Eichelberger, J.C., Carrigan, C.R., Westrich, H.R., Price, R.H., 1986. Non-explosive silicic volcanism. *Nature* 323, 598–602. <https://doi.org/10.1038/323598a0>
- Farquharson, J.I., Heap, M.J., Lavallée, Y., Varley, N.R., Baud, P., 2016. Evidence for the development of permeability anisotropy in lava domes and volcanic conduits. *Journal of Volcanology and Geothermal Research* 323, 163–185.  
<https://doi.org/10.1016/j.jvolgeores.2016.05.007>

- Gardner, J.E., Befus, K.S., Watkins, J., Hesse, M., Miller, N., 2012. Compositional gradients surrounding spherulites in obsidian and their relationship to spherulite growth and lava cooling. *Bulletin of Volcanology* 74, 1865–1879. <https://doi.org/10.1007/s00445-012-0642-9>
- Gauthier, P.-J., Condomines, M., 1999.  $^{210}\text{Pb}$ – $^{226}\text{Ra}$  radioactive disequilibria in recent lavas and radon degassing: inferences on the magma chamber dynamics at Stromboli and Merapi volcanoes. *Earth and Planetary Science Letters* 172, 111–126. [https://doi.org/10.1016/S0012-821X\(99\)00195-8](https://doi.org/10.1016/S0012-821X(99)00195-8)
- Gonnermann, H.M., Manga, M., 2003. Explosive volcanism may not be an inevitable consequence of magma fragmentation. *Nature* 426, 432–435. <https://doi.org/10.1038/nature02138>
- Heiken, G., Wohletz, K., Eichelberger, J., 1988. Fracture fillings and intrusive pyroclasts, Inyo Domes, California. *Journal of Geophysical Research: Solid Earth* 93, 4335–4350. <https://doi.org/10.1029/JB093iB05p04335>
- Henley, R.W., Berger, B.R., 2013. Nature's refineries — Metals and metalloids in arc volcanoes. *Earth-Science Reviews* 125, 146–170. <https://doi.org/10.1016/j.earscirev.2013.07.007>
- Hinkley, T.K., Le Cloarec, M.-F., Lambert, G., 1994. Fractionation of families of major, minor, and trace metals across the melt-vapor interface in volcanic exhalations. *Geochimica et Cosmochimica Acta* 58, 3255–3263. [https://doi.org/10.1016/0016-7037\(94\)90053-1](https://doi.org/10.1016/0016-7037(94)90053-1)
- Kendrick, J.E., Lavallée, Y., Varley, N.R., Wadsworth, F.B., Lamb, O.D., Vasseur, J., 2016. Blowing Off Steam: Tuffisite Formation As a Regulator for Lava Dome Eruptions. *Frontiers in Earth Science* 4:41. <https://doi.org/10.3389/feart.2016.00041>

- Kolzenburg, S., Heap, M.J., Lavallée, Y., Russell, J.K., Meredith, P.G., Dingwell, D.B., 2012. Strength and permeability recovery of tuffisite-bearing andesite. *Solid Earth* 3, 191–198. <https://doi.org/10.5194/se-3-191-2012>
- MacKenzie, J.M., Canil, D., 2008. Volatile heavy metal mobility in silicate liquids: Implications for volcanic degassing and eruption prediction. *Earth and Planetary Science Letters* 269, 488–496. <https://doi.org/10.1016/j.epsl.2008.03.005>
- Mather, T.A., Witt, M.L.I., Pyle, D.M., Quayle, B.M., Aiuppa, A., Bagnato, E., Martin, R.S., Sims, K.W.W., Edmonds, M., Sutton, A.J., Ilyinskaya, E., 2012. Halogens and trace metal emissions from the ongoing 2008 summit eruption of Kīlauea volcano, Hawai‘i. *Geochimica et Cosmochimica Acta* 83, 292–323. <https://doi.org/10.1016/j.gca.2011.11.029>
- Pallister, J.S., Diefenbach, A.K., Burton, W.C., Muñoz, J., Griswold, J.P., Lara, L.E., Lowenstern, J.B., Valenzuela, C.E., 2013. The Chaitén rhyolite lava dome: Eruption sequence, lava dome volumes, rapid effusion rates and source of the rhyolite magma. *Andean Geology* 40, 277–294. <https://doi.org/10.5027/andgeoV40n2-a06>
- Papale, P., Moretti, R., Barbato, D., 2006. The compositional dependence of the saturation surface of H<sub>2</sub>O+CO<sub>2</sub> fluids in silicate melts. *Chemical Geology* 229, 78–95. <https://doi.org/10.1016/j.chemgeo.2006.01.013>
- Plail, M., Edmonds, M., Humphreys, M.C.S., Barclay, J., Herd, R.A., 2014. Geochemical evidence for relict degassing pathways preserved in andesite. *Earth and Planetary Science Letters* 386, 21–33. <https://doi.org/10.1016/j.epsl.2013.10.044>
- Pokrovski, G.S., Borisova, A.Y., Bychkov, A.Y., 2013. Speciation and Transport of Metals and Metalloids in Geological Vapors. *Reviews in Mineralogy and Geochemistry* 76, 165–218. <https://doi.org/10.2138/rmg.2013.76.6>

- Saubin, E., Tuffen, H., Gurioli, L., Owen, J., Castro, J.M., Berlo, K., McGowan, E.M., Schipper, C.I., Wehbe, K., 2016. Conduit Dynamics in Transitional Rhyolitic Activity Recorded by Tuffsite Vein Textures from the 2008–2009 Chaitén Eruption. *Frontiers in Earth Science* 4:59. <https://doi.org/10.3389/feart.2016.00059>
- Schipper, C.I., Castro, J.M., Tuffen, H., James, M.R., How, P., 2013. Shallow vent architecture during hybrid explosive–effusive activity at Cordón Caulle (Chile, 2011–12): Evidence from direct observations and pyroclast textures. *Journal of Volcanology and Geothermal Research* 262, 25–37. <https://doi.org/10.1016/j.jvolgeores.2013.06.005>
- Sparks, R.S.J., 1978. The dynamics of bubble formation and growth in magmas: A review and analysis. *Journal of Volcanology and Geothermal Research* 3, 1–37. [https://doi.org/10.1016/0377-0273\(78\)90002-1](https://doi.org/10.1016/0377-0273(78)90002-1)
- Stasiuk, M.V., Barclay, J., Carroll, M.R., Jaupart, C., Ratté, J.C., Sparks, R.S.J., Tait, S.R., 1996. Degassing during magma ascent in the Mule Creek vent (USA). *Bulletin of Volcanology* 58, 117–130. <https://doi.org/10.1007/s004450050130>
- Tuffen, H., Dingwell, D., 2005. Fault textures in volcanic conduits: evidence for seismic trigger mechanisms during silicic eruptions. *Bulletin of Volcanology* 67, 370–387. <https://doi.org/10.1007/s00445-004-0383-5>
- Tuffen, H., Dingwell, D.B., Pinkerton, H., 2003. Repeated fracture and healing of silicic magma generate flow banding and earthquakes? *Geology* 31, 1089–1092. <https://doi.org/10.1130/G19777.1>
- van Hinsberg, V., Vigouroux, N., Palmer, S., Berlo, K., Mauri, G., Williams-Jones, A., Mckenzie, J., Williams-Jones, G., Fischer, T., 2015. Element flux to the environment of the passively degassing crater lake-hosting Kawah Ijen volcano, Indonesia, and implications for estimates of the global volcanic flux. *Geological Society, London, Special Publications* 437, 9–34. <https://doi.org/10.1144/SP437.2>

- Wei, L., Mosley-Thompson, E., Gabrielli, P., Thompson, L.G., Barbante, C., 2008. Synchronous deposition of volcanic ash and sulfate aerosols over Greenland in 1783 from the Laki eruption (Iceland). *Geophysical Research Letters* 35, L16501. <https://doi.org/10.1029/2008GL035117>
- Williams-Jones, A.E., Migdisov, A.A., Archibald, S.M., Xiao, Z., 2002. Vapor-transport of ore metals, in: *The Water-Rock Interactions, Ore Deposits, and Environmental Geochemistry: A Tribute to David A. Crerar*, Geochemical Society, Special Publications. pp. 279–305.
- Zhang, Y., Ni, H., 2010. Diffusion of H, C, and O Components in Silicate Melts. *Reviews in Mineralogy and Geochemistry* 72, 171–225. <https://doi.org/10.2138/rmg.2010.72.5>
- Zhang, Y., Ni, H., Chen, Y., 2010. Diffusion Data in Silicate Melts. *Reviews in Mineralogy and Geochemistry* 72, 311–408. <https://doi.org/10.2138/rmg.2010.72.8>
- Zhang, Y., Xu, Z., Zhu, M., Wang, H., 2007. Silicate melt properties and volcanic eruptions: SILICATE MELT PROPERTIES. *Reviews of Geophysics* 45, RG4004. <https://doi.org/10.1029/2006RG000216>